le cnam

Conservatoire national des arts et métiers

ÉCOLE DOCTORALE SCIENCES DES MÉTIERS DE L'INGÉNIEUR

Laboratoire Modélisation Mathématiques et Numérique - M2N

Thèse de doctorat

Présentée par : **Marthe DE CROUY-CHANEL**

Soutenue le : **4 juillet 2025**

Discipline : **Mathématiques appliquées et applications des mathématiques**

Spécialité : **Sciences pour l'ingénieur - Mathématiques appliquées**

SUBGRID-SCALE MODELING FOR TURBULENT FLOW SIMULATION WITH A REMESHED VORTEX METHOD

THÈSE dirigée par :
M. Iraj MORTAZAVI Professeur, M2N, CNAM

et co-encadrée par :
Mme. Chloé MIMEAU Maître de conférences, M2N, CNAM

Jury

M. Éric LAMBALLAIS	Professeur, Institut P', Université de Poitiers	Rapporteur
M. Spencer SHERWIN	Professeur, Department of Aeronautics, Imperial College London	Rapporteur
M. Guillaume BALARAC	Professeur, LEGI, Institut National Polytechnique de Grenoble	Examinateur
M. Simon MARIÉ	Maître de conférences, DynFluid, CNAM	Examinateur
M. Grégory PINON	Professeur, LOMC, Université Le Havre Normandie	Examinateur
Mme. Maria Vittoria SALVETTI	Professeur, DICI, Université de Pise	Examinatrice
M. Iraj MORTAZAVI	Professeur, M2N, CNAM	Directeur de thèse
Mme. Chloé MIMEAU	Maître de conférences, M2N, CNAM	Encadrante de thèse
M. Alessandro MARIOTTI	Professeur, DICI, Université de Pise	Invité

Remerciements

Un grand merci à Eric Lamballais et Spencer Sherwin pour avoir accepté d'être rapporteurs de cette thèse, leur relecture attentive et leurs retours très pertinents. Merci aux autres membres de mon jury, Guillaume Balarac, Simon Marié, Grégory Pinon, Maria Vittoria Salvetti et Alessandro Mariotti, d'avoir accepté d'évaluer mon travail. Merci en particulier à Guillaume et Simon d'avoir été membres de mon comité de suivi, cette thèse n'aurait pas été la même sans leur regard extérieur et leurs questions pertinentes qui ont orienté mon travail. Merci à Maria Vittoria et Alessandro d'avoir suivi mon travail tout au long de cette thèse et pour m'avoir très gentiment accueilli à Pise pendant deux semaines pour me former aux méthodes de quantification d'incertitude et rédiger notre premier article. Je suis honorée d'avoir un tel jury.

Cette thèse n'aurait jamais vu le jour sans ma super équipe d'encadrement. Merci à Iraj et Chloé, qui m'accompagnent depuis mon stage de master. Merci pour votre confiance et votre soutien tout au long de cette thèse, en particulier dans mes moments d'anxiété. Merci en particulier à Chloé pour sa relecture rigoureuse de tous mes travaux et pour toujours avoir sa porte ouverte quand j'avais une "petite" question. Je n'aurais pas pu rêver d'une meilleure encadrante et j'espère être la première d'une longue lignée de doctorants qu'elle encadrera.

Merci à mes compagnons de thèse, en particulier Azzeddine et Nicolas qui m'ont accompagné quasiment tout du long de l'aventure, entre pauses cafés et conférences tout autour de l'Europe. Merci aussi à toute la dream team du bureau des doctorants, Awa, Yasmine, Riccardo, Kashish, Boubacar, Houda et Lamine et les nombreux stagiaires qui ont partagé notre salle. Merci d'avoir créé une super ambiance inter-labos! C'était un plaisir de venir travailler tous les jours avec vous.

Merci à Sofia et Laure pour leur disponibilité et leur précieuse aide face à l'administration du CNAM et à Olivier pour son support technique et pour maintenir imathr940 sans lequel cette thèse n'aurait pas pu être faite. Merci à Chloé, Camilla, Cécile, Josselin, Sigrid, Arnaud, Myriam, Raissa et tous les membres du GBCM2N pour les grandes discussions aux pauses déjeuner, les verres au Léo du vendredi et pour mettre le feu (aucun lien avec la fermeture temporaire de la cantine) aux pots de soutenance et autres concerts de uku-guitare avec leur bonne humeur et leur inventivité. Je mesure la chance d'être dans un labo avec un si bonne ambiance et des membres aussi sympas!

Un grand merci à ma famille, à mes parents pour leur soutien constant et leur efforts pour comprendre mon sujet de thèse, à mes frères et soeurs, Jacques, François, Anne et Edith. C'est un bonheur de vous voir grandir et devenir de plus en plus des gens supers, je suis très fière de vous tous. Un merci tout particulier à Matidie et Papinus qui m'ont donné le goût de la science.

Merci à mes amis de Pontoise (et associés) pour les soirées nanards et jeux de société, les Quiplashs jusqu'à overdose, toutes les blagues et les références, et merci d'être là après toutes ces années. Merci à Yann pour ton humour et ta capacité à intégrer et améliorer toutes les soirées. Merci à Ted et Louis de nous accueillir si souvent à Asnières (avec des super plats!). Merci à Enora pour ta sensibilité et ta créativité et ta capacité à faire de ta vie une aventure passionnante. Merci plus général à Térence, Hélo, Théa et Axel. Merci aussi à Alyx et Edern de nous avoir accueilli lors d'un super weekend à Angoulême. Merci Mario pour tes mariosmes et ta passion pour des sujets étranges qui rend chaque conversation avec toi passionnante (pas merci pour m'avoir fait découvrir les variantes de sudoku et la perte de productivité qui en a résulté).

Merci à la bande de Jussieu pour les bières au Piano Vache et les vacances au bord de la Mayenne. J'ai énormément de chance de vous connaitre et vous avez été un grand soutien dans les moments difficiles de la thèse. Merci à Mathilde H. pour les soirées à Montreuil, les longues discussions téléphoniques, tous les films et livres que j'ai découvert grâce à elle, et pour cette amitié qui dure depuis cinq ans entre quatre villes différentes! Merci à Mathilde C., que j'ai rencontré par le hasard d'un dortoir berlinois et qui est maintenant une super amie, merci pour ton humour, ta franchise et ta passion douteuse pour les crânes. Merci à Charlène et Victor, c'est génial de vous voir évoluer depuis la licence et je suis très heureuse d'être toujours en contact avec vous malgré la distance (même si je doute que Victor soit vraiment parti en Allemagne tellement on le voit à Paris...). Merci aussi Charlène pour le super accueil à Vienne! Merci à Sara M. pour tous les concerts, ta sensibilité, ta gentillesse, ton enthousiasme et ton amitié. Merci à Céleste pour les BDs, ta passion et ton humour. Enfin merci à Robin (l'étoile de $\overset{*}{\searrow}$), Helen (et Tsuki) et Esther!

Merci à mes amis de la Cave, Nono, Henry, Simon, Jonjon (et Ted encore), qui sont toujours là pour rigoler ou débattre, virtuellement ou au Nid. Merci aussi à Hugo, Basile et toute la bande de Montreuil, au copains du CEA, Wissam, Grégoire et Lucas, à Roro, Sara P., Eleanor, Elliot et Blanche, Frederik et Sabrina et à mes amis de Vienne, Mikaela, Vittoria et Khachick.

Merci à Black Country, New Road d'avoir sorti leur dernier album pendant que j'étais en train d'écrire ce manuscrit, c'est très gentil de leur part.

Lors de cette thèse j'ai déménagé deux fois, merci à mes colocs successifs, Céleste (encore), Leo, Vittalia et Anna, pour m'avoir écouté râler sur mes simulations.

Enfin merci à Baptiste, mon meilleur ami et le meilleur coloc de tous pour ton amour, tes attentions et ton soutien au quotidien.

Abstract

Among the many numerical methods developed to simulate incompressible flows, particle or Lagrangian methods are well positioned thanks to their stability and low numerical diffusion in advection-dominated flows. The Navier-Stokes equations are solved by discretizing the problem's physical quantities on numerical particles following the fluid dynamics. Vortex methods, based on the vorticity-velocity formulation of the Navier-Stokes equations, belong to this class of Lagrangian methods. However, purely Lagrangian Vortex Methods suffer from issues such as particle distortion. Remeshed Vortex Methods (RVM), a hybrid Eulerian-Lagrangian approach, address these limitations by periodically repositioning particles on a fixed mesh. This hybridization enabled by the particle remeshing allows for the use of Eulerian methods in an initially Lagrangian algorithm.

This thesis investigates the applicability of RVM for Large Eddy Simulation (LES) of turbulent flows. While Direct Numerical Simulation (DNS), where all the flow's spatial and temporal scales are resolved, remains infeasible in most cases for high Reynolds numbers, LES offers a practical compromise between accuracy and cost by solving the large scales of the flow, the small scales being modeled by a subgrid-scale (SGS) model. The present work evaluates various subgrid-scale modeling strategies adapted to the vorticity-velocity formulation of the Navier-Stokes equations, assessing their performance across both isotropic and wall-bounded turbulent flows. Special attention is given to the models' sensitivity and calibration through uncertainty quantification techniques. The results highlight the potential of RVM as an effective tool for LES, especially for coarse resolutions, and delineates the limitations of modeling and calibration practices, particularly in complex flow configurations.

Keywords : Remeshed Vortex Methods, Turbulent flows, Large Eddy Simulation, Subgrid-Scale Modeling, Variational Multi-Scale, Spectral Vanishing Viscosity, Uncertainty quantification, Polynomial Chaos Expansion

Résumé

Parmi les nombreuses méthodes numériques développées pour simuler les écoulements incompressibles, les méthodes particulaires ou lagrangiennes sont bien positionnées grâce à leur stabilité et à leur faible diffusion numérique dans les écoulements dominés par l'advection. Les équations de Navier-Stokes sont résolues en discrétisant les quantités physiques du problème sur des particules numériques suivant la dynamique de l'écoulement. Les méthodes vortex, basées sur la formulation vorticité-vitesse des équations de Navier-Stokes, appartiennent à cette classe de méthodes lagrangiennes. Cependant, les méthodes vortex purement lagrangiennes présentent des problèmes tels que la distorsion du champs de particules. Les méthodes vortex remaillées (MVR), une approche hybride eulérienne-lagrangienne, permettent de pallier ces limitations en repositionnant périodiquement les particules sur une grille fixe. Cette hybridation permet l'utilisation de méthodes eulériennes dans un algorithme initialement lagrangien.

Cette thèse étudie l'applicabilité des MVR à la simulation des grandes échelles de la turbulence (ou Large Eddy Simulation (LES)). Alors que la simulation numérique directe, qui résout toutes les échelles spatiales et temporelles de l'écoulement, reste généralement irréalisable pour les nombres de Reynolds élevés, la LES offre un compromis pratique entre précision et coût en résolvant les grandes échelles de l'écoulement, les petites échelles étant modélisées par un modèle de sous-maille. Ce travail étudie différentes stratégies de modélisation des échelles de sous-maille adaptées à la formulation vorticité-vitesse des équations de Navier-Stokes, en évaluant leurs performances pour les écoulements turbulents isotropes et avec parois. Une attention particulière est portée à la sensibilité et à la calibration des modèles grâce à des méthodes de quantification des incertitudes. Les résultats soulignent le potentiel des MVR comme outil efficace pour la LES, notamment pour les résolutions grossières, et montrent les limites des pratiques de modélisation et de calibration, notamment dans les configurations d'écoulement les plus complexes.

Mots-clés : Méthodes vortex remaillées, Écoulements turbulents, Simulation des grandes échelles de la turbulence, Modélisation des échelles de sous-maille, Méthodes multi-échelles, Viscosité spectrale évanescente, Quantification des incertitudes, Chaos polynomial

Contents

List of Figures

List of Tables

Nomenclature

Operations

For $f : \mathbb{R}^d \to \mathbb{R}$, $\mathbf{u}, \mathbf{v} : \mathbb{R}^d \to \mathbb{R}^d$, $\mathbf{R} : \mathbb{R}^d \to \mathbb{R}^{d\times d}$,

- $\mathbf{u} \cdot \mathbf{v} = \sum\limits_{1\leq i\leq d} \mathbf{u}_i \mathbf{v}_i$
- $\mathbf{u} \times \mathbf{v} = \begin{cases} (\mathbf{u}_2\mathbf{v}_3 - \mathbf{u}_3\mathbf{v}_2, \mathbf{u}_3\mathbf{v}_1 - \mathbf{u}_1\mathbf{v}_3, \mathbf{u}_1\mathbf{v}_2 - \mathbf{u}_2\mathbf{v}_1)^T & d = 3 \\ (0, 0, \mathbf{u}_1\mathbf{v}_2 - \mathbf{u}_2\mathbf{v}_1)^T & d = 2 \end{cases}$
- $\mathbf{u} \otimes \mathbf{v} = (\mathbf{u}_i \mathbf{v}_j)_{1\leq i,j\leq d}$
- $\nabla f = \left(\frac{\partial f}{\partial \mathbf{x}_i}\right)_{1\leq i\leq d}$
- $\nabla \mathbf{u} = \left(\frac{\partial \mathbf{u}_i}{\partial \mathbf{x}_j}\right)_{1\leq i,j\leq d}$
- $\nabla \cdot \mathbf{u} = \sum\limits_{1\leq i\leq d} \frac{\partial \mathbf{u}_i}{\partial \mathbf{x}_i}$
- $\nabla \cdot \mathbf{R} = (\sum\limits_{1\leq j\leq d} \frac{\partial \mathbf{R}_{ij}}{\partial \mathbf{x}_j})_{1\leq i\leq d}$
- $\nabla \times \mathbf{u} = \begin{cases} \left(\frac{\partial \mathbf{u}_3}{\partial \mathbf{x}_2} - \frac{\partial \mathbf{u}_2}{\partial \mathbf{x}_3}, \frac{\partial \mathbf{u}_1}{\partial \mathbf{x}_3} - \frac{\partial \mathbf{u}_3}{\partial \mathbf{x}_1}, \frac{\partial \mathbf{u}_2}{\partial \mathbf{x}_1} - \frac{\partial \mathbf{u}_1}{\partial \mathbf{x}_2}\right)^T & d = 3 \\ \left(0, 0, \frac{\partial \mathbf{u}_2}{\partial \mathbf{x}_1} - \frac{\partial \mathbf{u}_1}{\partial \mathbf{x}_2}\right)^T & d = 2 \end{cases}$
- $\Delta f = \nabla \cdot (\nabla f) = \sum\limits_{1\leq i\leq d} \frac{\partial^2 f}{\partial \mathbf{x}_i^2}$
- $\Delta \mathbf{u} = (\Delta \mathbf{u}_i)_{1\leq i\leq d}$
- $(\mathbf{u} \cdot \nabla)\mathbf{v} = (\sum\limits_{j=1}^{d} \mathbf{u}_j \frac{\partial \mathbf{v}_i}{\partial \mathbf{x}_j})_{1\leq i\leq d}$

In the following, Einstein's notation for sums will be used.

Physical quantities

Coefficients

- ν - kinematic viscosity
- Re - Reynolds number
- Ra - Rayleigh number
- Pr - Prandtl number

Scalars

- ω - vorticity (scalar)
- p - pressure

Vectors

- $\mathbf{u}$ - velocity
- $\boldsymbol{\omega} = \nabla \times \mathbf{u}$ - vorticity (field)
- $\overline{\mathbf{u}}$ - (grid-) filtered velocity
- $\overline{\boldsymbol{\omega}}$ - (grid-) filtered vorticity
- $\widehat{\overline{\mathbf{u}}}$ - (test-) filtered velocity
- $\widehat{\overline{\boldsymbol{\omega}}}$ - (test-) filtered vorticity

Tensors

- $\mathbf{S} = \frac{1}{2}(\nabla \mathbf{u} + \nabla \mathbf{u}^T)$ - Strain-rate tensor
- τ - Subgrid stress tensor
- $\mathbf{R}$ - Subgrid scale vorticity stress

Acronyms

- CFD - Computational Fluid Dynamics
- CFL - Courant–Friedrichs–Lewy
- CPU - Central Processing Unit
- DES - Detached Eddy Simulations
- DNS - Direct Numerical Simulation
- FD - Finite Differences
- FFT - Fast Fourier Transform
- FLOPS - Floating-Point Operations Per Second
- FV - Finite Volumes
- GPC - Generalized Polynomial Chaos
- GPU - Graphic Processing Unit
- HIT - Homogeneous Isotropic Turbulence
- HPC - High Performance Computing
- IBM - Immersed Boundary Method
- ILES - Implicit Large Eddy Simulation
- KH - Kelvin-Helmholtz
- LBM - Lattice-Boltzmann Method
- LCFL - Lagrangian Courant–Friedrichs–Lewy
- LES - Large Eddy Simulation
- NS - Navier-Stokes
- ODE - Ordinary Differential Equation
- PCE - Polynomial Chaos Extension
- PDF - Probability Density Function
- PS - Pseudo-Spectral
- PSE - Particle Strength Exchange
- RANS - Reynolds-Averaged Navier-Stokes equations
- RK - Runge-Kutta
- RVM - Remeshed Vortex Method
- SEV - Spectral Eddy Viscosity
- SGS - SubGrid-Scale
- SVV - Spectral Vanishing Viscosity
- TGV - Taylor-Green Vortex

- TKE - Turbulent Kinetic Energy
- UQ - Uncertainty Quantification
- VIC - Vortex-In-Cell
- VM - Vortex Method
- VMS - Variational Multi-Scale
- VPM - Vortex Particle Method
- VPMM - Vortex Particle-Mesh Method
- VTE - Vorticity Transport Equation
- WALE - Wall-Adapting Local Eddy-viscosity

Introduction

Motivation

Accurately modeling turbulent flow is one of the most important and challenging problem in computational fluid dynamics (CFD), as turbulence plays a critical role in a wide range of applications—from minimizing aerodynamic drag in aircraft and automobiles, to predicting pollutant dispersion in the atmosphere, and ensuring the structural stability of buildings and bridges under wind or water loads. While Direct Numerical Simulation (DNS), where all spatial and temporal scales of turbulence are resolved is the most precise approach, it becomes computationally infeasible for flows at high Reynolds numbers typical in real-world engineering problems [CS10].

For that reason, techniques such as Reynolds-Averaged Navier-Stokes equations (RANS) and Large Eddy Simulation (LES) are widely used to reduce the cost of turbulent flow simulation. RANS models average the effects of turbulence over time, making them computationally efficient and suitable for steady-state problems. LES, on the other hand, resolves large turbulent structures while modeling only the smaller scales and offers a good compromise between accuracy and computational cost. Although RANS is favored in industry due to its low cost, LES is becoming increasingly viable outside of academic research as computation becomes more energy efficient and accessible [Zhi15]. Current research in Large Eddy Simulation (LES) explores several interconnected areas. One key focus is the complex interaction between numerical and artificial diffusion, with the rise in popularity of implicit LES (ILES) [GMR07]. Other active areas include the sensitivity of the subgrid-scale models to their parameters and their calibration [XC19], as well as the emerging field of data-driven turbulence modelling [NLdLK21].

A major challenge in LES is the development of robust, low-dissipation numerical methods that can accurately capture the resolved large-scale structures of the flow. This must be done in tandem with the design of effective SGS models. Importantly, LES modeling is inherently coupled with the numerical scheme: the performance and evaluation of SGS models cannot be separated from the numerical methods used to simulate the resolved scales.

In this context, Vortex Methods are particularly well positioned. Although they are among the oldest approaches for solving the Navier–Stokes equations for incompressible flows, they remain relatively underused and less widely known. They solve the vorticity-velocity formulation of the Navier-Stokes equations by discretizing the vorticity field on numerical particles advected with the flow. The velocity is then recovered as the solution of a Poisson equation. Derived in the 1920s [Pra28], they have been developed since the 1970s and still occupy an important place in computational fluid dynamics (CFD) thanks to their precision in the description of advection-dominated flows, their stability and reduced numerical diffusion. Recent developments in high performance computing (HPC) and especially the use of GPUs in scientific computing

increased the interest in particle methods as they are well adapted to this kind of architecture [RBCK10, Eta14] due to their highly parallelizable nature. In particular, in Vortex Methods the timestep is not constrained by the grid size, making high resolution simulations more affordable.

However, purely Lagrangian Vortex Methods suffer from the distortion of particles distribution in the computational domain and also face difficulties to handle boundary conditions and diffusion effects. To remedy to these drawbacks, Remeshed Vortex Methods were introduced. Remeshed Vortex methods (RVM) [KL95] can be seen as the semi-Lagrangian, or hybrid, variant of these approaches. In RVM, particles are regularly repositioned or "remeshed" on a fixed Cartesian grid to control their positions. This remeshing step enables the introduction of Eulerian methods in an initially Lagrangian algorithm, which allows to tackle the diffusion step and the Poisson equation in a more efficient way than in the purely Lagrangian approach. This method combines the advantages of Lagrangian and Eulerian schemes, and because of its low diffusivity property [CK00], represents a good candidate to perform Large Eddy Simulations of turbulent flows. Furthermore, RVM is based on the vorticity-velocity formulation of the Navier-Stokes equations, thus directly handling vorticity, a key component in turbulent flows.

Works using the Remeshed Vortex Methods have long focused on academic flows, and in the last decades have started to be applied to more realistic flows, from optimization of fish schooling [GHK14, NVA+17] to turbulent flows past aircraft [CCB+08, CBD+17, CCW20] and wind turbines [CBWK13, CDZ+17, CDC+17], as well as sediment flows [Kec19]. Still, works applying the RVM to turbulent flows are rare and few study have been made on the comparative performance of subgrid-scale models in this context, and none for our present RVM algorithm.

This thesis thus aims to assess the capacity of Remeshed Vortex Methods to handle Large Eddy Simulations of turbulent flows, starting from homogeneous isotropic flows and continuing with more complex wall-bounded flows. Different subgrid-scale modeling strategies, adapted to the present vorticity-velocity formulation will be assessed to find the ones that are the best adapted in this context. A particular attention is given to the sensitivity of the models to their coefficients and to changes in configurations. Indeed, in LES, uncertainties arising from Subgrid-Scale (SGS) modeling can interact in a complex manner with those related to the numerical discretization. Therefore, it is not guaranteed that model parameters calibrated for the classical velocity-based framework are suitable for the RVM as well. To evaluate the impact of the LES model coefficients on the simulations results, stochastic approaches based on the polynomial chaos expansion [XK02] are used.

Thesis structure

Figure 0.1 schematizes the structure of the thesis, which is as follow:

- Chapter 1 is dedicated to Vortex Methods, from their Lagrangian origin to the present hybrid Eulerian-Lagrangian Remeshed Vortex Method. The numerical method used throughout this work and its implementation in the `HySoP` library is described in details.

- Chapter 2 presents turbulence modeling, with a focus on Large Eddy Simulation and an overview of the main subgrid-scale models used in the literature for classical velocity-pressure formulation of the Navier-Stokes equations. An extensive literature review on

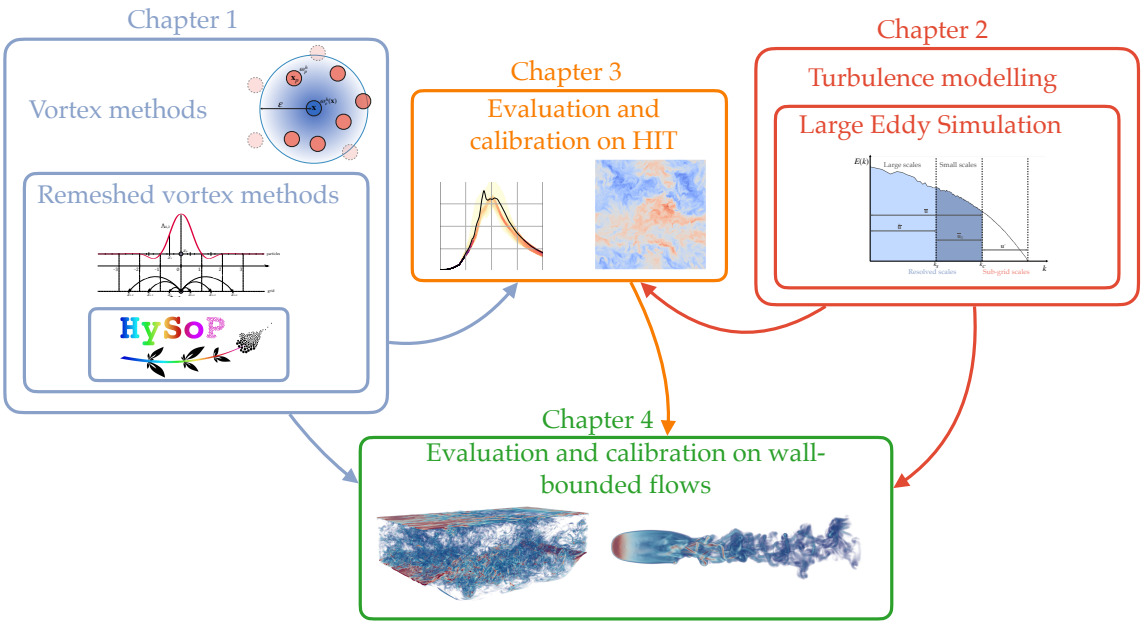

Figure 0.1: Overview of the thesis

subgrid-scale modeling for the present vorticity-velocity formulation is then conducted, and the capacity of the Remeshed Vortex Method for LES is assessed.

- Chapter 3 is an adaptation of a paper published in Computers&Fluids [dMM+24]: various subgrid-scale models from the ones presented in chapter 2 are evaluated on the Taylor-Green vortex benchmark and two of them are calibrated through an Uncertainty Quantification procedure. The calibration is shown to be robust to resolution and Reynolds numbers. The model are then evaluated on the decay of homogeneous isotropic turbulence.

- Chapter 4 is an extension of the work of chapter 3, which was limited to homogeneous isotropic turbulence, to more complex wall-bounded flows. Two cases are considered: a turbulent flow over periodic hills and a turbulent flow past a sphere. This chapter highlights the capacity of RVM for the simulation of wall-bounded turbulent flows, even with the limitation of a Cartesian grid, uniform by direction. However, the Uncertainty Quantification procedure proves to be limited in those contexts.

Chapter 1

Vortex Methods

Contents

Introduction

Fluid movements are described by the Navier-Stokes equations that are derived from the mass and momentum conservation laws. In fluid dynamics, the fluid can be considered from a Lagrangian point of view, where one follows the trajectory of individual fluid particles and we denote $\mathbf{x}(\mathbf{x}_0, t)$ the position of a particle with initial position $\mathbf{x}_0$ at time t. In the Eulerian perspective, however, the point of view is the one of an exterior fixed observer and the fluid is described by its velocity field $\mathbf{u}(\mathbf{x}, t)$ at point $\mathbf{x}$ and time t.

Both specifications are connected through the material derivative defined for a quantity f as

$$\frac{Df}{Dt} = \frac{\partial f}{\partial t} + \mathbf{u} \cdot \nabla f. \tag{1.1}$$

The material derivative represents the rate of variation of f following a fluid particle in the Lagrangian formalism. In this formalism, the advection term appears as a linear term, whereas in the Eulerian formalism, it is nonlinear.

This distinction leads to two different classes of numerical methods, namely the Eulerian and Lagrangian methods. The Eulerian methods (e.g. finite differences, finite volumes, finite elements, spectral methods, ...) are the most widely used. The velocity and pressure fields are discretized on a fixed grid or mesh. In a Lagrangian scheme (e.g. SPH methods [GM77], Vortex Methods), the approach is mesh-free and the flow is discretized using numerical particles whose positions vary over time and which carry local quantities such as momentum, vorticity, or density.

Vortex Methods, originally developed as Lagrangian approaches, follow this principle by discretizing the vorticity field on moving particles. They were first derived in the 1920s and are the first numerical methods used in fluid dynamics in the 1970s. Although the original formalism of the Vortex Methods is Lagrangian, very early, due to the inherent difficulties of handling a mesh-free method, versions of Vortex Methods integrating a Cartesian grid were developed in parallel with their Lagrangian counterpart and are today among the most popular families of Vortex Methods.

Our work is based on an hybrid Eulerian-Lagrangian Vortex Method, where the advection part of the Navier-Stokes equation is solved in a Lagrangian way and the other terms are solved in an Eulerian way, combining the advantages of both methods.

In this chapter we will give an overview of Vortex Methods, highlighting both fully Lagrangian and hybrid (or remeshed) approaches. We will then describe the specific numerical method and library used throughout this work.

1.1 Overview of Vortex Methods

This first section gives an overview of Vortex Methods, from their creation as purely Lagrangian methods to the hybrid Lagrangian-Eulerian schemes as the one used in this thesis, also called semi-Lagrangian schemes, and their applications.

1.1.1 Lagrangian Vortex Methods

1.1.1.1 Governing equations

Let us start from the adimensional incompressible Euler equations, with constant density, in their classical velocity($\mathbf{u}$)-pressure(p) formulation

$$\frac{\partial \mathbf{u}}{\partial t} + \mathbf{u} \cdot \nabla \mathbf{u} = -\nabla p \tag{1.2}$$

completed with the incompressibility condition

$$\nabla \cdot \mathbf{u} = 0 \tag{1.3}$$

as well as initial and boundary conditions.

Let us consider first the three dimensional case. By applying the curl operator to (1.2), we obtain

$$\nabla \times (\frac{\partial \mathbf{u}}{\partial t} + \mathbf{u} \cdot \nabla \mathbf{u}) = 0 \tag{1.4}$$

Introducing the vorticity $\boldsymbol{\omega}$, defined as the curl of the velocity

$$\boldsymbol{\omega} = \nabla \times \mathbf{u} = \begin{pmatrix} \partial_y \mathbf{u}_z - \partial_z \mathbf{u}_y \\ \partial_z \mathbf{u}_x - \partial_x \mathbf{u}_z \\ \partial_x \mathbf{u}_y - \partial_y \mathbf{u}_x \end{pmatrix}, \tag{1.5}$$

we can rewrite the above equation as

$$\frac{\partial \boldsymbol{\omega}}{\partial t} + \mathbf{u} \cdot \nabla \boldsymbol{\omega} - \boldsymbol{\omega} \cdot \nabla \mathbf{u} = 0. \tag{1.6}$$

This is the vorticity($\boldsymbol{\omega}$)-velocity($\mathbf{u}$) formulation of the incompressible Euler equations. Instead of only one non-linear term, we now have two: the vorticity advection term ($\mathbf{u} \cdot \nabla \boldsymbol{\omega}$) and the so-called "stretching" term ($\boldsymbol{\omega} \cdot \nabla \mathbf{u}$) representing the deformation of vortices in three-dimensional flows. This equation is completed by a Poisson equation

$$-\Delta \mathbf{u} = \nabla \times \boldsymbol{\omega}. \tag{1.7}$$

This equation is derived from the definition of vorticity and the incompressibility equation

$$\nabla \times \boldsymbol{\omega} = \nabla \times \nabla \times \mathbf{u} = \nabla(\nabla \cdot \mathbf{u}) - \Delta \mathbf{u} = -\Delta \mathbf{u}. \tag{1.8}$$

In two dimensions the curl operator is not properly defined, we use in the following the notation

$$\nabla \times \mathbf{u} = \begin{pmatrix} 0 \\ 0 \\ \partial_x \mathbf{u}_y - \partial_y \mathbf{u}_x \end{pmatrix} \tag{1.9}$$

and define $\omega = (\nabla \times \mathbf{u})_z$, keeping in mind that in this case ω is a scalar. The stretching term disappears and the vorticity-velocity Euler equation is now simply a scalar advection equation

$$\frac{\partial \omega}{\partial t} + \mathbf{u} \cdot \nabla \omega = 0. \tag{1.10}$$

As for the Poisson equation we now have

$$\nabla \times \nabla \times \mathbf{u} = \begin{pmatrix} \partial_y \omega \\ -\partial_x \omega \\ 0 \end{pmatrix} = \begin{pmatrix} \partial_x(\nabla \cdot \mathbf{u}) - \Delta \mathbf{u}_x \\ \partial_y(\nabla \cdot \mathbf{u}) - \Delta \mathbf{u}_y \\ 0 \end{pmatrix} = - \begin{pmatrix} \Delta \mathbf{u}_x \\ \Delta \mathbf{u}_y \\ 0 \end{pmatrix} \tag{1.11}$$

and the system to solve is

$$-\Delta \mathbf{u} = \begin{pmatrix} \partial_y \omega \\ -\partial_x \omega \end{pmatrix}. \tag{1.12}$$

1.1.1.2 2D Vortex Methods

The Vortex Method is one of the oldest approach in computational fluid dynamics, the calculations used to derive it dating back from 1928 [Pra28] and 1931 [Ros31]. The Vortex Method solves the 2D Euler equation (1.10) with a Lagrangian, i.e. meshless, approach. This

approach consists in discretizing the vorticity on a set $\mathcal{P}$ of numerical particles p characterized by their position $\mathbf{x}_p^h(t)$ at a given time t, their volume (assumed here to be constant in time) v_p and the vorticity they carry $\omega_p^h(t)$. ω is thus discretized at a given point $\mathbf{x}$ of the domain and a given time t as

$$\omega^h(\mathbf{x},t) = \sum_{p\in\mathcal{P}} \omega_p^h(t) v_p \delta(\mathbf{x} - \mathbf{x}_p^h(t)). \tag{1.13}$$

where δ is the Dirac distribution. From this discretization, we deduce the following set of Ordinary Differential Equations (ODEs)

$$\frac{d\mathbf{x}_p^h}{dt} = \mathbf{u}^h(\mathbf{x}_p^h(t),t) \tag{1.14}$$

$$\frac{d\omega_p^h}{dt} = 0. \tag{1.15}$$

This system of linear ODEs corresponds exactly to the Lagrangian discretization of the 2D Euler equation (1.10) given above. The first equation represents the evolution of the material position $\mathbf{x}_p$ of a particle (i.e. a fluid element) as a function of the velocity field $\mathbf{u}(\mathbf{x}_p,t)$. The second equation is a consequence of the Kelvin's circulation theorem stating that in an inviscid flow, the circulation around a closed curve moving with the fluid is constant with respect to time. As for the Poisson equation, it can be solved in a Lagrangian way through the following Biot-Savart law

$$\mathbf{u}^h = \mathbf{K}(\mathbf{x},\mathbf{x}') \star \omega(\mathbf{x}') + \mathbf{u}_\infty^h(\mathbf{x}) \tag{1.16}$$

where $\mathbf{K}$ is the rotational counterpart of G, Green's function for the Poisson equation, given by $G(\mathbf{x}) = -\frac{1}{2\pi}\ln(|\mathbf{x}|)$, such that

$$\mathbf{K} \star \boldsymbol{\omega} = \nabla \times (G \star \omega). \tag{1.17}$$

As previously said, this Lagrangian discretization allows to solve the non-linear incompressible Euler equations (1.10) as a system of linear ODEs (1.14)-(1.15). However, due to the Dirac distribution, this discretization is unaffordable in practise. For that reason, Chorin and Bernard introduced the Vortex blob method [CB73], where instead of being discretized at a single point, the vorticity is discretized on a disc of radius $\varepsilon > 0$. The Dirac distribution is then approximated by a mollified function ζ_ε of the form

$$\zeta_\varepsilon(x) = \frac{1}{\varepsilon^n}\zeta(\frac{x}{\varepsilon}) \tag{1.18}$$

where ζ is a symmetric smoothly decaying cutoff function and $n > 0$. The sequence $(\zeta_\varepsilon)_\varepsilon$ converges to the Dirac distribution δ as ε goes to 0. In that framework, and as represented in figure 1.1, the discretized vorticity is defined as

$$\omega_\varepsilon^h(\mathbf{x},t) = \sum_{p\in\mathcal{P}} \omega_p^h(t) v_p \zeta_\varepsilon(\mathbf{x} - \mathbf{x}_p^h(t)). \tag{1.19}$$

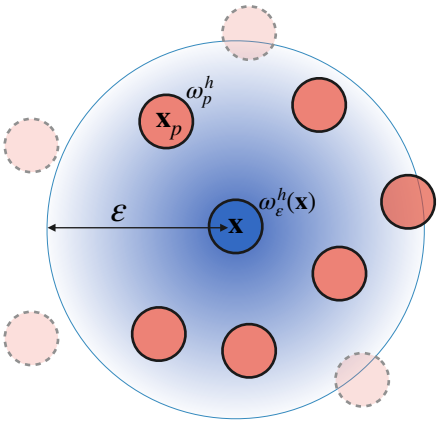

Figure 1.1: Illustration of the Vortex blob method. The gradient of color around the particle p represents the value of $\zeta_\varepsilon(\mathbf{x}_p - \mathbf{x})$. The vorticity at point $\mathbf{x}$ is approximated as the sum of the local circulations of the particles at a distance ε of $\mathbf{x}$.

1.1.1.3 3D Vortex Methods

In three dimensions, the vorticity is now a 3-dimensional vector and the stretching term appears in the Euler equations. The first 3D Vortex Methods are the filament Vortex Methods, introduced by Leonard [Leo75b, Leo80]. The vorticity is discretized on deformable lines or tubes that form closed path or extend to infinity. Then, according to Kelvin's theorem and Helmholtz's first theorem, the vorticity circulation is constant along those filaments as in 2D and there is thus no need to include the stretching component of the vorticity equation. However, these methods have many flaws: they are difficult to initialize, require "surgeries" to remove tiny loops and the inclusion of a diffusion term is not straightforward [CK00].

On the other hand, the Vortex particle method, formalized by Anderson and Greengard [AG85] and Cottet [Cot88] can be seen as a more direct, despite less physically natural, extension of the two-dimensional Vortex Method. The fluid is discretized on particles carrying the vorticity. Using the same discretization as above, the ODEs to solve are now

$$\frac{d\mathbf{x}_p^h}{dt} = \mathbf{u}^h(\mathbf{x}_p^h(t), t) \tag{1.20}$$

$$\frac{d\boldsymbol{\omega}_p^h}{dt} = \boldsymbol{\omega}_p^h \cdot \nabla \mathbf{u}^h(\mathbf{x}_p, t). \tag{1.21}$$

Discretizing the spatial derivative from (1.21) by using the Vortex blob framework, we obtain (omitting the superscript h for clarity)

$$(\partial_{\mathbf{x}_i}\mathbf{u}(\mathbf{x}))_\varepsilon = \sum_{p\in\mathcal{P}} v_p \partial_{\mathbf{x}_{p_i}}\mathbf{u}(\mathbf{x}_p)\zeta_\varepsilon(\mathbf{x}-\mathbf{x}_p) \tag{1.22}$$

and by using that we are sufficiently distant from the boundary and the symmetry of ζ_ε,

$$\sum_{p\in\mathcal{P}} v_p \partial_{\mathbf{x}_{p_i}}\mathbf{u}(\mathbf{x}_p)\zeta_\varepsilon(\mathbf{x}-\mathbf{x}_p) = -\sum_{p\in\mathcal{P}} v_p \mathbf{u}(\mathbf{x}_p)\partial_{\mathbf{x}_{p_i}}\zeta_\varepsilon(\mathbf{x}-\mathbf{x}_p) = \sum_{p\in\mathcal{P}} v_p \mathbf{u}(\mathbf{x}_p)\partial_{\mathbf{x}_i}\zeta_\varepsilon(\mathbf{x}-\mathbf{x}_p) \tag{1.23}$$

and thus (1.21) is solved with

$$\frac{d\boldsymbol{\omega}_p}{dt} = \sum_{1\leq i\leq 3} \boldsymbol{\omega}_p^i \partial_i \mathbf{u}(\mathbf{x}_p) = \sum_{1\leq i\leq 3, q\in\mathcal{P}} \boldsymbol{\omega}_p^i v_q \mathbf{u}(\mathbf{x}_q) \partial_i \zeta_\varepsilon(\mathbf{x}_p - \mathbf{x}_q). \tag{1.24}$$

As for the Poisson equation, it is solved in the same way with a Biot-Savar law, with now $G(\mathbf{x}) = (4\pi|x|)^{-1}$.

1.1.1.4 Viscous Vortex Methods

So far we have only considered the Euler equations. However, to be able to simulate turbulent flows, it is essential to be able to represent viscous effects. To that effect, we now consider the Navier-Stokes equations in their dimensionless vorticity-velocity formulation in 2D,

$$\frac{\partial \omega}{\partial t} + \mathbf{u}\cdot\nabla\omega - \frac{1}{Re}\Delta\omega = 0 \tag{1.25}$$

$$-\Delta\mathbf{u} = \begin{pmatrix} \partial_y \omega \\ -\partial_x \omega \end{pmatrix}, \tag{1.26}$$

or in 3D,

$$\frac{\partial \boldsymbol{\omega}}{\partial t} + \mathbf{u}\cdot\nabla\boldsymbol{\omega} - \boldsymbol{\omega}\cdot\nabla\mathbf{u} - \frac{1}{Re}\Delta\boldsymbol{\omega} = 0 \tag{1.27}$$

$$-\Delta\mathbf{u} = \nabla\times\boldsymbol{\omega}, \tag{1.28}$$

where Re is the Reynolds number, a dimensionless quantity characterizing the fluid's regime defined as

$$Re = \frac{UL}{\nu} \tag{1.29}$$

with U the characteristic flow velocity, L the characteristic length and ν the fluid's kinematic viscosity. In the following of this section we will consider the 2D case but the methods presented can be extended to the 3D case.

Several types of Vortex Methods were used to treat the diffusion term in a purely Lagrangian framework, starting from the Random Walk method, introduced by Chorin [Cho73]. In this approach, a viscous splitting method is used, dividing one timestep of the algorithm in two sub-steps: the convection step, where the inviscid equations (1.14) and (1.15) are first solved, and then the diffusion step, where the equations solved are

$$\frac{d\mathbf{x}_p^h}{dt} = 0 \tag{1.30}$$

$$\frac{d\omega_p^h}{dt} = \frac{1}{Re}\Delta\omega(\mathbf{x}_p). \tag{1.31}$$

In the Random Walk approach, once the inviscid advection equation is solved, the diffusive effects are modeled by imposing a Brownian motion to the particles by updating the particle's positions with

$$\mathbf{x}_p^{n+1} = \mathbf{x}_p^n + \Delta t\mathbf{u}(\mathbf{x}_p^n) + \xi_p^n \tag{1.32}$$

where ξ_p^n are Gaussian independent random variables with mean 0 and variance $2\Delta t/Re$. As the number N of particles grows, the particle field converges to the Green's function, solution of the diffusion equation. This method is able to conserve the total circulation of the fluid flow and can handle flows around complicated boundaries. However, due to its probabilistic nature, it can lead to noisy solutions. Furthermore, its convergence is only of order $O(1/\sqrt{N})$ and to obtain a good accuracy, a high number of particles is needed, leading to a high computational cost.

A common deterministic approach is the Particle Strengh Exchange (PSE) method [DMG89], based on the idea that diffusion induces a change in the vorticity strength of the particles. The second-order operator $\Delta\omega_p$ is approximated by an integral operator, better suited for particle methods. Let us consider the mollified kernel $\eta_\varepsilon = \varepsilon^2\eta(\mathbf{x}/\varepsilon)$ with η satisfying for some order r

$$\begin{cases} \int x_i x_j \eta(\mathbf{x})d\mathbf{x} = 2\delta_{ij} & i,j = 1,2 \\ \int x_1^{i_1} x_2^{i_2}\eta(\mathbf{x})d\mathbf{x} & \text{if } i_1+i_2 = 1 \text{ or } 3 \le i_1+i_2 \le r+1 \\ \int |\mathbf{x}|^{r+2}|\eta(\mathbf{x})|d\mathbf{x} < \infty & \end{cases} \tag{1.33}$$

then for

$$\Delta_\varepsilon\omega(\mathbf{x}) = \varepsilon^{-2}\int(\omega(\mathbf{y})-\omega(\mathbf{x}))\eta_\varepsilon(\mathbf{y}-\mathbf{x})d\mathbf{y} \tag{1.34}$$

and if $\omega \in W^{r+2,p}(\mathbb{R}^2)$ for some $p \in [1,\infty[$, we have the following estimate

$$\|\Delta_\varepsilon\omega - \Delta\omega\|_{0,p} \le C\varepsilon^r\|\omega\|_{r+2,p}. \tag{1.35}$$

A proof can be found in [CK00]. Replacing $\Delta\omega$ by $\Delta_\varepsilon\omega$ and replacing the integral by a numerical quadrature, we obtain the following scheme for equation (1.31)

$$\frac{d\omega_p^h}{dt} = \frac{1}{Re}\varepsilon^{-2}\sum_{q\in\mathcal{P}}(v_q\omega_q^h - v_q\omega_p^h)\eta_\varepsilon(\mathbf{x}_q^h - \mathbf{x}_p^h). \tag{1.36}$$

This scheme is deterministic and does not require a viscous splitting, however, because of the quadrature used to approximate the integral, it requires a large particle overlapping leading to a large computational cost for flows with small vorticity scales, especially in three dimensions. Other deterministic approaches to treat the diffusion term in a purely Lagrangian way have been explored (see a review in [MM21]) but they all suffer from the necessity to maintain a permanent particle overlapping.

1.1.2 From Lagrangian Vortex Methods to Hybrid Lagrangian-Eulerian Vortex Methods

1.1.2.1 Particle field distortion issues

Because the vorticity field is discretized on particles and not on fixed grid point, it is essential for these particles to be representative of the flow, i.e. that the vortex blobs overlap. This means that the distance between particles must be maintained to the order of ε, the cutoff size. As we saw earlier, this overlapping issue is also important to ensure the convergence of the Particle Strength Exchange method used to include viscous effects. An important issue is thus preventing distortion effects that arises in cases where the particles are clustered in some areas of the domain

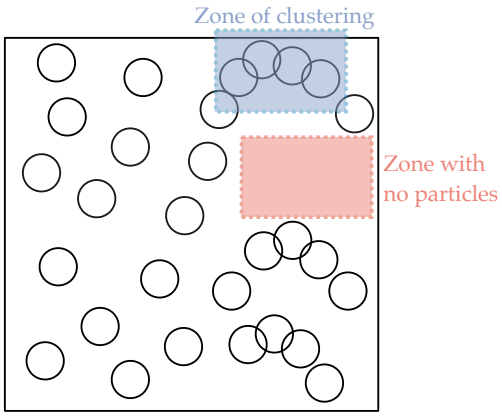

Figure 1.2: Illustration of particle distortion effects arising in Lagrangian Vortex Methods.

and are missing in other parts (see figure 1.2). In such cases, the Vortex Method ceases to provide an accurate representation of the flow physics and numerical instabilities may appear.

In order to solve this issue, different techniques are used. The first type of approaches allow the Vortex Method to remain purely meshless, and involve either a correction of the particle strength [Bea88, CLD88, BLA05], creating a triangulation whose nodes are the particle location and use it to interpolate the vorticity [RS94, Str97], or a generalization of the PSE method [SRS10]. A review of these approaches is presented in [MM21]. However, these methods often suffer from a limited convergence.

The second family of approaches, called "remeshing" or "regridding" methods, introduced by [HJ90, KL95], consist in frequently re-initializing the particles positions by repositioning them on the nodes of an underlying Cartesian grid. Let us consider as an illustration the one-dimensional case: denoting x_i the position of a grid node with $i \in \mathbb{N}$ and Δx the grid step size, the redistributed vorticity at node i, $\omega_i = \omega(x_i)$, is obtained using an interpolation kernel Γ with compact support

$$\omega_i = \sum_{p \in \mathcal{P}} \omega_p \Gamma \left(\frac{x_p - x_i}{\Delta x} \right). \tag{1.37}$$

In other words, the remeshed particle carries a vorticity value ω_i which is equal to the sum of the weighted values of the vorticity ω_p carried by the particles p located in the support of Γ. A schematic illustration of the two-dimensional remeshing procedure is presented in figure 1.3. This procedure ensures the control of the distance between particles and avoids distortion effects at the cost of a new operation and the need for a fixed grid in an originally mesh-free method. Since we are interested in hybrid Eulerian-Lagrangian methods, this procedure is naturally at the center of our approach, as it links both frameworks. In the following, we will thus present in details the construction of the remeshing kernels that will be used throughout this work.

1.1.2.2 Remeshing kernels

We consider symmetric kernels Γ with compact support $[-M_s, M_s]$. One key feature we desire from these kernels is the conservation of the first p moments of the discrete vorticity field,

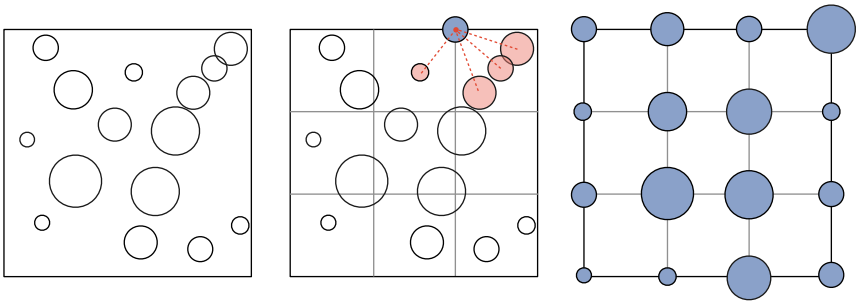

Figure 1.3: Illustration of the 2D remeshing procedure. The empty circles depict the particles before remeshing and the blue circles represent the remeshed particles, the size of the circles being proportional to the vorticity intensity they carry. During the remeshing step (figure in the middle), the vorticity at each grid point is computed as the sum of the vorticities carried by the nearby grid particles, lying in the remeshing kernel support, using equation (1.37).

namely

$$\sum_{q\in\mathcal{P}} \Gamma\left(\frac{x_q - x}{\Delta x}\right) x_q^\alpha = x^\alpha, \quad 0 \leq \alpha \leq p, \quad \alpha \in \mathbb{N}. \tag{1.38}$$

Γ is therefore an interpolation kernel of order p. We note that the equation for $\alpha = 0$ represent the mass conservation and the kernels' symmetry ensure automatically the satisfaction of the equation for $\alpha = 1$.

A first family of kernels based on the satisfaction of $p(p+1)$ conditions (coming from (1.38)) can then be constructed with piecewise polynomial functions of degree p. They are the ordinary interpolation kernels, denoted Λ_p, where Λ_1 is the linear interpolation kernel, ensuring mass conservation and defined as: $\Lambda_1(x) = 1 - |x|$ if $|x| \leq 1$ and 0 otherwise. However, the Λ_p kernels are not regular or even necessarily continuous (see few examples on figure 1.4), leading to inaccurate solutions.

A second family of kernels are the B-splines kernels [Sch46]. They are usually denoted M_n and are defined as

$$M_n(x) = \frac{1}{2\pi}\int_{\mathbb{R}} \left(\frac{\sin(\xi/2)}{\xi/2}\right)^n e^{ix\xi} d\xi. \tag{1.39}$$

M_1 is the top hat function and for $n > 1$, M_n is the convolution of M_{n-1} with M_1 (with notably $M_2 = \Lambda_1$) and is of class $\mathcal{C}^{n-2}$. For $n \geq 2$, the kernels M_n preserve the first two moments with increased regularity (see figure 1.4). However, they are limited to these two moments.

To increase the order of the B-splines remeshing kernels, while conserving their regularity, Monaghan [Mon85] proposed an extrapolation of the B-splines kernels, denoted M'_n, by constructing linear combinations $M'_n(x) = \sum_{k=0}^{\lfloor n/2 \rfloor - 1} c_k x^k M_n^{(k)}(x)$ of the M_n kernels and their derivatives $M_n^{(k)}$ such that their successive moments are cancelled, i.e.

$$\int x^\alpha M'_n(x) dx = \begin{cases} 1 & \text{if} \quad \alpha = 0 \\ 0 & \text{if} \quad 1 \leq \alpha \leq n-1 \end{cases} \tag{1.40}$$

which requires a linear system to be solved. Since the kernels are symmetric, we only need to check the cases where α is even, leading to a system of $\lfloor n/2 \rfloor$ equations. For instance, a widely used kernel is the M'_4 kernel defined as

$$M'_4(x) = \frac{1}{2}\left(3M_4(x) + x\frac{dM_4}{dx}(x)\right) = \begin{cases} 1 - \frac{5}{2}|x|^2 + \frac{3}{2}|x|^3 & \text{if} \quad |x| < 1 \\ 2 - 4|x| + \frac{5}{2}|x|^2 - \frac{1}{2}|x|^3 & \text{if} \quad 1 \leq |x| < 2 \\ 0 & \text{otherwise.} \end{cases} \tag{1.41}$$

By construction, this kernel is of class $\mathcal{C}^1$ and conserves moments up to $p = 2$. However, the construction of the M'_n kernels does not guarantee in general the interpolation condition

$$\Gamma(i) = \mathbb{1}_{\{i=0\}} \quad \forall i \in \mathbb{Z} \tag{1.42}$$

which ensures the conservation of a particle's transported quantity if it does not move from its starting position on the grid (for example, the M'_4 and M'_6 kernels do satisfy this property, but M'_5 does not, as can be seen on figure 1.4). For that reason, Cottet *et al.* [CEPP14] introduced a systematic way to derive high order kernels satisfying this property. This new family of kernels $\Lambda_{p,r}$ preserving $p+1$ moments and of class $\mathcal{C}^r$ is constituted of even and piecewise polynomial of degree M in intervals of the form $[i, i+1]$. These kernels are determined by $M_s(M+1)$ coefficients. Because we require r-regularity on a piecewise even polynome defined on $2M_s$ segments, there is $M_s(r+1)$ interface conditions at integer values to satisfy and since we want the odd order derivative to vanish at 0, this leads to further $\lfloor \frac{r+1}{2} \rfloor$ conditions. The conservation of moments imposes $p+1$ conditions and the interpolation property imposes M_s conditions. Therefore, we can expect to find kernels with the desired properties under the condition

$$M_s(M+1) \geq (r+1)Ms + \left\lfloor \frac{r+1}{2} \right\rfloor + p + 1 + M_s. \tag{1.43}$$

We note that the kernel $\Lambda_{2,1}$ obtained from this framework is the same as the kernel M'_4 presented above. Table 1.1 summarizes the properties of some of the kernels presented in this section and figure 1.4 depicts a few for each family.

The remeshing step can also be used to solve the diffusion equation: Wee and Ghoniem [WG06] modified some of the remeshing kernels presented above to include diffusive effects and thus remove the need for an additional diffusion scheme on the grid.

1.1.2.3 Hybrid Vortex Methods

Due to the drawbacks inherent to the purely Lagrangian methods presented above (solving the diffusion equation, distortion effects...) and due to the presence of a Cartesian grid introduced by the remeshing procedure exposed previsouly, it seems natural to construct hybrid Eulerian-Lagrangian, or semi-Lagrangian, Vortex Methods based on a splitting of the Navier-Stokes equations where the advection equation is solved in a Lagrangian way whereas the stretching, diffusion and Poisson equations, as well as possible external forces, are solved on the Eulerian grid, with grid-based methods such as finite-differences, finite-volume schemes or spectral methods. This is the principle behind the Vortex-in-Cell (VIC) methods, introduced by Christiansen in 1973 [Chr73].

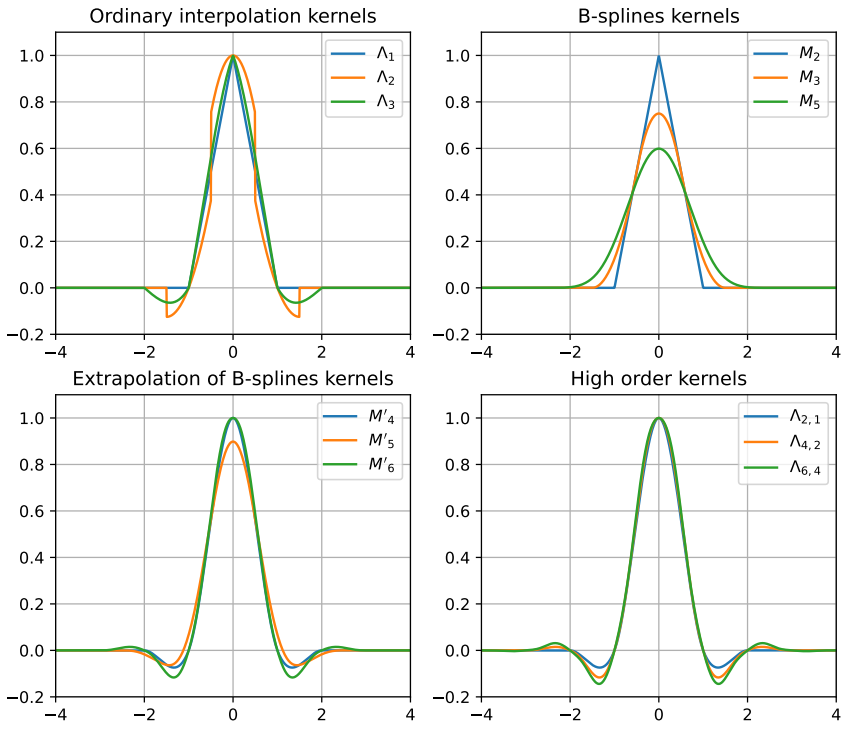

Figure 1.4: Plots of common remeshing kernels (inspired from [Mim15])

Name(s)	Maximal preserved moment	Regularity	Support	Degree	(1.42) satisfied
Λ_1 / M_2	1	$\mathcal{C}^0$	$[-1,1]$	1	✓
Λ_2	2	-	$[-1.5,1.5]$	2	✓
Λ_3	3	$\mathcal{C}^0$	$[-2,2]$	3	✓
Λ_4	4	-	$[-2.5,2.5]$	4	✓
M_3	1	$\mathcal{C}^1$	$[-1.5,1.5]$	2	✓
M_4	1	$\mathcal{C}^2$	$[-2,2]$	3	
M_5	1	$\mathcal{C}^3$	$[-2.5,2.5]$	4	
M_8	1	$\mathcal{C}^6$	$[-4,4]$	7	
M'_4 / $\Lambda_{2,1}$	2	$\mathcal{C}^1$	$[-2,2]$	3	✓
M'_5	3	$\mathcal{C}^2$	$[-2.5,2.5]$	4	
M'_6 / $\Lambda_{4,2}$	4	$\mathcal{C}^2$	$[-3,3]$	5	✓
M'_8	4	$\mathcal{C}^4$	$[-4,4]$	7	
$\Lambda_{2,2}$	2	$\mathcal{C}^2$	$[-2,2]$	5	✓
$\Lambda_{4,4}$	4	$\mathcal{C}^4$	$[-3,3]$	9	✓
$\Lambda_{6,4}$	6	$\mathcal{C}^4$	$[-4,4]$	9	✓
$\Lambda_{6,6}$	6	$\mathcal{C}^6$	$[-4,4]$	13	✓
$\Lambda_{8,4}$	8	$\mathcal{C}^4$	$[-5,5]$	9	✓

Table 1.1: Summary of the properties of common remeshing kernels.

These methods rely on interpolation schemes, to interpolate the vorticity from the particles to the mesh (P2M schemes) and from the mesh to the particles (M2P schemes). In practice, the basis function used for P2M-M2P schemes is often one of the remeshing kernels described previously, with $M'_4/\Lambda_{2,1}$ being the most popular in literature. Although they were approximately proposed at the same time as purely Lagrangian Vortex methods, the VIC methods, also called Vortex Particle-Mesh Methods (VPMM) or Remeshed Vortex Methods (RVM) are today the most commonly used type of Vortex Methods due to their flexibility and ease of implementation. They vary in the methods used within the Eulerian part of the fractional step algorithm and the frequency of the particles remeshing. This thesis is precisely based on a Remeshed Vortex Method (RVM).

As for other hybrid approaches combining both Lagrangian and Eulerian frameworks, we can cite domain decomposition methods [Cot91, GHS93, CKS00, HV02], where Lagrangian and Eulerian methods are used in different parts of the domain, usually to better impose boundary conditions near immersed obstacles. We refer to [CK00] for more details. Finally, another more recent hybrid approach was introduced by Kornev in 2018 [Kor18] based on separating the large scale field, solved on the grid, and the small scale field, solved through a pure Lagrangian Vortex Method. This method is by construction closer to a Large Eddy Simulations (LES) approach and will be detailed later, in Chapter 2, when studying more specifically turbulence modeling with Vortex Methods.

In summary, the advantages of using a RVM instead of a purely Lagrangian VM or another hybrid approach are as follow:

- The particle overlapping condition is satisfied all throughout the simulation thanks to the remeshing procedure
- The viscous effects can easily be handled by using Eulerian-based schemes on the underlying grid for the resolution of the diffusion equation, while the Lagrangian treatment of the convective effects is conserved.
- The Poisson equation is solved with a lower computational cost compared to the classical particle-particle interactions computed in the resolution of the Biot-Savart law.
- They are easier to implement compared to domain decomposition approaches in the other hybrid Vortex Methods.

1.1.3 Remeshed Vortex Methods

1.1.3.1 Treatment of boundary conditions

In purely Lagrangian Vortex Methods, the treatment of boundary conditions is not straightforward as the no-slip boundary condition, frequent when dealing with wall-bounded flows, needs to be rewritten as a condition on the vorticity field. A first approach is the vortex sheet method introduced by Chorin [Cho73, Cho80]. The boundary conditions are treated by creating a vortex sheet on the surface of the body which strength is set so that the tangential velocity in the body goes to zero. The vortex sheet method has been used for example to study flows past a cylinder [SS88, GG98], a backward-facing step [SG88] or airfoils [Che83]. Another, more accurate, approach consists in using vorticity flux boundary conditions [KLP94, Cot95] to enforce the no-slip

condition instead of creating new vortex blobs or vortex sheets. This method has been applied to 2D cylinder flow in various regimes [KL95] and for 3D simulations of the flow past a sphere at different Reynolds [PWS+02].

However, difficulties may arise when using these methods, especially when dealing with complex geometries. In hybrid Eulerian-Lagrangian Vortex Methods, however, the Eulerian grid allows to easily add penalization terms to the Navier-Stokes equations. This leads to the family of Immersed Boundary Methods (IBM), where the boundary conditions are not explicitly prescribed but added through an additional term in the equation solved on the whole domain. This type of method can also deal with arbitrary geometries.

In particular, the Brinkman penalization, developed by Caltagirone [Cal94] and Angot *et al.* [ABF99], was first used for the velocity-vorticity formulation of the Navier-Stokes equations by Kevlahan and Ghidaglia [KG01] and in the context of remeshed Vortex Methods by Coquerelle and Cottet [CC08a]. It is a first order Immersed Boundary Method.

It consists in adding a forcing term to the Navier-Stokes equations (1.49) so that we solve

$$\frac{\partial \boldsymbol{\omega}}{\partial t} + \mathbf{u} \cdot \nabla \boldsymbol{\omega} - \boldsymbol{\omega} \cdot \nabla \mathbf{u} - \frac{1}{Re} \Delta \boldsymbol{\omega} = \nabla \times (\lambda \chi (\mathbf{u}_b - \mathbf{u})) \tag{1.44}$$

where χ is the characteristic function of the immersed body, equal to 1 inside the solid parts, and equal to 0 in the fluid parts of the domain, $\mathbf{u}_b$ is the rigid velocity of the solid parts immersed in the fluid ($\mathbf{u}_b = 0$ in the present thesis since we will only consider fixed obstacles), and where λ is the penalization factor, inversely proportional to the medium permeability (thus equal to 0 in the fluid and very high in solid regions). In the context of flow past solid obstacles, the force is therefore activated only inside the solid parts, making the velocity vanish in these regions, and the no-slip boundary condition is automatically satisfied.

This approach is not the only one (see for example [CP04, MCW16, GMWC19]) but has been validated for many RVM simulations of wall-bounded flows and will be the one used in this work for the treatment of boundary conditions.

1.1.3.2 Convergence studies

The convergence of Lagrangian Vortex Methods has been established in the late 1970s and 1980s. Historically, Hald [Hal79] gave the first convergence result in the context of 2D vortex blob methods and showed that under the overlapping condition $h << \varepsilon$, where h is the distance between particles and ε the size of the blobs, as described in section 1.1.1.2, the vortex blob trajectories tend to the exact one as the number of eddies grows. Beale and Majda [BM82] generalized this result for $h = O(\varepsilon)$ and to three dimensions. Another convergence proof was found by Beale [Bea86] by assuming a smooth vorticity with compact support and with a cutoff of at least 4th order. This proof was later generalized by [Cot88].

These proofs were only considering a spatially-discretized scheme. The time-stepping scheme was first analyzed by Anderson and Greengard [AG85] and exhibited a stability condition for the Lagrangian advection, constraining the timestep to the velocity gradient

$$\Delta t = \frac{C}{\|\nabla \mathbf{u}\|_\infty} \tag{1.45}$$

where C is a constant lower or equal to 1, also called LCFL number (for Lagrangian CFL, as opposed to the Eulerian CFL that ties Δt to the grid size).

As for remeshed Vortex Methods, a proof of stability and consistence for a directional splitting scheme (described in detail in subsection 1.2.2.1) can be found in [CEPP14] in the case of Euler equations with a constant velocity field using the class of high order kernels $\Lambda_{p,r}$ presented in subsection 1.1.2.2. More precisely, writing ω the solution of Euler equations and $\mathcal{T}_i\omega(\cdot, t_n)$ the result of the scheme at point x_i, given kernels Γ satisfying the moment property for $p > 1$ moments and with $\Gamma \in W^{r+1,\infty}(\mathbb{R})$ for some $r > 1$ and $\Gamma \in \mathcal{C}^\infty(]l, l+1[)$ for $l \in \mathbb{Z}$ and provided the condition (1.45) is satisfied, we have

$$\omega(x_i, t_{n+1}) = \mathcal{T}_i\omega(\cdot, t_n) + O(\Delta t^2) + O(\Delta t \Delta x^\beta + \Delta x^{\beta+1} + \Delta t^{\beta+1}) \tag{1.46}$$

where $\beta = \inf(p, r)$. In other words, using the classical kernel $\Lambda_{4,2} = M_6'$, the advection-remeshing scheme is theoretically of order 2 in time and space. The space convergence can be further improved using higher order kernels.

However, this demonstration does not take into account the schemes discretizing the viscous and the stretching terms involved when solving the 3D Navier-Stokes equations (1.49). To our knowledge, there is no complete proof of convergence of the Remeshed Vortex methods in such complete case, where the numerical analysis is significantly complicated by the heterogeneous and hybrid aspects. Numerical studies of the convergence can still be useful to estimate the global order of convergence of the complete algorithm used to solve Navier-Stokes and will be presented in the following chapters.

1.1.3.3 Comparison with classical methods

Since the Remeshed Vortex methods are not widespread in the Computational Fluid Dynamics (CFD) community, it is natural to ask ourselves how they compare to classical Eulerian methods and whether they represent a good candidate to challenge or complete them.

A few authors have recently performed comparison studies on classical benchmarks: van Rees *et al.* [vRLPK11] compared a Remeshed Vortex Method and a pseudo-spectral (PS) method on the Taylor-Green vortex (TGV) at $Re = 1600$ and the collision of two vortex tubes at $Re = 10,000$ and concluded that the RVM matched the performance of the PS method when the 4th order remeshing kernel, M_6', is used. The study remarked that since the Vortex Method allows for larger timesteps since it does not constrain the timestep to the grid size but to the velocity gradient (condition (1.45)), its time to solution is smallest than for a spectral method. It is also expected to have a better scaling at a larger number of cores due to its lesser number of FFT operations per timestep.

More recently, Mimeau *et al.* [MMM21] compared a Remeshed Vortex Method with a lattice-Boltzmann method (LBM) on three reference test cases: the advection of a simple vortex, the Taylor-Green vortex and the simulation of three-dimensional flows past a solid cube. The study showed the low dissipative behaviour of the RVM, obtaining a better accuracy at low spatial resolutions. However, at higher resolutions, the LBM had a better accuracy and a better convergence order overall.

From these studies and the intrinsic characteristics of the Vortex Methods, we can exhibit the desirable features of the Remeshed Vortex Methods compared to Eulerian-based schemes:

- The use of vorticity as the main variable formulation of the NS equations.

- Pressure, in flows with constant density such as the ones studied in this work, is not a variable of the governing equations solved by the RVM, there is therefore no need for a pressure solver (however, the pressure field can always be retrieved by solving a Poisson equation).
- The diffusive effects in the advection/remeshing step are limited due to the Lagrangian treatment of the vorticity transport. This leads the RVM to be less dissipative than most non-spectral Eulerian schemes, allowing for a better approximation of the flow at coarse resolutions, especially of the vorticity which is the main variable in our method. Figure 1.5 shows the comparison of a RVM (with remeshing kernel $\Lambda_{4,2}$ and global convergence order ≈ 1.5) to literature results obtained with a fourth order Finite Differences (FD) [JJS16], a second order Finite Volumes (FV) and Lattice Boltzmann (LB) (using the D3Q19 lattice and with global convergence order ≈ 2) solvers for the TGV test case at $Re = 1600$.
- The stability condition for the advection step is less restrictive: contrary to the classical CFL condition, the Lagrangian stability condition do not tie the time step to the grid step but to the velocity gradients (1.45), thus allowing for larger Δt and lower computational cost.
- The modular aspect offered by the fractional step resolution approach allows to easily discretize additional source terms (on the Cartesian grid), at the desired order.

1.1.4 Remeshed Vortex Method applications

1.1.4.1 Wall-bounded flows and fluid-structure interactions

Bluff-body flows are very important test cases in computational fluid mechanics as they allow to test the ability of a numerical method to solve complex separated flow fields, to handle significant pressure gradients, and to predict the wake dynamics accurately.

In semi-Lagrangian methods, the cylinder flow was further investigated in 3D by Cottet and Poncet [CP04] in the context of a Vortex-In-Cell method. The diffusion is treated with a PSE scheme. The boundary conditions are imposed in two different ways: either while solving the Poisson equation on the grid or by using an Immersed Boundary Method. The penalization method was used with the present method in [MGCM15] for 2D bluff body flows and in [MMC17] to investigate the flow past a porous hemisphere.

The RVM was also widely used to model fluid-structure interactions in the context of fish schooling. The use of Remeshed Vortex Methods combined with a level-set method for the two-way coupling of a fluid with rigid bodies was introduced by Coquerelle and Cottet [CC08b] and was subsequently applied to simulation of articulated bodies [BGRC19] by coupling the RVM with a multi-body solver and to the optimization of the motion [GvRK12] and shape [vRGK13] of self-propelled swimmers. The RVM was also coupled with a reinforcement learning procedure [GHK14, NVA$^+$17] to optimize fish swimming in a tandem configuration.

Finally, concerning industrial applications, we can cite simulations of flow past aircraft wings and wind turbines. Pioneer work considered the instability created by counter-rotating vortices present in aircraft wakes [CCB$^+$08] and showed that the RVM method demonstrated a very good efficiency and scalability. Further work allowed to model rotor wakes [CBD$^+$17, CCW20]

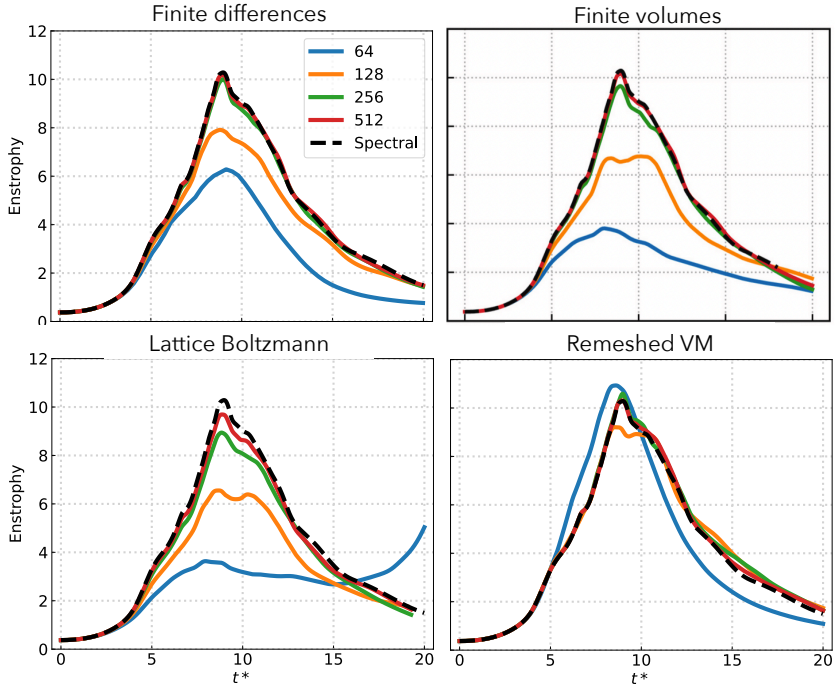

Figure 1.5: Comparison of the numerical grid-convergence of the Taylor-Green vortex solution at $Re = 1600$ for different schemes: (top left) Finite differences, from Jammy *et al.* [JJS16], (top right) Finite volumes, from Suss *et al.* [SMLGM23], (bottom left) Lattice Boltzmann Method and (bottom right) Remeshed Vortex Method, from Mimeau *et al.* [MMM21]. The solid colored curves indicate the solution obtained with a grid resolution of N^3, with $N = 64, 128, 256, 512$. The spectral solution from Wang *et al.* [WFA$^+$13] is given as reference in each case, depicted by the dotted black line.

and wind turbine wakes [CBWK13, CDZ+17, CDC+17] using the RVM. Recently, the RVM was coupled with an immersed lifting and dragging line model [CWC20] to model more efficiently the effect of the immersed body on the flow.

1.1.4.2 Scalar transport

Another family of applications of the Vortex Methods are scalar transport problems. Numerous physical phenomena can be modeled through the transport of a scalar quantity, for example the transport of pollutants through water or air, or the transfer of heat through convection. This is translated mathematically by the coupling of Navier-Stokes equation with an advection-diffusion equation

$$\partial_t \theta + \mathbf{u} \cdot \nabla \theta = \kappa \Delta \theta \tag{1.47}$$

where θ is the transported scalar quantity and κ its diffusivity. If there is a coupling between the scalar field θ and the flow governing equations through the adding of a source term $\mathbf{f}(\theta, \mathbf{x}, t)$ in the Navier-Stokes equations, the scalar influences the flow properties, and is said to be active. Otherwise, without any coupling, the scalar is defined as passive.

Due to their Lagrangian nature, the Vortex Methods are particularly well suited for transport equations. Lagaert *et al.* [LBC14] coupled in a multi-grid approach a spectral Navier-Stokes solver to a Remeshed Vortex Method for the passive scalar transport and showed an increased efficiency compared to a fully spectral approach. Since the timestep is not constrained by the grid size, the semi-Lagrangian approach scales well when considering small scalar diffusivity requiring fine grids. Later, Etancelin [Eta14], considered the same approach but used a RVM (also called semi-Lagrangian Vortex Method) for the Navier-Stokes solver as well. The Navier-Stokes equations were solved in parallel on multiple CPUs whereas the passive scalar transport was solved on GPUs.

As for active scalar transport, we can cite Keck's [Kec19] work on the transport of sediments. In the case considered, a fresh water carrying sediments meets a salt water, requiring the coupling of the Navier-Stokes equations with two transport-diffusion equations, one for the salinity and the other for the concentration of sediments. The use of a semi-Lagrangian method and of CPU-GPU hybrid computations allowed to attain high Schmidt numbers, i.e. high ratios between the fluid viscosity and the scalar diffusivity.

1.2 Numerical algorithm and implementation

We aim to solve the 3D Navier-Stokes equation in their vorticity-velocity formulation

$$\frac{\partial \boldsymbol{\omega}}{\partial t} + \mathbf{u} \cdot \nabla \boldsymbol{\omega} - \boldsymbol{\omega} \cdot \nabla \mathbf{u} - \frac{1}{Re} \Delta \boldsymbol{\omega} = 0 \tag{1.48}$$

$$-\Delta \mathbf{u} = \nabla \times \boldsymbol{\omega}, \tag{1.49}$$

using a remeshed Vortex Method. The present RVM algorithm is semi-Lagrangian and is based on an operator splitting, meaning that, within one current time step of the time-running algorithm, the vorticity is evolved at fixed velocity with 1) the Lagrangian advection of vorticity and the remeshing of particles on a fixed Cartesian grid (which is therefore performed at every time

step as opposed to classical VIC methods), 2) the discretization of the other operators (stretching, diffusion, penalization) on the Cartesian grid with Eulerian methods (finite differences or FFT-based). The velocity is then evolved from the new vorticity with a Poisson equation solved using a FFT-based method on the Cartesian grid. In the following sections we present the numerical solver used in this thesis and we detail the present RVM algorithm.

1.2.1 Hysop

1.2.1.1 Presentation

In the following, we will use the in-house and research open source `HySoP` (HYbrid SimulatiOn with Particles) library[1], dedicated to solving fluid related problems using the RVM approach described previously. It is a `Python` parallel solver, interfaced with compiled languages such as `Fortran`, `OpenCL` and `C++`. This choice allows to have an easier and well-known interpreted language for the higher-level code of the library and for the user interface while retaining the efficiency of `Fortran` and `C`-based compiled languages implementations.

The library was created as a high performance and multi-architecture framework for simulations of scalar transport with the semi-Lagrangian particle methods [Eta14] from a former `Fortran` code called `SCALES` [LBCB12, MC12]. The library was further developped to include the treatement of boundary conditions with a penalization method to handle flows past immersed obstacles by Mimeau [Mim15] and was then deeply enriched by Keck [Kec19] to further optimize simulations on hybrid CPU-GPU architecture.

1.2.1.2 Library structure

`Hysop`'s structure is based on four main objects: domains, variables, operators and problems.

The user needs first to specify the rectangular domain on which the simulation is defined with the `Domain` object by specifying its dimension (usually 2 or 3), the lengths of its sides, its origin and, if needed, boundary conditions. By default, the domain is considered periodic. This domain is then discretized on a Cartesisian `Mesh` with a given resolution. In the case of a multi-resolution simulation, a `Mesh` is created for each resolution.

The user also needs to define the variables of the problem. There are two main objects for this purpose: `Field` objects, which can be scalar fields (such as a pressure or a temperature) or vector fields (like the vorticity or velocity field) and `Parameter` objects (which can be constant, like the viscosity, or time-dependent, like an adaptive time-step, but are uniform across the domain). Once the `Domain` and the `Mesh` are defined, each `Field` can then be discretized to be used in numerical schemes.

`Operator` objects represent the fractional steps to solve within the overall mathematical problem, like solving the advection equation or the Poisson equation (i.e. computing the velocity from the vorticity). They take variables (`Field` and `Parameter`) as input and provide in output a modification of these variables or a computation of other ones, such as quantities for post-processing (e.g. kinetic energy, enstrophy, ...) or an update of the time step if it is adaptive. For each numerical method used in the temporal and spacial discretization of an operator,

[1] `https://particle_methods.gricad-pages.univ-grenoble-alpes.fr/hysop-doc/`

multiple scheme orders are available, therefore the user can choose the order of each operator independently.

The `Problem` object represents the physical problem to be solved. To create the `Problem` object, the user gives the ordered sequence of operators to be applied to the variables discretized on the domain. To solve the problem, the user also needs to define a `Simulation` object that will handle the time-marching of the algorithm. Given a final time or a maximum number of iteration, the `Simulation` will update the current iteration, the current simulation time, and will stop the simulation at the required final time or iteration.

1.2.1.3 High performance computing

`Hysop` makes use of different techniques to solve the numerical problem in the most efficient way adapted to the architecture on which it is deployed. Once the operators are defined by the user, the library creates an acyclic graph operator in order to optimize their memory usage and execution. The use of the `OpenCL` library also allows to generate different code variants for one operator and compare them to select the best candidates. The reader is refered to [Kec19] for more details.

Futhermore, in `Hysop`, in order to make use of multiple cores, the domain on which the problem is solved is divided in multiple parts in the x direction. Each core then solves the problem on one part of the domain and communicates, via MPI communicators, with the cores assigned to neighboring sub-domains to exchange ghost cells information at each step. Because of the discretization on a regular Cartesian grid, this parallelization is very straightforward and computationally efficient.

It can also be noted that `Hysop` also supports computations on a hybrid CPU-GPU architecture [Eta14]. The GPUs (Graphics Processing Units) are highly efficient for computational tasks that are strongly parallelizable. Their increased number of floating-point operations per second (FLOPS) makes them powerful computation accelerators. In the context of Lagrangian methods, they are particularly effective for particle operations (transport, remeshing) [RK08]. For Eulerian-Lagrangian approaches, the hybrid architecture is well-suited, as CPUs provide sufficient memory for the Eulerian operators, while GPUs handle the Lagrangian part of the algorithm. Furthermore, when considering multiscale scalar transport simulations, where the number of particles becomes significant compared to the size of the grid, GPUs offer considerable advantages.

The use of hybrid CPU-GPU computation is not exploited in this thesis, where parallel computations were only performed on multiple CPU cores, and would constitute an important short-term perspective.

1.2.2 Physical space operators

1.2.2.1 Strang splitting

The operator splitting realized in the present fractional step algorithm is further decomposed by using a directional Strang splitting [Str68] where 1D advection-remeshing-stretching problems are successively solved, direction by direction. This directional splitting allows to reduce the computational effort compared to a tensorial approach since it reduces the multi-dimensional partial differential equations to a sum of one-dimensional problems, leading to a

reduction in computational cost. In particular, as opposed to a tensorial remeshing performed in most remeshed Vortex Methods, remeshing directionally reduces the cost (in 3D for a first order splitting algorithm) from $O(N \times S^3)$ to $O(N \times 3S)$ with N the number of particles and S the stencil size in one direction.
Let us write our operator $\mathcal{L}$ (where $\mathcal{L}$ could be for instance the advection operator or the remeshing operator) such that the operation to solve in 3D is

$$\partial_t \boldsymbol{\omega} = \mathcal{L}(\boldsymbol{\omega}) = \mathcal{L}_x(\boldsymbol{\omega}) + \mathcal{L}_y(\boldsymbol{\omega}) + \mathcal{L}_z(\boldsymbol{\omega}), \tag{1.50}$$

the first order Strang splitting consists in solving successively $\partial_t \boldsymbol{\omega} = \mathcal{L}_x(\boldsymbol{\omega})$, $\partial_t \boldsymbol{\omega} = \mathcal{L}_y(\boldsymbol{\omega})$ and $\partial_t \boldsymbol{\omega} = \mathcal{L}_z(\boldsymbol{\omega})$ where x, y, z respectively denote the streamwise, vertical and spanwise direction in the computational domain. Writing L the numerical counterpart of $\mathcal{L}$ and $TI(\boldsymbol{\omega}, \Delta t)$ the result of the time integration scheme applied to $\boldsymbol{\omega}$ with step Δt, we solve

$$\boldsymbol{\omega}^{n+1,*} = TI(L_x(\boldsymbol{\omega}^n), \Delta t) \tag{1.51}$$
$$\tilde{\boldsymbol{\omega}}^{n+1,*} = TI(L_y(\boldsymbol{\omega}^{n+1,*}), \Delta t) \tag{1.52}$$
$$\boldsymbol{\omega}^{n+1} = TI(L_z(\tilde{\boldsymbol{\omega}}^{n+1,*}), \Delta t). \tag{1.53}$$

This scheme introduces an error of order $O(\Delta t^2)$. However, this procedure can be extended to the second order by introducing two extra steps with half the time step

$$\boldsymbol{\omega}^{n+1/2,*} = TI(L_x(\boldsymbol{\omega}^n), \Delta t/2) \tag{1.54}$$
$$\tilde{\boldsymbol{\omega}}^{n+1/2,*} = TI(L_y(\boldsymbol{\omega}^{n+1/2,*}), \Delta t/2) \tag{1.55}$$
$$\boldsymbol{\omega}^{n+1,*} = TI(L_z(\tilde{\boldsymbol{\omega}}^{n+1/2,*}), \Delta t) \tag{1.56}$$
$$\tilde{\boldsymbol{\omega}}^{n+1,*} = TI(L_y(\boldsymbol{\omega}^{n+1,*}), \Delta t/2) \tag{1.57}$$
$$\boldsymbol{\omega}^{n+1} = TI(L_x(\tilde{\boldsymbol{\omega}}^{n+1,*}), \Delta t/2). \tag{1.58}$$

This scheme is second-order accurate, provided that L is an approximation of $\mathcal{L}$ at, at least, the second order.

More details about the Strang splitting procedure and its algorithmic advantages can be found in [Eta14] and [Kec19]. So far we have presented the case where the direction x is treated first, then y, then z. However, this order can be modified and its impact on the simulation will be discussed in the following chapters and will be the subject of a numerical study.

1.2.2.2 Advection and remeshing

In this work, the particles are initialized on a Cartesian grid and remeshed every timestep, meaning that the particles' position at the beginning of a timestep coincide with the grid points. The particle positions are time-integrated using a second order Runge-Kutta scheme. The advection and remeshing operators are solved with a directional Strang splitting (explained in section 1.2.2.1), meaning that the advection and remeshing steps are jointly treated through a one-dimensional procedure, first performed in the x-axis, then in the y-axis and finally in the z-axis. Since

$$\partial_t \boldsymbol{\omega} = \mathbf{u} \cdot \nabla \boldsymbol{\omega} = u_x \partial_x \boldsymbol{\omega} + u_y \partial_y \boldsymbol{\omega} + u_z \partial_z \boldsymbol{\omega}, \tag{1.59}$$

the advection operator can be split into three different operators

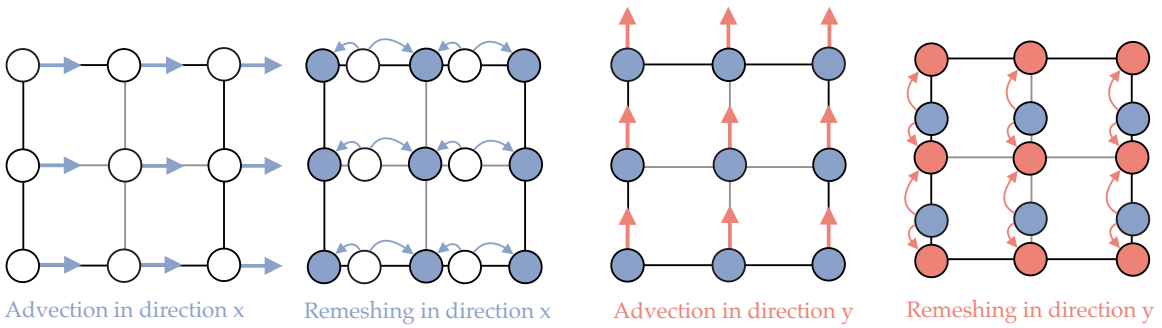

Figure 1.6: 2D directional advection and remeshing.

1. x-axis splitting: $\partial_t \boldsymbol{\omega} = u_x \partial_x \boldsymbol{\omega}$
2. y-axis splitting: $\partial_t \boldsymbol{\omega} = u_y \partial_y \boldsymbol{\omega}$
3. z-axis splitting: $\partial_t \boldsymbol{\omega} = u_z \partial_z \boldsymbol{\omega}$

each directional operator representing the advection of the particles along the given axis. Every directional step of the advection algorithm is followed by a directional remeshing step using one of the high-order 1D-remeshing kernel formulas described in section 1.1.2.2. See figure 1.6 for an illustration of this procedure in 2D.

1.2.2.3 Stretching

The stretching equation is considered in its conservative formulation

$$\partial_t \boldsymbol{\omega} = \nabla \cdot (\boldsymbol{\omega} \otimes \mathbf{u}) = \boldsymbol{\omega} \cdot \nabla \mathbf{u} + \mathbf{u}(\nabla \cdot \boldsymbol{\omega}) \tag{1.60}$$

which is equivalent to the usual formulation

$$\partial_t \boldsymbol{\omega} = \boldsymbol{\omega} \cdot \nabla \mathbf{u} \tag{1.61}$$

as long as the vorticity is divergence-free, i.e. $\nabla \cdot \boldsymbol{\omega} = 0$. It is important to note that numerically, the divergence free of the vorticity may not be satisfied through the different stages of the solver. A solenoidal projection of the vorticity field is therefore performed at each time step within the algorithm, as will be presented in see section 1.2.3.2.

The equation (1.60) is solved with a centered explicit finite difference scheme, usually of the 4^{th} order, although the order can be changed. The stencil coefficients are automatically computed using symbolic expressions [Kec19]. Like for the advection, the stretching equation is split directionally, meaning that we successively solve

1. x-axis splitting: $\partial_t \boldsymbol{\omega} = \partial_x (\omega_x \mathbf{u})$
2. y-axis splitting: $\partial_t \boldsymbol{\omega} = \partial_y (\omega_y \mathbf{u})$
3. z-axis splitting: $\partial_t \boldsymbol{\omega} = \partial_z (\omega_z \mathbf{u})$

1.2.2.4 Penalization of the vorticity field to enforce no-slip boundary conditions

As described in section 1.1.3.1, the no-slip boundary conditions are treated in the present RVM method by using the Brinkman penalization method. Discretizing the Brinkman penalization equation

$$\partial_t \boldsymbol{\omega} = -\nabla \times (\lambda \chi \mathbf{u}) \tag{1.62}$$

with an implicit Euler scheme we obtain

$$\boldsymbol{\omega}^{n+1} = \boldsymbol{\omega}^n - \Delta t \nabla \times (\lambda \chi \mathbf{u}^{n+1}) \tag{1.63}$$

which can be rewritten using that $\boldsymbol{\omega}^{n+1} = \nabla \times \mathbf{u}^{n+1}$

$$\boldsymbol{\omega}^{n+1} = \boldsymbol{\omega}^n - \Delta t \lambda \chi \boldsymbol{\omega}^{n+1} \tag{1.64}$$

$$(1 + \Delta t \lambda \chi)\boldsymbol{\omega}^{n+1} = \boldsymbol{\omega}^n \tag{1.65}$$

$$= (1 + \Delta t \lambda \chi)\boldsymbol{\omega}^n - \Delta t \lambda \chi \boldsymbol{\omega}^n \tag{1.66}$$

and finally by writing the second $\boldsymbol{\omega}^n$ on the left hand side of the previous equation as $\nabla \times \mathbf{u}^n$, we obtain the explicit expression

$$\boldsymbol{\omega}^{n+1} = \boldsymbol{\omega}^n - \nabla \times \left(\frac{\lambda \chi \Delta t \mathbf{u}^n}{1 + \lambda \chi \Delta t} \right) \tag{1.67}$$

which is solved by discretizing the curl operator with 4^{th} order centered finite differences.

1.2.3 FFT operators

1.2.3.1 Fast Fourier Transform

The one-dimensional discrete Fourier transform (DFT) of a signal u on N points writes

$$\hat{u}_p = \frac{1}{N} \sum_{j=0}^{N-1} u_j e^{-2i\pi \frac{jp}{N}} \tag{1.68}$$

Numerically, this is calculated using the Fast Fourier Transform (FFT) algorithm [CT65], with a complexity of $O(N \log(N))$ (instead of $O(N^2)$ for a naive implementation). The algorithm is based on a divide-and-conquer strategy and works optimally when N is power of two.

The FFT operations in `Hysop` are usually computed with the `FFTW` (for Fastest Fourier Transform in the West) [FJ05] library written in Fortran, interfaced with the python frontend through the wrapper `pyfftw` but numerous other implementations exist (`FFTPACK`, `MKL-FFT`, `clFFT` or `cuFFT` for example).

1.2.3.2 Solenoidal reprojection

The solenoidal reprojection ensures that the vorticity is a solenoidal field (ie. $\nabla \times \boldsymbol{\omega} = 0$) by projecting $\boldsymbol{\omega}$ on the space of divergence-free fields. The solenoidal reprojection step is here to ensure one always has $\nabla \cdot \boldsymbol{\omega} = 0$ throughout the different steps of the fractionnal step algorithm. Indeed, numerical errors can accumulate and to prevent that, we correct the vorticity regularly. Let us recall that any vector field can be expressed as the sum of a solenoidal (divergence-free) and an irrotational (curl-free) field. The irrotational component can be written as the gradient of a scalar potential e. Let $\boldsymbol{\omega}^*$ be the vorticity to be corrected and $\boldsymbol{\omega}$ its solenoidal part, thus the correction we seek. We write then

$$\boldsymbol{\omega}^* = \boldsymbol{\omega} + \nabla e \tag{1.69}$$

then

$$\nabla \cdot \boldsymbol{\omega}^* = \nabla \cdot \boldsymbol{\omega} + \nabla \cdot \nabla e \tag{1.70}$$

and since $\nabla \cdot \boldsymbol{\omega} = 0$,

$$\Delta e = \nabla \cdot \boldsymbol{\omega}^* \tag{1.71}$$

and by applying the Laplacian operator to (1.69) we get

$$\Delta \boldsymbol{\omega}^* = \Delta \boldsymbol{\omega} + \nabla \Delta e \tag{1.72}$$

which means $\boldsymbol{\omega}$ is solution to

$$\Delta \boldsymbol{\omega} = \Delta \boldsymbol{\omega}^* - \nabla(\nabla \cdot \boldsymbol{\omega}^*) \tag{1.73}$$

which is a Poisson equation that can easily be solved in the Fourier space.

1.2.3.3 Poisson equation

The Poisson equation allows to compute the velocity field from the vorticity field. Whereas all the other operators modify the vorticity field, this is the only operator updating the velocity field. This equation is solved in the Fourier space. In the physical space, the equation is

$$\Delta \mathbf{u}(\mathbf{x}) = -\nabla \times \boldsymbol{\omega}(\mathbf{x}) \tag{1.74}$$

and in the Fourier space

$$-(k_x + k_y + k_z)^2 \hat{\mathbf{u}}(k) = i \begin{pmatrix} k_y \hat{\boldsymbol{\omega}}_z(k) - k_z \hat{\boldsymbol{\omega}}_y(k) \\ k_z \hat{\boldsymbol{\omega}}_x(k) - k_x \hat{\boldsymbol{\omega}}_z(k) \\ k_x \hat{\boldsymbol{\omega}}_y(k) - k_y \hat{\boldsymbol{\omega}}_x(k) \end{pmatrix} \tag{1.75}$$

where $\hat{\mathbf{u}}$ and $\hat{\boldsymbol{\omega}}$ respectively denote the Fourier transform of $\mathbf{u}$ and $\boldsymbol{\omega}$. Since in the Fourier space, the derivatives are transformed in simple pointwise multiplications, a high level of precision can be attained. The reprojection of the vorticity on a solenoidal field through a Poisson equation (cf previous section) is solved in a similar way.

1.2.3.4 Diffusion

In the same way, we write the diffusion equation

$$\partial_t \boldsymbol{\omega}(\mathbf{x}) = \frac{1}{Re}\Delta\boldsymbol{\omega}(\mathbf{x}) \tag{1.76}$$

in the Fourier space

$$\partial_t \hat{\boldsymbol{\omega}}(k) = -\frac{1}{Re}(k_x + k_y + k_z)^2\hat{\boldsymbol{\omega}}(k) \tag{1.77}$$

This equation is solved in the Fourier space with an implicit Euler integration scheme

$$\hat{\boldsymbol{\omega}}^{n+1}(k) = \frac{\hat{\boldsymbol{\omega}}^{n}(k)}{1 + \frac{\Delta t}{Re}(k_x + k_y + k_z)^2}. \tag{1.78}$$

For computationally efficiency, the forward and backward FFT are only computed once on the quantities of interest $\mathbf{u}$ and $\boldsymbol{\omega}$ and the three FFT-based operator are thus solved consecutively in the general algorithm.

1.2.4 Algorithmic issues

1.2.4.1 Adaptive time step

As explained in section 1.1.3.2, in Vortex methods, instead of a CFL condition constraining the advection time step depending on the grid size, we have the so-called LCFL condition where the time step now depends on the infinity norm of the velocity gradient

$$\Delta t \leq \Delta t_{adv,1} = \frac{C_{LCFL}}{\|\nabla \mathbf{u}\|_\infty}, \tag{1.79}$$

and where the constant C_{LCFL}, called the LCFL number, must be lower or equal to 1. In practice, one also sometimes computes

$$\Delta t_{adv,2} = \frac{C_{LCFL}}{\|\boldsymbol{\omega}\|_\infty} \quad \text{and} \quad \Delta t_{adv,3} = \frac{C_{LCFL}}{\|\mathbf{S}\|_\infty}, \tag{1.80}$$

where $\mathbf{S}$ is the strain tensor. The gradients used in those expressions are computed with finite differences. Concerning the stretching equation, the stability of the time discretization is ensured by the condition [Mim15]

$$\Delta t \leq \Delta t_{stretch} = \frac{C_{stretch}}{\max\limits_i \left(\sum\limits_j \left| \frac{\partial u_i}{\partial x_j} \right| \right)} \tag{1.81}$$

where $C_{stretch}$ is a constant depending on the time-integration scheme. The diffusion and the penalization step, who are solved implicitly, do not constrain the time step. The simulation time step Δt is thus adapted at each iteration k of the overall algorithm as follows:

$$\Delta t^k = \min(\Delta t^k_{adv}, \Delta t^k_{stretch}) \tag{1.82}$$

In practice, the advection stability is found to be the most restrictive and thus the one driving the evolution of the time step.

1.2.4.2 General algorithm summary

The algorithm as well as the different numerical methods used for each step are summarized in table 1.2. The general algorithm is given by

$t^0, \Delta t^0, k \leftarrow t_{start}, \Delta t_{start}, 0$
$\boldsymbol{\omega}^0 \leftarrow \boldsymbol{\omega}(t = t_{start})$
while $t^k < t_{end}$ **do**
  $\hat{\boldsymbol{\omega}}^{*,k} \leftarrow \mathcal{F}(\boldsymbol{\omega}^k)$
  $\hat{\boldsymbol{\omega}}^k \leftarrow \texttt{reprojection}(\hat{\boldsymbol{\omega}}^{*,k})$
  $\hat{\mathbf{u}}^k, \hat{\boldsymbol{\omega}}^k \leftarrow \texttt{poisson}(\hat{\boldsymbol{\omega}}^k), \texttt{diffusion}(\hat{\boldsymbol{\omega}}^k)$
  $\boldsymbol{\omega}^k, \mathbf{u}^k \leftarrow \mathcal{F}^{-1}(\hat{\boldsymbol{\omega}}^k), \mathcal{F}^{-1}(\hat{\mathbf{u}}^k)$
  $\boldsymbol{\omega}^{k,0} \leftarrow \boldsymbol{\omega}^k$
  for i from 0 to D-1 (with D the number of directions) **do**
    $\boldsymbol{\omega}^{k,2i+1} \leftarrow \texttt{directional-advec}_{\texttt{i+1}}(\boldsymbol{\omega}^{k,2i}, \Delta t^k, u^k_{i+1})$
    $\boldsymbol{\omega}^{k,2i+2} \leftarrow \texttt{directional-remesh}_{\texttt{i+1}}(\boldsymbol{\omega}^{k,2i+1})$
  end for
  for i from 0 to D-1 (with D the number of directions) **do**
    $\boldsymbol{\omega}^{k,i+7} \leftarrow \texttt{directional-stretch}_{\texttt{i+1}}(\boldsymbol{\omega}^{k,i+6}, \Delta t^k, \mathbf{u}^k)$
  end for
  $\boldsymbol{\omega}^{k+1} \leftarrow \boldsymbol{\omega}^{k,3i+3}$
  $\Delta t^{k+1} \leftarrow \texttt{adapt-dt}(\boldsymbol{\omega}^{k+1}, \mathbf{u}^k, \Delta t^k)$
  $t^{k+1} \leftarrow t^k + \Delta t^{k+1}$
  $k \leftarrow k + 1$
end while

Fractional steps		Time integration	Space discretization	Subsection
1) Solenoidal reprojection	$\Delta\boldsymbol{\omega} = \Delta\boldsymbol{\omega}^* - \nabla(\nabla \cdot \boldsymbol{\omega}^*)$	-	spectral method (`FFTW`) (grid)	1.2.3.2
2) Poisson equation	$\Delta\mathbf{u} = -\nabla \times \boldsymbol{\omega}$	-	spectral method (`FFTW`) (grid)	1.2.3.3
3) Diffusion	$\partial_t\boldsymbol{\omega} = \frac{1}{Re}\Delta\boldsymbol{\omega}$	implicit Euler	spectral method (`FFTW`) (grid)	1.2.3.4
4) Advection-remeshing (directional)				1.2.2.2
a) Advection	$\begin{cases} d_t\mathbf{x}_p &= \mathbf{u}(\mathbf{x}_p(t), t) \\ d_t\boldsymbol{\omega} &= 0 \end{cases}$	RK2	Lagrangian (particles)	1.1.1.2
b) Remeshing	$\boldsymbol{\omega}(\mathbf{x}) = \sum_p \boldsymbol{\omega}_p(\mathbf{x})\Lambda(\frac{\mathbf{x}_p - \mathbf{x}}{\Delta\mathbf{x}})$	-	$\Lambda_{4,2}$ kernel (particles to grid)	1.1.2.2
5) Stretching (directional)	$\partial_t\boldsymbol{\omega} = (\boldsymbol{\omega} \cdot \nabla)\,\mathbf{u}$	RK3	4^{th} order centered FD (grid)	1.2.2.3
6) Adaptive time step	$\Delta t(t)$	-	4^{th} order centered FD (grid)	1.2.4.1

Table 1.2: Summary of the algorithm defining the different steps of the solution of the Navier-Stokes equations in the present RVM approach.

1.2.4.3 Remaining issues

The `Hysop` library is a scientific research software that is continuously upgraded and some developments are still needed to allow its usage as a general fluid dynamics software.

The range of boundary conditions that can be prescribed is still limited due to the inherent difficulty of implementing non-periodic boundary conditions in a FFT code (one recalls that the

Poisson solver is essentially implemented on a FFT-based topology in `Hysop`). The work from Keck [Kec19] has allowed to extend FFT operators to Dirichlet and Neumann homogeneous boundary conditions by transforming the discrete Fourier transform in a discrete sine transform or a discrete cosine transform [Mar94] but `Hysop` still misses the implementation of general non-homogeneous boundary conditions. Furthermore, no-slip boundary conditions are currently handled with a Brinkman penalization method that is only first order. This method could be improved with the Image Point Correction method (IPC) [BHI14] ensuring a second-order accuracy. In the following, we will only consider periodic or uniform Dirichlet boundary conditions (which will be enforced with penalization).

Finally, the current version of `Hysop` only proposes a grid discretization on a fixed regular Cartesian grid (i.e. $\Delta x, \Delta y, \Delta z$ are constant in space and time), while not necessarily uniform (i.e. one may have $\Delta x \neq \Delta y \neq \Delta z$). This configuration therefore does not allow, currently, for grid refinement near walls or adaptation to complex domain geometries. Although the remeshing step naturally imposes a Cartesian grid, work on adaptive mesh refinement has been done in the context of remeshed Vortex Methods relying on dividing the domain in blocks of different refinements that are modified dynamically depending on the velocity or vorticity gradients [BCK05, EOP10, RCW11] or on wavelet fields decomposition [BK06, RHvR$^+$15]. Such mesh refinement techniques are strongly envisioned as future developments within the `Hysop` library.

Conclusion

In this chapter we presented in a first part the method on which this thesis is based to solve the incompressible Navier-Stokes equations: the Remeshed Vortex Methods (RVM). They are based on the vorticity-velocity formulation of the governing equations. The advection of vorticity is solved by discretizing the field on numerical particles. The particles are then remeshed on an underlying Cartesian grid to ensure a control of the particles distancing and to avoid the numerical instabilities related to the phenomenon of particle clustering. The introduction of a Cartesian mesh allows the use of Eulerian methods to solve the other operators constituting the governing equations, i.e. the diffusion, the stretching and the Poisson equation and to solve the issue of particle field distortion while retaining the low diffusivity inherent to Lagrangian approaches as well as the lack of a CFL condition. In a second part, we presented the library `Hysop` used throughout this work and we detailed the different numerical operators which constitute the different stages of our fractional-step algorithm.

In the following chapter, we will discuss the question of subgrid scale modeling in the context of Remeshed Vortex Methods for the simulation of turbulent flows.

Chapter 2

Subgrid-Scale Modeling

Contents

Introduction

In this work we are interested in modeling turbulent flows using the Remeshed Vortex Method introduced in the previous chapter. Turbulence modeling is a complex and active area of research in computational fluid mechanics, with most studies relying on the velocity-pressure formulation of the Navier-Stokes equations. Given its prevalence, we begin by presenting turbulence models in that context before narrowing our focus to approaches based on the vorticity-velocity formulation.

In this chapter we will first introduce turbulence, its key characteristics, and the challenges associated with its numerical simulation. We will then give an overview of the methods and models used in the velocity-pressure and vorticity-velocity formulation of the Navier-Stokes equations. Finally, we will make an assessment of the advantages and challenges of Remeshed Vortex Methods in the context of turbulence simulations.

2.1 Turbulence modeling

2.1.1 Introduction to turbulence

Before introducing the numerical aspect of turbulence modeling, we briefly introduce turbulence from a physical point of view.

2.1.1.1 Characterization

Turbulence is a physical phenomenon arising in flow motions. Although there is no definitive definition of turbulence, it is often characterized by the chaotic evolution of the flow's velocity field and the wide range of scales involved which are coupled in a non-trivial way. Turbulence is inherently 3D. These characteristics make a turbulent flow difficult to predict and numerically simulate, as opposed to a laminar flow.

The main tool in characterizing turbulence is the Reynolds number. Given a typical length scale L and a mean velocity U, it is defined as

$$Re = \frac{UL}{\nu} \tag{2.1}$$

The higher the Reynolds number, the more turbulent a flow is. The limit between laminar and turbulent is not clearly defined and depends on the test case considered. Usually, there is a first critical Reynolds number that marks the shift from a laminar to a transitional state and another for the shift to a turbulent state.

2.1.1.2 The energy cascade

Although the characterization of turbulence is a difficult task, an important notion in the theory of turbulence is the energy cascade, i.e. the idea that, in turbulence, different scales of eddies co-exist and that energy is transmitted from the largest to the smallest scales. As Lewis F. Richardson [Ric22] famously puts it:

"Big whirls have little whirls
that feed on their velocity,
And little whirls have lesser whirls
and so on to viscosity."

The point, referred in the poem as "viscosity", where little whirls cease to have lesser whirls is the Kolmogorov scale, where energy is dissipated into heat due to viscous forces. The higher the viscosity, the larger this scale is.

The energy spectrum is defined in a homogeneous isotropic turbulent flow as $E(k) = 2\pi k^2 |\hat{\mathbf{u}}(k)|^2$ where $\hat{\mathbf{u}}$ is the Fourier transform of the velocity $\mathbf{u}$ and k represent the eddies' wavenumber. It is represented in figure 2.1. Kolmogorov's hypothesis states that in the inertial range, where the transfer of energy between scales occurs, the energy spectrum has the form

$$E(k) \sim k^{-5/3}. \tag{2.2}$$

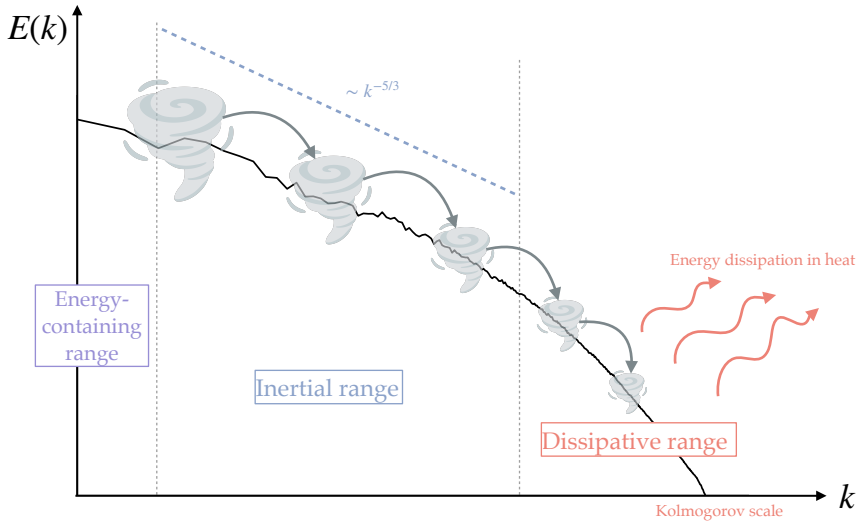

Figure 2.1: Schematic representation of the energy cascade in turbulence

The energy cascade explains the difficulty to solve numerically turbulent flows: to have a good representation of the physics of the flow, one must solve the whole range of spatial and temporal scales, up to the Kolmogorov scale where the energy is dissipated, otherwise there will be a build-up of energy at the smallest resolved scales since they will not be able to transfer their energy to smaller scales. This build up can lead to instabilities. Furthermore, the interactions between large and small scales are complex and although the main mechanism is the energy transfer from larger to smaller scales, there is a back-scatter effect that can be important to capture the physics of a flow. Lacking small scales can thus result in inaccurate results.

For these reasons, we need a a fine resolution of the spatial scales to capture the Kolmogorov scale if we want a complete and stable simulation of the flow. The Kolmogorov scale being related to the Reynolds number, this means that the more turbulent the flow is, the finer the spatial resolution must be. More precisely, in the context of a three dimensional flow disctretized on a Cartesian grid, the relation between the number of mesh points N^3 and the Reynolds number Re is

$$N^3 \gtrapprox Re^{9/4} \tag{2.3}$$

meaning that for most industrial applications involving turbulent flows, where Re is very large, between 10^4 and 10^8, a direct approach would be either very expensive or not feasible with current computational and memory capacities. For that reason, a number of approaches to reduce the cost of turbulent flow simulations have been introduced.

2.1.2 Approximation methods

In the following, we will present the filtered Navier-Stokes equations and the two main families of approaches based on theses equations (see figure 2.2): methods based on statistical averaging of the flow (RANS) and based on scale-separation (LES). RANS remain the most widely used techniques in industry due to its lower cost whereas LES, requiring finer resolutions, is currently

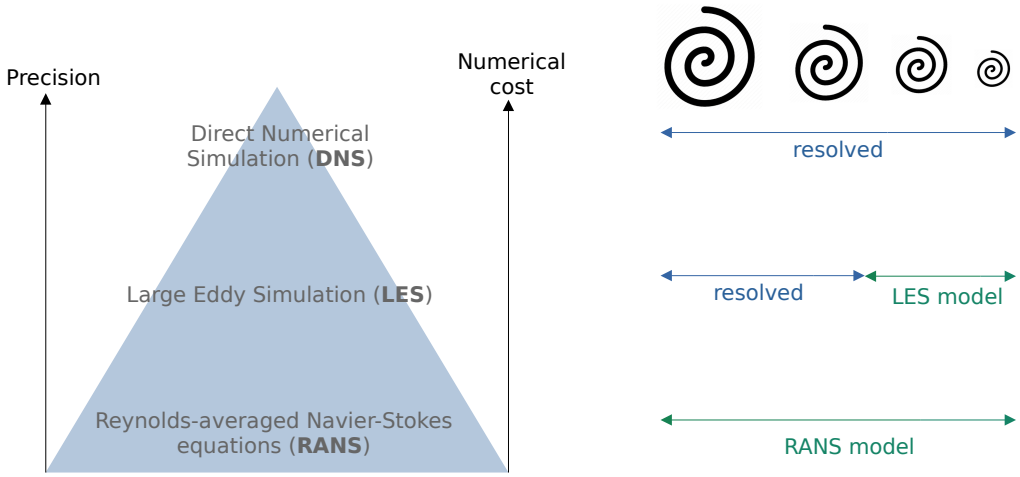

Figure 2.2: Strategies to model turbulence.

mostly used for academic applications, although its popularity is growing with the increase of computational capacities. Hybrid RANS-LES approaches, such as Detached Eddy Simulations (DES) [SJSA97], where wall-bounded flows are solved with RANS near the boundary and with LES away from the boundary, have also been successful for several years now.

2.1.2.1 Filtered Navier-Stokes equations

Most methods for turbulence modeling make use of a scale separation operator $\mathcal{F}$, which is required to be linear and to commute with derivatives. In this setting, a variable of the problem will be decomposed as follows:

$$f = \bar{f} + f' \tag{2.4}$$

where $\bar{f} = \mathcal{F}(f)$ is the resolved part of the variable and f' the unresolved part. We can then rewrite the Navier-Stokes:

$$\begin{cases} \dfrac{\partial \overline{\mathbf{u}}}{\partial t} + (\overline{\mathbf{u}} \cdot \nabla)\overline{\mathbf{u}} = -\dfrac{1}{\rho}\nabla \bar{p} + \dfrac{1}{Re}\Delta \overline{\mathbf{u}} - \nabla \cdot \tau \\ \nabla \cdot \overline{\mathbf{u}} = 0 \end{cases} \tag{2.5}$$

where $\tau = \overline{\mathbf{u} \otimes \mathbf{u}} - \overline{\mathbf{u}} \otimes \overline{\mathbf{u}}$ is called the subgrid stress tensor and represents the interactions between the resolved and unresolved scales. Since it depends on information we do not have access to, it needs to be approximated.

We can further decompose τ in the following way

$$\tau = \overline{\overline{\mathbf{u}} \otimes \overline{\mathbf{u}}} - \overline{\mathbf{u}} \otimes \overline{\mathbf{u}} + \overline{\mathbf{u}' \otimes \overline{\mathbf{u}}} + \overline{\overline{\mathbf{u}} \otimes \mathbf{u}'} + \overline{\mathbf{u}' \otimes \mathbf{u}'} \tag{2.6}$$

where $L = \overline{\overline{\mathbf{u}} \otimes \overline{\mathbf{u}}} - \overline{\mathbf{u}} \otimes \overline{\mathbf{u}}$ is the Leonard tensor, which represents the fluctuations within the resolved scales and can be computed from the resolved quantities, $C = \overline{\mathbf{u}' \otimes \overline{\mathbf{u}}} + \overline{\overline{\mathbf{u}} \otimes \mathbf{u}'}$ is the cross stress tensor that represents the interactions between the resolved and subgrid scales and $R = \overline{\mathbf{u}' \otimes \mathbf{u}'}$ is the Reynolds subgrid stress tensor which represents the effect of the subgrid scales on the resolved field.

2.1.2.2 Reynolds-Averaged Navier-Stokes (RANS)

Reynolds-Averaged Numerical Simulation (RANS) are based on an averaging of the flow. The scale separation operator F is here a statistical averaging operator. In that case $\bar{f}$ represents the time-averaged value of f,

$$\bar{f}(t) = \int_{t-T}^{T} f(s)ds \tag{2.7}$$

and f' its fluctuations. This decomposition was first proposed by Reynolds [Rey95], hence its name. The Reynolds-averaged Navier-Stokes thus write

$$\begin{cases} \dfrac{\partial \overline{\mathbf{u}}}{\partial t} + (\overline{\mathbf{u}} \cdot \nabla)\overline{\mathbf{u}} = -\dfrac{1}{\rho}\nabla \bar{p} + \dfrac{1}{Re}\Delta \overline{\mathbf{u}} - \nabla \cdot \tau_{RANS} \\ \nabla \cdot \overline{\mathbf{u}} = 0 \end{cases} \tag{2.8}$$

with $\tau_{RANS} = \overline{\mathbf{u}' \otimes \mathbf{u}'}$ the Reynolds stress tensor. We have in this approach $L = C = 0$. τ_{RANS} cannot be expressed using the resolved field and a closure model has to be introduced.

2.1.2.3 Large Eddy Simulation (LES)

Large Eddy Simulations (LES) rely on a separation of the large and small scales of the flow (see figure 2.3) using a low-pass filter G_Δ, where Δ is the cutoff scale, usually proportional to the grid size. We have then

$$\bar{f} = G_\Delta \star f \tag{2.9}$$

Because the smallest scales are ignored, a Sub-Grid Scale (SGS) model is needed to model their

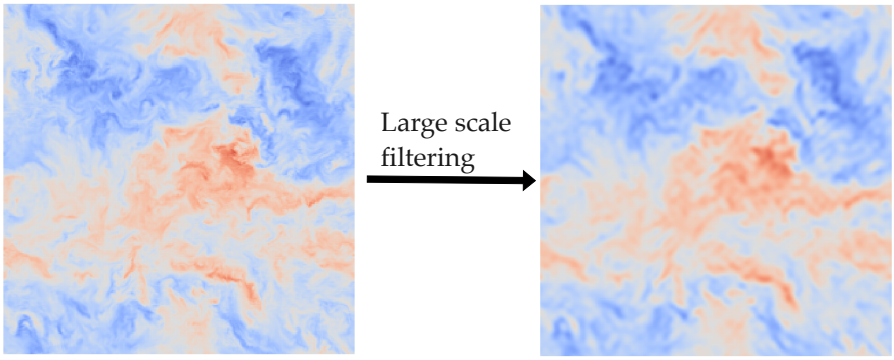

Figure 2.3: Example of a filtered velocity field.

effects. The filtered Navier-Stokes equations write

$$\begin{cases} \dfrac{\partial \overline{\mathbf{u}}}{\partial t} + (\overline{\mathbf{u}} \cdot \nabla)\overline{\mathbf{u}} = -\dfrac{1}{\rho}\nabla \bar{p} + \dfrac{1}{Re}\Delta \overline{\mathbf{u}} - \nabla \cdot \tau_{SGS} \\ \nabla \cdot \overline{\mathbf{u}} = 0 \end{cases} \tag{2.10}$$

with $\tau_{SGS} = \overline{\mathbf{u} \otimes \mathbf{u}} - \overline{\mathbf{u}} \otimes \overline{\mathbf{u}}$ representing the interactions between the resolved larger scales and the unresolved sub-grid smaller scales.

Among common filters, we can cite

- the box or top-hat filter
$$\hat{G}(k) = \frac{\sin(k\Delta/2)}{k\Delta/2},$$
- the cutoff filter
$$\hat{G}(k) = \begin{cases} 1 & \text{if } |k| \leq \frac{\pi}{\Delta} \\ 0 & \text{otherwise} \end{cases},$$
- the Gaussian filter
$$\hat{G}(k) = \exp\left(\frac{-D^2k^2}{24}\right).$$

Other filters which can be applied both in Fourier and physical space are the filters based on finite difference stencils [Lel92].

In practise, G is implicit: the filtering of the small scales is done by using a resolution too coarse to reach Kolmogorov's scale, although explicit filters are used when needing a further separation of the resolved scales.

2.2 Subgrid-Scale modeling for velocity-pressure methods

In this section, we present a brief overview of the subgrid-scale models used in LES for classical methods based on the velocity-pressure $(\mathbf{u} - p)$ formulation of the Navier-Stokes equations. These models are usually classified in two categories: functional and structural [Sag06] (see figure 2.4).

Functional modeling of small scales is based on the idea that the importance of the subgrid scales is the dissipation of the energy transfered from the resolved scales. Therefore, these models are purely disssipative models and are usually based on adding a non-constant artificial viscosity term to the filtered Navier-Stokes equations. These models do not account for backscatter, which is usually considered negligible compared to the transfer of energy from large to small scales [VM22].

On the other hand, structural models are based on modeling directly the subgrid-scale tensor. This modeling can be done through a formal series expansion or using self-similarity. It is to be noted that, although they are the most accurate in *a priori* tests, they are often not dissipative enough on their own. For that reason they are often coupled with a clipping procedure or with a functional model.

Some models fall in between these two categories as for example, mixed models combining a structural and a functional modeling approach or the dynamic version of the Smagorinsky model [GPMC91, Lil92] that uses structural assumptions for its parameter computation procedure.

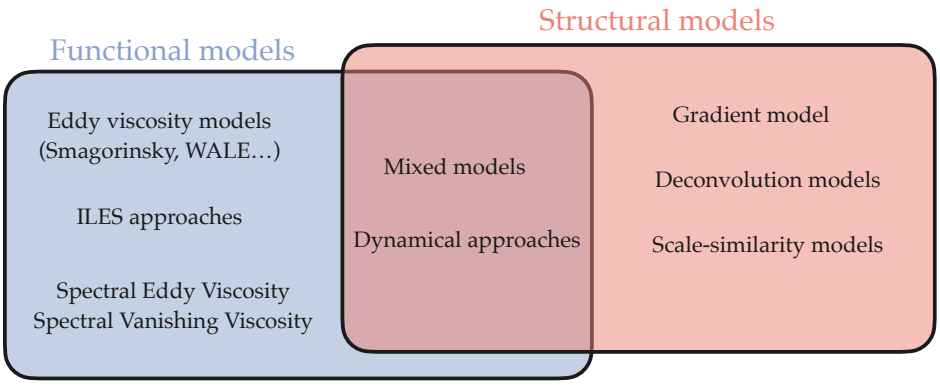

Figure 2.4: Families of subgrid-scale models for LES.

2.2.1 Eddy-viscosity models

In eddy-viscosity (also called artificial viscosity) models, the subgrid scales are modelled by a term of the form

$$\tau_{ij}^{SGS} = -2\nu_{SGS}\overline{\mathbf{S}}_{ij}, \tag{2.11}$$

meaning that the dissipation is proportional to the strain rate tensor, as stated by the Boussinesq hypothesis [Bou77]. This model lead to a symmetric, Galilean invariant tensor.

Models differ in the expression of the viscosity term ν_{SGS}, which is often written as a function of a coefficient, a length scale $\overline{\Delta}$ related to the implicit grid filtering and a velocity scale. We present in the following two of the most well-known of these models, applied in the physical space, and their variations. Other well-known eddy-viscosity models include the Structure-Function model introduced by Metais and Lesieur [ML92] and Vreman's model [Vre04].

2.2.1.1 Smagorinsky

The most well-known closure model for the scale-filtered Navier-Stokes is a functional model introduced by Smagorinsky [Sma63]. It is written as

$$\nu_{SMAG} = 2(C_S\overline{\Delta})^2|\bar{\mathbf{S}}|. \tag{2.12}$$

Here $\bar{\mathbf{S}} = \frac{1}{2}(\nabla\overline{\mathbf{u}} + \nabla^T\overline{\mathbf{u}})$ denotes the strain tensor, $|\bar{\mathbf{S}}| = \sqrt{\bar{\mathbf{S}}_{pq}\bar{\mathbf{S}}_{pq}}$ is the magnitude of $\mathbf{S}$, C_S is the model coefficient and $\overline{\Delta}$ the characteristic scales. Classically, C_S is taken to be around 0.16 and, on a regular Cartesian grid, $\overline{\Delta}$ is usually the space step.

This model is one of the simplest and cheapest that yields a realistic decay of kinetic energy. However this model assumes that the smallest scales are purely dissipative and therefore does not account for backscatter. Furthermore, it is known to be over-dissipative for moderate Reynolds flows and its coefficient needs to be adapted to the turbulent flow considered (which can be done in a dynamical way). Finally, it does not have a good behavior near a wall, as the subgrid-scale viscosity does not go to 0 in that case.

2.2.1.2 Wall-Adapting Local Eddy-viscosity (WALE)

The WALE model was introduced by Nicoud and Ducros [ND99] to solve the issue of the asymptotic behaviour of the flow near a wall. Its eddy viscosity was designed to vanish near solid surfaces and is given by

$$\nu_{WALE} = C_W \overline{\Delta}^2 \frac{(\overline{\mathcal{S}}_{ij}^d \overline{\mathcal{S}}_{ij}^d)^{3/2}}{(\overline{S}_{ij}\overline{S}_{ij})^{5/2} + (\overline{\mathcal{S}}_{ij}^d \overline{\mathcal{S}}_{ij}^d)^{5/4}} \tag{2.13}$$

where C_W is a coefficient to be chosen, $\overline{\mathcal{S}} = \overline{S}_{ik}\overline{S}_{kj} + \overline{\Omega}_{ik}\overline{\Omega}_{kj}$ with $\overline{\Omega} = \frac{1}{2}(\nabla\overline{\mathbf{u}} - \nabla\overline{\mathbf{u}}^T)$ the rotation rate tensor and $\overline{\mathcal{S}}_{ij}^d = \overline{\mathcal{S}}_{ij} - \frac{1}{3}\overline{\mathcal{S}}_{kk}\delta_{ij}$. This model is well adapted to near-wall flows since its viscosity is equal to 0 in that case. However, in pure rotational flows its viscosity is proportional to the vorticity. It is therefore less adapted to cases without wall boundary conditions and where we wish to preserve the largest vortex structures.

2.2.1.3 Dynamical coefficients

Smagorinsky and other eddy-viscosity model depend on an arbitrary coefficient. However, the optimal coefficient vary depending on the test case considered or the regime of the flow and may not be the same in the whole simulation domain when considering strongly inhomogeneous flows. The optimal coefficient can also vary in time when simulating the growth of turbulence. For these reasons, dynamical procedures have been developed to adapt the coefficient in time and space.

The most well-known use of a dynamical coefficient is Germano *et al.* 's dynamic Smagorinsky model [GPMC91] that uses test-filtering to dynamically adapt the Smagorinsky model's coefficient in time and space. It can however be applied to other models and we will present the approach for a generic model that writes

$$\tau_{SGS} = Cf(\bar{\Delta}, \overline{\mathbf{u}}), \tag{2.14}$$

with C the coefficient to be optimized.

The Germano approach is based on explicitly filtering the resolved velocity field with some filter G such that

$$\hat{\overline{\mathbf{u}}} = G * \overline{\mathbf{u}} \tag{2.15}$$

The explicitly filtered Navier-Stokes equations write

$$\begin{cases} \dfrac{\partial\hat{\overline{\mathbf{u}}}}{\partial t} + (\hat{\overline{\mathbf{u}}}\cdot\nabla)\hat{\overline{\mathbf{u}}} = -\dfrac{1}{\rho}\nabla\widehat{\overline{p}} + \dfrac{1}{Re}\Delta\hat{\overline{\mathbf{u}}} - \nabla\cdot\hat{\tau} \\ \nabla\cdot\hat{\overline{\mathbf{u}}} = 0 \end{cases} \tag{2.16}$$

with

$$\widehat{\tau} = G * (\overline{\mathbf{u}\otimes\mathbf{u}} - \overline{\mathbf{u}}\otimes\overline{\mathbf{u}}) + \widehat{\overline{\mathbf{u}}\otimes\overline{\mathbf{u}}} - \hat{\overline{\mathbf{u}}}\otimes\hat{\overline{\mathbf{u}}} = G*\tau + L \tag{2.17}$$

which correspond to the sum of the explicit filter applied to the subgrid scale tensor τ and the subgrid scale Leonard tensor L arising from the explicit filtering. The assumption being made

in this model is that the optimal subgrid scale model coefficient for the second level of filtering is the same as for the first (implicit) level of filtering.

Writing the subgrid scale model for the implicit filtering,

$$\tau_{SGS} = Cf(\bar{\Delta}, \overline{\mathbf{u}}), \tag{2.18}$$

we search for C such that C is optimal for the subgrid scale model for the explicit filtering

$$\tau^G_{SGS} = Cf(\widehat{\bar{\Delta}}, \widehat{\overline{\mathbf{u}}}). \tag{2.19}$$

In order to do that, we define the residual E that we seek to minimize

$$E = \tau^G_{SGS} - G * (\tau_{SGS}) - \tau^G = C(f(\widehat{\bar{\Delta}}, \widehat{\overline{\mathbf{u}}}) - G * f(\bar{\Delta}, \overline{\mathbf{u}}) - L = CM - L. \tag{2.20}$$

The least-square optimization problem to be solved is thus "find $C(x,t)$ such that $E_{ij}E_{ij}$ is minimal". We write

$$\frac{\partial E_{ij}E_{ij}}{\partial C} = 0 \tag{2.21}$$

and obtain

$$C = \frac{L_{ij}M_{ij}}{M_{ij}M_{ij}}. \tag{2.22}$$

However this procedure can lead to divisions by zero in certain parts of the domain. For that reason, averaging procedures have been developed by [Lil92, GLMA95]. In this modified method, the coefficient is given by

$$C = \frac{\langle L_{ij}M_{ij}\rangle}{\langle M_{ij}M_{ij}\rangle}, \tag{2.23}$$

where the brackets usually represent averaging over directions of statistical homogeneity. Other averaging approaches exists, Meneveau *et al.* [MLC96] introduced for example an averaging based on the time-average of the path lines of flow particles. Although the Smagorinsky model remains the most widely used subgrid-scale model, dynamical approaches have be used for other models, such as the Vreman model [YM07].

2.2.1.4 Variational multi-scale models

Another variant of classical models is the variational multiscale (VMS) family of models. VMS models, introduced by Hughes *et al.* [HMOW01] aim to circumvent the excessive diffusion of the largest scales introduced by classical eddy-viscosity models. This is done by applying the artificial viscosity only to the smallest of the resolved scales, thus requiring an additional explicit small-scale filtering (see figure 2.5).

Let f be some resolved field, we define, in Fourier space, the largest resolved scales of f by $\widehat{f}(k) = \widehat{G}(k)f(k)$ where $\widehat{G}$ is some test filter, and the smallest resolved scales f_S by $f_S = f - \widehat{f}$. One therefore defines the VMS-Smag model by:

$$\tau_{SGS} = -\nu_{SGS}(\nabla\overline{\mathbf{u}}_S + \nabla\overline{\mathbf{u}}_S^T) \tag{2.24}$$

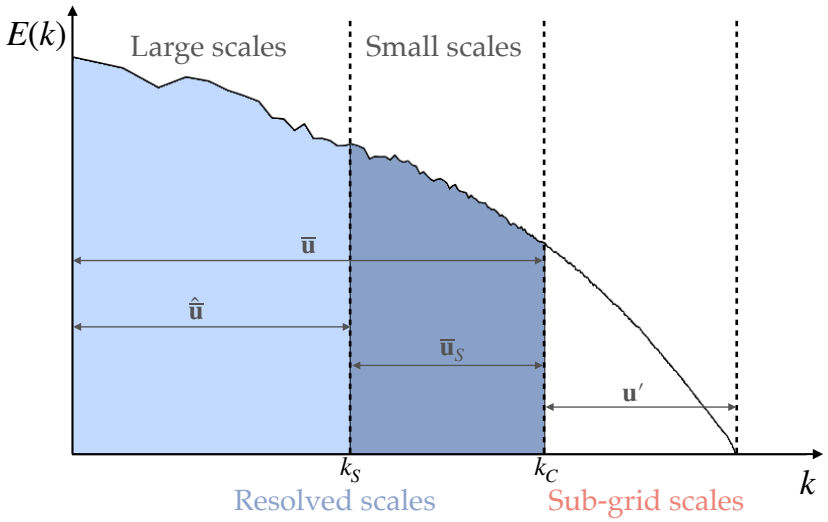

Figure 2.5: Schematic representation of the scale-separation principle behind VMS approaches.

where $\overline{\mathbf{u}}_S$ denotes the small scales of the resolved velocity field and where the eddy viscosity ν_{SGS} is defined as in the Smagorinsky model, either from the filtered large scales of the velocity fields $\widehat{\overline{\mathbf{u}}}$, in which case the model is said to be 'large-small', or from the small scales of the velocity fields $\overline{\mathbf{u}}_S$, which leads to the 'small-small' model.

2.2.1.5 Extension to anisotropic grids

Subgrid-scales models were conceived with isotropic Eulerian grids in mind. In that case, the length scale $\overline{\Delta}$ is simply defined as the step size. However, for most applications, anisotropic or unstructured grids are used for computational efficiency reasons. Very soon, the question of how to define a length scale in that context was posed.

The simplest answer consist in taking simply either the geometric mean [Dea70] or the maximum [SJSA97] of the directional step sizes

$$\overline{\Delta}_{vol} = \sqrt{\Delta x \Delta y \Delta z} \qquad \overline{\Delta}_{max} = \max(\Delta x, \Delta y, \Delta z). \tag{2.25}$$

Chauvet *et al.* [CDJ07] proposed an approach based on the vorticity vector,

$$\overline{\Delta}_{\boldsymbol{\omega}} = \frac{1}{|\boldsymbol{\omega}|}\sqrt{\boldsymbol{\omega}_x^2 \Delta y \Delta z + \boldsymbol{\omega}_y^2 \Delta x \Delta z + \boldsymbol{\omega}_z^2 \Delta x \Delta y}, \tag{2.26}$$

which was then improved by Mockett *et al.* [MFG+15]. Trias *et al.* [TGS+17] recently introduced another length scale based on the subgrid stress tensor.

A comparison of these different options for strongly anisotropic grids with different models and different grid configurations was conducted by [STL20] and concluded that while no scale was better than the other in every configuration, $\overline{\Delta}_{max}$ was generally the most robust to the grid anisotropy and $\overline{\Delta}_{vol}$ the least robust.

2.2.2 Other functional approaches

Other, less classical approaches can be considered functional in the sense that they are based on mimicking the diffusive effect of the small scales, and do not stem from the analytical expression of the subgrid-scale tensor.

2.2.2.1 Spectral Eddy Viscosity and Spectral Vanishing Viscosity models

Spectral Eddy Viscosity (SEV) and Spectral vanishing viscosity (SVV) models are based on a similar idea than eddy-viscosity models, they add a new viscosity term to the Navier-Stokes equation to model the subgrid scales. This viscosity term is added in the spectral domain and is scale-dependant.

SEV models were introduced by Chollet and Leiseur [CL81] to evaluate the viscosity needed at the cutoff to reproduce the $k^{-5/3}$ energy spectrum of homogeneous turbulence. This viscosity is dependant on the kinetic energy at the cutoff. It is the basis for the structure function model [ML92] in the physical space.

SVV models, on the other hand, were first introduced in another context by [Tad89, MT89, MKT93] to regularize hyperbolic problems solved by spectral methods. They were then used for LES of Navier-Stokes [KK00, KK02, KS06, Pas06, Pas05]. They consists in adding progressively viscosity to the end of the spectrum, where non-physical oscillations may occur. The coarser scales remain untouched, which makes them similar to the VMS model presented previously.

In Fourier space, the modified diffusion operator writes:

$$\partial_t \hat{\mathbf{u}} = -k_x^2(1/Re + \nu_S(k_x)) + k_y^2(1/Re + \nu_S(k_y)) + k_z^2(1/Re + \nu_S(k_z)))\hat{\mathbf{u}} \tag{2.27}$$

in Chollet and Leiseur's SEV method the spectral viscosity ν_S is given by

$$\nu_s(k) = (0.267 + 9.21e^{-3.03k_c/k})\sqrt{E_{kc}/k_c} \tag{2.28}$$

and in SVV, ν_S is given by the expression introduced by [MKT93]:

$$\nu_s(k) = \begin{cases} 0 & \text{if } k < k_m \\ \nu_0 \exp\left[-\left(\frac{k_c - k}{k_m - k}\right)^2\right] & \text{if } k_m \leq k \leq k_c \end{cases} \tag{2.29}$$

where k_c is the wavenumber at the cutoff scale. The SVV technique depends then on two parameters: the artificial viscosity intensity ν_0 and the cutoff wavenumber k_m from which the artificial viscosity is added.

In the literature, a scaling of the SVV viscosity ν_0 by $\frac{1}{kc}$ (meaning that the SVV viscosity becomes negligible as the resolution increases) has been studied by Pasquetti [Pas05] in the context of a LES of the turbulent wake around a cylinder. Other approaches include scaling the viscosity with the velocity field [KK02], the ratio of the Kolmogorov scale to the resolved scale [DLLV17] or using the artificial viscosity given by the Smagorinsky model [MFRV20].

2.2.2.2 Implicit Large Eddy Simulations

Implicit Large Eddy Simulation (ILES) relies on the idea that the numerical diffusion introduced by the numerical method used to solve the filtered Navier-Stokes equations is sufficient

to account for the missing energy diffusion. Consequently, this approach does not require an explicit subgrid-scale (SGS) model.

The core principle of ILES is that since LES inherently under-resolves the Navier-Stokes equations, subgrid-scale modeling must be considered in conjunction with the numerical method employed [Bor90]. In some cases, the SGS model can be of the same order of magnitude as the truncation error of the method [Gho96]. In ILES, this truncation error itself serves as the SGS model. A well-known variant of this approach is the Monotone Integrated LES (MILES) [BGOK92]. We refer to the book by Grinstein *et al.* [GMR07] for an overview of the different ILES approaches and their applications.

Recently, Lamballais *et al.* [LFL11] introduced an ILES approach based on finite difference methods: the stencil used for the diffusion equation is modified to introduce a SVV-like artificial viscosity to the smaller scales of the flow. The SVV method can thus be used in a non-spectral code. A comparison between this approach and a classical eddy-viscosity model is presented in [DLLV17].

2.2.3 Structural models

2.2.3.1 Self-Similarity approaches

Bardina *et al.* 's [BFR80] self-similarity model is based on the idea that scales in turbulence are self similar, thus the relationship between resolved and subgrid scales is the same as the one between explicitely filtered and non filtered scales.

The model thus writes

$$\tau_{ij} = \widehat{\overline{\mathbf{u}}_i\overline{\mathbf{u}}_j} - \widehat{\overline{\mathbf{u}}}_i\widehat{\overline{\mathbf{u}}}_j. \tag{2.30}$$

However, in practise, the model is found to be not dissipative enough. For that reason, Bardina combines it with an eddy-viscosity model such that the new, mixed model writes

$$\tau_{ij} = C_B\widehat{\overline{\mathbf{u}}_i\overline{\mathbf{u}}_j} - \widehat{\overline{\mathbf{u}}}_i\widehat{\overline{\mathbf{u}}}_j - 2\nu_{SGS}\mathbf{S}_{ij}. \tag{2.31}$$

This mixed approach was used by Zang *et al.* with a dynamical Smagorinsky model as the eddy-viscosity model [ZSK93] and Salvetti and Banerjee [SB95] further improved it by introducing a second dynamical coefficient for the structural part of the model.

2.2.3.2 Deconvolution models

Deconvolution models are based on the idea that one can reconstruct the subgrid scales from the filter's analytic expression. The assumption made is that the filter G can be reversed, i.e. there exist an inverse operation G^{-1} such that

$$\mathbf{u} = G^{-1} \star \overline{\mathbf{u}} = G^{-1} \star G \star \mathbf{u}. \tag{2.32}$$

The subgrid-scale term can thus be reconstructed from the resolved fields. In practise, the exact expression of the filter is not known and the inverse operation is thus an approximated one.

An example of such an approach is the Approximate Deconvolution Model (ADM) proposed by Stolz *et al.* [SAK01] where the inverse filtering operation is approximated through a polynomial expansion of the filter kernel.

2.2.3.3 Gradient model

A special case of a deconvolution model is the gradient model, first derived by Leonard [Leo75a] and Clark *et al.* [CFR79] and modified by Vreman [Vre95]. It is based on the Taylor expansion of the filtered fields. We make the assumption that our filter G of size $\bar{\Delta}$ is such that

$$\overline{\mathbf{u}} = G \star \mathbf{u} = \mathbf{u} + \frac{\bar{\Delta}^2}{24}\partial_k^2 \mathbf{u} + O(\bar{\Delta}^4). \tag{2.33}$$

This holds for example for the top-hat and the Gaussian filter. Using this expression now to evaluate the subgrid-scale tensor

$$\tau_{ij} = \overline{\mathbf{u}_i \mathbf{u}_j} - \overline{\mathbf{u}}_i \overline{\mathbf{u}}_j \tag{2.34}$$

$$= \mathbf{u}_i \mathbf{u}_j + \frac{\bar{\Delta}^2}{24}\partial_k^2(\mathbf{u}_i \mathbf{u}_j) + O(\bar{\Delta}^4) - (\mathbf{u}_i + \frac{\bar{\Delta}^2}{24}\partial_k^2 \mathbf{u}_i + O(\bar{\Delta}^4))(\mathbf{u}_j + \frac{\bar{\Delta}^2}{24}\partial_k^2 \mathbf{u}_j + O(\bar{\Delta}^4)) \tag{2.35}$$

$$= \mathbf{u}_i \mathbf{u}_j + \frac{\bar{\Delta}^2}{24}(\mathbf{u}_i \partial_k^2 \mathbf{u}_j + 2\partial_k \mathbf{u}_i \partial_k \mathbf{u}_j + \mathbf{u}_j \partial_k^2 \mathbf{u}_i) - \mathbf{u}_i \mathbf{u}_j - \frac{\bar{\Delta}^2}{24}\mathbf{u}_i \partial_k^2 \mathbf{u}_j - \frac{\bar{\Delta}^2}{24}\mathbf{u}_j \partial_k^2 \mathbf{u}_i + O(\bar{\Delta}^4) \tag{2.36}$$

$$= \frac{\bar{\Delta}^2}{12}\partial_k \mathbf{u}_i \partial_k \mathbf{u}_j + O(\bar{\Delta}^4). \tag{2.37}$$

The model thus writes

$$\tau_{SGS}(i,j) = \frac{\bar{\Delta}^2}{12}\partial_k \overline{\mathbf{u}}_i \partial_k \overline{\mathbf{u}}_j. \tag{2.38}$$

This model, as most structural models, performs well in *a priori* test but has been found to overestimate backscatter effects, for that reason, it is often completed with a regularization procedure, for example in [CJM03], the strain directions leading to a growth of enstrophy are removed and in [LPA13, VBC16], a clipping procedure ensures the dissipation rate is non-negative.

2.3 Subgrid-Scale modeling for vorticity-velocity methods

Works on subgrid-scale models in the vorticity-velocity ($\boldsymbol{\omega} - \mathbf{u}$) formulation are scarcely represented in the literature, particularly when using a semi-Lagrangian numerical method like the present one. We present here a review of some models used in the literature. Although most of the models presented are used in Lagrangian or semi-Lagrangian codes, some authors have also used the $\boldsymbol{\omega} - \mathbf{u}$ formulation in LES with Eulerian methods. We will discuss at the end of the chapter the advantages of using the semi-Lagrangian method and the $\boldsymbol{\omega} - \mathbf{u}$ formulation for Large Eddy Simulations.

2.3.1 Closure problem in velocity-vorticity

Let $\mathcal{F}$ be our filter function, then by making the same assumptions as those made for the $\mathbf{u}-p$ formulation (the filter is linear and commutes with derivatives), we obtain

$$\mathcal{F}\left(\frac{\partial \boldsymbol{\omega}}{\partial t}+\nabla\cdot(\boldsymbol{\omega}\otimes\mathbf{u}-\mathbf{u}\otimes\boldsymbol{\omega})\right)=\mathcal{F}\left(\frac{1}{Re}\Delta\mathbf{u}\right) \tag{2.39}$$

$$\mathcal{F}\left(\frac{\partial \boldsymbol{\omega}}{\partial t}\right)+\mathcal{F}(\nabla\cdot(\boldsymbol{\omega}\otimes\mathbf{u}-\mathbf{u}\otimes\boldsymbol{\omega}))=\mathcal{F}\left(\frac{1}{Re}\Delta\mathbf{u}\right) \tag{2.40}$$

$$\frac{\partial \overline{\boldsymbol{\omega}}}{\partial t}+\nabla\cdot(\overline{\boldsymbol{\omega}}\otimes\overline{\mathbf{u}}-\overline{\mathbf{u}}\otimes\overline{\boldsymbol{\omega}}+[\mathcal{F},\mathcal{B}](\boldsymbol{\omega},\mathbf{u})-[\mathcal{F},\mathcal{B}](\mathbf{u},\boldsymbol{\omega}))=\frac{1}{Re}\Delta\overline{\mathbf{u}} \tag{2.41}$$

where $\mathcal{B}(\mathbf{u},\boldsymbol{\omega})=\mathbf{u}\otimes\boldsymbol{\omega}$, $\mathcal{B}(\boldsymbol{\omega},\mathbf{u})=\boldsymbol{\omega}\otimes\mathbf{u}$ and $\bar{(\cdot)}$ denotes the quantities filtered by $\mathcal{F}$.

We now write

$$\mathbf{R}=[\mathcal{F},\mathcal{B}](\boldsymbol{\omega},\mathbf{u})-[\mathcal{F},\mathcal{B}](\mathbf{u},\boldsymbol{\omega})=\overline{\boldsymbol{\omega}\otimes\mathbf{u}}-\overline{\boldsymbol{\omega}}\otimes\overline{\mathbf{u}}-\overline{\mathbf{u}\otimes\boldsymbol{\omega}}+\overline{\mathbf{u}}\otimes\overline{\boldsymbol{\omega}} \tag{2.42}$$

such that

$$\mathbf{R}_{ij}=\overline{\boldsymbol{\omega}_i\mathbf{u}_j}-\overline{\boldsymbol{\omega}}_i\overline{\mathbf{u}}_j-\overline{\mathbf{u}_i\boldsymbol{\omega}_j}+\overline{\mathbf{u}}_i\overline{\boldsymbol{\omega}}_j \tag{2.43}$$

and we have the filtered equations:

$$\frac{\partial \overline{\boldsymbol{\omega}}}{\partial t}+\nabla\cdot(\overline{\boldsymbol{\omega}}\otimes\overline{\mathbf{u}}-\overline{\mathbf{u}}\otimes\overline{\boldsymbol{\omega}})=\frac{1}{Re}\Delta\overline{\mathbf{u}}-\nabla\cdot\mathbf{R} \tag{2.44}$$

where $\mathbf{R}$ is called the subgrid scale vorticity stress.

We note that since the Navier-Stokes equations in the $\boldsymbol{\omega}-\mathbf{u}$ formulation have two non-linear terms, the subgrid tensor can be decomposed in two parts: one related to the advection term and the other to the stretching term. According to an *a priori* analysis in [MKM98], both non-linear terms play a role in the growth of turbulence and are not correlated with each other and thus need to be both modelled.

2.3.2 Eddy-viscosity models

2.3.2.1 Derivation

One approach is to simply model the subgrid scale tensor by using the same models as for the $\mathbf{u}-p$ formulation and taking their curl. For instance, the $\boldsymbol{\omega}-\mathbf{u}$ equivalent of an eddy-viscosity model writes

$$-\nabla\cdot\mathbf{R}^{SGS}=-\nabla\times\nabla\cdot\tau^{SGS}=\nabla\times\nabla\cdot(2\nu_{SGS}\overline{\mathbf{S}})=\nabla\times(2\nu_{SGS}\nabla\cdot\overline{\mathbf{S}})+\nabla\times(2\nabla\nu_{SGS}\cdot\overline{\mathbf{S}}), \tag{2.45}$$

neglecting the second term of this expression, we obtain

$$-\nabla\cdot\mathbf{R}^{SGS}=\nabla\times(2\nu_{SGS}\nabla\cdot\overline{\mathbf{S}})=\nabla\times(\nu_{SGS}\nabla\cdot(\nabla\overline{\mathbf{u}}+\nabla\overline{\mathbf{u}}^T))=\nabla\times(\nu_{SGS}\Delta\mathbf{u})=-\nabla\times(\nu_{SGS}\nabla\times\overline{\boldsymbol{\omega}}) \tag{2.46}$$

This model was introduced by Mansour *et al.* [MFR78] and preserves the antisymmetry of $\mathbf{R}$. It can be written equivalently as

$$\mathbf{R}^{SGS} = -\nu_{SGS}(\nabla\overline{\boldsymbol{\omega}} - \nabla\overline{\boldsymbol{\omega}}^T) \tag{2.47}$$

This model has the advantage to be simple to implement and has a structure similar to classical $\mathbf{u} - p$ eddy-viscosity models. This model is the most widely used in Vortex Methods.

Mansfield *et al.* [MKM98] noted that the subgrid-scale tensor in the $\boldsymbol{\omega} - \mathbf{u}$ formulation modeled by the eddy-viscosity model above can be decomposed in two terms corresponding to the gradient diffusion term $\mathbf{g}^D = \nabla \cdot (\nu_{SGS}\nabla\overline{\boldsymbol{\omega}})$ and an additional term $\mathbf{g}^Z = -\nabla \cdot (\nu_{SGS}\nabla\overline{\boldsymbol{\omega}}^T)$ that can be simplified as $-\nabla\nu_{SGS} \cdot \nabla\overline{\boldsymbol{\omega}}^T$ since the vorticity is divergence-free. The authors then study the relative importance of each term and find that $\mathbf{g}^Z$ is roughly one order of magnitude smaller than $\mathbf{g}^D$ and weakly correlates with the subgrid-stress term $\mathbf{r} = \nabla \cdot \mathbf{R}$ and can thus be neglected in the application of the model. Furthermore, they show that the partial correlation between $\mathbf{g}$ and $\mathbf{r}$ is due to the correlation between $\mathbf{g}^D$ and $\mathbf{r}^C$ (the part of $\mathbf{r}$ stemming from convective effects), while the alignement between $\mathbf{g}^D$ and $\mathbf{r}^S$ (the part of $\mathbf{r}$ due to stretching), remains basically random.

2.3.2.2 Smagorinsky

A first application of the eddy-viscosity model was done by Winckelmans [Win95]. In this case, a Lagrangian Vortex Method is used and the diffusion is treated with a particle strength exchange scheme (see section 1.1.1.4). The regularization is done through a Λ_2 remeshing scheme. Although different expressions of ν_{SGS} are proposed, the ν_{SGS} used in practise is given by the classical Smagorinsky model (equation (2.12)). The test case is a six rings compact vortex system.

While little is said in this first paper of the performance of the model, a more systematic comparison is done in [WLCW96]. In this paper, different models, both in $\mathbf{u} - p$ and $\boldsymbol{\omega} - \mathbf{u}$, are compared *a priori* on $(\mathbf{u} - p)$ DNS databases of isotropic turbulence. Other than the eddy-viscosity in $\boldsymbol{\omega} - \mathbf{u}$ a hyper eddy-viscosity model of the form $\mathbf{R}^{SGS} = -\overline{\Delta}^2\nabla \times (\nu_{SGS}\nabla^4\overline{\boldsymbol{\omega}}))$ is investigated. The authors find that "the eddy-viscosity model in the $\boldsymbol{\omega} - \mathbf{u}$ formulation produces significantly higher correlations than its counterpart in the $\mathbf{u} - p$ formulation". However, these results hold for *a priori* comparison and do not take into account the effect of the numerical method used when using those models in LES.

An *a posteriori* test of an eddy-viscosity model for LESs with a $\boldsymbol{\omega} - \mathbf{u}$ method is given in Mansfield *et al.* [MKM96]. The simulations use a 3D vortex element core method, where an element splitting algorithm ensure the overlapping of the particles and a Smagorinsky eddy-viscosity model. The test case considered is a vortex ring and the results show the positive impact of the eddy-viscosity model.

A modification of the Smagorinsky model is proposed by Cottet *et al.* [CJM03], where the over-dissipation of the model is corrected by a selective function Ψ based on the angle between the vorticity at a given grid point and the average vorticity of its neighbours. The model is written as

$$\mathbf{R}^{SGS} = -\Psi(\mathbf{x}, t)\nu_{SGS}\nabla\overline{\boldsymbol{\omega}} \tag{2.48}$$

where ν_{SGS} is given by the Smagorinsky model.

Recently, Whitehouse and Boschitsch [WB21] tested the Smagorinsky model as well as Mansour's vorticity model where $\nu_{SGS} = C_S^2\overline{\Delta}|\overline{\boldsymbol{\omega}}|$, on the inviscid Kida–Pelz vortex [Kid85] and the Taylor-Green vortex [TG37] at $Re = 100$ and $Re = 1600$. On the first test case, Mansour's vorticity-based model is shown to be more diffusive than the traditional Smagorinsky model. On the Taylor-Green vortex, both models perform very similarly and are able to reproduce the reference enstrophy and kinetic energy better than the simulations with no models, although the flows investigated are not very challenging at the resolutions considered.

2.3.2.3 Dynamical models

Based on the same eddy-viscosity model (2.47), Mansfield *et al.* [MKM98, MKM99] have adapted Germano's dynamical Smagorinsky coefficient in the context of a Lagrangian Vortex Method.

Since the method is grid-free, the filtering is done through the use of a blob discretization, with the core radius $\overline{\Delta}$ being the equivalent of the filter size. Let $\overline{q}$ be some quantity discretized on particles, the test filtered quantity has the form

$$\widehat{\overline{q}}(\mathbf{x}) = \frac{\sum_i \overline{q}(\mathbf{x}_i) e^{-(c|\mathbf{x}-\mathbf{x}_i|/\widehat{\overline{\Delta}})^3}}{\sum_i e^{-(c|\mathbf{x}-\mathbf{x}_i|/\widehat{\overline{\Delta}})^3}} \tag{2.49}$$

The dynamical coefficient C_S is given by

$$C_S^2 = \frac{\langle \ell \cdot m \rangle}{\langle m \cdot m \rangle} \tag{2.50}$$

where the brackets represent an averaging over homogeneous directions and where

$$\ell_i = \widehat{\overline{\mathbf{u}}_j \partial_j \overline{\boldsymbol{\omega}}_i} - \widehat{\overline{\boldsymbol{\omega}}_j \partial_j \overline{\mathbf{u}}_i} - \widehat{\overline{\mathbf{u}}_j} \partial_j \widehat{\overline{\boldsymbol{\omega}}_i} + \widehat{\overline{\boldsymbol{\omega}}_j} \partial_j \widehat{\overline{\mathbf{u}}_i} \tag{2.51}$$

and

$$m = \nabla \cdot M = \widehat{\overline{\Delta}}^2 |\widehat{\overline{\mathbf{S}}}| (\nabla \widehat{\overline{\boldsymbol{\omega}}} - (\nabla \widehat{\overline{\boldsymbol{\omega}}})^T) - \widehat{\alpha} \tag{2.52}$$

where $\hat{\Delta}$ denotes the test filter size, $\widehat{\overline{\mathbf{S}}} = \frac{1}{2}(\nabla \widehat{\overline{\mathbf{u}}} + (\nabla \widehat{\overline{\mathbf{u}}})^T)$ and $\alpha = \overline{\Delta}^2 |\overline{\mathbf{S}}| (\nabla \overline{\boldsymbol{\omega}} - (\nabla \overline{\boldsymbol{\omega}})^T)$.

In practise, this is not actually how C_S is computed, following *a priori* tests from [MKM98] (see subsection 2.3.2.1), the authors choose to simplify ℓ to keep only the term arising from convection

$$\ell^C = \widehat{\overline{\mathbf{u}}_j \partial_j \overline{\boldsymbol{\omega}}_i} - \widehat{\overline{\mathbf{u}}_j} \partial_j \widehat{\overline{\boldsymbol{\omega}}_i} \tag{2.53}$$

and to use only the term $\nu_{SGS} \nabla \overline{\boldsymbol{\omega}}$ in the eddy-viscosity model, leading to

$$m^D = \widehat{\overline{\Delta}}^2 |\widehat{\overline{\mathbf{S}}}| \nabla \widehat{\overline{\boldsymbol{\omega}}} - \overline{\Delta}^2 \widehat{|\overline{\mathbf{S}}| \nabla \overline{\boldsymbol{\omega}}}. \tag{2.54}$$

In [MKM99], the model is applied to colliding vortex rings and show a good agreement with experimental data.

Another dynamic procedure was recently introduced in the context of a Lagrangian Vortex Method by Valentin [Val24], where the Smagorinsky coefficient is adapted with the variations of local enstrophy.

2.3.2.4 Variational Multi-Scale models

Variational Multi-Scale (VMS) models were introduced in the context of a Remeshed Vortex Method by Cocle *et al.* [CDW07, CBW08, CBW09]. In [CDW07], a Vortex-In-Cell (VIC) method is used with various eddy-viscosity models, which are split in four categories depending on which scales are used to compute the artificial viscosity ν_{SGS} and on which scales the artificial viscosity is applied (see table 2.1 for a complete breakdown). It is to be noted that in these studies the eddy-viscosity formulation is

$$\mathbf{R}^{SGS} = -\nu_{SGS}(\nabla\overline{\boldsymbol{\omega}} + \nabla\overline{\boldsymbol{\omega}}^T) \tag{2.55}$$

which is a symmetric tensor and thus differ from the anti-symmetric formulation (2.47).

		ν_{SGS} is computed from the	
		full resolved field ($\bar{\cdot}$)	filtered small scales ($\bar{\cdot}_s$)
(2.55) is applied to the	full resolved field ($\bar{\cdot}$)	"complete-complete"	"small-complete"
	filtered small scales ($\bar{\cdot}_s$)	"complete-small"	"small-small"

Table 2.1: Classification of VMS modeling approaches introduced in [CDW07] (see Fig. 2.5 for notations)

The models used are Smagorinsky, WALE and Structure-Function [ML92] , the Structure-Function being considered in its "small-complete" and "small-small" formulations whereas the Smagorinsky model is studied in the four configurations presented in table 2.1. The WALE model is only studied in a complete-complete (i.e. non VMS) formulation. Beside the eddy viscosity models, simulations with a hyper-viscosity model are also presented. The LES are compared with a simulation from a Pseudo-Spectral method with a hyper-viscosity model. The test case considers two pairs of counter-rotating vortices, a structure developing quickly into the Crow instability (we refer to [CCB$^+$08] for more details and a DNS of this test case using a Vortex Method).

The "complete-complete" (i.e. non-VMS) approaches perform the worse due to their high dissipation whereas the multi-scale approaches perform well, the hyper-viscosity model's performance lands in between as they tend to over-diffuse at the high wavenumbers. The authors also compare different order of filters and conclude that the filters using the highest order (i.e. retaining the least small scales) perform the best. The small-scale filtering seem to matter the most, independent of the model used. The same approach is tested in [CBW08, CBW09], where almost the same models (except WALE) are once again compared on LES of decaying homogeneous isotropic turbulence (HIT) with no viscosity term and the authors reach the same conclusions. In [CBW09], the authors note that for homogeneous and isotropic cases, the effective viscosity scaling is not as important as for more complex flows, and thus "complete-complete" and "complete-small" (respectively "small-complete" and "small-small") approaches give similar results. A scale dependency of the model's coefficients is also extrapolated from the simulations. Finally, the asymptotic spectral behavior of the approaches is considered and a "bump" is observed in the energy spectra at the end of the inertial range, this "bump" is more pronounced in "x-small" approaches.

The complete-small variant of Smagorinsky in RVM has been applied to high-fidelity LES of

rotor wakes [CWD08, CBD$^+$17, CCW20, CWC20] and wind turbine wakes [CDZ$^+$17, CDC$^+$17], showing its versatility and capacity to handle challenging flows.

2.3.2.5 A mixed eddy-viscosity model

Finally, we can cite a model based on Mansour's eddy viscosity formulation that uses a mixed formulation for the artificial viscosity ν_{SGS}. In the context of an Eulerian velocity-vorticity method, Tenaud *et al.* [TPDT05] introduced the following model, mixing Mansour's vorticity model [MFR78] and Bardina's TKE model [BFR80]

$$(C_S^2\bar{\Delta}^2\|\overline{\boldsymbol{\omega}}\|)^{\alpha}(C_B^2\bar{\Delta}^2\|\overline{\mathbf{u}}-\widehat{\overline{\mathbf{u}}}\|)^{1-\alpha} \tag{2.56}$$

where α is a parameter between 0 and 1 determining the relative importance of each model. The model is used in LES of mixing layers, where the velocity-vorticity formulation is useful as there is no pressure boundary condition.

2.3.3 Structural models

2.3.3.1 Scale-similarity and deconvolution models

In a very recent article, Hou *et al.* [HCY$^+$25] compare with a $\boldsymbol{\omega}-\mathbf{u}$ spectral method several structural models, namely the gradient model, the scale similarity model, the approximate deconvolution model and the dynamic iterative approximate deconvolution model [YWXW21]. Their formulation is adapted to the $\boldsymbol{\omega}-\mathbf{u}$ formulation by re-deriving them from the vorticity stress tensor. The models are tested on decaying homogeneous isotropic turbulence, first *a priori* and are regularized with a hyper-viscosity term for *a posteriori* tests. In *a posteriori* tests, they are also compared to a dynamical Smagorinsky model and a mixed model combining the dynamical Smagorinsky model and a scale-similarity model. The structural model perform well both *a priori*, showing high correlation with the subgrid-scale tensor and *a posteriori*, outperforming the dynamical and mixed model.

2.3.3.2 Gradient model

Following the same derivation as in subsection 2.2.3.3, the gradient model in $\boldsymbol{\omega}-\mathbf{u}$ writes

$$\mathbf{R}_g(i,j)=\frac{\Delta^2}{12}(\partial_k\overline{\boldsymbol{\omega}}_i\partial_k\overline{\mathbf{u}}_j-\partial_k\overline{\boldsymbol{\omega}}_j\partial_k\overline{\mathbf{u}}_i). \tag{2.57}$$

This model is well known for its good *a priori* performances and its low cost, but tends to overestimate back-scatter effects and leads to unstable simulations. The gradient model is implemented, among other structural models (see subsection 2.3.3.1) in [HCY$^+$25] within a spectral method and stabilized with a hyper-viscosity term.

2.3.4 Other approaches

In this section we present approaches that are not directly derived from models developed for the $\mathbf{u}-p$ Navier-Stokes equations but directly use the properties of the Vortex Methods to model sub-grid scales.

2.3.4.1 Anisotropic subgrid-scale models

Cottet [Cot96] introduced a subgrid-scale model based on analysing the truncation error introduced by the 2D Vortex Method.

In the pure Lagrangian formalism (see subsection 1.1.1.2) we solve

$$\frac{\partial \boldsymbol{\omega}}{\partial t} + \nabla \cdot (\boldsymbol{\omega} \mathbf{u}_\varepsilon) = 0 \tag{2.58}$$

where $\mathbf{u}_\varepsilon = K_\varepsilon \star \boldsymbol{\omega} = K \star \zeta_\varepsilon \star \boldsymbol{\omega}$.

However, in blob Vortex Methods, the vorticity is discretized using a mollifying kernel ζ_ε, which plays here the role of a LES filter. Thus, writing $\boldsymbol{\omega}_\varepsilon = \zeta_\varepsilon \star \boldsymbol{\omega}$, the equation that should be solved in theory is

$$\frac{\partial \boldsymbol{\omega}_\varepsilon}{\partial t} + \nabla \cdot ((\boldsymbol{\omega} \mathbf{u})_\varepsilon) = 0. \tag{2.59}$$

Starting from the convolution of ζ_ε with (2.58), which is the equation that is actually solved for the regularized vorticity

$$\zeta_\varepsilon \star (\frac{\partial \boldsymbol{\omega}}{\partial t} + \nabla \cdot (\boldsymbol{\omega} \mathbf{u}_\varepsilon)) = 0, \tag{2.60}$$

we obtain

$$\frac{\partial \boldsymbol{\omega}_\varepsilon}{\partial t} = -\nabla \cdot (\zeta_\varepsilon \star (\boldsymbol{\omega} \mathbf{u}_\varepsilon)) \tag{2.61}$$

$$\frac{\partial \boldsymbol{\omega}_\varepsilon}{\partial t} + \nabla \cdot (\boldsymbol{\omega}_\varepsilon \mathbf{u}_\varepsilon) = \nabla \cdot (\boldsymbol{\omega}_\varepsilon \mathbf{u}_\varepsilon - \zeta_\varepsilon \star (\boldsymbol{\omega} \mathbf{u}_\varepsilon)) \tag{2.62}$$

$$= \nabla \cdot \left(\int \zeta_\varepsilon(\mathbf{x} - \mathbf{y}) \boldsymbol{\omega}(\mathbf{y}) (\mathbf{u}_\varepsilon(\mathbf{x}) - \mathbf{u}_\varepsilon(\mathbf{y})) d\mathbf{y} \right) =: E_{adv} \tag{2.63}$$

Cottet's method rely on studying this truncation term E to determine the conditions leading to an increase in enstrophy in order to construct a model that annihilates the production of enstrophy under these conditions. Some more computations lead to (dropping the subscript ε for clarity)

$$\frac{d}{dt} \int \boldsymbol{\omega}^2 d\mathbf{x} = - \iint (\boldsymbol{\omega}(\mathbf{x}) - \boldsymbol{\omega}(\mathbf{y}))^2 (\mathbf{u}(\mathbf{x}) - \mathbf{u}(\mathbf{y})) \cdot \nabla \zeta(\mathbf{x} - \mathbf{y}) d\mathbf{x} d\mathbf{y}. \tag{2.64}$$

The left-hand side corresponds to the evolution of enstrophy with respect to time. Thus, from the right-hand side, one deduces that in the regions of the domain where

$$(\mathbf{u}(\mathbf{x}) - \mathbf{u}(\mathbf{y})) \cdot \nabla \zeta(\mathbf{x} - \mathbf{y}) < 0 \tag{2.65}$$

the enstrophy increases. In order to cancel out the increase of enstrophy induced by the truncation error and using a positive radial function vanishing at infinity for ζ, we get the minimal scheme

$$\frac{d\boldsymbol{\omega}_p}{dt} = \sum_q \mathrm{v}_q (\boldsymbol{\omega}_p - \boldsymbol{\omega}_q) \min(0, (\mathbf{u}_p - \mathbf{u}_q) \cdot (\mathbf{x}_p - \mathbf{x}_q) \zeta'(|\mathbf{x}_p - \mathbf{x}_q|) |\mathbf{x}_p - \mathbf{x}_q|^{-1}) \tag{2.66}$$

This model is anisotropic and less diffusive than usual functional models. Although it is derived from the 2D equations, an extension to the 3D formulation is introduced in [Cot98] and has been used in the context of "two-level" simulations of the Navier-Stokes equations in $\boldsymbol{\omega} - \mathbf{u}$ formulation [MCM18] where the velocity and vorticity are discretized at different grid sizes, coarser for velocity and finer for vorticity.

Recently Alvarez *et al.* [AN24] adapted this approach to model stretching effects a purely Lagrangian Vortex Method. The subgrid stress tensor is written as

$$\nabla \cdot \mathbf{R} = E_{adv} + E_{stretch} \tag{2.67}$$

where E_{adv} can be modelled with Cottet's model described above. As the authors focus on stretching effects, they neglect it and derive the following model for the stretching subgrid term

$$E_{stretch} \approx C_d \sum_q \zeta(\mathbf{x}_p - \mathbf{x}_q)(v_q \boldsymbol{\omega}_q \cdot \nabla)(\mathbf{u}(\mathbf{x}_p) - \mathbf{u}(\mathbf{x}_q)) \tag{2.68}$$

where C_d is a dynamic coefficient computed with a Germano procedure. The model is further regularized with a clipping procedure based on enstrophy backscatter control. The model is validated on a turbulent round jet and, although it does not stabilize a classical Vortex Method, it does stabilize a new version of the Vortex Method introduced in the same article that does not, as classical Vortex Methods do, assume a constant particle volume. The model is further applied to the rotation of blades in a hover; once again, it stabilizes the new Vortex Method and shows similar accuracy to that of a mesh-based LES with less computation time. The performance of the model on higher resolutions was also tested with a simulation of the wake of an aircraft propeller.

Although the authors give a grid-based formulation of their model, it remains tailored to purely Lagrangian Vortex Method as it is based on the truncation error that stems from solving the Navier-Stokes equations fully on particles.

2.3.4.2 Domain decomposition

A hybrid approach using Lagrangian discretization for the small scales of the flow fields and Eulerian discretization for the large scales was developed by Kornev and Samarbakhsh [Kor17, KS19, SK19, KSD24]. At each timestep, the flow is separated into large and small scales similarly as for VMS methods and the small scales velocity field with strong vortices, denoted $\mathbf{u}^v$, are discretized with vortex elements, the remaining scales are discretized on a grid and are denoted $\mathbf{u}^g$.

The Navier-Stokes equations are re-written as the coupled system

$$\partial_t \mathbf{u}^g + (\mathbf{u}^g \cdot \nabla)\mathbf{u}^g = -\frac{1}{\rho}\nabla P^g + \frac{1}{Re}\Delta \mathbf{u}^g + (\mathbf{u}^v \times \boldsymbol{\omega}^g) \tag{2.69}$$

$$\partial_t \boldsymbol{\omega}^v + ((\mathbf{u}^g + \mathbf{u}^v) \cdot \nabla)\boldsymbol{\omega}^g = (\boldsymbol{\omega}^v \cdot \nabla)(\mathbf{u}^g + \mathbf{u}^v) + \frac{1}{Re}\Delta \boldsymbol{\omega}^v. \tag{2.70}$$

The two equations are solved successively, first (2.69) is solved on the grid using a semi-implicit finite difference method, then the particle strength update in (2.70) is done using the Vortex Method of [FK05] and the velocity $\mathbf{u}^v$ is updated from $\boldsymbol{\omega}^v$ using the Biot-Savart law. The

method can be linked to LES due to its use of scale-filtering, instead of using a model for the subgrid scales, they are directly solved on the particles, the Lagrangian framework allowing for their efficient and accurate representation.

The method was applied to decaying homogeneous isotropic turbulence and free jet flows. Although these method are more costly than their LES counterparts for a given resolution, due to the Biot-Savart sum and the transfer of information from grid to particles, they are more accurate and thus more efficient compared to higher-resolution LES.

In the same spirit, Stock *et al.* [SGS10] performed Large Eddy Simulations of rotorcraft wakes using a Lagrangian discretization in the wake region and an Eulerian discretization for the near-body region. The LES model used in the Lagrangian regions was the one proposed by Cottet [Cot96]. A similar approach was used recently by Valentin [Val24].

2.3.5 Assessement of the remeshed method for LES

2.3.5.1 Lessons from literature

We can gather the following lessons from our literature review of LES with $\boldsymbol{\omega} - \mathbf{u}$ methods:

- The first studies seem to validate Mansour's eddy-viscosity formulation [MFR78] where $\mathbf{R}^{SGS} = -\nu_{SGS}(\nabla\overline{\boldsymbol{\omega}} - \nabla\overline{\boldsymbol{\omega}}^T)$, as it performs well *a priori* (exceeding even the correlation obtained with the classical $\mathbf{u} - p$ formulation [Win95]) as well as *a posteriori* [WLCW96, MKM96, MKM99].

- Interestingly, while most authors use Mansour's antisymmetric formulation, others use the symmetric formulation $\mathbf{R}^{SGS} = -\nu_{SGS}(\nabla\overline{\boldsymbol{\omega}} + \nabla\overline{\boldsymbol{\omega}}^T)$ [CDW07, CBW08, CBW09] or simply $\mathbf{R}^{SGS} = -\nu_{SGS}\nabla\overline{\boldsymbol{\omega}}$ [MKM98, CJM03]. While using an antisymmetric formulation to model an antisymmetric tensor seems the most relevant choice according to Mansfield *et al.* [MKM98], the leading term in the eddy-viscosity model is $\nu_{SGS}\nabla\overline{\boldsymbol{\omega}}$ and thus the three formulations can be considered close.

- From the studies comparing different models, it seems that the formulation used for ν_{SGS} does not matter so much as complete-complete (non-multiscale) eddy-viscosity model perform about the same [WB21, CDW07]. However, what does seem to make a difference is the use of a variational multiscale method (VMS) [CDW07, CBW08, CBW09], which reduces the diffusivity of classical eddy-viscosity models.

- Non-classical eddy-viscosity or structural models are rare in literature and seem to always require a regularization procedure, like a clipping based on enstrophy [Cot96, AN24] or a mixing with a hyper-viscosity model [HCY$^+$25].

- Except from VMS models, which have been applied to many cases involving fluid-structure interactions [CWD08, CBD$^+$17, CCW20, CWC20, CDZ$^+$17, CDC$^+$17], most of the benchmarks have been done, to our knowledge, on flows with no boundaries. It remains therefore unclear how the presented models compare in their performance near walls.

2.3.5.2 Vorticity-velocity formulation

It is interesting that some of the studies described in this chapter use the $\boldsymbol{\omega} - \mathbf{u}$ formulation (sometime called vorticity transport equation or VTE) in an Eulerian code. The authors' justifications for their choice give us insight in the advantage of this formulation, inherent to Vortex Methods, for LES.

Speziale [Spe87] and Tenaud *et al.* [TPDT05] note the advantage of the lack of boundary conditions on the pressure (as this quantity is absent from the $\boldsymbol{\omega} - \mathbf{u}$ formulation) and the direct access to the vorticity vector which is central to turbulence. Notably, the enstrophy has been used as a measure of turbulence in sensor models [CJM03, CWS18]. In Chapelier *et al.* 's [CWS18] coherent-vorticity preserving approach, not based on a vorticity-velocity formulation, the model's coefficient is modulated with a sensor function dependant on the ratio of the test-filtered to the resolved enstrophy. This choice is justified by the shape of the enstrophy spectrum, which grows as $k^{1/3}$ in the inertial range, meaning that the turbulence growth is driven by the small-scales of vorticity.

Duraisamy and Lele [DL08] used the $\boldsymbol{\omega} - \mathbf{u}$ formulation for DNS of low swirl-number turbulent Batchelor vortex using a pseudo-spectral method. They justified their choice by its ability to naturally handle spatially compact vorticity distributions where periodicity can be assumed, thereby eliminating the difficulty of setting explicit pressure and velocity boundary conditions.

Other authors point out the reduced numerical diffusion and dissipation of the vorticity field [BL05, WB21] and the higher numerical accuracy in the computation of the wall vorticity [MF00].

2.3.5.3 Lagrangian advection

The Lagrangian treatment of the advection term in Vortex Method is also an advantage for LES as it limits diffusive effects (see chapter 1 for more details), unlike Eulerian methods, where numerical dissipation can excessively dampen small-scale structures, the Lagrangian approach preserves vorticity dynamics more effectively, leading to a more faithful representation of turbulence, particularly in under-resolved regions. This leads to a better approximation of the flow at coarse resolutions. Since LES relies on under-resolving the flow on a coarse grid, obtaining an accurate coarse-scale approximation is crucial for capturing large-scale turbulence structures while minimizing artificial dissipation.

Furthermore, the Lagrangian stability condition do not tie the time step to the grid step but to the velocity gradients, leading to larger time-steps and further computational cost reduction compared to traditional Eulerian LES approaches, where stability is often constrained by the Courant–Friedrichs–Lewy (CFL) condition.

2.3.5.4 Hybrid framework

Our hybrid Lagrangian-Eulerian framework is furthermore adapted to implement SGS models as the modular aspect of the algorithm allows to easily create new operators to solve the additional terms stemming from the models on the grid, without requiring an adaptation to the particle method. Furthermore, since we already use an FFT algorithm to solve the Poisson and the diffusion equations, we can use explicit filters in the Fourier space without a large added computational cost and thus implement easily multiscale methods. The FFT can also be used to

add, again with no important additional cost, an artificial viscosity like in the methods described in subsection 2.2.2.1.

2.3.5.5 Disadvantages

The remeshed vortex have however disadvantages for LES, the $\boldsymbol{\omega} - \mathbf{u}$ formulation requires more variables and thus uses more memory (two 3D fields vs one 3D field and one scalar field in the classical $\mathbf{u} - p$ formulation), the solenoidality of the vorticity field is not guaranteed and thus the method requires regular vorticity re-projections to be stable. The boundary conditions are not easily implemented and the uniform Cartesian grid, although simplifying the parallelization of the solver, limits the ability of the method to solve flows in complicated geometries as it imposes an uniform resolution in the whole domain.

Finally, our Remeshed Vortex Method has a global accuracy of order under 2 [MMM21] (this accuracy, however, depends on the specific numerical schemes employed in the various operators, and higher-order accuracy can be attained by using higher-order schemes, though this requires greater computational effort), which may not be sufficient for LES. However, whether a high-order method is necessary for accurate LES—and even whether high-order methods are desirable in LES—remains a subject of debate (see Chapter 8 of [Sag06] for an overview of this discussion).

Conclusion

In this chapter we briefly presented the main numerical approaches to turbulence modeling. Since it is the method used in our work, we focused on Large Eddy Simulations techniques. We then presented the main models used in the context of numerical methods based on the $\mathbf{u} - p$ formulations. Finally, we conducted a literature review of models adapted or developed for the $\boldsymbol{\omega} - \mathbf{u}$ formulation, some of them being implemented in Eulerian solvers and some of them being inherently tied to a Lagrangian framework. This literature review allowed us to already conclude on the ability and relative performance of these models in benchmark test cases. We then analysed the strengths of weaknesses of our present Remeshed Vortex Method (RVM) for LES by considering its $\boldsymbol{\omega} - \mathbf{u}$ formulation, its Lagrangian treatment of advection and its hybrid Lagrangian-Eulerian framework. This analysis supports the conclusion that the proposed RVM is a relevant candidate for performing LES.

In the following chapter, we implement, compare and calibrate some of the models presented in our present method for Large Eddy Simulations of homogeneous, isotropic and periodic turbulent test cases.

Chapter 3

Homogeneous, isotropic, periodic turbulent test cases

Contents

Introduction

In the previous chapter, we introduced different subgrid-scale modeling strategies, both in the velocity-pressure and the velocity-vorticity formulation. In this chapter we investigate and compare some of these subgrid-scale models in the context of the present RVM (i.e. models solely expressed in vorticity-velocity formulation) to study their performance. More specifically, in this chapter, the SGS models analysis will be conducted on a single test case of homogeneous isotropic turbulence, namely the classical test case of the Taylor-Green vortex [TG37]. Once the best models have been selected from this specific benchmark, we will evaluate the sensitivity to their parameters. Indeed, in LES, uncertainties arising from SGS modeling can interact in a complex manner with those related to the numerical discretization. Therefore, it is not guaranteed that model parameters calibrated for the classical Eulerian and velocity-based framework are suitable for the RVM as well. To evaluate the impact of model coefficients on the LES-RVM results, we adopt a stochastic Uncertainty Quantification approach based on the polynomial chaos expansion

[XK02], that provides response surfaces of the LES output quantities in the parameter space requiring only a limited number of simulations. This technique allows an affordable calibration of the model parameters against reference DNS data.

After the SGS models calibration, the robustness of calibration to changes in Reynolds number, grid resolution, and flow configuration (with the decaying homogeneous isotropic turbulence test case) will finally be investigated.

3.1 Subgrid-scale modeling

In this section, we assess artificial viscosity models (the standard Smagorinsky model as well as its dynamic and variational multiscale (VMS) variants), and structural models with the gradient model [Leo75a, CFR79, Vre95]. We also consider the Spectral Vanishing Viscosity (SVV) approach which, as will be shown, is especially well suited to the present RVM algorithm. All these models, adapted to the vorticity-velocity formulation, are hereafter described under the expressions actually implemented and used in our `HySoP` RVM solver. For all the SGS models (except from SVV), the differential operators implied in these models are discretized on the Cartesian grid, with fourth-order finite differences.

3.1.1 Eddy viscosity models

3.1.1.1 Smagorinsky

We use the following eddy viscosity model, presented in subsection 2.2.1.1 and 2.3.2.1:

$$\mathbf{R} = -\nu_{SGS}(\nabla\overline{\boldsymbol{\omega}} - \nabla\overline{\boldsymbol{\omega}}^T) \tag{3.1}$$

with ν_{SGS} given by the classical Smagorinsky model, that is:

$$\nu_{SGS} = (C_S\Delta)^2|\mathbf{S}| \tag{3.2}$$

where C_S is a coefficient to be a-priori assigned, Δ the LES filter size, $\mathbf{S} = \frac{1}{2}(\nabla\overline{\mathbf{u}} + (\nabla\overline{\mathbf{u}})^T)$ and $|\mathbf{S}| = \sqrt{2\mathbf{S}_{ij}\mathbf{S}_{ij}}$ the magnitude of the strain tensor $\mathbf{S}$.

The dynamic variant of this model [MKM98, MKM99], presented in subsection 2.3.2.3 will also be considered.

3.1.1.2 Variational multiscale models

Another variant of the Smagorinsky model explored is the variational multiscale (VMS) family of models presented in subsections 2.2.1.4 and 2.3.2.4. Contrary to the VMS models used by Cocle *et al.*, and presented in the literature review section 2.3.2.4, the VMS models considered in the present work are based on the anti-symmetric formulation of the subgrid scale vorticity tensor, i.e.:

$$\mathbf{R}_{SGS} = -\nu_{SGS}(\nabla\overline{\boldsymbol{\omega}}_S - \nabla\overline{\boldsymbol{\omega}}_S^T) \tag{3.3}$$

where $\overline{\boldsymbol{\omega}}_S$ denotes the small scales of the resolved vorticity field. These smallest resolved scales are defined as $\overline{\boldsymbol{\omega}}_S = \overline{\boldsymbol{\omega}} - \widehat{\overline{\boldsymbol{\omega}}}$, with $\widehat{\overline{\boldsymbol{\omega}}}(k) = \widehat{G}(k)\overline{\boldsymbol{\omega}}(k)$ the largest resolved scales of the vorticity

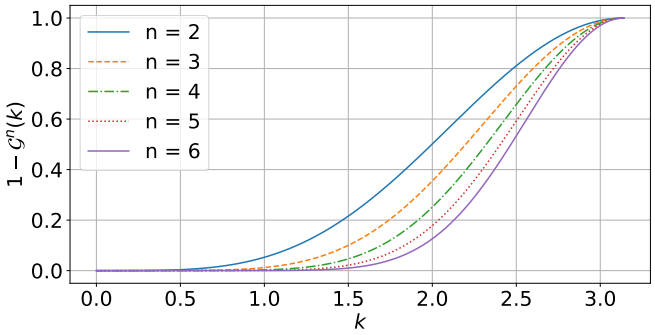

Figure 3.1: Explicit filtering. Plot of $(1 - \mathcal{G}^n)$ with respect to the wavenumer k for different values of filter order n.

field selected with a $\widehat{G}$ test filter. In particular, we will focus on the "complete-small" variant of this approach where the Smagorinsky SGS viscosity ν_{SGS} (3.2) is computed from the complete range of scales of the velocity field, as opposed to "small-small" and "small-complete" approaches where ν_{SGS} is computed from the small scales of the velocity field (the "small-small" variant was tested in the present study and was found to be more expensive as it required an additional explicit small-scale filtering for both the $\boldsymbol{\omega}$ and the $\mathbf{u}$ fields while not improving significantly the results). In the following, as there is no ambiguity with another VMS approach, we will denote the selected "complete-small" variant by "VMS Smagorinsky model" or "VMS-Smag model". One therefore defines the VMS-Smag model by:

$$\mathbf{R}_{SGS} = -\nu_{SGS}(\nabla\overline{\boldsymbol{\omega}}_S - \nabla\overline{\boldsymbol{\omega}}_S^T), \quad \text{with} \quad \nu_{SGS} = (C_S\Delta)^2|\mathbf{S}|. \tag{3.4}$$

3.1.1.3 Filtering

In the context of the VMS-Smag model described previously, one needs to define an appropriate test filter $\widehat{G}$. In the following we will filter the large resolved scale using the filter presented in [WJ01]. It is based on the stencil:

$$\widehat{\boldsymbol{\omega}}^{(n)} = \left[\left(I - \left(-\delta_x^2/4\right)^n\right)\left(I - \left(-\delta_y^2/4\right)^n\right)\left(I - \left(-\delta_z^2/4\right)^n\right)\right]\boldsymbol{\omega} \tag{3.5}$$

where $\delta_x^2 f_{i,j,k} = f_{i+1,j,k} - 2f_{i,j,k} + f_{i-1,j,k}$. In Fourier space, the filtered field is then

$$\widehat{\boldsymbol{\omega}}^{(n)}(\mathbf{k}) = G^n(\mathbf{k})\boldsymbol{\omega}(\mathbf{k}) = G^n(k_x h_x)G^n(k_y h_y)G^n(k_z h_z)\boldsymbol{\omega}(\mathbf{k}) \tag{3.6}$$

with h the grid step and

$$G^n(k) = \left(1 - \sin^{2n}(k/2)\right). \tag{3.7}$$

The small scales are then obtained as follows:

$$\boldsymbol{\omega}_S^{(n)} = \boldsymbol{\omega}(\mathbf{k}) - \widehat{\boldsymbol{\omega}}^{(n)}(\mathbf{k}) = (1 - G^n(\mathbf{k}))\boldsymbol{\omega}(\mathbf{k}). \tag{3.8}$$

Figure 3.1 shows the evolution of $1 - G^n$ with the wavenumber k for different values of n. In this work we performed all filtering operations in the Fourier space, taking advantage of the

interfacing of the `HySoP` library with the Fortran `FFTW` library, already used to solve the diffusion and the Poisson equations (see subsection 1.2.3.4). It has to be noticed that this type of filtering has the property of being also applicable in the physical space, under the condition of taking integer values of filter order n, as done in [CDW07] for a variant of the hybrid Vortex method.

3.1.2 A structural model: the clipped gradient model

Among structural models, which aim to directly model the subgrid-scale tensor, we explore the gradient model from subsections and 2.2.3.3 and 2.3.3.2 based on a Taylor series expansion. It writes:

$$\mathbf{R}_g(i,j) = \frac{\Delta^2}{12}(\partial_k\overline{\boldsymbol{\omega}}_i\partial_k\overline{\mathbf{u}}_j - \partial_k\overline{\boldsymbol{\omega}}_j\partial_k\overline{\mathbf{u}}_i). \tag{3.9}$$

This model is well known for its good *a-priori* performances and its low cost, but we observed that it tends to overestimate back-scatter effects and leads to unstable simulations. We therefore propose to add the following clipping procedure:

$$\mathbf{R}_g^{clip}(i,j) = \frac{\Delta^2}{12}(\partial_k\overline{\boldsymbol{\omega}}_i\partial_k\overline{\mathbf{u}}_j - \partial_k\overline{\boldsymbol{\omega}}_j\partial_k\overline{\mathbf{u}}_i) \times \begin{cases} 1 & \text{if } \mathbf{R}_g(i,j)\Omega_{ij} < 0 \\ -1 & \text{otherwise} \end{cases} \tag{3.10}$$

where $\overline{\Omega_{ij}} = \frac{1}{2}(\partial_j\overline{\boldsymbol{\omega}}_i - \partial_i\overline{\boldsymbol{\omega}}_j)$. In this clipping approach, we focus on the directions where the model leads to an energy transfer from the small to the large scales, inverting the sign of the model in those specific directions. In the $\mathbf{u}-p$ formulation, it corresponds to the directions where $\tau_{ij}S_{ij} > 0$ [PCML91]. In our $\boldsymbol{\omega}-\mathbf{u}$ formulation, we consider the enstrophy-producing directions: writing the scalar product of $\overline{\boldsymbol{\omega}}$ with the filtered Navier-Stokes equations

$$\overline{\boldsymbol{\omega}} \cdot (\partial_t\overline{\boldsymbol{\omega}} + \overline{\mathbf{u}} \cdot \nabla\overline{\boldsymbol{\omega}} - \overline{\boldsymbol{\omega}} \cdot \nabla\overline{\mathbf{u}}) = \overline{\boldsymbol{\omega}} \cdot (\nu\Delta\overline{\boldsymbol{\omega}} - \nabla \cdot \mathbf{R}) = 0 \tag{3.11}$$

we obtain the enstrophy transport equation

$$\frac{1}{2}\partial_t\zeta + \overline{\mathbf{u}} \cdot \nabla\zeta - \overline{\boldsymbol{\omega}}_i\overline{\boldsymbol{\omega}}_j\partial_j\overline{\mathbf{u}}_i = \nu\Delta\zeta - \nu(\partial_j\overline{\boldsymbol{\omega}}_i)^2 - \partial_j(\overline{\boldsymbol{\omega}}_i\mathbf{R}_{ij}) + \mathbf{R}_{ij}\partial_j\overline{\boldsymbol{\omega}}_i = 0 \tag{3.12}$$

the term $\mathbf{R}_{ij}\partial_j\overline{\boldsymbol{\omega}}_i$ represents the energy transfer between the resolved and subgrid scales and can be rewritten, using the anti-symmetry of $\mathbf{R}$,

$$\mathbf{R}_{ij}\partial_j\overline{\boldsymbol{\omega}}_i = \frac{1}{2}\left(\mathbf{R}_{ij}\partial_j\overline{\boldsymbol{\omega}}_i - \mathbf{R}_{ij}\partial_i\overline{\boldsymbol{\omega}}_j\right) = \frac{1}{2}\mathbf{R}_{ij}\left(\partial_j\overline{\boldsymbol{\omega}}_i - \partial_i\overline{\boldsymbol{\omega}}_j\right). \tag{3.13}$$

3.1.3 Spectral vanishing viscosity

Spectral vanishing viscosity approaches are a type of regulation of spectral methods that modify the diffusion operator to add viscosity to the end of the spectrum. Similarly as for the previously described VMS methods, the coarser scales remain untouched. To further the analogy, we choose to use the same small-scale filtering for both VMS-Smag and SVV models (i.e. eq. (3.8)).

The two methods differ however in that the VMS-Smag model viscosity is computed from the whole resolved velocity field (cf eq. (3.2)) whereas in SVV, as detailed below, the viscosity is simply taken to be proportional to the cutoff scale. Furthermore, from a computational point

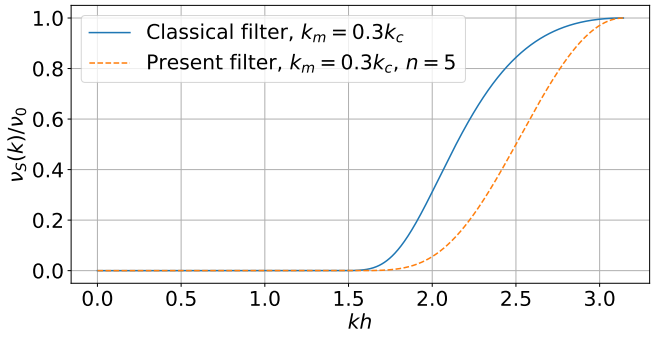

Figure 3.2: Evolution of the spectral artificial viscosity with respect to the wavenumber (eqs. (3.15) (blue curve) and (3.16) (orange curve)).

of view, the SVV is directly integrated in the Fourier part of our solver whereas the VMS-Smag model (3.4) requires a new discretization operator (performed with finite differences in the present case). This makes the SVV particularly well adapted to our RVM algorithm.
In Fourier space, the modified diffusion operator writes:

$$\partial_t \hat{\boldsymbol{\omega}} = -(k_x^2(1/Re + \nu_S(k_x)) + k_y^2(1/Re + \nu_S(k_y)) + k_z^2(1/Re + \nu_S(k_z)))\hat{\boldsymbol{\omega}} \tag{3.14}$$

with the spectral viscosity ν_S given by the expression introduced by [MKT93]:

$$\nu_s(k) = \begin{cases} 0 & \text{if } k < k_m \\ \nu_0 \exp\left[-\left(\frac{k_c - k}{k_m - k}\right)^2\right] & \text{if } k_m \leq k \leq k_c \end{cases} \tag{3.15}$$

where k_c is the wavenumber at the cutoff scale.

In the present formulation, the SVV operator (3.14) is anisotropic. In the present chapter, where we only consider homogeneous and isotropic turbulent flows, we found very little variation in the results between the present formulation and an isotropic operator (i.e. one that introduces the same viscosity for each direction). However, we believe that having a flexible operator with the ability to introduce a different viscosity amplitude at a different rate in each direction can be a useful feature for more complex flow configurations. As argued in [VCL23], anisotropy can also be an asset to correct anisotropic errors due to numerical differentiation in the physical space.

As previously said, instead of using a cutoff at k_m, and in order to simplify the comparison with the other models and the following Uncertainty Quantification study, the filter used for the SVV operator is chosen to be the same as the one used for the VMS-Smag model:

$$\nu_s(k,h) = \nu_0 \exp\left[-\left(\frac{k_c - k}{k_m - k}\right)^2\right](1 - G^n(kh)) =: \nu_0 Q_{SVV}(k)(1 - G^n(kh)) \tag{3.16}$$

with h the grid step. The evolution of ν_S with the wavenumber k is shown in figure 3.2 and compared to the one of the classical formulation (3.15). Table 3.1 presents a summary of the different filters presented above, showing the link between the VMS and SVV approaches.

Model	Small scale filter
Smag	none
VMS-Smag	G^n
classical SVV	Q_{SVV}
present SVV	$Q_{SVV} \star G^n$

Table 3.1: Summary of the different filters considered in the present study.

Indeed, the SVV approach can be seen as an anisotropic variant of the VMS-Smag model, with a different filter and a constant viscosity.

The SVV approach requires the definition of two parameters, namely k_m (or, in the present study, the order n of the explicit filter (3.16)) and ν_0. In the literature, a scaling of the SVV viscosity ν_0 by $1/k_c$ (meaning that the SVV viscosity becomes negligible as the resolution increases) has been studied by [Pas05] in the context of a LES of the turbulent wake around a cylinder. Other approaches consist in scaling the viscosity with the velocity field [KK02], the ratio of the Kolmogorov scale to the resolved scale [DLLV17] or using the artificial viscosity given by the Smagorinsky model [MFRV20]. In our context, since we are applying the SVV operator directly in the Fourier space, it is not appropriate to scale the artificial viscosity with a quantity varying in space. In the following, we therefore study viscosities ν_0 of the form:

$$\nu_0 = \frac{C_{SVV}}{k_c} \tag{3.17}$$

where C_{SVV} is a coefficient to be set.

3.2 Model comparison on the Taylor-Green Vortex

3.2.1 Taylor-Green test case

3.2.1.1 Presentation

The Taylor-Green vortex (TGV) [TG37] is a well-established test case and is very often used as a benchmark for LES models due to its setup simplicity. From simple initial conditions, large vortex break into smaller and smaller structures under the influence of vortex stretching and turbulence grows (see figure 3.3). The domain is a cubic box of length 2π with periodic boundary conditions and the initial vorticity is given by

$$\boldsymbol{\omega}(\mathbf{x}, t=0) = \boldsymbol{\omega}(x, y, z, t=0) = \begin{pmatrix} -\cos(x)\sin(y)\sin(z) \\ -\sin(x)\cos(y)\sin(z) \\ 2\sin(x)\sin(y)\cos(z) \end{pmatrix} \tag{3.18}$$

3.2.1.2 Previous works with RVM

The Taylor-Green vortex was already investigated with the present method at the transitional Reynolds number of 1600. The performance of the Remeshed Vortex Method was compared against spectral methods [vRLPK11] and the Lattice Boltzman method [MMM21] (see

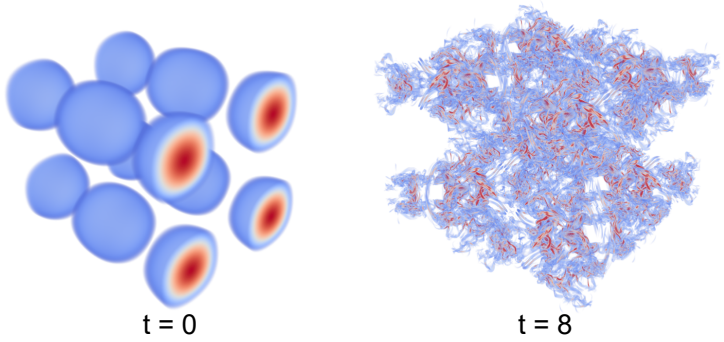

Figure 3.3: Vorticity norm for the Taylor-Green vortex at $Re = 5000$ at times $t = 0$ and $t = 8$.

subsection 1.1.3.3 for more details). The convergence of the present method on the TGV was also numerically demonstrated [Kec19, MMM21]. In particular Keck [Kec19] compared the influence of the remeshing kernel and the timestep on the solution.

However, as these studies were conducted on a relatively low Reynolds number, no subgrid-scale model was necessary. To our knowledge, no tests on higher Reynolds were conducted with the RVM.

3.2.2 Numerical results

3.2.2.1 A posteriori comparison of model performances

The different models are first compared in the context of the TGV test case, at $Re = 5000$. The results are compared against those of a DNS conducted with the present RVM and a 768^3 grid resolution. For the purpose of comparison, the DNS enstrophy data are filtered on the same grid used for LES using a sharp cutoff filter. For the specific quantity of dissipation, the results are compared against available reference DNS at a higher resolution of 1280^3 from [DLLV17]. We start by comparing the LES results obtained with our RVM approach with those of a LES conducted with a purely Eulerian method. Figure 3.4 presents a comparison of the dimensionless-time history of kinetic energy dissipation of a 72^3 LES with RVM and the standard Smagorinsky model with that obtained by Chapelier *et al.* [CWS18], using high-order finite differences with the Smagorinsky model as well. The model coefficient for both simulations is $C_S = 0.172$. We observe in both cases a shift in the time evolution of kinetic energy dissipation but our method seems to better represent the peak of dissipation, demonstrating its low-diffusivity.

In figure 3.5, the time history of the kinetic energy E_k (a), the kinetic energy dissipation $-dE_k/dt$ (b), the enstrophy $\langle \boldsymbol{\omega} \cdot \boldsymbol{\omega} \rangle$ (c), and the energy spectrum at non-dimensional time $t = 8.5$ (d) are used to evaluate the different models by comparison to the non-filtered DNS results from [DLLV17] for the dissipation (b) and to the present DNS results for the other quantities (a, c, d).

The LESs are performed with $N_{LES} = 96$. The model coefficients used are the classical $C_S = 0.16$ for Smagorinsky and coefficients close to the ones suggested in [CBW09] for VMS-Smag and in [Pas05] for SVV ($C_S = 0.245$ and $n = 3$ and $C_{SVV} = 0.25$ and $n = 5$ respectively).

As can be seen, the no-model simulation (i.e. under-resolved simulation with no SGS model) is characterized by the classical pile up of energy at the small scales and is unstable. In all

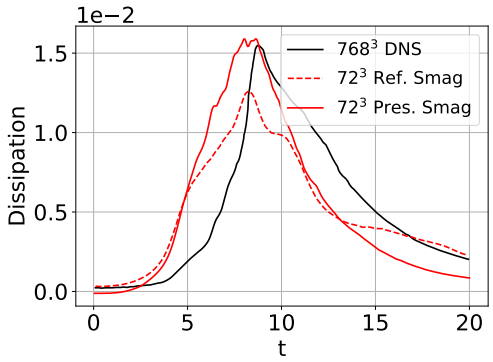

Figure 3.4: Comparison of standard Smagorinsky simulation from the present RVM approach with a standard Smagorinsky simulation from [CWS18]: time history of kinetic energy dissipation for TGV at $Re = 5000$ and $N_{LES} = 72$, comparison with filtered 768^3 DNS.

cases, the introduction of a SGS model leads to stable simulations. The standard Smagorinsky seems to damp excessively the large scales, while energy pile up is still present at the smallest resolved scales (figure 3.5(d)). Moreover, the peak in dissipation occurs earlier than in DNS, and, consequently, the kinetic energy decay is more rapid in the first phase of the evolution. The gradient model gives results very similar to those obtained with the Smagorinsky model. In has to be noticed that the dynamic Smagorinsky model also behaves similarly to the Smagorinsky model, as shown in figure 3.6(a). This may be due to the considered test case. Indeed, in the absence of walls or strong inhomogeneities in the flow, the advantage of adapting the model coefficient in space is less visible. When observing the evolution of the dynamic coefficient in time (figure 3.6(b)), we find that it quickly stabilises to a constant coefficient close to the one used for the standard Smagorinsky model, namely $C_S = 0.16$. Finally, the SVV and VMS-Smag models give a kinetic energy spectrum in good agreement with the one obtained in DNS (figure 3.5(d)), thus confirming the benefit of introducing SGS viscosity only at the smallest resolved scales of the flow without adding dissipation to the largest scales. The SVV gives the best global agreement with DNS, in particular for the kinetic energy decay (figure 3.5(a)) and the energy spectrum (figure 3.5(d)).

3.2.2.2 Comparison of computational times

Table 3.2 compares the CPU-time per iteration for various models. This study was performed on sequential (non-parallel) runs of the TGV test case at $Re = 1600$ and $N_{LES} = 64$ over 2000 iterations, in order to have a stable baseline simulation with no SGS model. Indeed, the simulation of the TGV test case at $Re = 1600$ and $N_{LES} = 64$, with the RVM approach and without any SGS model, is stable and does not blow up.s All simulations were performed on the same hardware (Xeon E5-2650L v3 1.8GHz). The CPU times are normalized by the no-model runtime.

As anticipated, all models imply an increase in computational time compared to the baseline simulation without any model. However, the impact is almost negligible when adopting the SVV approach, given that it does not require the introduction of a new term to be discretized but only

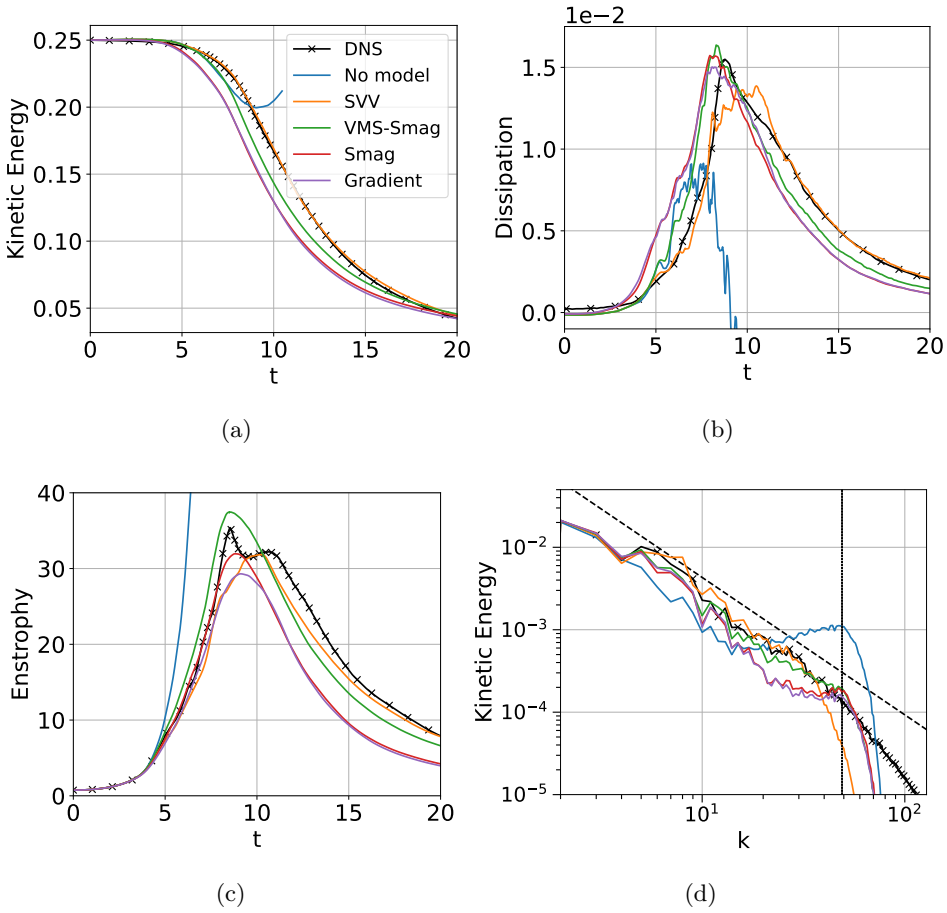

Figure 3.5: Time history of (a) kinetic energy, (b) kinetic energy dissipation, (c) enstrophy and (d) kinetic energy spectrum at $t = 8.5$ for the TGV with $Re = 5000$ and $N_{LES} = 96$. Comparison with 768^3 DNS for (a), (c) and (d) (filtered for (a) and (c)), and with non-filtered reference 1280^3 DNS from [DLLV17] for (b).

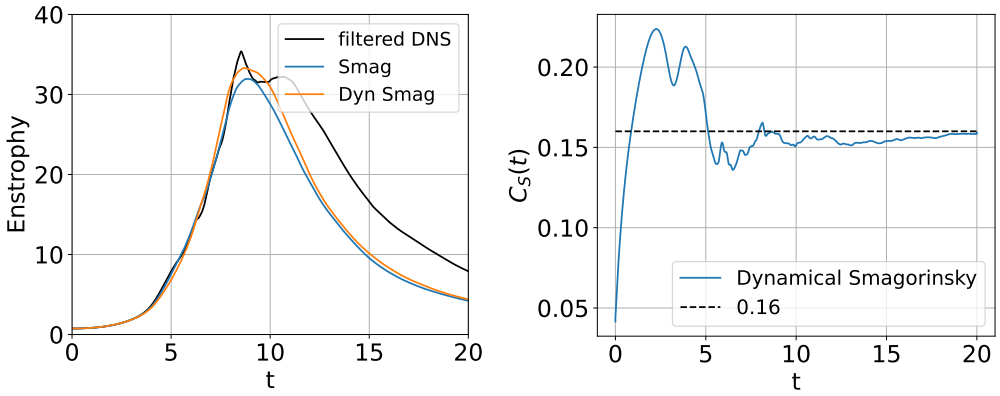

(a) (b)

Figure 3.6: Comparison of standard Smagorinsky and dynamical Smagorinsky in the present RVM approach for TGV at $Re = 5000$ and $N_{LES} = 96$: (a) time history of enstrophy, comparison with filtered 768^3 DNS, (b) time history of dynamical Smagorinsky coefficient, comparison with constant standard Smagorinsky coefficient.

a modification of the existing Fourier-based diffusion operator. The VMS Smagorinsky model requires a higher computational cost than the standard Smagorinsky due to the explicit filtering operation needed to separate the smallest resolved scales from the largest ones. However, the additional increase in computational time is relatively minor, especially when considering the enhanced performance achieved compared with the standard Smagorinsky model (see figure 3.5). The dynamic Smagorinsky model is the least efficient in terms of computational costs. This can be attributed to the numerous filtering and derivative operations required by equations (2.51)-(2.50), particularly within the context of the vorticity-velocity formulation. Therefore, while our current implementation of the dynamic Smagorinsky model may benefit from optimization, we do not expect to be able to reduce the computational costs at the same level of that of the other considered models, due to the inherent required number of filtering operations and additional differential terms to be discretized.

Model	normalised averaged time per iteration
Smag	1.14
Dynamical Smag	1.81
VMS Smag	1.2
Gradient	1.19
SVV	1.02

Table 3.2: Time per iteration for LESs of TGV at $Re = 1600$ and $N_{LES} = 64$ normalised by the time per iteration for a no-model simulation.

Based on the simulation results and computational cost comparison, the VMS-Smag and the SVV models come out as the most adapted models in our framework. However, both SGS models involve a set of parameters that can or must be assigned a priori. The main ones are the

model coefficients, C_S and C_{SVV}, which directly regulate the amount of SGS viscosity, and the order n of the filter in equations (3.7) and (3.16), which determines the range of the smallest resolved scales in which the SGS viscosity is introduced. While testing different values of these parameters in LES of the TGV case, we observed significant changes in the results even with a slight variation in the parameter values. To systematically study the sensitivity of both models to their parameters while keeping the number of needed simulations reasonable, an Uncertainty Quantification procedure is performed and presented in the following section.

3.3 Parameter sensitivity estimation and model calibration

3.3.1 Uncertainty quantification

3.3.1.1 Polynomial Chaos Expansion

We perform an Uncertainty Quantification study using the Polynomial Chaos Expansion (PCE) [XK02] to analyze the stochastic sensitivity of the results given by the VMS-Smag and the SVV models to their main parameters. This technique has been used in numerous study of the sensitivity of LES models to their coefficients (see for example [LMS07] for a study of the uncertainties associated with the Smagorinsky constant in HIT and section 5 of Xiao and Cinnella's review [XC19]). An illustration of the procedure is presented in figure 3.7.

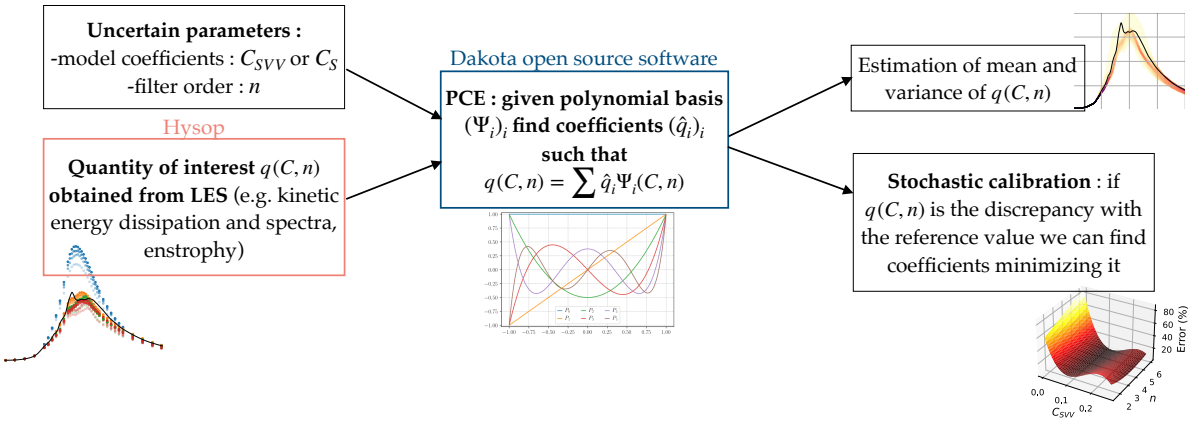

Figure 3.7: Illustration of the PCE procedure used in this work.

Uncertainty quantification is based on considering the model parameters as uncertain random variables. By assuming their PDFs, one can propagate those uncertainties and evaluate the sensitivity of the results to the variation of the parameters. PCE is based on modeling the response surface as a combination of polynomials in the considered variables. We choose a polynomial basis Ψ_p and write the response surface u as a function of the parameters y:

$$u(y) = \sum_{i=0}^{\infty} \hat{u}_i \Psi_i(y) \tag{3.19}$$

the coefficients $\hat{u}_i$ are computed by

$$\hat{u}_i = \int u(y)\Psi_i(y)dy \tag{3.20}$$

To practically obtain the response surface, it is necessary to truncate the sum in equation (3.19). This finite limit L is here determined as follows:

$$L = \prod_{k=1}^{M}(P_k + 1) - 1 \tag{3.21}$$

where M is the number of uncertain variables considered in the problem and P_k is the highest polynomial order selected for the variable of index k.
Once the coefficients $\hat{u}_i$ computed, the mean value and the variance of u can be computed as:

$$\mathbb{E}[u] = \hat{u}_0 \tag{3.22}$$

$$Var[u] \approx \sum_{i=0}^{L} \hat{u}_i^2 - \hat{u}_0^2 \tag{3.23}$$

The partial sensitivities, i.e. the contribution of each parameter (or combination of them) to the total variance, are evaluated through the partial variances [Sob01]:

$$S_{i_1,i_2...,i_S} = \int u^2_{i_1,i_2...,i_S} dy_{i_1} dy_{i_2} ... = \sum_{p \in \mathcal{P}_{i_1,i_2...}} \hat{u}_p^2 \tag{3.24}$$

3.3.1.2 Present Uncertainty quantification procedure

In the present work, the uncertain parameters of the numerical simulations are the following: model coefficient C_S (eqs. (3.4) and (3.2)) and filter order n (eq. (3.7)) for the VMS-Smag model and model coefficient C_{SVV} (eq. (3.17)) and filter order n for the SVV approach (eq. (3.16)). We consider the following ranges of variation of the parameters $C_S \in [0.1949, 0.7]$, $C_{SVV} \in [0, 0.2685]$ and $n \in [1.5223, 6]$ and uniform input PDF within these ranges. These intervals were determined as follows: we started from the values recommended in the literature and we first checked whether the introduced SGS viscosity could be decreased while maintaining a stable simulation. For SVV, also for very low values of C_{SVV} the simulations were stable and, thus, the value proposed in the literature, $C_{SVV} = 0.25$, is the largest quadrature point in the considered interval. Conversely, for the VMS-Smag model, LESs became unstable for values of C_S slightly lower than the value recommended in the literature, $C_S = 0.23$; therefore, we also included significantly larger values in the C_S variation range. In the above intervals, a constant probability density function (PDF) is postulated because, among the traditionally employed distributions, it is the least informative, exhibiting the highest variance within specified intervals. We choose the Legendre polynomial family for the gPC expansion, which is the optimal one when dealing with uniform PDF distributions. For all the uncertainty parameters, the expansion in equation (3.19) is truncated to the third order ($P_k = 3$ for all k). Thus, four quadrature points are needed for each parameter, as summarized in table 3.3. Since we consider two parameters

n	1.8332	3.0000	4.5223	5.6891
C_S	0.23	0.3617	0.5335	0.6652
C_{SVV}	0.0187	0.0887	0.18	0.25

Table 3.3: Quadrature points used for the Uncertainty Quantification study performed for the VMS-Smag model (with parameters n and C_S) and for the SVV model (with parameters n and C_{SVV}).

for each model ($M = 2$), we have $L = 15$ which corresponds to 16 simulations to be performed for each model. The polynomial chaos expansion was performed using the `Dakota` library[1].

Figure 3.8 shows the average absolute value of the polynomial coefficients obtained for the PCE in the case of the SVV and VMS-Smag models for each order of polynomial. As one can see, the average absolute values for coefficients associated to polynomial with order > 3 are about an order of magnitude smaller than the coefficients associated with polynomials of order 3. This justifies our choice in the truncation order.

3.3.2 Sensitivity to parameters

3.3.2.1 Sensitivity to parameters for the VMS-Smagorinsky model

Figure 3.9 and 3.10 present the sensitivity analysis of the VMS-Smag model for the TGV test case at $Re = 5000$ with $N_{LES} = 96$. The impact of the two parameters is studied for three quantities of interest: kinetic energy dissipation (figures 3.9(a)(c)), enstrophy (figures 3.9(b)(d)) and kinetic energy spectrum at $t = 8.5$ (figure 3.10). In both figures 3.9 and 3.10, the probability density functions (PDFs) of each quantity are shown and compared with the DNS from [DLLV17] for dissipation and present DNS with $N_{DNS} = 768$ for the other quantities. The PDFs for the quantities of interest are visually represented through a color gradient, where each segment of the plot is shaded following the likelihood of the quantity falling within that specific range. Hence, the darkest part of the plot identifies where the analyzed quantities show the lowest variation. One observes a strong variability at the peak of enstrophy (figure 3.9(b)) and at the tail of the spectrum (figure 3.10(a)), where the model is the most active. In figures 3.9(c)-(d) and 3.10(b), the partial variances are plotted as a function of time for enstrophy and dissipation (figure 3.9) and of wavenumber for the spectrum (figure 3.10). They represent the relative sensitivity to each of the two parameters and to the interaction between those parameters. The impact of the interaction is always quite low, showing the independence of the two parameters. The model seems to be sensitive to both parameters and in regions of high variability, the coefficient C_S is the dominant one.

Figure 3.11 represents the computed polynomial chaos expansion interpolation of the relative ℓ^2-error for enstrophy and kinetic energy spectrum obtained in LES compared with the 768^3 DNS. The error is represented as a function of coefficients C_S and n. The minima for the reconstructed response surfaces of the error for the energy spectrum and the enstrophy being close to each another, we identified the optimal values by taking their average. This led to $n = 6$ and $C_S = 0.41$.

[1] `https://dakota.sandia.gov/`

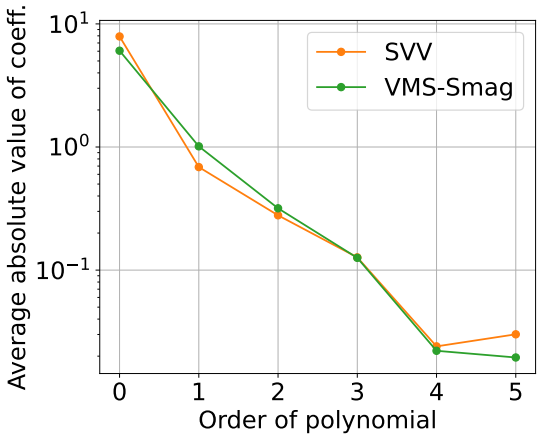

Figure 3.8: Average absolute value of polynomial coefficients with the order of the polynomial, evaluated over 120 surfaces responses in the Uncertainty Quantification for the SVV and VMS-Smag models.

3.3.2.2 Sensitivity to parameters for the SVV model

In a similar way, the PDFs and partial variances for kinetic energy dissipation, enstrophy (fig. 3.12), and kinetic energy spectrum at $t = 8.5$ (fig. 3.13) are shown for the SVV model. The quantities of interest given by the LES with the SVV model show a lower variability than for the VMS-Smag model. The agreement with the reference DNS is generally good, i.e., except for the peaks of dissipation for which the DNS value stands lightly outside of the PDF. When considering the partial variances, we observe that the model is much more sensitive to the coefficient C_{SVV} than to the filter order n. This is also observed in figure 3.14, showing the relative ℓ^2-error for enstrophy and kinetic energy spectrum compared with the DNS. The error does not vary much along the n axis. The two quantities show a local minimum in the same region, around $C_{SVV} = 0.09$ favoring small values of viscosity as observed in [KS06, KSB12]. Since the order of the filter was observed to be minor compared to that of the coefficient value and since the optimal value of the filter order is not clear, for further comparisons with VMS-Smag, we chose $n = 6$.

3.3.3 Simulations with calibrated coefficients

3.3.3.1 Taylor-Green Vortex

The Uncertainty Quantification conducted on the TGV test case at $Re = 5000$ with a resolution of $N_{LES} = 96$ revealed specific regions in the space of the parameters involved in the VMS-Smag and SVV models, corresponding to low errors in the quantities of interest compared with DNS. This allowed us to identify two "optimal" couples of parameters $(C_S, n) = (0.41, 6)$ and $(C_{SVV}, n) = (0.09, 6)$ for the two SGS models. To evaluate the robustness of this calibration, we assess the results obtained in LES with the two SGS models and the calibrated parameters, for various resolutions and Reynolds numbers.

Figure 3.15 shows the kinetic energy spectra for $Re = 1600$, 3000 and 5000 (along rows)

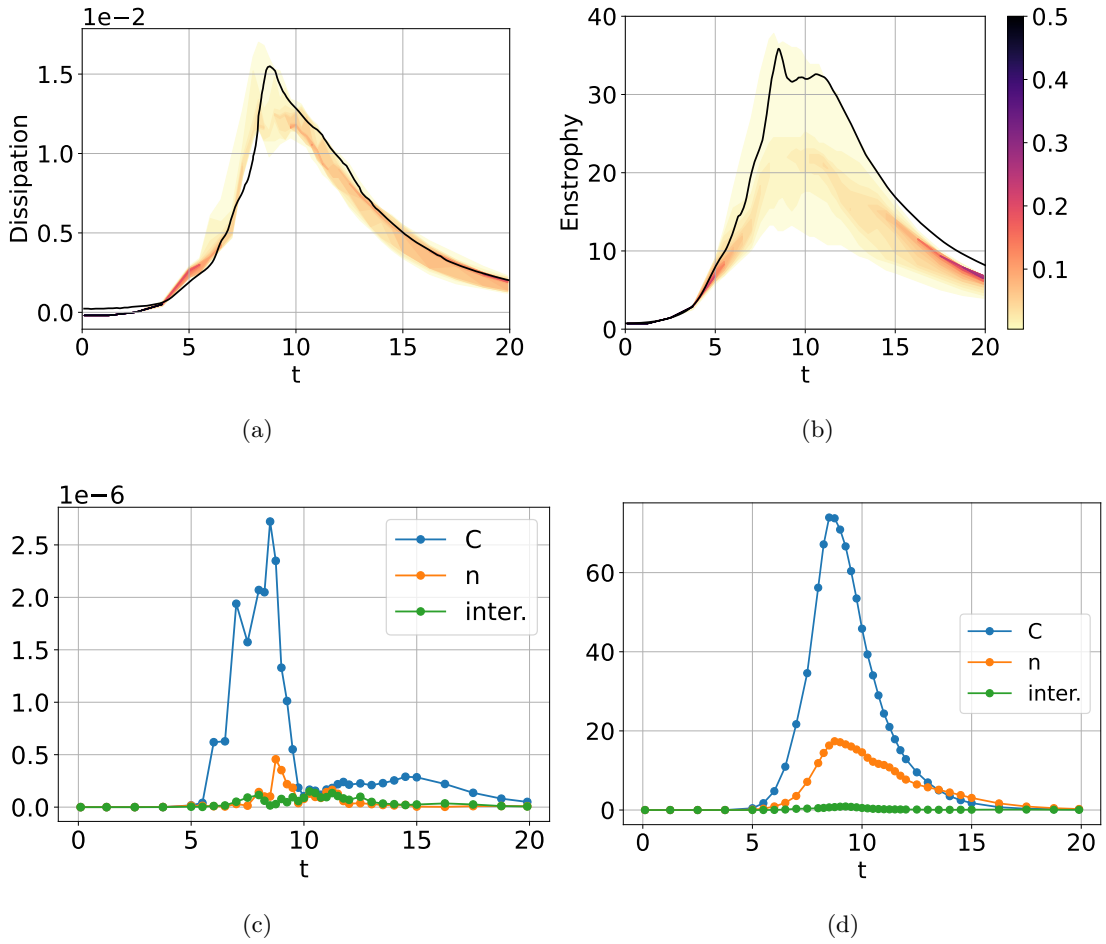

Figure 3.9: Sensitivity analysis of the VMS-Smag model for the TGV test case at $Re = 5000$ with $N_{LES} = 96$. (a)-(b) Probability density functions and (c)-(d) partial variances (for C_S, n, and their interaction) for time history of (left) kinetic energy dissipation and (right) enstrophy. Comparison with a reference DNS (solid black curve): (a) non-filtered 1280^3 DNS from [DLLV17], (b) filtered 768^3 DNS.

and $N_{LES} = 64$, 96 and 128 (along columns). We recall that the calibration was performed for the $Re = 5000$ and $N_{LES} = 96$ case (figure 3.15(h)). A comparison with DNS is shown (with $N_{DNS} = 512$ at $Re = 1600$ and $N_{DNS} = 768$ otherwise). For every configuration, the no-model case overestimates the energy in the small scales and over-dissipates the large scales. The VMS-Smag and SVV models with the "optimal" parameters show a very good agreement with the reference spectra until the cutoff.

Figure 3.16 shows the time history of the enstrophy in the following three configurations: $(Re = 1600, N_{LES} = 64)$, $(Re = 3000, N_{LES} = 64)$ and $(Re = 5000, N_{LES} = 96)$. A comparison with filtered DNS is shown (with $N_{DNS} = 512$ at $Re = 1600$ and $N_{LES} = 768$ otherwise). The same conclusions as before hold, with a slightly better performance in the peak and the decay of turbulence for SVV, the maximum value of enstrophy for SVV having a relative error with

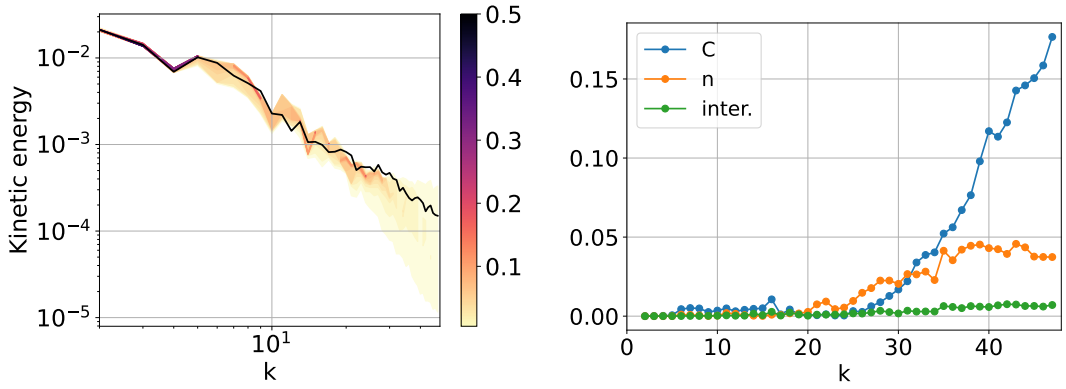

(a) (b)

Figure 3.10: (a) Probability density functions and (b) partial variances (for C_S, n, and their interaction) for kinetic energy spectrum at $t = 8.5$ for VMS-Smag simulations of TGV with $Re = 5000$ and $N_{LES} = 96$. Comparison with the present reference 768^3 DNS (solid black curve).

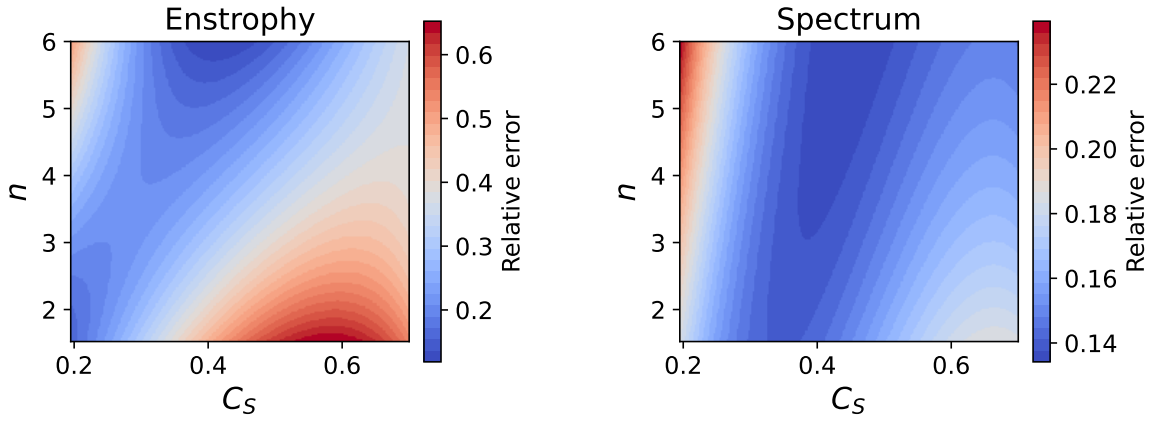

Figure 3.11: Surface response for the ℓ^2-error for time history of (left) enstrophy and (right) kinetic energy spectrum at $t = 8.5$ for VMS-Smag simulations of TGV with $Re = 5000$ and $N_{LES} = 96$.

the peak of enstrophy for the filtered DNS of 5%, 2% and 0.9% for $Re = 1600, 3000$ and 5000 respectively (although the peak is shifted for $Re = 5000$).

Figure 3.17 shows the time history of kinetic energy dissipation in the configuration for $Re = 1600$, 3000 and 5000 (along rows) and $N_{LES} = 64$, 96 and 128 (along columns). A comparison with non-filtered DNS is shown (with $N_{DNS} = 512$ for $Re = 1600$ and $N_{LES} = 768$ for $Re = 3000$ and the reference DNS from [DLLV17] for $Re = 5000$). It has to be noticed that this quantity was not included in our optimization procedure. Interestingly, the same conclusions

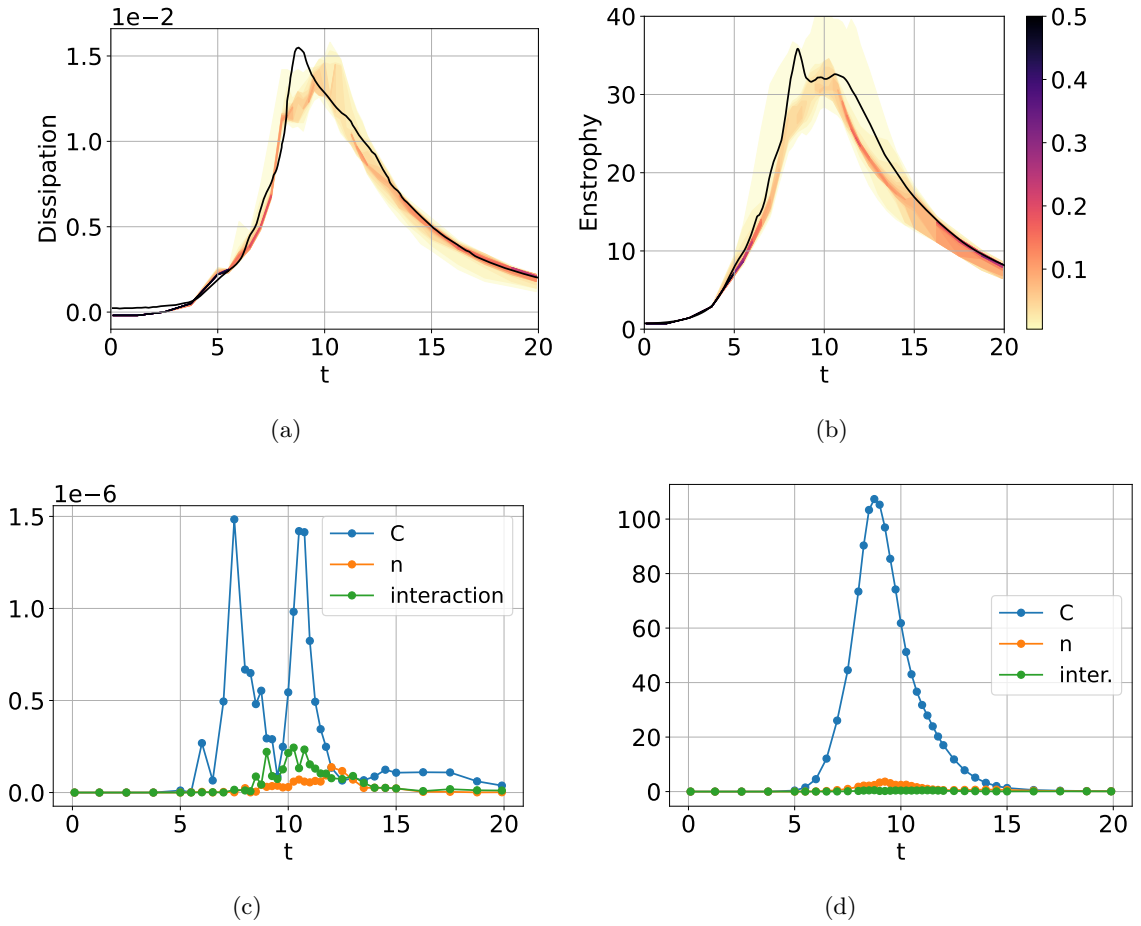

Figure 3.12: Sensitivity analysis of the SVV model on the TGV test case at $Re = 5000$ with $N_{LES} = 96$. (a)-(b) Probability density functions and (c)-(d) partial variances (for C_{SVV}, n, and their interaction) for time history of (left) kinetic energy dissipation and (right) enstrophy. Comparison with a reference DNS (solid black curve): (a) non-filtered 1280^3 DNS from [DLLV17], (b) filtered 768^3 DNS.

as for enstrophy and kinetic energy spectra hold for the dissipation: the VMS-Smag is slightly more dissipative in the coarser resolutions, however, contrary to enstrophy, it shows a better agreement with the DNS in the higher resolutions. The "double bump" observed near the peak of dissipation has already been observed for intermediate resolutions in other DNS performed with RVM (see for example Figure 9 of [MMM21]) and is certainly a feature due to the remeshing kernel order as shown in [Kec19] (section 3.2.8). In summary, these results indicate that the calibrated parameter values for both the VMS-Smag and SVV SGS models perform well even for Reynolds numbers, grid resolutions and physical quantities different from those they were initially optimized for.

Finally, figure 3.18 depicts the qualitative performance of the VMS-Smag and SVV models for the TGV test case at $Re = 5000$ with $N_{LES} = 128$. The flow structures drawn by the

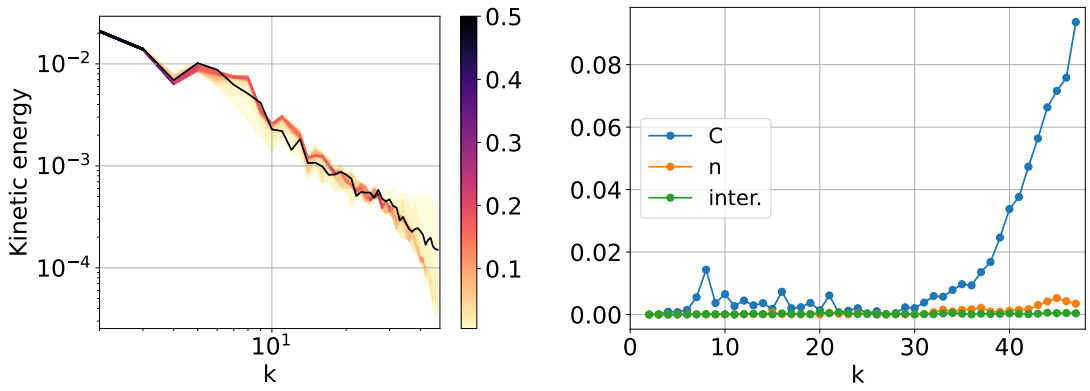

(a) (b)

Figure 3.13: (a) Probability density functions and (b) partial variances (for C_{SVV}, n, and their interaction) for kinetic energy spectrum at $t = 8.5$ for SVV simulations of TGV with $Re = 5000$ and $N_{LES} = 96$. Comparison with the present reference 768^3 DNS (solid black curve).

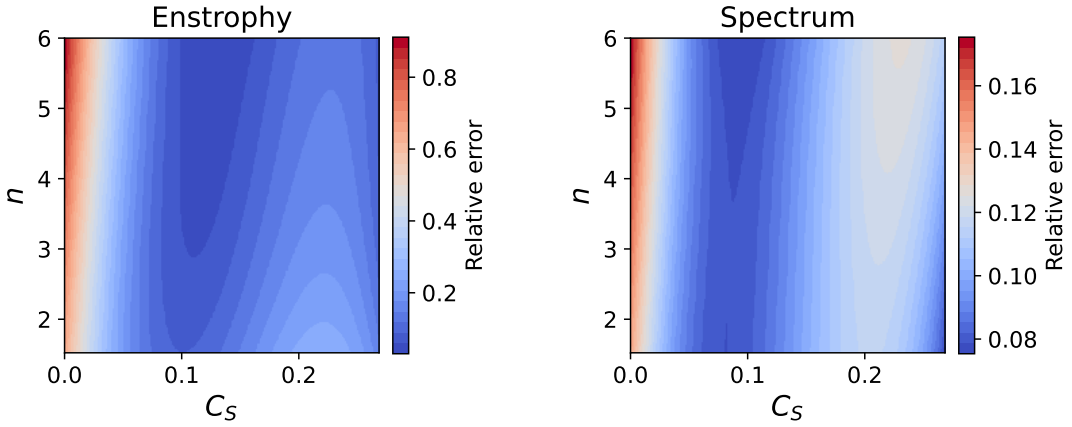

Figure 3.14: Surface response for the ℓ^2-error for time history of (left) enstrophy and (right) kinetic energy spectrum at $t = 8.5$ for SVV simulations of TGV with $Re = 5000$ and $N_{LES} = 96$.

streamwise velocity component u_x at the slice $x = \pi/8$ are compared with the DNS structures with $N_{DNS} = 768$. The no-model case is under-resolved and although it manages to capture the macro scales of the flow, it exhibits spurious oscillations. The structures for the VMS-Smag and SVV models confirm the previous results by showing a good qualitative agreement with DNS, with the VMS-Smag model being slightly more diffusive.

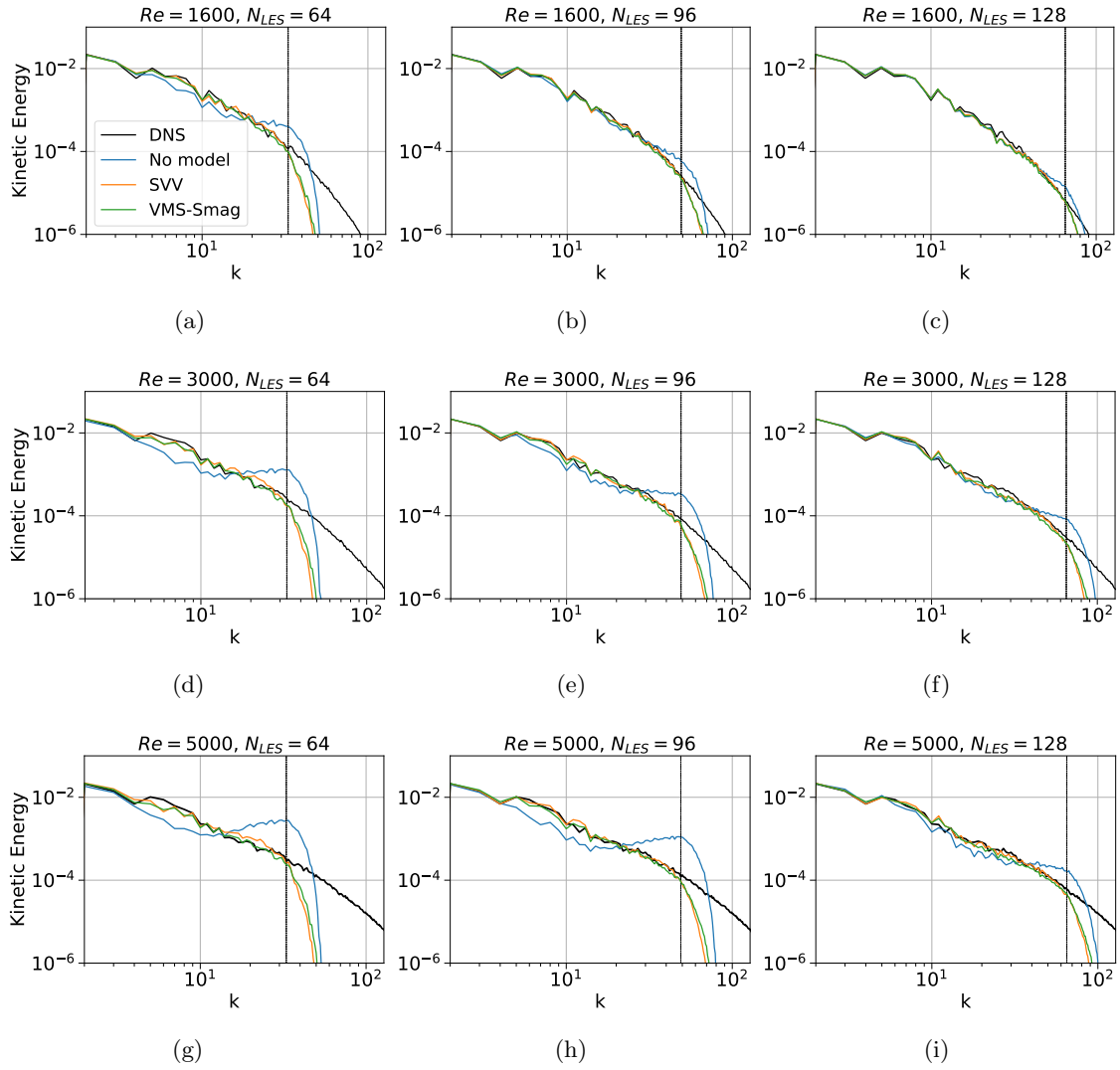

Figure 3.15: Kinetic energy spectrum at $t = 8.5$ for TGV at different Reynolds and resolutions, comparison with (a)-(c) 512^3 DNS, (d)-(i) 768^3 DNS. Uncertainty quantification was performed on case (h).

3.3.3.2 Decay of homogeneous isotropic turbulence (HIT)

The SVV and VMS-Smag models together with their "optimal" parameter values are then tested for a different test case. First, we aim to assess whether the model coefficients calibrated for the TGV case yield accurate results for a different flow configuration as well. As in the case of the TGV, we also investigate whether the parameter calibration is robust to changes in numerical resolution or Reynolds number. To these aims, we considered another classical test case: the decay of homogeneous isotropic turbulence (HIT).

The initial velocity and vorticity fields are obtained using the procedure described by Rogallo

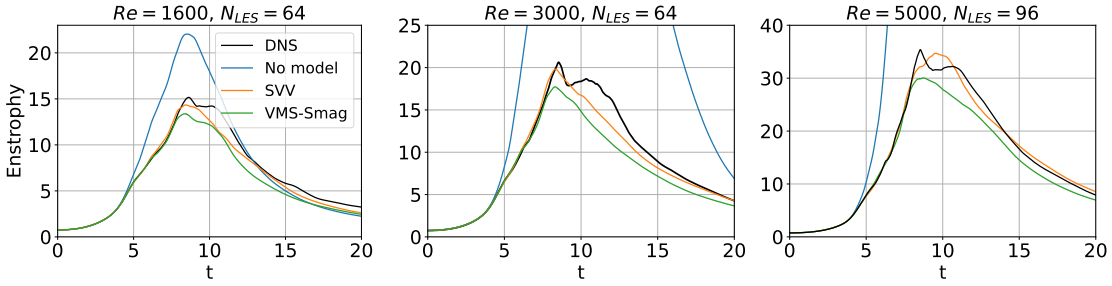

(a) (b) (c)

Figure 3.16: Time history of enstrophy for TGV at (a) $Re = 1600$, (b) $Re = 3000$ and (c) $Re = 5000$, comparison with filtered (a) 512^3 DNS, (b) and (c) 768^3 DNS. Uncertainty quantification was performed on case (c).

[Rog81] in a cubic box of size $2\pi^3$ with a 512^3 grid resolution from the initial spectrum given by:

$$E_{init}(|\mathbf{k}|, 0) = 16\sqrt{2/\pi}k_f^{-5}|\mathbf{k}|^4 e^{-2(|\mathbf{k}|/k_f)^2} \tag{3.25}$$

where here $k_f = 3$. The turbulence is then forced in Fourier space [LCP05] with:

$$\partial_t \hat{\boldsymbol{\omega}} = \frac{\mathbf{1}_{[|\mathbf{k}| \leq k_f]}}{2 \sum\limits_{|\mathbf{k}| \leq k_f} E(|\mathbf{k}|)} \hat{\boldsymbol{\omega}} \tag{3.26}$$

Once a statistically steady flow has been reached, the turbulent state is interpolated on a coarser grid, used as the initial state for the LES. Two cases with different viscosities are explored. The Reynolds numbers based on the Taylor microscale and considered in the following are $Re_\lambda = 140$ and $Re_\lambda = 210$.

The VMS-Smag model with the coefficients calibrated for the TGV case, namely $(C_S, n) = (0.41, 6)$, was found to give satisfactory results also for HIT without any adaptation, and the results will be compared against DNS in the following. Conversely, we found that the SVV SGS model with the previously calibrated parameters does not provide enough dissipation, yielding inaccurate results for all Reynolds numbers and resolutions studied. A new sensitivity analysis was then conducted with SVV for the case $Re_\lambda = 210$ and $N_{LES} = 64$. Figure 3.19 shows the response surfaces in the parameter space of the error compared with DNS with $N_{DNS} = 256$ for enstrophy and kinetic energy spectrum. It can be seen that the minimum of the error is around $C_{SVV} = 0.3$ independently of n.

The results obtained with the new calibrated value $(C_{SVV}, n) = (0.3, 6)$ are shown in figure 3.20 together with those given by the VMS-Smag model with the parameters calibrated for TGV and a reference DNS performed on a 256^3 grid. The figure shows the time history of enstrophy normalized with initial enstrophy at $Re_\lambda = 140$ and 210 and for three different resolutions, $N_{LES} = 16, 32$ and 96. As for the TGV case, the no-model simulations overestimate the enstrophy, except for the highest resolution and the lowest Reynolds number considered, where the cutoff scale is closer to Kolmogorov scale. Both models give results in good agreement with the DNS for all Re and resolutions, with VMS-Smag being slightly more diffusive.

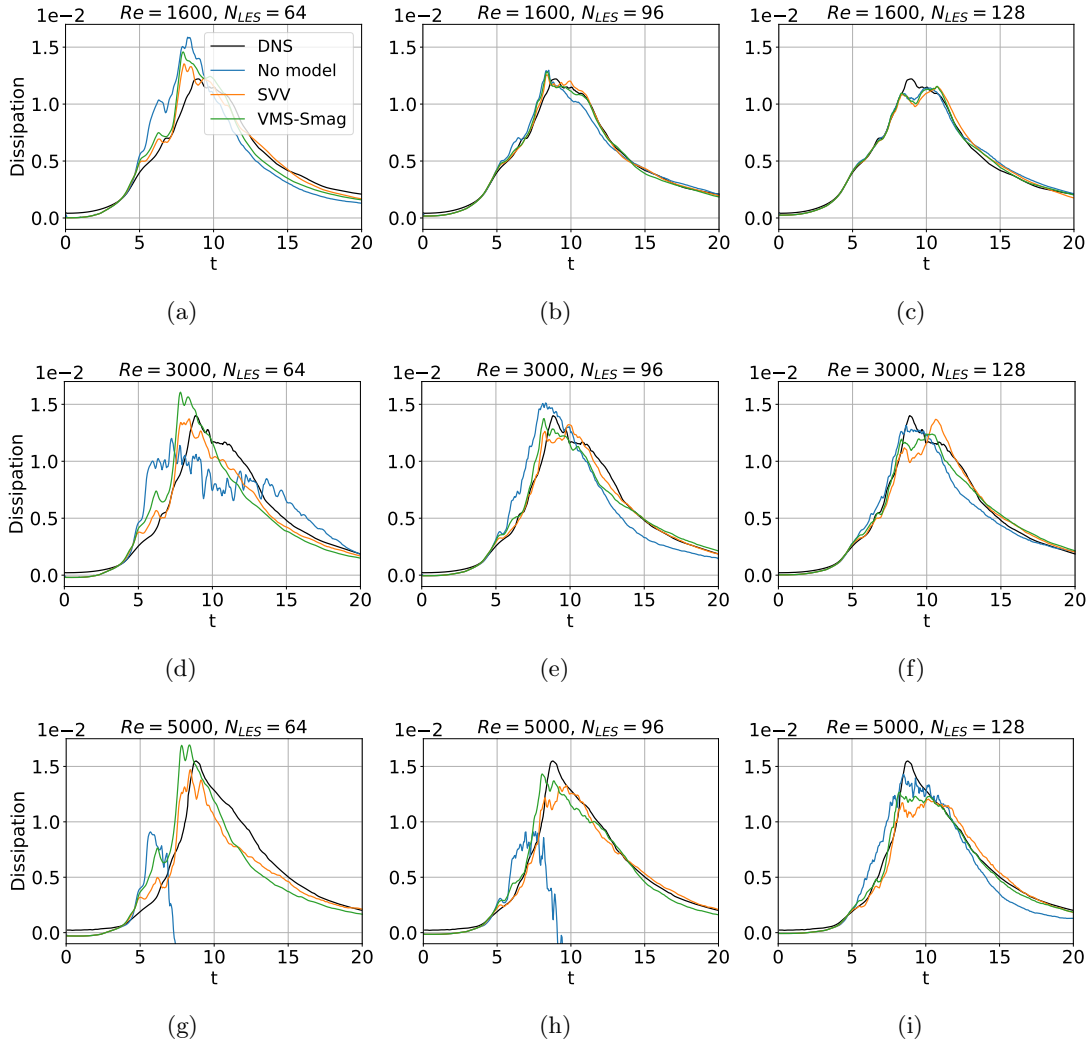

Figure 3.17: Time history of kinetic energy dissipation for TGV at different Reynolds and resolutions, comparison with (a)-(c) 512^3 DNS, (d)-(f) 768^3 DNS, and (g)-(i) reference 1280^3 DNS from [DLLV17]. Uncertainty quantification was performed on case (h).

Figure 3.21 compares the kinetic energy spectra obtained at $t = 1$ for the different Re and LES resolutions considered. The no-model simulation is characterized by energy pile-up at the smallest resolved scales, while the energy content of the largest ones is underestimated. This observation holds true in all cases except for the lowest Reynolds number and finer resolution, consistent with what was previously noted for enstrophy. The VMS-Smag and SVV SGS models with calibrated coefficients give spectra in good agreement with DNS up to the cut-off for all the considered Reynolds numbers and resolutions. Thus, as already observed for the TGV case, the model coefficient calibration is robust to changes in Reynolds number and resolution. However, the SVV model requires a further tuning of C_{SVV} for the HIT case. This can be explained by the method of computing artificial viscosity: in the VMS-Smag model, it is computed using the

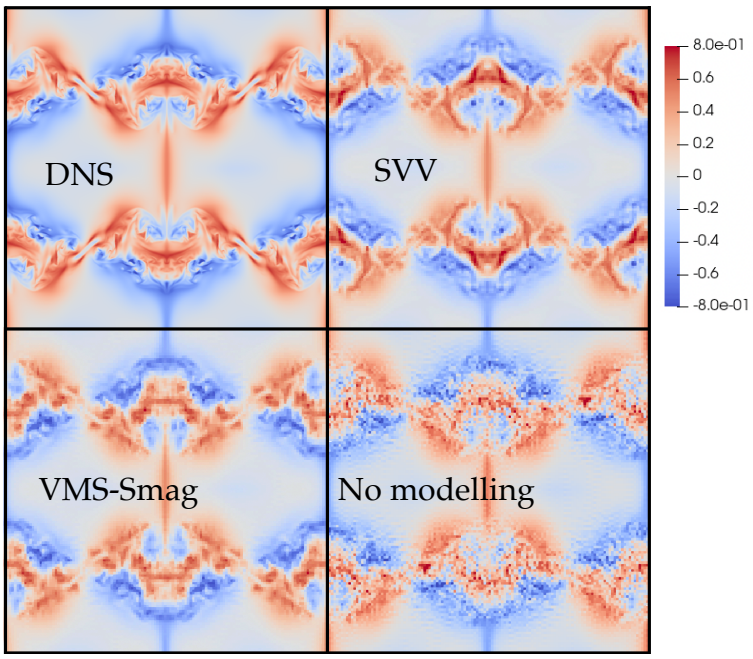

Figure 3.18: Qualitative comparison of the performance of the models on the flow structure depicted by the u_x velocity component at the slice $x = \pi/8$ for TGV at $Re = 5000$ and at $t = 8.5$. The no-model case, the SVV and the VMS-Smag results obtained with a $N_{LES} = 128$ resolution are compared to the DNS result with $N_{DNS} = 768$.

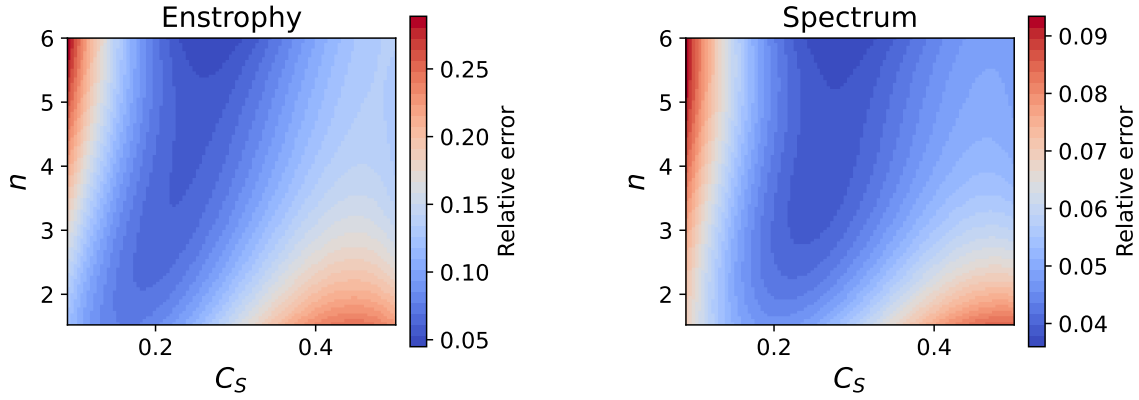

Figure 3.19: Surface response for the ℓ^2-error for (left) time history of enstrophy (right) and kinetic energy spectrum at $t = 1$ for SVV simulation of decaying HIT.

velocity field whereas in the SVV model, it depends solely on the cutoff scale.

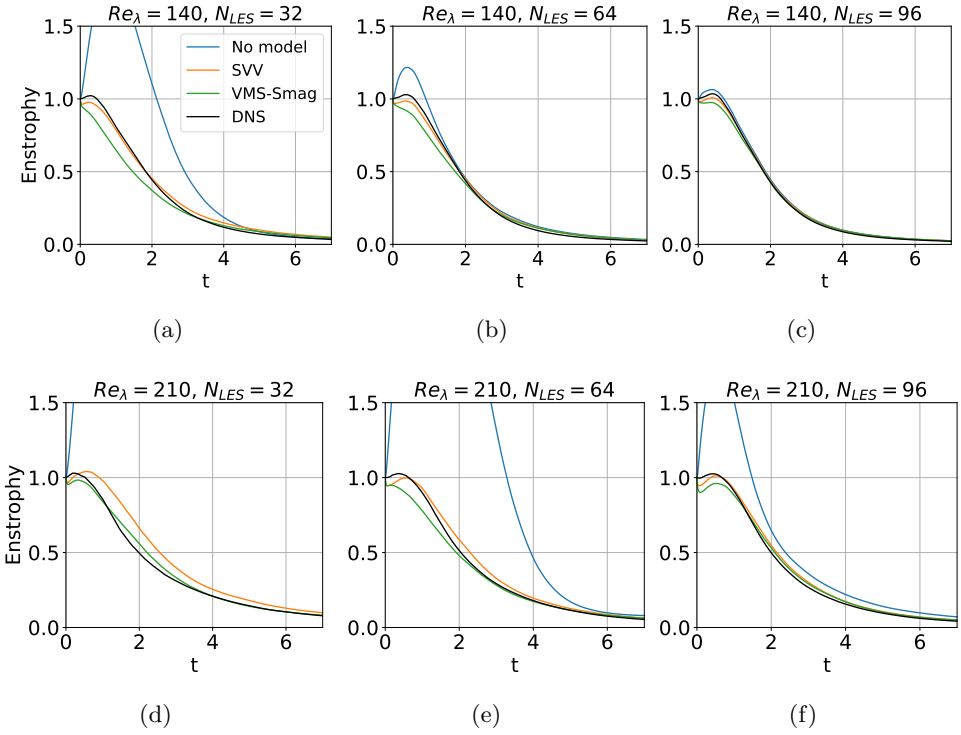

Figure 3.20: Time history of normalized enstrophy for the decay of HIT, comparison with filtered 256^3 DNS. Uncertainty quantification was performed on case (e).

Conclusion

In this chapter, we aimed to study various SGS models in the specific case of homogeneous isotropic turbulent flows.

Firstly, we evaluated various subgrid scale models for the TGV benchmark at $Re = 5000$. We first considered the standard and dynamic Smagorinsky models as well as a clipped gradient model. They were found to be over-dissipative in the large scales and not enough in the small scales. In contrast, the VMS approach, which introduces the SGS viscosity only in the smallest scales of the resolved field, turned out to be well adapted to the present RVM method employing vorticity as the main variable. Finally, we appraised the SVV model, which, to our knowledge, has never been explored within RVM. It was also found to be well suited, thanks to its multiscale nature as well as its easy integration in a fractional step algorithm already including spectral operators, making it a very low-cost approach.

Then, based on accuracy and computational cost considerations, the VMS-Smag and SVV models were selected for a further study of their sensitivity to parameters that must be a-priori assigned, i.e. model coefficients regulating the amount of introduced SGS viscosity, C_S and C_{SVV}, and filter order. This analysis was conducted again for TGV at $Re = 5000$ by using polynomial chaos expansion, that gives continuous response surfaces for the quantities of interest in the parameter space with a limited number of simulations. A remarkable variability of the results was observed, with C_S and C_{SVV} having the greatest impact, while the sensitivity to the

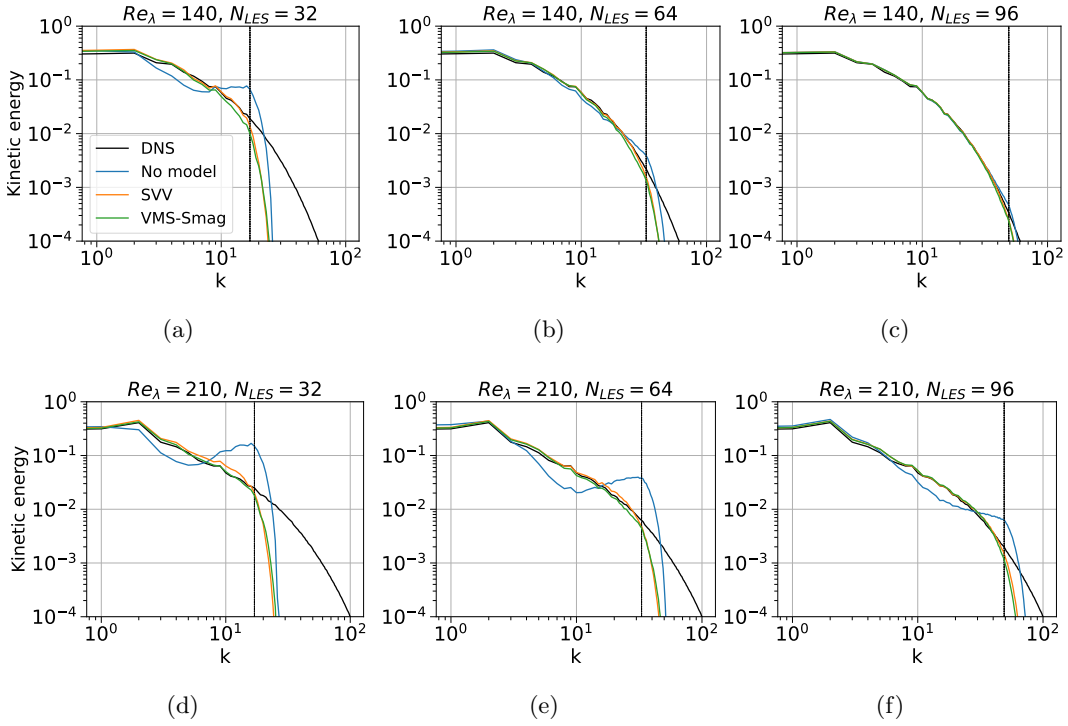

Figure 3.21: Kinetic energy spectrum at $t = 1$ for the decay of HIT, comparison with 256^3 DNS. Uncertainty quantification was performed on case (e).

filter used being relatively less important. Thanks to the response surfaces of the error respect to reference DNS data, "optimal" values of the parameters, in particular of C_S and C_{SVV}, could be identified for each SGS model. The so calibrated coefficients were then tested in LES of TGV and of decaying HIT, for different Reynolds numbers and grid resolutions. For the VMS-Smag model, the value of C_S calibrated for the TGV case yielded accurate results also for decaying HIT, while recalibration of C_{SVV} was needed for the SVV model in LES of the decaying HIT. For both SGS models and flow configurations, the parameter calibration is robust to changes in the flow regime (Reynolds number) and LES grid resolution.

Summarizing, the Variational Multi-Scale Smagorinsky and the Spectral Vanishing Viscosity SGS models appear well-suited for LES of turbulent homogeneous and isotropic flows with the remeshed Vortex method. This is attributed to their low computational cost and the fact that SGS viscosity is introduced only in the smallest resolved scales of the vorticity. As for the sensitivity to model parameters, it is dominated by the value of the coefficient regulating the amount of introduced SGS viscosity. This, together with the stochastic polynomial chaos expansion approach, simplifies the parameter calibration against DNS reference data. This calibration is robust to changes in Reynolds numbers and LES grid resolution, and, for the VMS-Smag model, also for a different flow configuration.

In the next chapter, we will focus on applying the present RVM approach to LESs of wall-bounded flows and checking to what extent the conclusions of the present SGS modeling assessment and calibration hold in presence of solid walls.

Chapter 4

Application to wall-bounded flows

Contents

Introduction

In the previous chapter, we compared and calibrated subgrid-scale models in the present vortex method. Our study exhibited two models, namely SVV and VMS-Smagorinsky, based on the filtering of small scales of vorticity, as well as optimal coefficients for these models in the context of homogeneous isotropic turbulence. This chapter aims to test the robustness of these findings on more challenging cases involving solid boundaries: a channel flow with hills at the bottom and the flow past a sphere.

4.1 Turbulent flow over periodic hills

4.1.1 Presentation

4.1.1.1 Test case setup

The test case considered is the classical channel flow over periodic hills[1]. It consists of a channel with two smooth hills at the bottom of the domain. The size of the domain is $9h \times 3.035h \times 4.5h$ where h is the height of the hills.

[1] kbwiki.ercoftac.org/w/index.php/Abstr:2D_Periodic_Hill_Flow

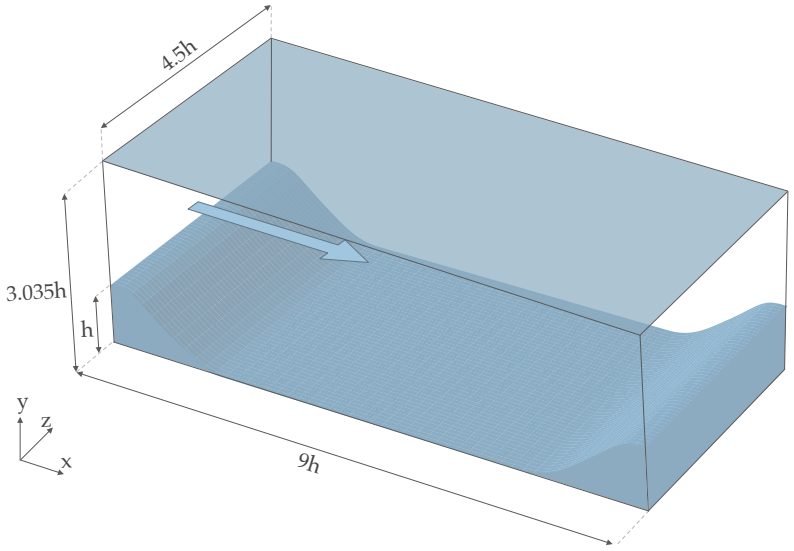

Figure 4.1: Test case configuration.

The profile of a hill is given by the polynomial

$$H(x) = \begin{cases} \min(h, h + 2.42h \times 10^{-4}x^2 - 7.588h \times 10^{-5}x^3) & \text{if } 0 \leq x \leq 0.3214h \\ 0.8955h + 3.484h \times 10^{-2}x - 3.629h \times 10^{-3}x^2 + 6.749h \times 10^{-5}x^3 & \text{if } 0.3214h \leq x \leq 0.5h \\ 0.9213h + 2.931h \times 10^{-2}x - 3.234h \times 10^{-3}x^2 + 5.809h \times 10^{-5}x^3 & \text{if } 0.5h \leq x \leq 0.7143h \\ 1.445h - 4.927h \times 10^{-2}x + 6.950h \times 10^{-4}x^2 - 7.394h \times 10^{-6}x^3 & \text{if } 0.7143h \leq x \leq 1.071h \\ 0.6401h + 3.123h \times 10^{-2}x - 1.988h \times 10^{-3}x^2 + 2.242h \times 10^{-5}x^3 & \text{if } 1.071h \leq x \leq 1.429h \\ \max(0, 2.0139h - 7.180h \times 10^{-2}x + 5.875h \times 10^{-4}x^2 + 9.553h \times 10^{-7}x^3) & \text{if } 1.429h \leq x \leq 1.929h \end{cases}$$

Periodic boundary conditions are imposed in the streamwise (x) and spanwise (z) directions and no-slip boundary conditions are prescribed in the vertical (y) direction. In the present simulations, the no-slip conditions are imposed with the Brinkman penalization method, described in 1.1.3.1 and 1.2.2.4. A constant flowrate is imposed at the entry of the domain with bulk velocity U_b. The Reynolds number is based on the hill height, h and U_b.

This test case was chosen to evaluate the capabilities of the RVM in resolving turbulent flows for multiple reasons. First, the turbulence stems from the hill profile, and thus does not require an additional forcing term or prescribed fluctuations to appear. The flow exhibits complex features such as flow separation and reattachment, a shear layer and a recirculation bubble, as well as a boundary layer at the top of the domain, making it a challenging test case.

4.1.1.2 Previous works

This configuration, slightly different than the present one, was introduced in an experiment by Almeida *et al.* [ADH93]. It was then chosen for an ERCOFTAC workshop in 1995 as a numerical test case, that highlighted issues with the original configuration, namely the low spanwise/vertical aspect ratio and the short distance between the hills. A new configuration was then proposed by Mellen *et al.* [MFR00].

The flow was since then studied extensively in literature. A key reference study is that of Breuer *et al.* [BPRM09] who explored different Reynolds numbers,performing DNS up to

$Re = 5600$ and LES for $Re = 5600$ and $Re = 10595$ using a dynamical Smagorinsky model (with averaging in the spanwise homogeneous direction), as well as experimentally using a water channel at $Re = 5600$ and $Re = 10595$. Two second-order finite-volumes codes were used for the DNS, one using a Cartesian grid (MGLET) and the other a curvilinear grid (LESOCC). The LES was only performed using LESOCC. Another reference experimental study is the one by Rapp and Manhart [RM11].

Among the more recent studies one can cite the DNSs performed by Krank *et al.* [KKW18] at $Re = 10595$ and $Re = 5600$ using a 7^{th} order spatial accuracy spectral discontinuous Galerkin scheme, and a comparison of different high-resolution LES configurations [GC19] and different subgrid-scale models, including a so-called MSM-ls (multi-scale large small) model which is directly comparable to our VMS-Smag. The flow has been also investigated a number of times in the context of ILES [HKA08, KKW18, WWXS21, SRCDB24]. In particular, in [WWXS21], a SVV method is compared to the LES of Fröhlich *et al.* [FMR$^+$05].

We will use in the following as references the LESOCC DNSs and LESs from Breuer *et al.* [BPRM09] as well as the DNSs from Krank *et al.* [KKW18]. The reason for using three references is that they do not perfectly coincide reflecting the variability introduced by the different simulation and measurement techniques, especially at higher Re.

4.1.2 Numerical results

4.1.2.1 Simulation setup

The major constraint of the present method when dealing with bounded flows is the regular Cartesian grid imposed by the remeshing and FFT operations. Due to the boundary layer developing at the ceiling of the domain, we opted for a smaller step size in the vertical direction compared to the other directions. The step size in the streamwise and spanwise directions is therefore chosen to be respectively twice and three times that in the vertical direction (i.e. $\Delta x/\Delta y = 2$ and $\Delta z/\Delta y = 3$) for the direct numerical simulations and respectively six and three times that in the vertical direction (i.e. $\Delta x/\Delta y = 6$ and $\Delta z/\Delta y = 3$) for the Large Eddy Simulations (see figure 4.2).

An important aspect of our code is its current constraint to Cartesian grids uniform by direction, leading to large cell size near the solid walls, compared to most references that use a non-uniform grid, at least in the vertical direction. Our uniform cell size in the vertical direction is about $\Delta y/h = 9 \times 10^{-3}$ for our finer DNS grid with $N_y = 342$ and $\Delta y/h = 1.2 \times 10^{-2}$ for our LES grid with $N_y = 256$. For comparison, Breuer *et al.* 's curvilinear grid, used both for DNS at $Re = 2800$ and LES at $Re = 10595$, has a cell size in the vertical direction of $\Delta y/h = 1.2 \times 10^{-3}$ at the crest of the hill, about 10 times finer. For $Re = 10595$ the number of grid points is small compared to the references: our LES grid has about 4.2 million points while Breuer *et al.* 's LESOCC LESs are performed on a grid with 13.1 million points and Krank *et al.* 's DNS uses about 180 million grid points.

Our simulations use a LCFL constant of 0.125 for the computation of the advection time step which is computed with

$$\Delta t_{advec} = \frac{C_{LCFL}}{\|\boldsymbol{\omega}\|_\infty}.$$

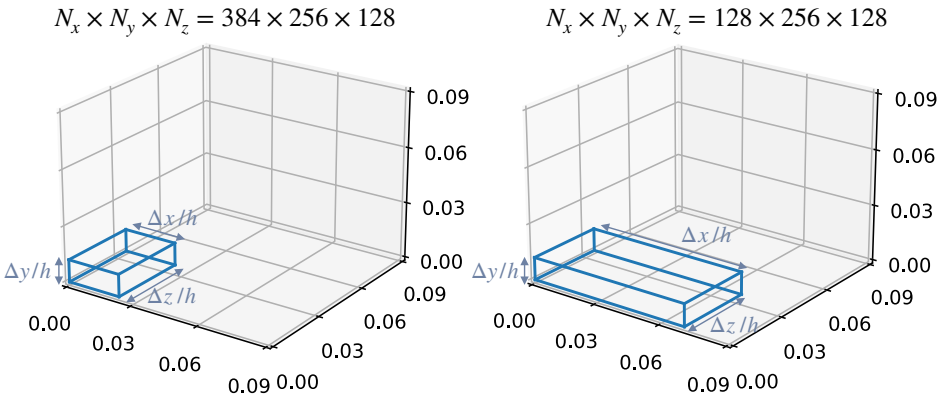

Figure 4.2: Shape of the computational Cartesian cells for DNS (left) and LES (right).

This leads to an average dimensionless timestep of about $\Delta t/h = 1.3 \times 10^{-3}$ for DNSs and $\Delta t/h = 2.2 \times 10^{-3}$ for the LESs, similar than Breuer *et al.* with $\Delta t/h = 2 \times 10^{-3}$ in DNS and $\Delta t/h = 1.8 \times 10^{-3}$ in LES. This is partly due to the low LCFL value, set at 0.125, which can be increased for future works, but also underlines that the advantage of the vortex method in this regard is limited in coarse simulations of turbulent flows as the high value of the velocity gradients constrain the time steps through the LCFL condition. However, since the timestep value is not tied to the grid size, it does not decrease as the resolution increases.

To ensure that the flow has reached a statistically steady state, data collection for the flow statistics begins after 20 flow-through times. Averaging is then performed over the following 60 flow-throughs, a duration during which the mean quantities exhibit minimal variation. Figure 4.3 illustrates the relative error between the final averaged quantities (i.e. mean velocities and Reynolds stresses) and those obtained after 10, 20, 30, 40, and 50 flow-throughs, for a representative simulation. The relative difference between the averages computed over 50 and 60 flow-throughs is on the order of 10^{-2}, indicating that 60 flow-throughs are sufficient to obtain statistically meaningful results.

4.1.2.2 Direct Numerical Simulation at Re=2800

We consider four grids of the same aspect ratio and with increasing resolution, 252×168×84, 288×192×96, 384×256×128 and 512×342×170. The flow quantities analyzed are the spanwise- and time-averaged velocities and Reynolds stresses, which are compared to reference DNS data from [BPRM09].

Figure 4.4 represents the averaged streamwise velocity field $\langle U \rangle / U_b$ and streamlines for the highest considered resolution. The figure shows the regions of separation, re-circulation and re-attachment.

Figures 4.5 and 4.6 represent the averaged velocity profiles and averaged Reynolds stresses profiles respectively. Despite the uniform Cartesian grid, the low-resolution results are close to the reference, with, in particular, a behavior in the vicinity of the upper-solid wall that is well reproduced (see the close-up views in figure 4.7).

The order of convergence of the the present RVM being related to the order of the particle

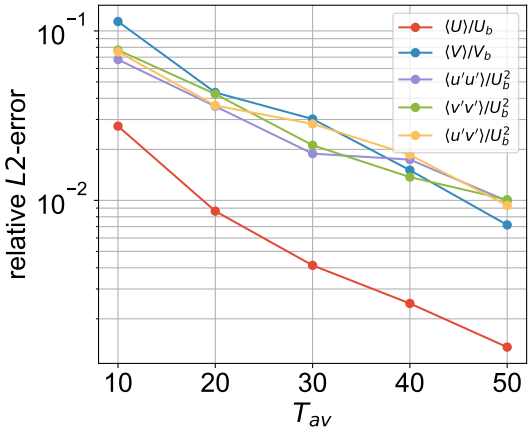

Figure 4.3: Relative error between the final averaged quantities (computed over 60 flow-throughs) and intermediate averages obtained after 10, 20, 30, 40, and 50 flow-throughs, for a 384×256×128 simulation of the flow over periodic hills at $Re = 2800$.

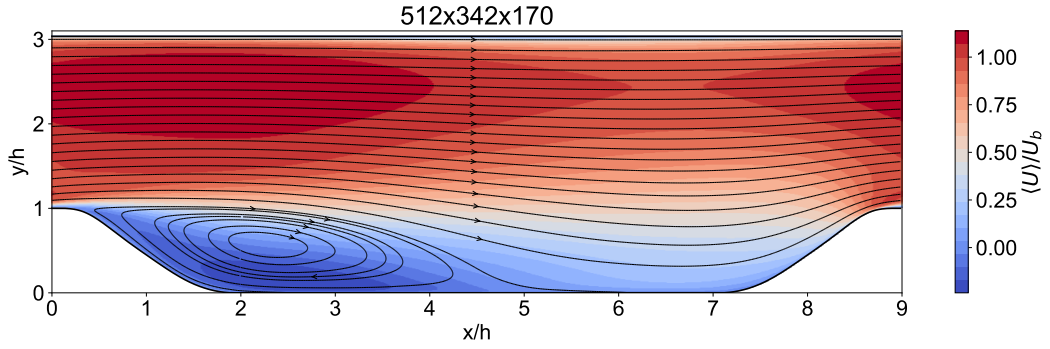

Figure 4.4: Averaged streamwise velocity field and streamlines for DNS at $Re = 2800$.

remeshing kernel, we tested two different kernels, namely $\Lambda_{4,2}$ (4^{th} order) and $\Lambda_{8,4}$ (8^{th} order) (see subsection 1.1.2.2). As shown in figure 4.8, increasing the order of the remeshing kernel leads to an increased accuracy on the flow statistics. In particular, the overshoot of the averaged streamwise Reynolds stress $\langle u'u'\rangle$ in the middle of the domain seems to be reduced by the higher order kernel. This effect is also visible on figure 4.9 representing the convergence study performed with $\Lambda_{4,2}$ (solid curves) and $\Lambda_{8,4}$ (dashed curves). Except for the last error-value of $\langle v'v'\rangle$ for $\Lambda_{8,4}$, the convergence order is between 1 and 2 for all the averaged quantities under consideration, in accordance with previous studies based on a similar RVM algorithm [MMM21].

Finally, figure 4.10 represents the time- and span-averaged wall shear stress close to the bottom boundary, obtained with the $\Lambda_{4,2}$ remeshing kernel and reconstructed with second order finite differences. Due to the reduced number of grid cells near the hills and the *a posteriori* nature of the reconstruction, this quantity is the least accurately reproduced by our simulations,

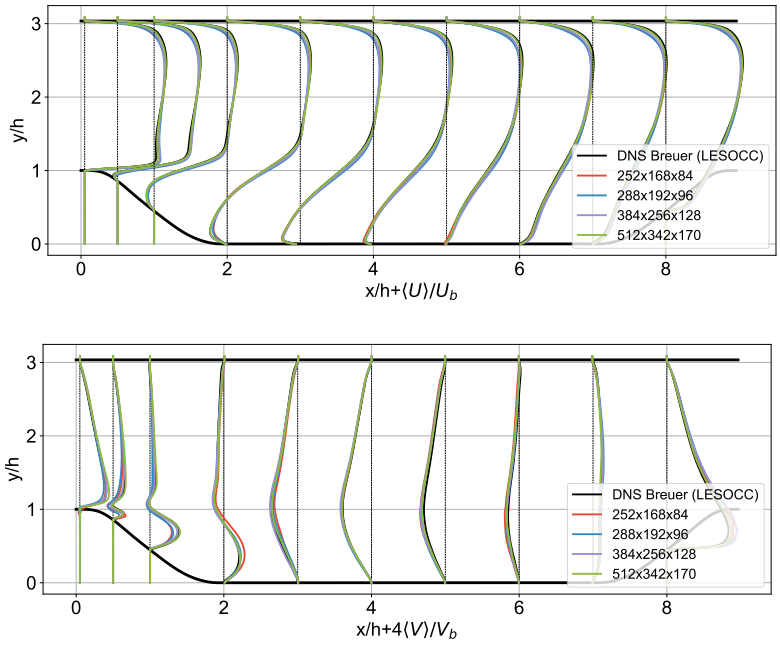

Figure 4.5: Time- and span-averaged streamwise ($\langle U \rangle / U_b$) and vertical ($\langle V \rangle / U_b$) velocity profiles for the different grid resolutions for the DNS of flow over periodic hills at $Re = 2800$ with remeshing kernel $\Lambda_{4,2}$, comparison with [BPRM09].

especially near the second hill, after flow reattachment. Considering the size of the recirculation bubble, although the separation point is recovered (0.24 for $\Lambda_{4,2}$ and 0.23 for $\Lambda_{8,4}$ vs 0.22 for [BPRM09]), the bubble is too short for both kernels, with a reattachement point 5.08 for $\Lambda_{4,2}$ and 5.15 for $\Lambda_{8,4}$ vs 5.41 for [BPRM09]. Once again, this is a limitation of our low resolution near the floor and of the first order Brinkman penalization procedure used to enforce the no-slip boundary conditions in the present RVM and confirms that the region near the second hill is the most challenging to solve.

This DNS study was performed without specifically considering the sequence of directional operations in the Strang splitting algorithm (subsection 1.2.2.1), i.e the sequence of directions chosen to subsequently solve the 1D problems in the splitting algorithm was taken as the default one implemented in `HySoP`: since the x (streamwise) direction is the parallelization direction in the solver, it is treated last in practice. In the Strang splitting algorithm, the directions were thus treated following this sequence: spanwise (z) - vertical (y) - streamwise (x). As we will see below, this sequence can lead to an increase of the method's numerical error and therefore to instabilities in the context of non-homogeneous and anisotropic flows, especially when considering high Reynolds numbers. The question of finding an optimal sequence of directions treatment in the present RVM's splitting algorithm is discussed in the following section.

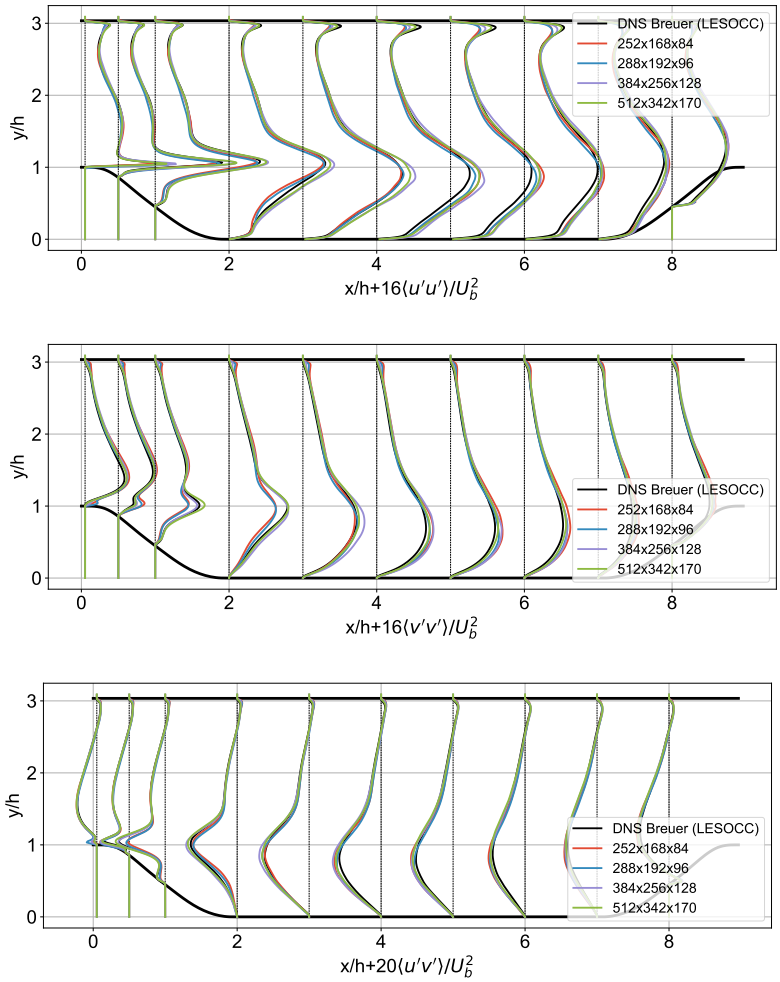

Figure 4.6: Time- and span-averaged streamwise normal ($\langle u'u' \rangle / U_b^2$), vertical ($\langle v'v' \rangle / U_b^2$) and shear ($\langle u'v' \rangle / U_b^2$) Reynold stress profiles for the different grid resolutions for the DNS of flow over periodic hills at $Re = 2800$ with remeshing kernel $\Lambda_{4,2}$, comparison with [BPRM09].

4.1.2.3 Directional splitting

In this section, we revisit a key component of the present RVM: the directional splitting algorithm where the advection, remeshing and stretching operators are treated as 1D problems solved successively (subsection 1.2.2.1). As opposed to chapter 3, we are no longer considering homogeneous isotropic flows and we are now working in a context where directional asymmetries exist. Therefore, an important numerical question we are faced with is the optimizing of the sequence of directions in the operators directional splitting.

As an illustration of a simple case, let us first study the 2D case, where the directional splitting only concerns the advection-remeshing operator. In the following we consider a directional Strang splitting that is of first-order in time. In this context, the advection operator can therefore be

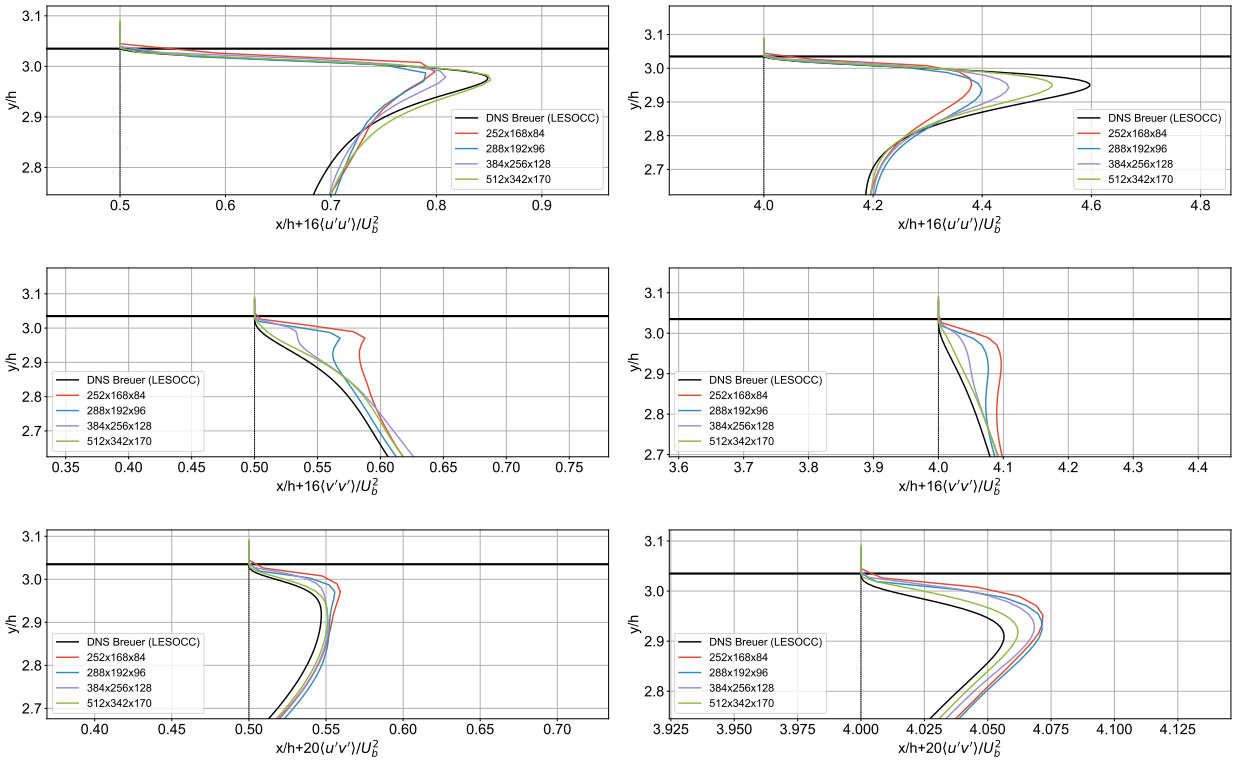

Figure 4.7: Close-up views of the $\langle u'u' \rangle / U_b$ (top), $\langle v'v' \rangle / U_b$ (center) and $\langle u'v' \rangle / U_b$ (bottom) profiles represented in figure 4.6, at two distinct positions $x/h = 0.5$ and $x/h = 4$, comparison with [BPRM09].

decomposed as:

$$\partial_t \boldsymbol{\omega} = \mathbf{u} \cdot \nabla \omega = u_x \partial_x \omega + u_y \partial_y \omega \tag{4.1}$$

which, following the first-order Strang splitting, can be split into two different 1D-advection sub-problems, by two means:
Case A:

1. x-axis splitting: $\partial_t \omega = u_x \partial_x \omega$
2. y-axis splitting: $\partial_t \omega = u_y \partial_y \omega$

Case B:

1. y-axis splitting: $\partial_t \omega = u_y \partial_y \omega$
2. x-axis splitting: $\partial_t \omega = u_x \partial_x \omega$

where each directional operator represents the advection of the particles along the given axis.

Considering an Euler scheme for time discretization, the directional splitting for the 2D advection in case A writes:

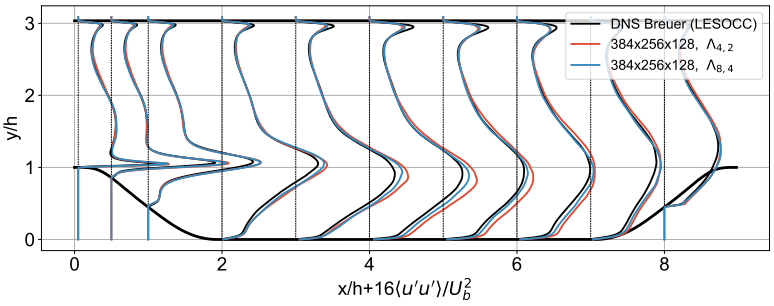

Figure 4.8: Comparison of the time- and span-averaged streamwise normal ($\langle u'u' \rangle / U_b^2$) Reynolds stress profiles for remeshing kernel $\Lambda_{4,2}$ and $\Lambda_{8,4}$ for the DNS of flow over periodic hills at $Re = 2800$, comparison with [BPRM09].

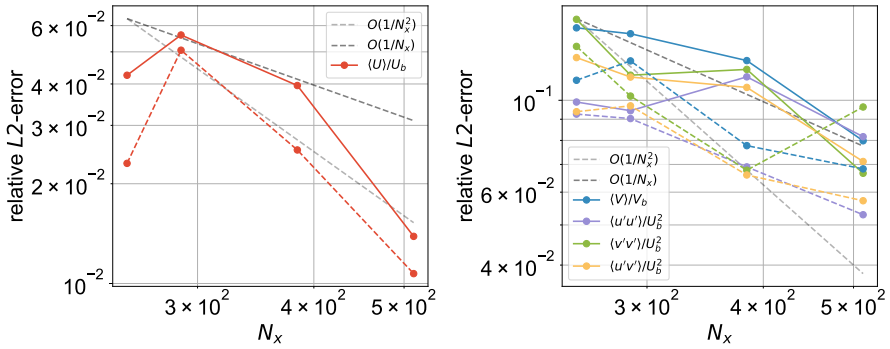

Figure 4.9: L^2 grid-convergence for simulations with remeshing kernel $\Lambda_{4,2}$ (solid lines) and $\Lambda_{8,4}$ (dashed lines).

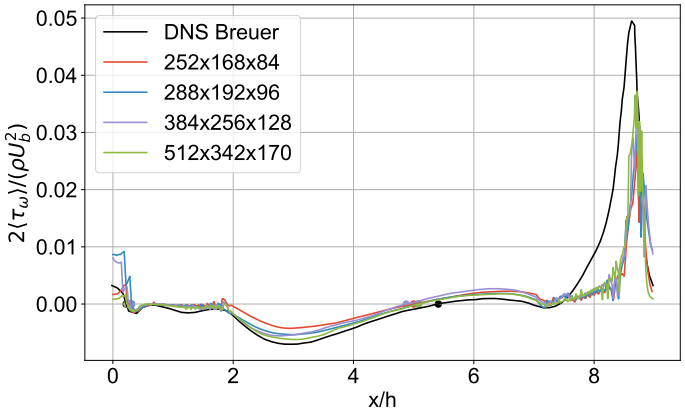

Figure 4.10: Time- and span-averaged wall shear stress close to the bottom boundary, reconstructed with second order finite differences for the different grid resolutions for the DNS of flow over periodic hills at $Re = 2800$ with remeshing kernel $\Lambda_{4,2}$, comparison with [BPRM09]. The round dots correspond to the change of sign of the wall shear stress, measuring the flow separation and reattachement points.

1. advection along the x direction:

$$\tilde{\omega}^{n+1} = \omega^n + \Delta t(u_x \partial_x \omega^n)$$

2. advection along the y direction:

$$\begin{aligned}\omega^{n+1} &= \tilde{\omega}^{n+1} + \Delta t(u_y \partial_y \tilde{\omega}^{n+1}) \\ &= \omega^n + \Delta t(u_x \partial_x \omega^n + u_y \partial_y \omega^n) + \mathbf{\Delta t^2}(\mathbf{u_y \partial_y u_x \partial_x \omega^n + u_y u_x \partial_y \partial_x \omega^n})\end{aligned}$$

The term in bold is an error term due to the directional splitting. This term is dependant on the sequence of directions chosen. Indeed, if instead we treat direction y first (Case B), we obtain after the second step:

$$\omega^{n+1} = \omega^n + \Delta t(u_x \partial_x \omega^n + u_y \partial_y \omega^n) + \mathbf{\Delta t^2}(\mathbf{u_x \partial_x u_y \partial_y \omega^n + u_x u_y \partial_x \partial_y \omega^n})$$

If instead of an Euler scheme, a Runge-Kutta scheme is used for the time integration, the same second-order term appears (and additional terms at higher orders). We observed that this sequence does have an influence on the quality of the solution when considering strongly anisotropic flows, such as the present periodic hills case.

In 3D, the situation is more complex: instead of one operator treated with directional splitting we have two: "advection-remeshing" and "stretching". And instead of two cases for the sequence of treatment of directions we now have 6 cases per operator, meaning 36 in total. The splitting error terms for the 6 different cases for the advection and stretching operators are presented in table 4.1 and 4.2 respectively. Since testing all of them *a posteriori* would be too costly, we calculated the splitting error term and evaluated it *a priori* on a low-resolution simulation of the 3D periodic hills at $Re = 2800$ using finite differences.

Cases (directions sequences)	Error term
x-y-z	$\mathbf{u}_y\partial_y(\mathbf{u}_x\partial_x\boldsymbol{\omega}^n) + \mathbf{u}_z\partial_z(\mathbf{u}_x\partial_x\boldsymbol{\omega}^n + \mathbf{u}_y\partial_y\boldsymbol{\omega}^n)$
x-z-y	$\mathbf{u}_z\partial_z(\mathbf{u}_x\partial_x\boldsymbol{\omega}^n) + \mathbf{u}_y\partial_y(\mathbf{u}_x\partial_x\boldsymbol{\omega}^n + \mathbf{u}_z\partial_z\boldsymbol{\omega}^n)$
y-x-z	$\mathbf{u}_x\partial_x(\mathbf{u}_y\partial_y\boldsymbol{\omega}^n) + \mathbf{u}_z\partial_z(\mathbf{u}_y\partial_y\boldsymbol{\omega}^n + \mathbf{u}_x\partial_x\boldsymbol{\omega}^n)$
y-z-x	$\mathbf{u}_z\partial_z(\mathbf{u}_y\partial_y\boldsymbol{\omega}^n) + \mathbf{u}_x\partial_x(\mathbf{u}_y\partial_y\boldsymbol{\omega}^n + \mathbf{u}_z\partial_z\boldsymbol{\omega}^n)$
z-x-y	$\mathbf{u}_x\partial_x(\mathbf{u}_z\partial_z\boldsymbol{\omega}^n) + \mathbf{u}_y\partial_y(\mathbf{u}_z\partial_z\boldsymbol{\omega}^n + \mathbf{u}_x\partial_x\boldsymbol{\omega}^n)$
z-y-x	$\mathbf{u}_y\partial_y(\mathbf{u}_z\partial_z\boldsymbol{\omega}^n) + \mathbf{u}_x\partial_x(\mathbf{u}_z\partial_z\boldsymbol{\omega}^n + \mathbf{u}_y\partial_y\boldsymbol{\omega}^n)$

Table 4.1: Advection error term for each splitting configuration.

Cases (directions sequences)	Error term
x-y-z	$\partial_y(\partial_x[\boldsymbol{\omega}_x^n\mathbf{u}_y]\mathbf{u}) + \partial_z(\partial_x[\boldsymbol{\omega}_x^n\mathbf{u}_z]\mathbf{u}) + \partial_z(\partial_y[\boldsymbol{\omega}_y^n\mathbf{u}_z]\mathbf{u})$
x-z-y	$\partial_z(\partial_x[\boldsymbol{\omega}_x^n\mathbf{u}_z]\mathbf{u}) + \partial_y(\partial_x[\boldsymbol{\omega}_x^n\mathbf{u}_y]\mathbf{u}) + \partial_y(\partial_z[\boldsymbol{\omega}_z^n\mathbf{u}_y]\mathbf{u})$
y-x-z	$\partial_x(\partial_y[\boldsymbol{\omega}_y^n\mathbf{u}_x]\mathbf{u}) + \partial_z(\partial_y[\boldsymbol{\omega}_y^n\mathbf{u}_z]\mathbf{u}) + \partial_z(\partial_x[\boldsymbol{\omega}_x^n\mathbf{u}_z]\mathbf{u})$
y-z-x	$\partial_z(\partial_y[\boldsymbol{\omega}_y^n\mathbf{u}_z]\mathbf{u}) + \partial_x(\partial_y[\boldsymbol{\omega}_y^n\mathbf{u}_x]\mathbf{u}) + \partial_x(\partial_z[\boldsymbol{\omega}_z^n\mathbf{u}_x]\mathbf{u})$
z-x-y	$\partial_x(\partial_z[\boldsymbol{\omega}_z^n\mathbf{u}_x]\mathbf{u}) + \partial_y(\partial_z[\boldsymbol{\omega}_z^n\mathbf{u}_y]\mathbf{u}) + \partial_y(\partial_x[\boldsymbol{\omega}_x^n\mathbf{u}_y]\mathbf{u})$
z-y-x	$\partial_y(\partial_z[\boldsymbol{\omega}_z^n\mathbf{u}_y]\mathbf{u}) + \partial_x(\partial_z[\boldsymbol{\omega}_z^n\mathbf{u}_x]\mathbf{u}) + \partial_x(\partial_y[\boldsymbol{\omega}_y^n\mathbf{u}_x]\mathbf{u})$

Table 4.2: Stretching error term for each splitting configuration.

The L^2-norm of the time-averaged error terms (computed *a priori*) are presented in figure 4.11. For the advection term, configurations where the x direction is handled before the y direction yield the lowest errors. In the case of the stretching term, the first position of the x direction in the splitting sequence appears to be the dominant factor. This could be attributed to the flow predominantly occurring along the x axis, making the $\mathbf{u}_x$ component more influential in the error terms (one notes the absence of the $\mathbf{u}_x$ component in the expression of the x-y-z and x-z-y error terms for the stretching operator in table 4.2) .

Based on these observations, we adopt the x-z-y ordering for the subsequent computations. A key remaining question is whether the use of a second order splitting procedure (i.e. considering half time steps (donner la ref de la section 1.2.2.1)) could reduce the sensitivity to the ordering of splitting operations, with an additional cost - requiring five directional operations per iteration, compared to three in the first-order splitting scheme.

4.1.2.4 Large Eddy Simulation at Re=10595

Large eddy simulations were performed on a higher Reynolds number of 10595 and on a 128×256×128 grid. At this Reynolds and resolution, a no-model simulation break down and a subgrid-scale model is necessary. The models considered are VMS-Smag and SVV, using coefficients calibrated on homogeneous isotropic turbulence, namely filter order $n = 6$ and coefficients $C_S = 0.4$ and $C_{SVV} = 0.09$ (see Chapter 3) . In the present context of a turbulent flow over solid walls, the consideration of the WALE model (2.13) is also interesting for our models comparison since, one recalls, WALE is a functional model designed in order to enforce a vanishing eddy viscosity near solid surfaces. A VMS-WALE is also examined. Both WALE and VMS-WALE are non calibrated, using the same coefficient $C_W = 0.25$. The explicit filter used for VMS-WALE is the same as VMS-Smag (3.7). For LES, the anisotropic grid chosen in this work,

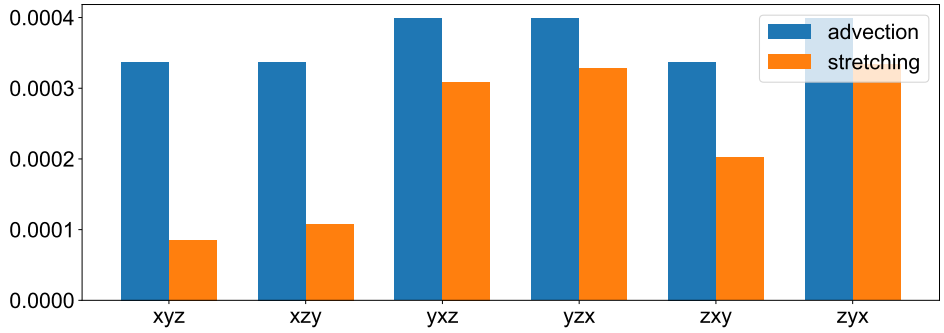

Figure 4.11: L^2-norm of time averaged error term related to each directional splitting configuration, for both advection and stretching operators.

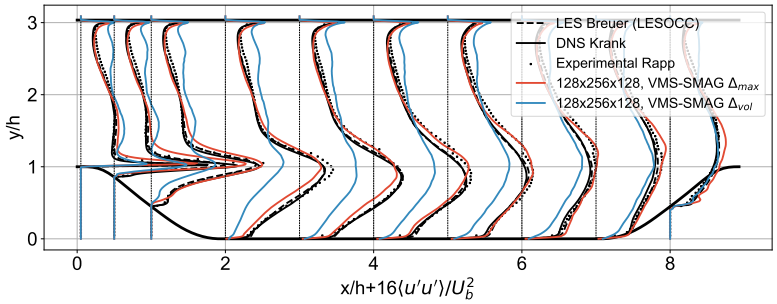

Figure 4.12: Comparison of the time- and span-averaged streamwise normal ($\langle u'u' \rangle / U_b$) Reynolds stress profiles for filter length Δ_{vol} and Δ_{max} for the LES of flow over periodic hills at $Re = 10595$, comparison with [BPRM09, KKW18, RM11].

and represented figure 4.2(right), means choosing appropriately the length scale used in subgrid-scale models (see subsection 2.2.1.5). A comparison of two choices, $\Delta_{max} = \max(\Delta x, \Delta y, \Delta z)$ and $\Delta_{vol} = \sqrt{\Delta x \Delta y \Delta z}$, is shown in figure 4.12, showing the poor performance of Δ_{vol} in this configuration.

Figure 4.13 and 4.14 show the averaged velocity and Reynolds stresses profiles respectively for the different sub-grid scales models. The results are compared with reference DNS from Krank *et al.* [KKW18], LES from Breuer *et al.* [BPRM09] and experimental data from Rapp and Manhart [RM11].

VMS-Smag and SVV focusing on the small scales of vorticity, although with parameters calibrated for different test cases (see Chapter 3), perform better than the WALE model, that tends to be too dissipative. VMS-WALE performs about as well as SVV but tends to be not dissipative enough close to walls; indeed the previously calibrated SVV model reproduces better the behavior of the fluid in the upper boundary (see zoomed details in figure 4.15).

Table 4.3 compares the location of the flow separation and reattachment points reported in literature, to the ones obtained from the different models used in the present LESs. Except

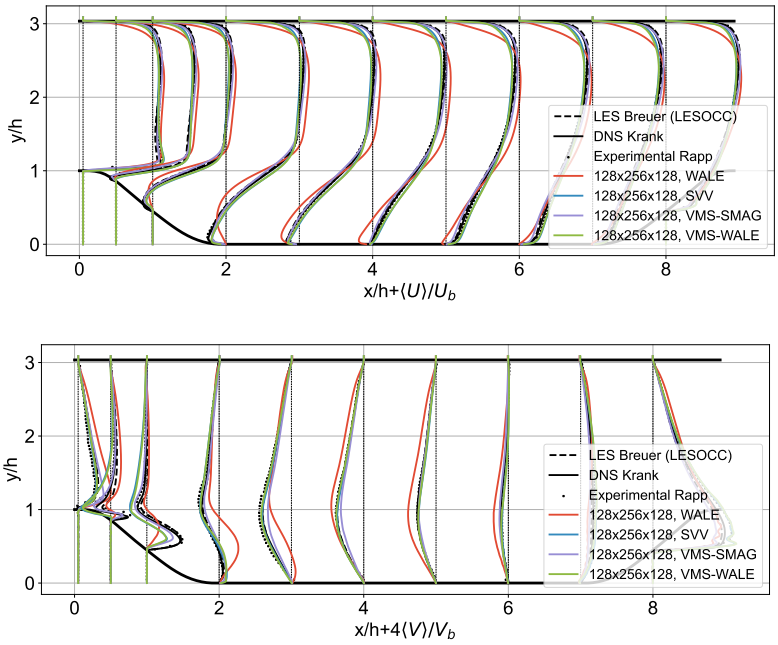

Figure 4.13: Time- and span-averaged streamwise ($\langle U \rangle / U_b$) and vertical ($\langle V \rangle / U_b$) velocity profiles obtained with the different subgrid-scale models in the LES of flow over periodic hills at $Re = 10595$, comparison with [BPRM09, KKW18, RM11].

for VMS-Smag, all simulations predict a shifted separation, downstream. Additionally, SVV and VMS-WALE show reattachment occurring upstream of the reference location, resulting in an undersized recirculation bubble, while WALE predicts a reattachment further downstream. Among all models, only VMS-Smag accurately reproduces the reference values.

	type	separation point	reattachment point
Rapp and Manhart [RM11]	Exp.	-	4.21
Krank et al. [KKW18]	DNS	0.2	4.51
Breuer et al. [BPRM09]	LES	0.19	4.69
Present	LES (WALE)	0.4	5.58
Present	LES (SVV)	0.41	3.89
Present	LES (VMS-Smag)	0.24	4.51
Present	LES (VMS-WALE)	0.41	3.88

Table 4.3: Flow separation and reattachment points (dimensionless position x/h).

Comparing to a similar subgrid-scale modeling strategy, we reach similar conclusions as Gloerfelt and Cinnella [GC19]. In this study, the flow is solved using an Eulerian finite volumes method and the velocity-pressure Navier-Stokes equation. A VMS-Smag model, similar to ours is used. The test filter is an 11-point filter with a cutoff at $kh = \pi$. The VMS model was found to perform better than models without explicit filtering of the small scales (i.e. Smagorinsky with or without a dynamic coefficient), which were found to be overly dissipative. The authors

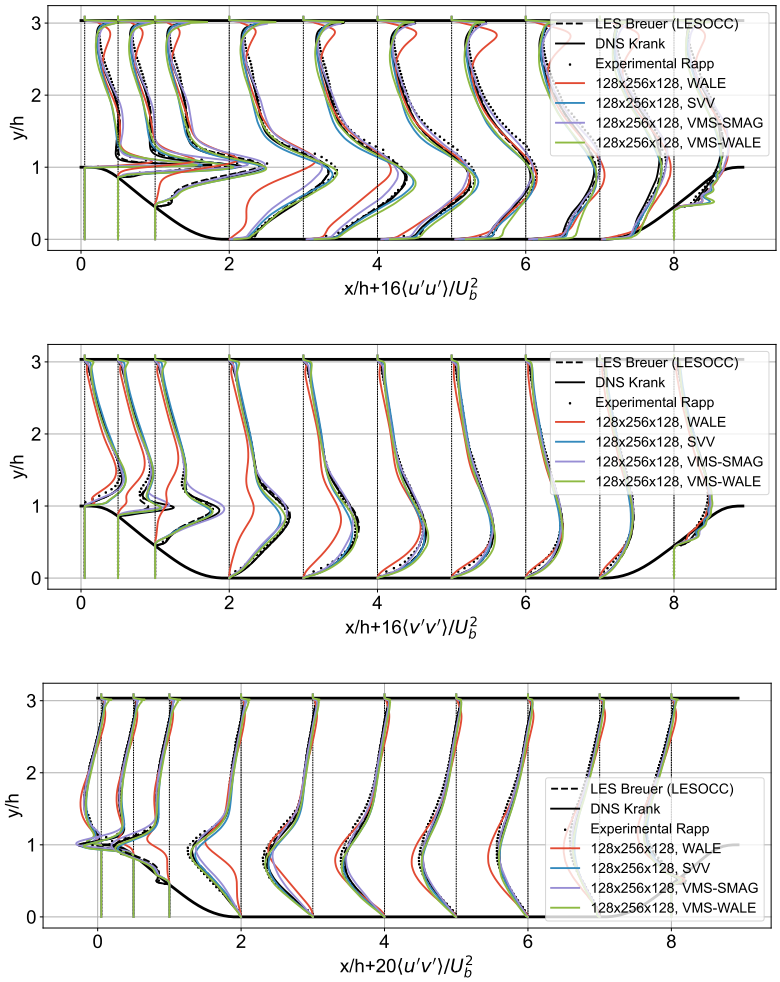

Figure 4.14: Time- and span-averaged streamwise normal ($\langle u'u' \rangle / U_b$), vertical normal ($\langle v'v' \rangle / U_b$) and shear ($\langle u'v' \rangle / U_b$) Reynold stress profiles obtained with the different grid subgrid-scale models in the LES of flow over periodic hills at $Re = 10595$, comparison with [BPRM09, KKW18, RM11].

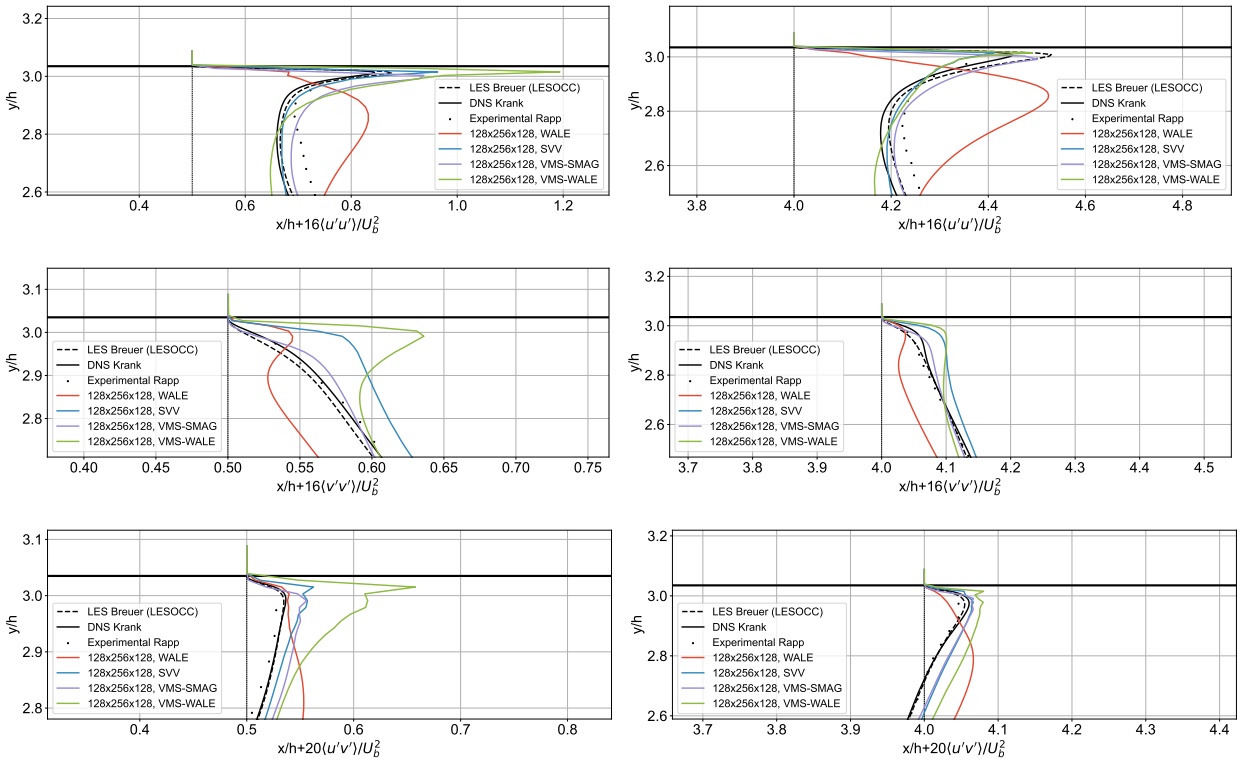

Figure 4.15: Close-up views of the $\langle u'u' \rangle / U_b$ (top), $\langle v'v' \rangle / U_b$ (center) and $\langle u'v' \rangle / U_b$ (bottom) profiles represented in figure 4.14, at two distinct positions $x/h = 0.5$ and $x/h = 4$, comparison with [BPRM09, KKW18, RM11].

also find that the VMS model performs similarly as a regularization strategy, whose principle can be compared to our SVV model.

In conclusion, VMS-Smag performs the best and appears to be well calibrated. It is followed by SVV, which likely suffers from suboptimal calibration. In Chapter 3 (dedicated to homogeneous isotropic turbulence), we showed that SVV required recalibration for a different test case, whereas VMS-Smag demonstrated greater robustness. This conclusion further supports our current findings in the case of turbulent flows over solid walls. VMS-WALE outperforms WALE and, despite not being specifically calibrated for this test case, highlights the benefits of small-scale filtering in subgrid-scale modeling. The results of VMS-WALE and SVV are comparables but in the context of our numerical method SVV requires a lower additional computational cost. Notably, no wall model was employed; instead, the small-scale filtering naturally adapted to the solid boundaries.

4.2 Flow past a sphere

Finally, we consider another wall-bounded flow: the case of a turbulent flow past a sphere at $Re = 3700$. The instantaneous vorticity field is represented in figure 4.16 as an illustration.

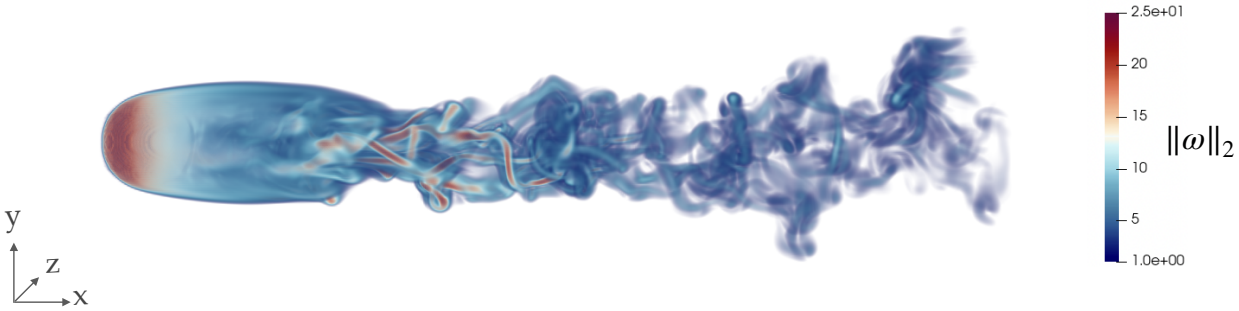

Figure 4.16: Instantaneous vorticity norm for the flow past a sphere at $Re = 3700$.

4.2.1 Setup

4.2.1.1 Case description

The case consists of a sphere of diameter D placed in a rectangular domain. The size of the domain is $12.8D \times 5.12D \times 5.12D$ and the origin is placed at the center of the sphere, located at a distance of 2.56 from the left, bottom and front boundaries of the domain. Periodic boundary conditions are imposed in all directions, no-slip boundary conditions are imposed on the surface of the sphere. A constant flowrate is imposed at the entry of the domain with bulk velocity U_b. The vorticity is absorbed within a sponge zone located at the end of the domain through a filter function (see figure 4.17). The Reynolds number is based on the sphere diameter, D and U_b and is set to $Re = 3700$. The quantities of interest presented below are averaged after the flow has reached a statistically steady state and over an averaging period of $\Delta T = 125$.

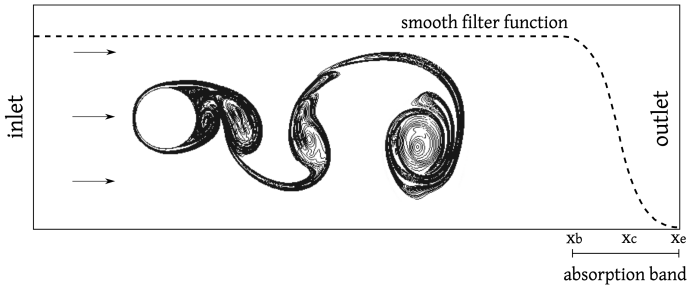

Figure 4.17: Smooth vorticity absorption performed at the outlet of the domain, figure from [Mim15]

In the following, we will use as reference the DNS by Rodriguez *et al.* [RLBO13] where a second-order symmetry-preserving scheme [VV03] is used on a cylindrical unstructured grid with about 9.48 million control volumes and a minimum of 12 grid points withing the boundary layer.

4.2.1.2 Directional splitting configuration

As in the case of periodic hills (subsection 4.1.2.3), we focus here on the effects of the sequence of directions in the splitting procedure applied to the advection operator and to the stretching one. This time, the impact of the directional splitting sequence on the solution will be evaluated *a posteriori* by measuring the added numerical dissipation, through the comparison of the mean enstrophy values obtained from 11 VMS-Smag LESs performed at resolution $320 \times 128 \times 128$ (the 11 LESs corresponding to each 6 splitting sequences applied to each operator, advection and stretching).

Figure 4.18 shows the mean enstrophy, computed after the flow has reached a statistically steady state, for each configuration. In the top figure, we first fixed the sequence of directions in the advection operator to z-y-x (the default configuration (implemented in the `HySoP` solver due to parallel computing issues) and considered all the 6 possible sequences of directions in the stretching operator. As can be seen, the minimal values of mean enstrophy are obtained with the directional sequences x-z-y and x-y-z. We therefore reach the same conclusion as in the *a priori* study carried out on the periodic hills test case for the stretching operator, that is: the position of the x direction (i.e. the predominant flow direction) in the splitting sequence seems to be the defining factor for the stretching operator.

Since the x-y-z sequence of directions in the stretching operator gives the lowest mean enstrophy, it was thus selected for the second study, where the sequence of directions in the stretching operator is fixed (i.e. x-y-z) and the 6 sequences of directions in the advection operator are studied (see bottom figure 4.18). We observe less variations in the mean enstrophy values in this case. For the large eddy simulations presented in this section, we will therefore keep the x-y-z sequence of directional splitting for the stretching operator while the sequence for the advection operator is left to the default one, z-y-x.

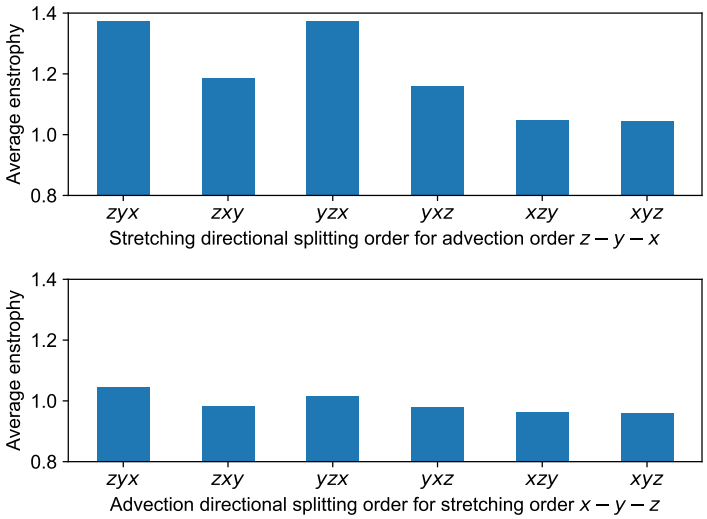

Figure 4.18: Mean enstrophy for each directional splitting configurations (*a posteriori* test).

4.2.2 Model calibration

4.2.2.1 Uncertainty Quantification

We aim to perform the same Uncertainty Quantification procedure than in the previous chapter dedicated to homogeneous isotropic turbulence (subsection 3.3.1.2). We focus here on the VMS-Smag model, which was performing the best on the periodic hills test case, and its sensitivity to model coefficient C_S^2 (eqs. (3.4) and (3.2)) and the small-scale filter order n (eq. (3.7)). The range of coefficients considered are for $C_S^2 \in [0.1949, 0.7]$ and $n \in [1.5223, 6]$. As opposed to the previous Uncertainty Quantification, the sensitivity of the model to its coefficient is evaluated through C_S^2 and not C_S, allowing us to consider higher values of C_S while keeping the same quadrature points. 16 simulations (i.e. 4 (for C_S^2) $\times$ 4 (for n) combinations) were performed to obtain the quadrature points needed for the polynomial chaos expansion.

Figure 4.19 presents the sensitivity analysis of the VMS-Smag model for the flow past a sphere at $Re = 3700$ with resolution $320 \times 128 \times 128$, which corresponds to 5.2 millions grid points, half that of Rodriguez *et al.* 's DNS study which uses a non-uniform grid. One notes that, at such Reynolds, the cell size associated to the present uniform grid is larger than the boundary layer thickness, compared to 12 points in the boundary layer in Rodriguez *et al.* . The quantity of interest here is the fluctuations of radial velocity spectra at $r/D = 0.6$ and $x/D = 1$ and $x/D = 3$, compared with [RLBO13].

The first spectrum (left hand side), evaluated close to the sphere at $r/D = 0.6$ and $x/D = 1$ represents the instabilities in the shear layer. Since this region is highly unstable, the LESs are very sensitive to their model coefficients and present a large variance on most frequencies. In Rodriguez *et al.* [RLBO13], a broadband peak located at $f_{KH} = 0.72U_b/D$ represents the signature of the Kelvin-Helmholtz shear-layer instability. In the present results, the broadness of such peak is recovered, however, one notes a shift in frequency to about $f_{KH} \approx 0.6U_b/D$ and in amplitude with respect to the reference. This peak does not seem to vary much with the model

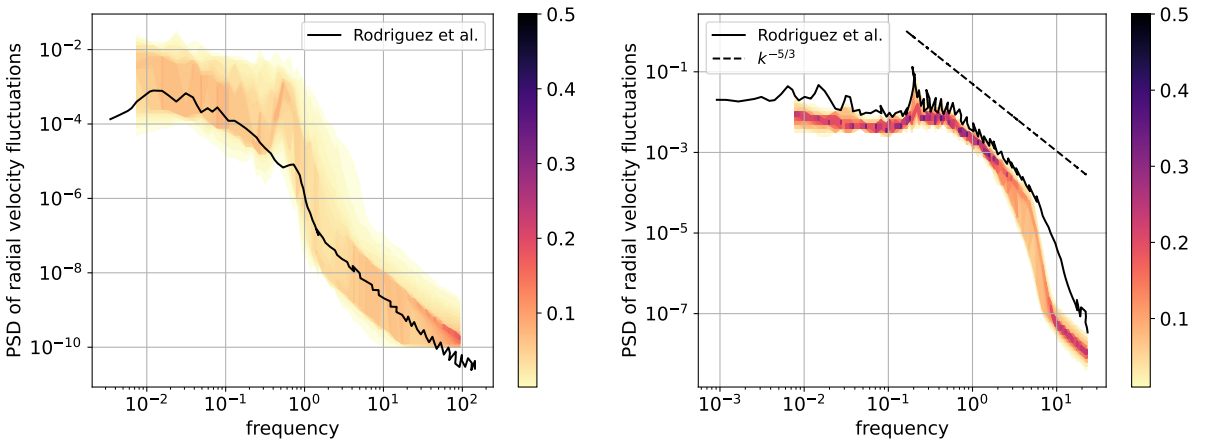

Figure 4.19: Probability density functions for energy spectra of radial velocity's fluctuations at $r/D = 0.6$ and $x/D = 1$ (left) and $x/D = 3$ (right) for VMS-Smag simulations of flow past a sphere with $Re = 3700$ and resolution $320 \times 128 \times 128$. Comparison with [RLBO13].

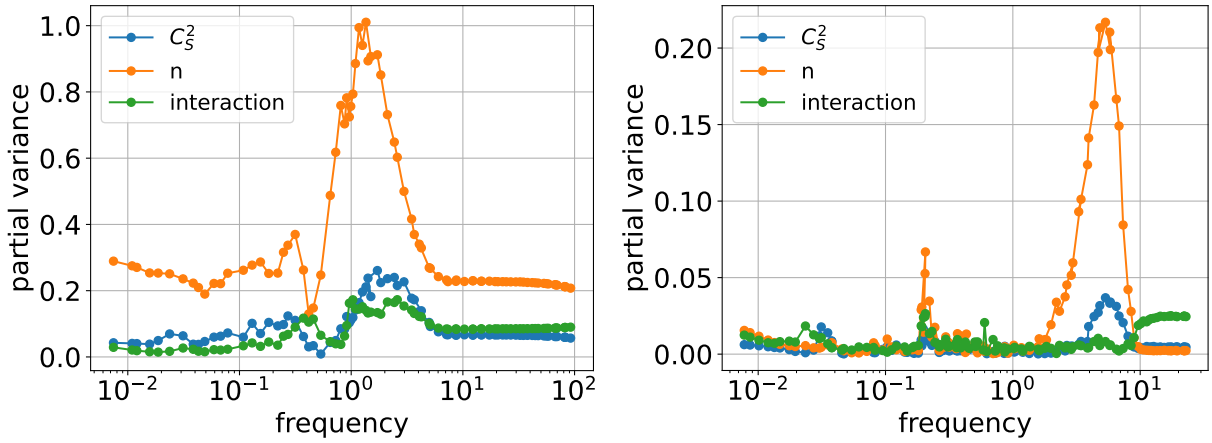

Figure 4.20: Partial variances (for C_S^2, n, and their interaction) for energy spectra of radial velocity's fluctuations at the radial distance from origin $r/D = 0.6$ and $x/D = 1$ (left) and $x/D = 3$ (right) for VMS-Smag simulations of flow past a sphere with $Re = 3700$ and resolution $320 \times 128 \times 128$.

coefficients, indicating a simulation error independent from the subgrid-scale model parameters.

The second spectrum (right hand side), on the other hand, is evaluated further downstream at $r/D = 0.6$ and $x/D = 3$, where the turbulence is more developed as demonstrated by the -5/3 law in the inertial range. At such position located further downstream, the frequency peak observed in the spectrum corresponds to the larger scale vortex shedding phenomenon. It is denoted f_{VS}. In the present LES results, $f_{VS} \approx 0.2U_b/D$ is in very good agreement with the

reference, reporting $f_{VS} = 0.215U_b/D$. The LESs are less sensitive in this area and recover the largest scale of the turbulence, with a drop in amplitude, especially at the highest frequencies.

In figure 4.20, the partial variances are plotted as a function of frequency. The model seems to more sensitive to coefficient n, contrary to the homogeneous isotropic case treated in the previous chapter, where C_S was shown to be the most sensitive parameter in the Uncertainty Quantification study. The greater variance is observed after the broadband peak, corresponding to a Kelvin-Helmholtz frequency of about $f_{KH} = 0.6U_b/D$ in the first spectrum and at the end of the second spectrum.

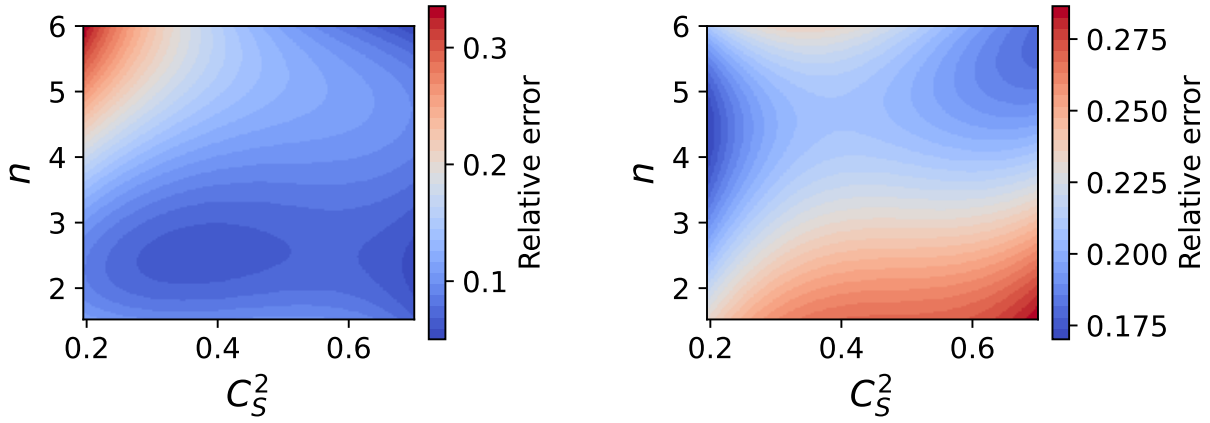

Figure 4.21: Surface response for the ℓ^2-error for the energy spectra of radial velocity's fluctuations at $r/D = 0.6$ and $x/D = 1$ (left) and $x/D = 3$ (right) for VMS-Smag simulations of flow past a sphere with $Re = 3700$ and resolution $320 \times 128 \times 128$.

Finally, figure 4.21 represents the computed polynomial chaos expansion interpolation of the relative ℓ^2-error for both spectrum compared with the reference [RLBO13]. The error is represented as a function of coefficients C_S^2 and n. Both spectra present different optimal coefficients regions. For the first spectrum, closer to the sphere, lower filter orders are favored whereas for the second spectrum, corresponding to a region of developed turbulence, higher order filters seem the best suited, similarly as for the Taylor-Green Vortex test case (see subsection 3.3.2.1), as in this region the spectrum is close to the one obtained in HIT.

Overall, our study shows that the non resolved boundary layer leads to stronger shear layers instabilities, visible in the spectra in a shift in amplitude and in the Kelvin-Helmholtz frequency. Further downstream, theses shifts are less important as the turbulence is more developped. This confirms that while not being wall-resolved, our LES-RVM can recover the large-scale physics of the flow.

4.2.2.2 Application to different resolutions

Finally, we try to use our Uncertainty Quantification (UQ) procedure to find an optimal coefficient for the VMS-Smag LES of the flow past a sphere at $Re = 3700$. Based on the surface responses of the discrepancy of the simulations spectrum with respect to the reference

(see fig. 4.21), we chose $C_S^2 = 0.7$ and $n = 4$ as the best compromise between the two spectra. Three simulations with these coefficients were then performed at resolutions $240 \times 96 \times 96$, $320 \times 128 \times 128$ (at which the UQ study was performed) and $640 \times 256 \times 256$.

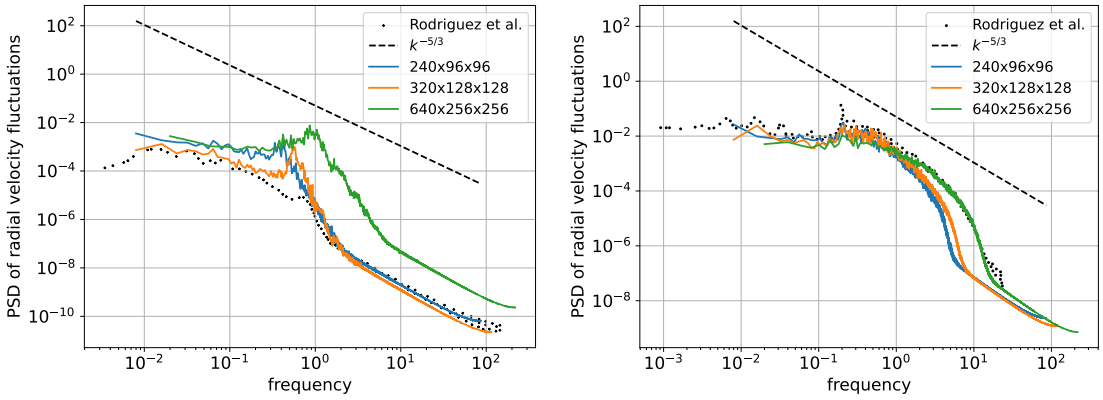

Figure 4.22: Energy spectra of radial velocity's fluctuations at $r/D = 0.6$ and $x/D = 1$ (left) and $x/D = 3$ (right) for VMS-Smag LES of flow past a sphere at $Re = 3700$ with $C_S^2 = 0.7$ and $n = 4$ for different resolutions. Comparison with [RLBO13].

Figure 4.22 presents the energy spectra of the flow's radial velocity fluctuations for the three resolutions considered. On the first spectrum, the simulation with resolution $320 \times 128 \times 128$ performs the best, which is expected as the coefficients were optimized for this configuration. The Kelvin-Helmholtz frequency is shifted to the left of the spectrum. This was the case for all coefficients tested in the UQ and is probably not due to the subgrid scale model itself. The Kelvin-Helmholtz frequency for the higher $640 \times 256 \times 256$ resolution seems better aligned to the reference but the spectrum is shifted upwards, revealing too high fluctuations' amplitude. The lower $240 \times 96 \times 96$ resolution has a better agreement with the reference, especially on the higher frequencies but the Kelvin-Helmholtz frequency is shifted to a lower value. This illustrates the high sensitivity of the shear layer's fluctuations to the grid resolution. On the other hand, the right spectrum, corresponding to a point further downstream of the sphere, the higher resolution is performing the best, with the shape of the reference solution recovered almost up to the highest frequencies.

Figure 4.23 shows the mean streamwise velocity and normal Reynolds stress profiles at two different positions, $x/D = 1.6$ and $x/D = 2.5$, with respect to the radial coordinate. For the mean streamwise velocity (top) the $320 \times 128 \times 128$ grid (used for the UQ) gives the best results. The coarser grid $240 \times 96 \times 96$ also performs well near the sphere but the $x/D = 2.5$ profile shows that the zone located at the end of the recirculation bubble deviates more from the reference. For, the highest $640 \times 256 \times 256$ resolution, the LES mean streamwise velocity solution is degraded both close to the sphere and at the recirculation bubble tip.

The mean normal Reynolds stress profiles (i.e. fluctuations of the streamwise velocity) show the same tendency as the one observed in the energy spectra of radial velocity fluctuations from figure 4.22: the calibration is robust to the change of resolution but only in the regions where the turbulent flow is developed. At $x/D = 2.5$, the LES performed with resolution $640 \times 256 \times 256$ presents the best results for this quantity. However, at $x/D = 1.6$, it fails to match the reference.

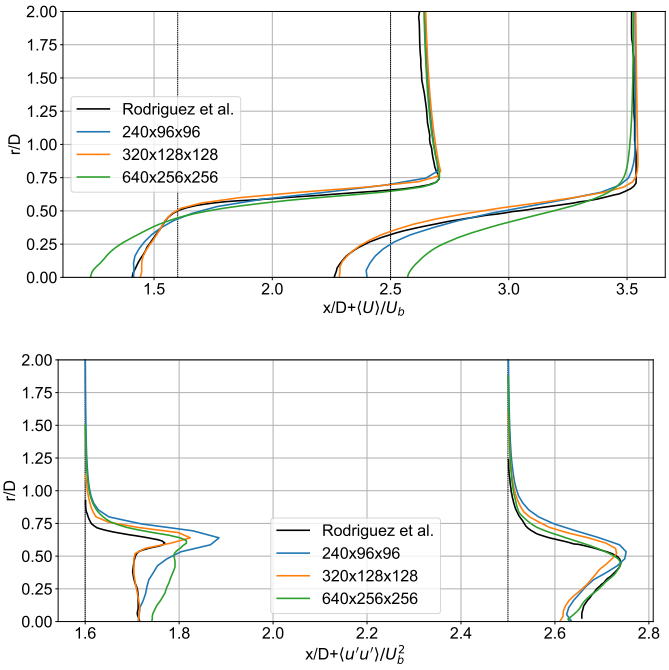

Figure 4.23: Time- and azimutal direction- averaged streamwise velocity (top) and normal Reynolds stress profiles (bottom) for VMS-Smag LES of the flow past a sphere at $Re = 3700$ with $C_S^2 = 0.7$ and $n = 4$ for different resolutions. Comparison with [RLBO13].

This seems to indicate that the present calibration is not fully robust to a change in resolution, as opposed to the previous TGV and HIT test cases presented in chapter 3, except for the fluctuations in regions further downstream from the sphere. This is due to the uniform Cartesian grid, which is too coarse to correctly capture the thin boundary layer at such Re and the shear effects close to the sphere boundary. Moreover, one recalls that the penalization method used in this study to prescribe the no-slip condition at the sphere surface can be considered as an immersed boundary method where the solid surface is represented in practice by a step-like rather than a smooth-curved shape. Notably, our simulation found a drag coefficient (computed during the penalization step through the procedure described in [MBG12]) for the $320 \times 128 \times 128$ resolution of about 0.55, much higher than the reference 0.39).

Figure 4.24 presents the mean streamwise velocity field in cylindrical coordinates for the different grid resolutions. The points at which the spectra were computed as well as the slice on which the profiles are compared to the reference DNS are also shown. The higher resolution VMS-Smag LES presents a smaller recirculation bubble compared to the two lower resolutions. We find the recirculation lengths (defined as the distance between the rear end of the sphere $(x/D = 0.5, r/D = 0)$ and the point $(x/D, r/D = 0)$ where the streamwise velocity changes sign) of 2.17, 2.42 and 1.42 for the $240 \times 96 \times 96$, $320 \times 128 \times 128$ and $640 \times 256 \times 256$ grids respectively, compared to a value of 2.28 for Rodriguez *et al.* Once again, although the calibrated coefficients lack robustness when applied to a higher resolution than that used for the UQ, they yield similar results when used at a lower resolution.

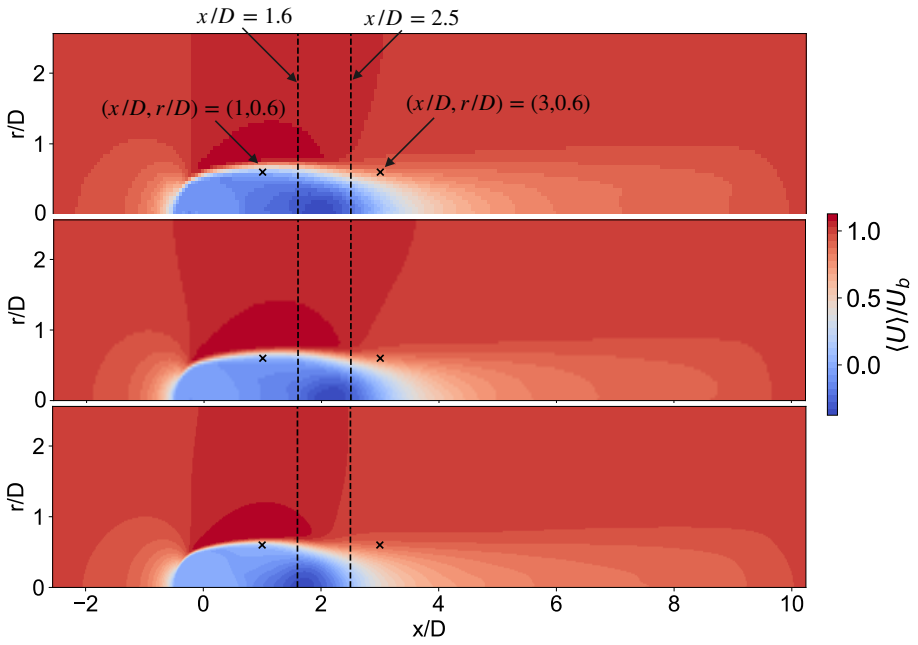

Figure 4.24: Time- and azimutal direction- averaged streamwise velocity field for VMS-Smag LES of the flow past a sphere at $Re = 3700$ with $C_S^2 = 0.7$ and $n = 4$ for resolutions $240 \times 96 \times 96$ (top) $320 \times 128 \times 128$ (middle) and $640 \times 256 \times 256$ (bottom). The dashed lines represent the slices at which the velocity profiles are compared to the reference in figure 4.23 and the crosses represent the points at which the spectra of the radial velocity fluctuations are represented in figure 4.22.

Since our Uncertainty Quantification shown that the model, in this configuration, was more sensitive to a variation in the filter order, we tried a lower filter order (i.e. the VMS-Smag model is applied to a broader range of scales) to try to reduce the amplitude of the radial velocity fluctuations near the sphere. Figures 4.25 and 4.26 show the mean velocity and Reynolds stress profiles and the spectra for the higher resolution LES with $n = 4$ (the "optimal" order) and a lower order of $n = 1$. The lower order performs better for the average streamwise velocity profiles and the spectrum near the sphere but the spectrum computed at a point further downstream from the sphere fails to accurately represent the higher frequencies.

Future work should perform the Uncertainty Quantification at a higher resolution to find better compromise between these two solutions, as the low resolution, despite its low computational cost, is probably too unrealistic to calibrate our model. The two coarse LESs (ie at $240 \times 96 \times 96$ and $320 \times 128 \times 128$) enable to successfully recover the mean flow field in good agreement with the DNS data available in the literature. This confirms that the VMS can effectively represent the global flow physics at coarse (and very coarse) resolutions.

This might also indicate that the VMS modeling, as used until this point, is limited in this kind of cases which presents distinct mechanisms close to the solid boundary (with Kelvin-Helmholtz instabilities) and in the wake (with vortex shedding). A dynamic or adaptive VMS could be considered, with the filter order varying with the domain zone solved.

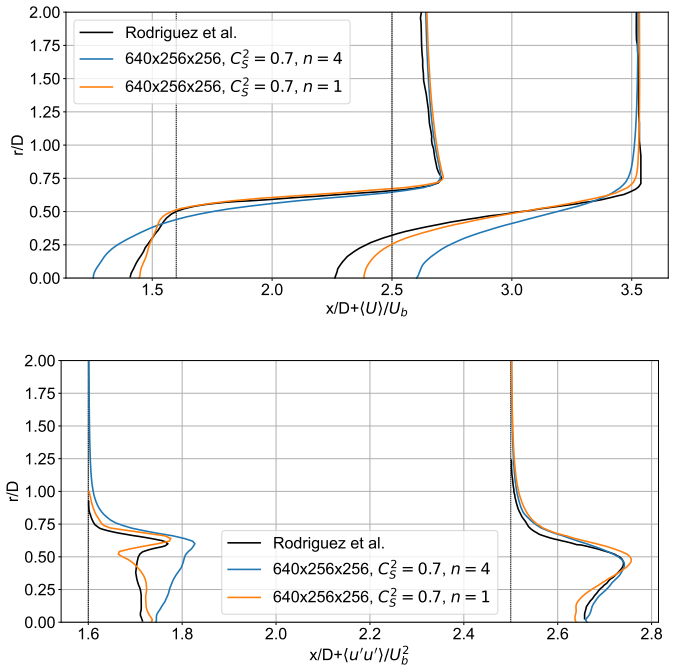

Figure 4.25: Time- and azimutal direction- averaged streamwise velocity (top) and normal Reynolds stress profiles (bottom) for $640 \times 256 \times 256$ VMS-Smag LES of the flow past a sphere at $Re = 3700$ with $C_S^2 = 0.7$ and two different filter orders. Comparison with [RLBO13].

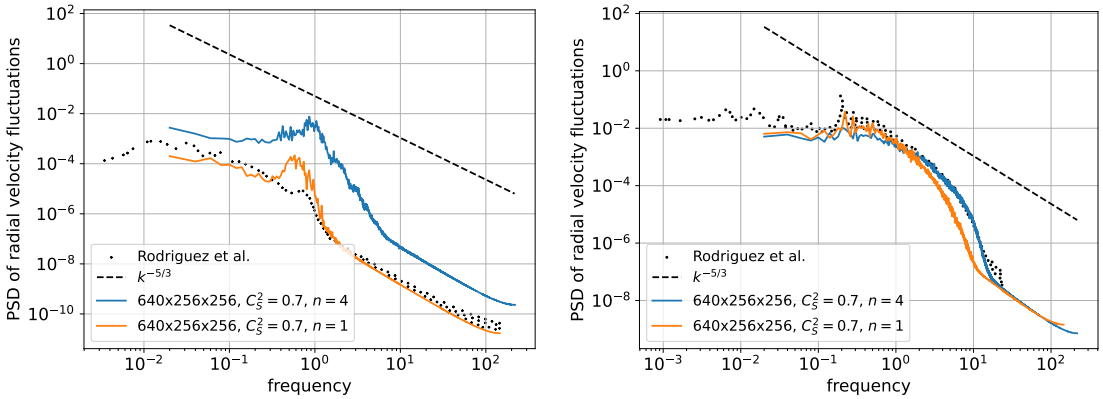

Figure 4.26: Energy spectra of radial velocity's fluctuations at $r/D = 0.6$ and $x/D = 1$ (left) and $x/D = 3$ (right) for $640 \times 256 \times 256$ VMS-Smag LES of the flow past a sphere at $Re = 3700$ with different filter orders. Comparison with [RLBO13].

Conclusion

The present RVM was applied first to a the channel flow over periodic hills. In DNS at $Re = 2800$, we obtained good precision, even with a wall treatment performed with a Cartesian grid and a first order immersed boundary method, confirming the interest of RVM for coarse grid simulations. In LES at $Re = 10595$, SGS models acting on the smallest resolved vorticity scales (VMS and SVV) provided good results in terms of averaged velocities and Reynolds stresses, with model parameters calibrated on different and simpler test cases (i.e. HIT benchmarks from chapter 3) without solid boundaries. The VMS-Smag is found again to be the best performing model, thus confirming our previous outcomes from chapter 3, that showed the robustness of VMS-Smag's coefficient whereas SVV's coefficient required adaptation to new test cases.

The VMS-Smag model was then tested on the flow past a sphere at $Re = 3700$. As in the previous chapter, a polynomial chaos expansion (PCE) method was used to perform an Uncertainty Quantification study and to calibrate the model with respect to its parameters. However, the uniform Cartesian grids considered do not enable to capture the thin boundary layer and the model was shown to be less robust to changes in resolution on this more complex test case, except for the fluctuations in regions further downstream from the sphere where the turbulence is more developed and thus where the flow is closer to a HIT configuration. A lower filter order for the highest resolution was then tested, which performed better for the average streamwise velocity profiles and near the sphere at the expense of a degraded performance on the fluctuations further downstream of the sphere.

Finally, as both these flow were characterized by a principal direction, this allowed us to test and calibrate the sequence of directions in the directional splitting, a key feature of our RVM algorithm.

Conclusion and perspectives

Conclusion

LES for Vortex Methods

In this work, we are interested in simulating incompressible turbulent flows with a Remeshed Vortex Method. This method solves the velocity-vorticity formulation of the Navier-Stokes equations using an hybrid, or semi-Lagrangian, approach where the vorticity advection is solved on numerical particles. The particle are then remeshed on a Cartesian grid where the rest of the operators are discretized. RVMs are characterized by a low numerical dispersion and diffusion and a good overall representation of flows at coarse resolutions. They also offer a direct access to vorticity, a key quantity in turbulence. In this work, the computations were performed using the research in-house solver `HySoP`, based on a fractional step algorithm.

An extensive study of various subgrid-scale models in Large Eddy Simulations using a Remeshed Vortex Method was conducted. The considered SGS models cover different types of modeling approaches, including classical models, like the Smagorinsky one, structural modeling and spectral regularization modeling. This study was motivated by the fact that the impact of closure modeling in LES in the context of vorticity-based formulation, and especially with a semi-Lagrangian approach such as the present RVM, has been much less explored than for classical velocity-pressure formulations. Furthermore, a key advantage of RVM is its low diffusivity, facilitated by the Lagrangian treatment of the advection step. It is crucial that the adopted subgrid-scale model does not compromise this feature.

From a study of literature and a benchmark on the Taylor-Green Vortex, it appeared that applying artificial viscosity models only to the smallest scales of vorticity allowed for efficient and precise simulations. Indeed, models applying viscosity to the whole range of scales of the flow were found to be too diffusive. By targeting small scales, one keeps the well-resolved large scales of the vorticity field intact while adding diffusion near the cutoff scale, where numerical instabilities arise. The Large Eddy Simulations of turbulent wall-bounded flows performed in this thesis showed that this conclusion still held true for such flows, where small-scales-filtering models performed better than a classical WALE model (which naturally reduces the subgrid viscosity near solid boundaries, without needing additional damping terms).

Two models, the variational multiscale version of the classical Smagorinsky (VMS-Smag) model as well as the spectral vanishing viscosity (SVV) approach were then selected. Both models are based on a small-scale filtering procedure but differ in their artificial viscosity definition: in VMS-Smag it is based on the strain tensor of the complete resolved velocity field whereas in SVV it is only a constant scaled on the cutoff scale k_c. The models also differ in their implementation

in `HySoP`: both are discretized in an Eulerian framework but the VMS-Smag is implemented through an additional finite differences operator whereas the SVV is directly included in the FFT-based diffusion operator, leading to a very low overhead cost.

As they both depend on two parameters (the model coefficient and the filter order), an Uncertainty Quantification procedure was carried out, first in the context of homogeneous isotropic turbulence (HIT) test cases, to evaluate their sensitivity to these parameters and to find an optimal configuration. The model coefficients calibrated from the Uncertainty Quantification study were found, for both VMS-Smag and SVV models, to be robust to a change of Reynolds number and grid resolution and, in the case of VMS-Smag, to a change of case test.

The present RVM with the two calibrated models was then applied to the channel flow over periodic hills at $Re = 10595$ and compared to DNS, LES and experimental results from literature on one side and to LESs performed in the present RVM framework with a WALE and VMS-WALE model on the other side. Again, SGS models acting on the smallest resolved vorticity scales (that is, VMS-Smag, SVV and VMS-WALE models) gave good results. The VMS-Smag model turns out to be the best performing model, confirming its robustness, while calibrated on HIT benchmarks and applied here to a very different flow, characterized by solid walls, a boundary layer, flow separation/reattachement and anisotropy.

Finally, Large Eddy Simulations of a turbulent flow past a sphere at $Re = 3700$ were performed, based on the VMS-Smag model. The flow, characterized by high-frequency Kelvin–Helmholtz instabilities in the shear layer and lower-frequency vortex shedding, served as the basis for another Uncertainty Quantification study. The latter turned out this time to provide a less robust calibration of the VMS-Smag parameters for accurately capturing instabilities close to the solid boundary. However, further downstream, where the turbulence is closer to a HIT configuration, the models were more robust to a change in resolution.

Overall, both the VMS-Smag and SVV models proved to be the best performing in the RVM approach, showing robustness, adaptability to both transitional and highly turbulent flows, both isotropic and anisotropic and were able to model developed turbulence in wall-bounded flows in very coarse resolutions, compared to literature. The SVV approach was the least computationally demanding in the context of our implementation but was not robust to a change of test case due to the simplicity of its artificial viscosity expression. VMS-Smag, on the other hand, was more robust to a change of test case as well as to a change of Reynolds number and grid-resolution, which enables its calibration at a low computational cost on simpler cases and coarse meshes.

Limitations

The present implementation of the RVM is however limited to Cartesian uniform grids for the particle remeshing schemes, which makes our Uncertainty Quantification procedure more complex when considering wall-bounded flows as the simulations are impacted by the coarse resolution of the boundary layer (as observed in the sphere case presented in chapter 4).

Furthermore, while the RVM has a competitive advantage in coarse resolutions due to its low diffusivity, its order of convergence (lower than 2 in practice) limits its efficiency for higher resolutions. Finally, since in Vortex Methods the Lagrangian stability condition on the timestep relies on the velocity gradients, the lack of a classical CFL condition (which constrains the timestep to the grid step) is not very advantageous in turbulent configurations. Indeed, while

in the context of laminar or transitional flow simulations the RVM allows for timesteps larger by one order of magnitude compared to those constrainted by the grid size in purely Eulerian methods, it was observed in the present analyzes to provide timesteps of similar values compared to Eurelian-based LES in the context of turbulent flows.

In the following, and taking into account the main outcomes of the present work, we present some mid and long term perspectives to develop Vortex methods to their full potential for subgrid-scale modeling.

Perspectives

In this section, we outline three perspectives of our work that relate to aspects of subgrid-scale modeling and potential applications beyond the scope of this thesis.

Decoupled subgrid-scale modeling

As highlighted in chapter 2, the vorticity-velocity formulation of the Navier-Stokes equation contains two non-linear terms: the advection term and the stretching term. Hence, the subgrid-scale tensor contains two terms, one for each non-linear operator. In this work, since we mostly derived our vorticity-velocity models from the functional models proposed in literature for the velocity-pressure formulation of the Navier-Stokes equations, a single subgrid-scale model was used to model both terms.

As far as we know, no decoupled modeling strategy, with each non-linear operator being modeled separately, has been tested in the context of RVM. Mansfield *et al.* [MKM98] studied *a priori* their relative importance and concluded that both terms play a role in the growth of turbulence and are not correlated, providing motivation for such a structural modeling approach. Cottet [Cot96] and Alvarez [AN24] have provided models for the advection and stretching term respectively, based on the vortex method. Structural models, such as those used in [HCY$^+$25] or the gradient model could also be the base of such a strategy.

Anisotropic spectral vanishing viscosity

An advantage of the present spectral vanishing viscosity implementation is the ability to easily adjust the artificial viscosity added to each direction. We recall the modified diffusion operator in the Fourier space

$$\partial_t \hat{\boldsymbol{\omega}} = -(k_x^2(1/Re + \nu_S(k_x)) + k_y^2(1/Re + \nu_S(k_y)) + k_z^2(1/Re + \nu_S(k_z)))\hat{\boldsymbol{\omega}}, \tag{5.2}$$

where the expression for ν_S depends on a constant ν_0 that can be chosen different depending on the direction where the artificial viscosity is added. This has not been exploited in the current work but could be useful to model flows where the numerical instabilities vary depending on direction, to avoid adding excessive viscosity in directions where it is not needed.

Bilevel simulations

An area where vortex methods possess an advantage is scalar transport (see subsection 1.1.4.2). Indeed, the lack of a CFL condition constraining the time step to the size of the grid inherent to the Lagrangian advection operator allows to use a fine grid for the transport of scalar with high diffusivity while retaining large time-steps. This is especially interesting when the ratio between the fluid viscosity and the scalar diffusivity is high, as the LCFL condition is tied to the velocity gradient. Hysop supports multi-grid simulations meaning that one can use a coarse grid to discretize the fluid quantities and a fine grid for the scalar field. However, in the case of an active scalar, the interpolation of the finely resolved scalar field on the coarse grid can lead to numerical instabilities.

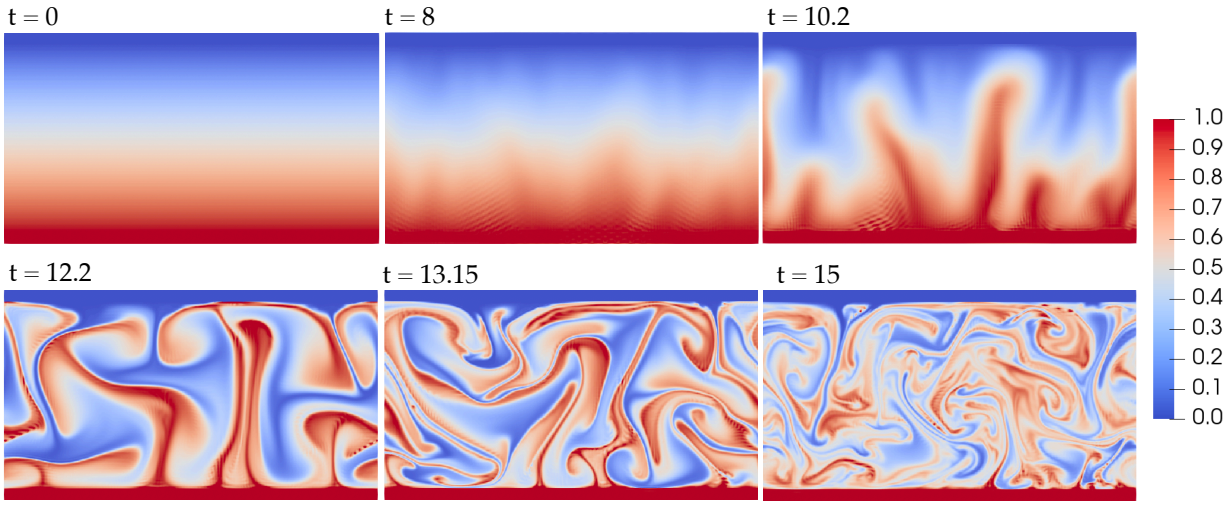

Figure 5.1: Temperature field at different times for the 2D Rayleigh-Benard instability for $T_0 = 1$, $T_1 = 0$, $Pr = 10$ and $Ra = 10^8$: the Navier-Stokes equations are solved on a 128×64 grid whereas the temperature advection and diffusion is solved on a 512×256 grid leading to the instabilities visible here.

As an illustration, we consider the Rayleigh-Bénard instability, where the fluid flow equations are coupled with an advection-diffusion equation of a temperature field. The instability develops as the fluid is constrained between two layers of constant temperature $\theta_0 < \theta_1$. The domain is $[0, 2] \times [0, 1]$ and in this domain, the equations write

$$\begin{cases} \dfrac{\partial \omega}{\partial t} + \mathbf{u} \cdot \nabla \omega - \sqrt{\dfrac{Pr}{Ra}} \Delta \omega + \partial_x \theta = 0 \\ -\Delta \mathbf{u} = \begin{pmatrix} \partial_y \omega \\ -\partial_x \omega \end{pmatrix} \\ \dfrac{\partial \theta}{\partial t} + \mathbf{u} \cdot \nabla \theta - \sqrt{\dfrac{1}{PrRa}} \Delta \theta = 0 \\ \theta(x, 0) = \theta_1 \quad \forall x \in [0, 2] \\ \theta(x, 1) = \theta_0 \quad \forall x \in [0, 2] \end{cases} \tag{5.3}$$

where θ denotes the temperature field, Pr the Prandlt number and Ra the Rayleigh number. The vorticity boundary conditions are periodic in the x-direction and no-slip in the y-direction. The temperature boundary conditions are also periodic in the x-direction. The Navier-Stokes equations are solved as described in chapter 1, with an added forcing term solved with finite differences. The advection of the temperature is solved using the same remeshed Lagrangian particle scheme than for the vorticity and the diffusion is solved using finite differences.

The Prandtl number is set to 10 and the Rayleigh number to 10^8, $\theta_0 = 0$ and $\theta_1 = 1$. Since the fluid viscosity is high, the Navier-Stokes equations are solved on a coarse grid. The temperature, with a low diffusivity, requires a finer grid. The vorticity field is discretized on a grid with resolution 128×64 whereas the temperature is discretized on a grid with resolution 512×256. The interpolation procedure is described in [Kec19].

Figure 5.1 shows the temperature field at different times on the finer grid. Turbulent structures develop as a result of the Rayleigh-Bénard instability. Numerical instabilities develop due to the multigrid procedure: the interpolation of the fine temperature on a coarse grid leads, through the forcing term, to errors in the time advancement of vorticity, which are further propagated during the temperature advection step. This instability are not present when the fluid is also solved on a fine grid.

One perspective to solve this issue would be to introduce an artificial viscosity to the temperature field before interpolating it, through a subgrid-scale model as one of those proposed and tested in this thesis work.

Bibliography

[ABF99] P. Angot, C.-H. Bruneau, and P. Fabrie. A penalization method to take into account obstacles in incompressible viscous flows. *Numerische Mathematik*, 81:497–520, 1999. (cit. on pp. 17 and 136).

[ADH93] GP Almeida, DFG Durao, and MV Heitor. Wake flows behind two-dimensional model hills. *Experimental Thermal and Fluid Science*, 7(1):87–101, 1993. (cit. on p. 80).

[AG85] C. Anderson and C. Greengard. On vortex methods. *SIAM Journal on Numerical Analysis*, 22(3):413–440, 1985. (cit. on pp. 9 and 17).

[AN24] E. J. Alvarez and A. Ning. Stable vortex particle method formulation for meshless large-eddy simulation. *AIAA Journal*, 62(2):637–656, 2024. (cit. on pp. 50, 51, 107, and 129).

[BCK05] M. Bergdorf, G.-H. Cottet, and P. Koumoutsakos. Multilevel adaptive particle methods for convection-diffusion equations. *Multiscale Modeling & Simulation*, 4(1):328–357, 2005. (cit. on p. 30).

[Bea86] J. T. Beale. A convergent 3-D vortex method with grid-free stretching. *Mathematics of Computation*, 46(174):401–424, 1986. (cit. on p. 17).

[Bea88] J. T. Beale. On the accuracy of vortex methods at large times. In *Computational Fluid Dynamics and Reacting Gas Flows*, pages 19–32. Springer, 1988. (cit. on p. 12).

[BFR80] J. Bardina, J. Ferziger, and W.C. Reynolds. Improved subgrid-scale models for large-eddy simulation. In *13th fluid and plasmadynamics conference*, page 1357, 1980. (cit. on pp. 42 and 48).

[BGOK92] J. P. Boris, F. F. Grinstein, E. S. Oran, and R. L. Kolbe. New insights into large eddy simulation. *Fluid dynamics research*, 10(4-6):199, 1992. (cit. on p. 42).

[BGRC19] C. Bernier, M. Gazzola, R. Ronsse, and P. Chatelain. Simulations of propelling and energy harvesting articulated bodies via vortex particle-mesh methods. *Journal of Computational Physics*, 392:34–55, 2019. (cit. on p. 19).

[BHI14] M. Bergmann, J. Hovnanian, and A. Iollo. An accurate cartesian method for incompressible flows with moving boundaries. *Communications in Computational Physics*, 15(5):1266–1290, 2014. (cit. on p. 30).

[BK06] M. Bergdorf and P. Koumoutsakos. A Lagrangian particle-wavelet method. *Multiscale Modeling & Simulation*, 5(3):980–995, 2006. (cit. on p. 30).

[BL05] R. E. Brown and A. J. Line. Efficient high-resolution wake modeling using the vorticity transport equation. *AIAA journal*, 43(7):1434–1443, 2005. (cit. on p. 52).

[BLA05] L. A. Barba, A. Leonard, and C. B. Allen. Advances in viscous vortex methods—meshless spatial adaption based on radial basis function interpolation. *International Journal for Numerical Methods in Fluids*, 47(5):387–421, 2005. (cit. on p. 12).

[BM82] J. T. Beale and A. Majda. Vortex methods. II. Higher order accuracy in two and three dimensions. *Mathematics of Computation*, 39(159):29–52, 1982. (cit. on p. 17).

[Bor90] J. P. Boris. On large eddy simulation using subgrid turbulence models, whither turbulence? *Turbulence at the Crossroads*, 1990. (cit. on p. 42).

[Bou77] J. Boussinesq. *Essai sur la théorie des eaux courantes*. Imprimerie nationale, 1877. (cit. on p. 37).

[BPRM09] M. Breuer, N. Peller, Ch. Rapp, and M. Manhart. Flow over periodic hills – Numerical and experimental study in a wide range of Reynolds numbers. *Computers & Fluids*, 38(2):433–457, February 2009. (cit. on pp. 80, 81, 82, 84, 85, 86, 87, 88, 90, 91, 92, 93, 136, 137, 138, and 139).

[Cal94] J.-P. Caltagirone. Sur l'intéraction fluide-milieu poreux; application au calcul des efforts exercés sur un obstacle par un fluide visqueux. *Comptes rendus de l'Académie des sciences. Série II, Mécanique, physique, chimie, astronomie*, 318(5):571–577, 1994. (cit. on pp. 17 and 136).

[CB73] A. H. Chorin and P. S. Bernard. Discretization of a vortex sheet, with an example of roll-up. *Journal of Computational Physics*, 13(3):423–429, 1973. (cit. on p. 8).

[CBD+17] D.-G. Caprace, S. Buffin, M. Duponcheel, P. Chatelain, and G. Winckelmans. Large eddy simulation of advancing rotor for near to far wake assessment. In *43rd European Rotorcraft Forum*, page 570, 2017. (cit. on pp. 2, 19, 48, and 51).

[CBW08] Roger Cocle, Laurent Bricteux, and Grégoire Winckelmans. Spectral behavior of various subgrid-scale models in LES at very high reynolds number. In *Quality and Reliability of Large-Eddy Simulations*, pages 61–68. Springer, 2008. (cit. on pp. 47, 51, 129, and 130).

[CBW09] R. Cocle, L. Bricteux, and G. Winckelmans. Scale dependence and asymptotic very high Reynolds number spectral behavior of multiscale subgrid models. *Physics of Fluids*, 21(8):085101, 08 2009. (cit. on pp. 47, 51, 61, 129, and 130).

[CBWK13] P. Chatelain, S. Backaert, G. Winckelmans, and S. Kern. Large eddy simulation of wind turbine wakes. *Flow, turbulence and combustion*, 91:587–605, 2013. (cit. on pp. 2 and 21).

[CC08a] M. Coquerelle and G.-H. Cottet. A vortex level set method for the two-way coupling of an incompressible fluid with colliding rigid bodies. *Journal of Computational Physics*, 227(21):9121–9137, 2008. (cit. on pp. 17 and 136).

[CC08b] M. Coquerelle and G.-H. Cottet. A vortex level set method for the two-way coupling of an incompressible fluid with colliding rigid bodies. *Journal of Computational Physics*, 227(21):9121–9137, 2008. (cit. on p. 19).

[CCB+08] P. Chatelain, A. Curioni, M. Bergdorf, D. Rossinelli, W. Andreoni, and P. Koumoutsakos. Billion vortex particle direct numerical simulations of aircraft wakes. *Computer Methods in Applied Mechanics and Engineering*, 197(13):1296–1304, 2008. (cit. on pp. 2, 19, and 47).

[CCW20] D.G. Caprace, P. Chatelain, and G. Winckelmans. Wakes of rotorcraft in advancing flight: A large-eddy simulation study. *Physics of Fluids*, 32(8), 2020. (cit. on pp. 2, 19, 48, and 51).

[CDC+17] P. Chatelain, M. Duponcheel, D.-G. Caprace, Y. Marichal, and G. Winckelmans. Vortex particle-mesh simulations of vertical axis wind turbine flows: from the airfoil performance to the very far wake. *Wind Energy Science*, 2(1):317–328, 2017. (cit. on pp. 2, 21, 48, and 51).

[CDJ07] N. Chauvet, S. Deck, and L. Jacquin. Zonal Detached Eddy Simulation of a controlled propulsive jet. *AIAA Journal*, 45(10):2458–2473, October 2007. Publisher: American Institute of Aeronautics and Astronautics. (cit. on p. 40).

[CDW07] R. Cocle, L. Dufresne, and G. Winckelmans. Investigation of multiscale subgrid models for LES of instabilities and turbulence in wake vortex systems. In *Complex Effects in Large Eddy Simulations*, 2007. (cit. on pp. xii, 47, 51, 58, 129, and 130).

[CDZ+17] P. Chatelain, M. Duponcheel, S. Zeoli, S. Buffin, D.-G. Caprace, G. Winckelmans, and L. Bricteux. Investigation of the effect of inflow turbulence on vertical axis wind turbine wakes. In *Journal of Physics: Conference Series*, volume 854(1), page 012011. IOP Publishing, 2017. (cit. on pp. 2, 21, 48, and 51).

[CEPP14] G.-H. Cottet, J.-M. Etancelin, F. Pérignon, and C. Picard. High order semi-Lagrangian particle methods for transport equations: numerical analysis and implementation issues. *ESAIM: Mathematical Modelling and Numerical Analysis*, 48(4):1029–1060, 2014. (cit. on pp. 14 and 18).

[CFR79] R.A. Clark, J.H. Ferziger, and W.C. Reynolds. Evaluation of subgrid-scale models using an accurately simulated turbulent flow. *Journal of Fluid Mechanics*, 91(1):1–16, March 1979. Publisher: Cambridge University Press. (cit. on pp. 43, 56, and 129).

[Che83] AY Cheer. Numerical study of incompressible slightly viscous flow past blunt bodies and airfoils. *SIAM journal on scientific and statistical computing*, 4(4):685–705, 1983. (cit. on p. 16).

[Cho73] A. J. Chorin. Numerical study of slightly viscous flow. *Journal of Fluid Mechanics*, 57(4):785–796, 1973. (cit. on pp. 10 and 16).

[Cho80] A.J. Chorin. Vortex models and boundary layer instability. *SIAM Journal on Scientific and Statistical Computing*, 1(1):1–21, 1980. (cit. on p. 16).

[Chr73] I. P. Christiansen. Numerical simulation of hydrodynamics by the method of point vortices. *Journal of Computational Physics*, 13(3):363–379, 1973. (cit. on p. 14).

[CJM03] G.-H. Cottet, D. Jiroveanu, and B. Michaux. Vorticity dynamics and turbulence models for large-eddy simulations. *ESAIM: Mathematical Modelling and Numerical Analysis*, 37(1):187–207, 2003. (cit. on pp. 43, 45, 51, 52, and 129).

[CK00] G.-H. Cottet and P. Koumoutsakos. *Vortex Methods: Theory and Practice*. Cambridge University Press, 2000. (cit. on pp. 2, 9, 11, and 16).

[CKS00] G.-H. Cottet, P. Koumoutsakos, and M. L. O. Salihi. Vortex methods with spatially varying cores. *Journal of Computational Physics*, 162(1):164–185, 2000. (cit. on pp. 16 and 125).

[CL81] J.-P. Chollet and M. Lesieur. Parameterization of small scales of three-dimensional isotropic turbulence utilizing spectral closures. *Journal of Atmospheric Sciences*, 38(12):2747–2757, 1981. (cit. on p. 41).

[CLD88] J.-P. Choquin and B. Lucquin-Desreux. Accuracy of a deterministic particle method for Navier-Stokes equations. *International journal for numerical methods in fluids*, 8(11):1439–1458, 1988. (cit. on p. 12).

[Cot88] G.-H. Cottet. A new approach for the analysis of vortex methods in two and three dimensions. *Annales de l'Institut Henri Poincaré C, Analyse non linéaire*, 5(3):227–285, 1988. (cit. on pp. 9 and 17).

[Cot91] G.-H. Cottet. Particle-grid domain decomposition methods for the Navier-Stokes equations in exterior domains. *Lectures in Applied Mathematics*, 28:103–117, 1991. (cit. on p. 16).

[Cot95] G.-H. Cottet. A vorticity creation algorithm for the navier-stokes equations in arbitrary domain. In *Navier—Stokes Equations and Related Nonlinear Problems*, pages 335–349. Springer, 1995. (cit. on p. 16).

[Cot96] G.-H. Cottet. Artificial viscosity models for vortex and particle methods. *Journal of Computational Physics*, 127(2):299–308, 1996. (cit. on pp. 49, 51, 107, and 129).

[Cot98] G-H Cottet. Anisotropic subgrid-scale numerical schemes for large eddy simulations of turbulent flows. Technical report, LMC-IMAG, 1998. (cit. on p. 50).

[CP04] G.-H. Cottet and P. Poncet. Advances in direct numerical simulations of 3D wall-bounded flows by vortex-in-cell methods. *Journal of computational physics*, 193(1):136–158, 2004. (cit. on pp. 17 and 19).

[CS10] G. N. Coleman and R. D. Sandberg. A primer on direct numerical simulation of turbulence-methods, procedures and guidelines. Technical report, University of Southampton, 2010. (cit. on p. 1).

[CT65] J. W. Cooley and J. W. Tukey. An algorithm for the machine calculation of complex fourier series. *Mathematics of computation*, 19(90):297–301, 1965. (cit. on p. 26).

[CWC20] D.-G. Caprace, G. Winckelmans, and P. Chatelain. An immersed lifting and dragging line model for the vortex particle-mesh method. *Theoretical and Computational Fluid Dynamics*, 34(1):21–48, 2020. (cit. on pp. 21, 48, and 51).

[CWD08] F. Cocle, G. Winckelmans, and G. Daeninck. Combining the vortex-in-cell and parallel fast multipole methods for efficient domain decomposition simulations. *Journal of Computational Physics*, 227(21):9091–9120, 2008. Special Issue Celebrating Tony Leonard's 70th Birthday. (cit. on pp. 48 and 51).

[CWS18] J. B. Chapelier, B. Wasistho, and C. Scalo. A Coherent vorticity preserving eddy-viscosity correction for Large-Eddy Simulation. *Journal of Computational Physics*, 359:164–182, April 2018. (cit. on pp. ix, 52, 61, and 62).

[Dea70] J. W. Deardorff. A numerical study of three-dimensional turbulent channel flow at large reynolds numbers. *Journal of Fluid Mechanics*, 41(2):453–480, 1970. (cit. on p. 40).

[DL08] K Duraisamy and S. K. Lele. Evolution of isolated turbulent trailing vortices. *Physics of Fluids*, 20(3), 2008. (cit. on p. 52).

[DLLV17] T. Dairay, E. Lamballais, S. Laizet, and J. Vassilicos. Numerical dissipation vs. subgrid-scale modelling for large eddy simulation. *Journal of Computational Physics*, 337, February 2017. (cit. on pp. 41, 42, 60, 61, 63, 67, 69, 70, 71, 75, 132, 133, and 134).

[DMG89] P. Degond and S. Mas-Gallic. The weighted particle method for convection-diffusion equations. I. The case of an isotropic viscosity. *Mathematics of computation*, 53(188):485–507, 1989. (cit. on p. 11).

[dMM+24] M. de Crouy-Chanel, C. Mimeau, I. Mortazavi, A. Mariotti, and M. V. Salvetti. Large-eddy simulations with remeshed vortex methods: An assessment and calibration of subgrid-scale models. *Computers & Fluids*, 277:106287, 2024. (cit. on p. 3).

[EOP10] M. El Ossmani and P. Poncet. Efficiency of multiscale hybrid grid-particle vortex methods. *Multiscale modeling & simulation*, 8(5):1671–1690, 2010. (cit. on p. 30).

[Eta14] J.-M. Etancelin. *Couplage de modèles, algorithmes multi-échelles et calcul hybride*. PhD thesis, Université de Grenoble, 2014. (cit. on pp. 2, 21, 22, 23, and 24).

[FDLS21] R. A. S. Frantz, G. Deskos, S. Laizet, and J. H. Silvestrini. High-fidelity simulations of gravity currents using a high-order finite-difference spectral vanishing viscosity approach. *Computers & Fluids*, 221:104902, May 2021. (cit. on p. 132).

[FJ05] M. Frigo and S. G. Johnson. The design and implementation of fftw3. *Proceedings of the IEEE*, 93(2):216–231, 2005. (cit. on p. 26).

[FK05] K Fukuda and K Kamemoto. Application of a redistribution model incorporated in a vortex method to turbulent flow analysis. *Proc. ICVFM2005, Yokohama, Japan*, pages 131–136, 2005. (cit. on p. 50).

[FMR+05] J. Fröhlich, C. P. Mellen, W. Rodi, L. Temmerman, and M. A. Leschziner. Highly resolved large-eddy simulation of separated flow in a channel with streamwise periodic constrictions. *Journal of Fluid Mechanics*, 526:19–66, March 2005. (cit. on p. 81).

[GC19] X. Gloerfelt and P. Cinnella. Large Eddy Simulation Requirements for the Flow over Periodic Hills. *Flow, Turbulence and Combustion*, 103(1):55–91, June 2019. (cit. on pp. 81 and 91).

[GG98] A Gharakhani and A.F. Ghoniem. Simulation of the piston driven flow inside a cylinder with an eccentric port. *Journal of fluids engineering*, 120(2):319–326, 1998. (cit. on p. 16).

[GHK14] M. Gazzola, B. Hejazialhosseini, and P. Koumoutsakos. Reinforcement learning and wavelet adapted vortex methods for simulations of self-propelled swimmers. *SIAM Journal on Scientific Computing*, 36(3):B622–B639, 2014. (cit. on pp. 2 and 19).

[Gho96] S. Ghosal. An analysis of numerical errors in large-eddy simulations of turbulence. *Journal of Computational Physics*, 125(1):187–206, 1996. (cit. on p. 42).

[GHS93] J.-L. Guermond, S. Huberson, and W.-Z. Shen. Simulation of 2D external viscous flows by means of a domain decomposition method. *Journal of Computational Physics*, 108(2):343–352, 1993. (cit. on p. 16).

[GLMA95] S. Ghosal, T. S. Lund, P. Moin, and K. Akselvoll. A dynamic localization model for large-eddy simulation of turbulent flows. *Journal of fluid mechanics*, 286:229–255, 1995. (cit. on pp. 39 and 129).

[GM77] R. A. Gingold and J. J. Monaghan. Smoothed particle hydrodynamics: theory and application to non-spherical stars. *Monthly notices of the royal astronomical society*, 181(3):375–389, 1977. (cit. on p. 6).

[GMR07] F. F. Grinstein, L. G. Margolin, and W. J. Rider. *Implicit large eddy simulation*, volume 10. Cambridge university press Cambridge, 2007. (cit. on pp. 1 and 42).

[GMWC19] T. Gillis, Y. Marichal, G. Winckelmans, and P. Chatelain. A 2D immersed interface Vortex Particle-Mesh method. *Journal of Computational Physics*, 394:700–718, 2019. (cit. on p. 17).

[GPMC91] M. Germano, U. Piomelli, P. Moin, and W.H. Cabot. A dynamic subgrid-scale eddy viscosity model. *Physics of Fluids A: Fluid Dynamics*, 3(7):1760–1765, 1991. (cit. on pp. 36, 38, and 129).

[GvRK12] M. Gazzola, W.M. van Rees, and P. Koumoutsakos. C-start: optimal start of larval fish. *Journal of Fluid Mechanics*, 698:5–18, 2012. (cit. on p. 19).

[Hal79] O. H. Hald. Convergence of vortex methods for Euler's equations. II. *SIAM Journal on Numerical Analysis*, 16(5):726–755, 1979. (cit. on p. 17).

[HCY+25] X. Hou, N. Chang, Z. Yuan, Y. Wang, H. Peng, R. Zhang, and J. Wang. Large eddy simulation modeling of incompressible turbulence governed by vorticity transport equations. *Physics of Fluids*, 37(1), 2025. (cit. on pp. 48, 51, 107, and 129).

[HJ90] S. Huberson and A. Jolles. Correction de l'erreur de projection dans les méthodes particules/maillage. *La recherche aérospatiale*, 4:1–6, 1990. (cit. on p. 12).

[HKA08] S Hickel, T. Kempe, and NA Adams. Implicit large-eddy simulation applied to turbulent channel flow with periodic constrictions. *Theoretical and Computational Fluid Dynamics*, 22:227–242, 2008. (cit. on p. 81).

[HMOW01] T.J. R. Hughes, L. Mazzei, A. A. Oberai, and A. A. Wray. The multiscale formulation of large eddy simulation: Decay of homogeneous isotropic turbulence. *Physics of Fluids*, 13(2):505–512, 2001. (cit. on pp. 39, 129, and 130).

[HV02] S. G. Huberson and S. G. Voutsinas. Particles and grid. *Computers & fluids*, 31(4-7):607–625, 2002. (cit. on p. 16).

[JJS16] S. Jammy, C. Jacobs, and N. Sandham. Enstrophy and kinetic energy data from 3D Taylor-Green vortex simulations, 2016. (cit. on pp. 19 and 20).

[Kec19] J.-B. Keck. *Numerical modelling and High Performance Computing for sediment flows*. PhD thesis, université grenoble alpes, 2019. (cit. on pp. 2, 21, 22, 23, 24, 25, 30, 61, 71, 109, and 127).

[KG01] N. K.-R. Kevlahan and J.-M. Ghidaglia. Computation of turbulent flow past an array of cylinders using a spectral method with brinkman penalization. *European Journal of Mechanics - B/Fluids*, 20(3):333–350, 2001. (cit. on pp. 17 and 136).

[Kid85] S Kida. Three-dimensional periodic flows with high-symmetry. *Journal of the Physical Society of Japan*, 54(6):2132–2136, 1985. (cit. on p. 46).

[KK00] G.-S. Karamanos and G.E. Karniadakis. A spectral vanishing viscosity method for large-eddy simulations. *Journal of Computational Physics*, 163(1):22–50, September 2000. (cit. on pp. 41 and 132).

[KK02] R. M. Kirby and G. E. Karniadakis. Coarse resolution turbulence simulations with spectral vanishing viscosity — large-eddy simulations (SVV-LES). *Journal of Fluids Engineering*, 124(4):886–891, December 2002. (cit. on pp. 41, 60, and 132).

[KKW18] B. Krank, M. Kronbichler, and W. A. Wall. Direct numerical simulation of flow over periodic hills up to ReH=10,595. *Flow, Turbulence and Combustion*, 101:521 – 551, 2018. (cit. on pp. 81, 90, 91, 92, 93, 136, 137, 138, and 139).

[KL95] P. Koumoutsakos and A. Leonard. High-resolution simulations of the flow around an impulsively started cylinder using vortex methods. *Journal of Fluid Mechanics*, 296:1–38, 1995. (cit. on pp. 2, 12, 17, and 127).

[KLP94] P. Koumoutsakos, A. Leonard, and F. Pepin. Boundary conditions for viscous vortex methods. *Journal of Computational Physics*, 113(1):52–61, 1994. (cit. on p. 16).

[Kor17] N. Kornev. Hybrid method based on embedded coupled simulation of vortex particles in grid based solution. *Computational Particle Mechanics*, 5:269 – 283, 2017. (cit. on pp. 50 and 129).

[Kor18] N. Kornev. Hybrid method based on embedded coupled simulation of vortex particles in grid based solution. *Computational Particle Mechanics*, 5(3):269–283, 2018. (cit. on p. 16).

[KS06] R. M. Kirby and S. J. Sherwin. Stabilisation of spectral/hp element methods through spectral vanishing viscosity: Application to fluid mechanics modelling. *Computer Methods in Applied Mechanics and Engineering*, 195(23):3128–3144, April 2006. (cit. on pp. 41, 68, and 132).

[KS19] N. Kornev and S. Samarbakhsh. Large eddy simulation with direct resolution of subgrid motion using a grid free vortex particle method. *International Journal of Heat and Fluid Flow*, 75:86–102, 2019. (cit. on pp. 50 and 129).

[KSB12] K. Koal, J. Stiller, and H. M. Blackburn. Adapting the spectral vanishing viscosity method for large-eddy simulations in cylindrical configurations. *Journal of Computational Physics*, 231(8):3389–3405, April 2012. (cit. on p. 68).

[KSD24] N Kornev, S Samarbakhsh, and J Darji. Hybrid grid-free and grid-based method for simulation of turbulent flows. *Physics of Fluids*, 36(7), 2024. (cit. on pp. 50 and 129).

[LBC14] J.-B. Lagaert, G. Balarac, and G.-H. Cottet. Hybrid spectral-particle method for the turbulent transport of a passive scalar. *Journal of Computational Physics*, 260:127–142, 2014. (cit. on p. 21).

[LBCB12] J.-B. Lagaert, G. Balarac, G.-H. Cottet, and P. Bégou. Particle method: an efficient tool for direct numerical simulations of a high Schmidt number passive scalar in turbulent flow. In *Summer Program 2012. Center of Turbulence Research*, pages 167–176, 2012. (cit. on p. 22).

[LCP05] A. G. Lamorgese, D. A. Caughey, and S. B. Pope. Direct numerical simulation of homogeneous turbulence with hyperviscosity. *Physics of Fluids*, 17(1):015106, 2005. (cit. on p. 74).

[Lel92] S.K. Lele. Compact finite difference schemes with spectral-like resolution. *Journal of computational physics*, 103(1):16–42, 1992. (cit. on p. 36).

[Leo75a] A. Leonard. Energy cascade in large-eddy simulations of turbulent fluid flows. In F.N. Frenkiel and R.E. Munn, editors, *Turbulent Diffusion in Environmental Pollution*, volume 18 of *Advances in Geophysics*, pages 237–248. Elsevier, 1975. (cit. on pp. 43, 56, and 129).

[Leo75b] A. Leonard. Numerical simulation of interacting three-dimensional vortex filaments. In *Proceedings of the Fourth International Conference on Numerical Methods in Fluid Dynamics*, pages 245–250. Springer Berlin Heidelberg, 1975. (cit. on p. 9).

[Leo80] A. Leonard. Vortex methods for flow simulation. *Journal of Computational Physics*, 37(3):289–335, 1980. (cit. on p. 9).

[LFL11] E. Lamballais, V. Fortuné, and S. Laizet. Straightforward high-order numerical dissipation via the viscous term for direct and large eddy simulation. *Journal of Computational Physics*, 230(9):3270–3275, 2011. (cit. on p. 42).

[Lil92] D.K. Lilly. A proposed modification of the germano sugrid-scale closure method. *Phys Fluids A*, 4:633–635, 1992. (cit. on pp. 36, 39, and 129).

[LMS07] D. Lucor, J. Meyers, and P. Sagaut. Sensitivity analysis of large-eddy simulations to subgrid-scale-model parametric uncertainty using polynomial chaos. *Journal of Fluid Mechanics*, 585:255–279, 2007. (cit. on p. 65).

[LPA13] H. Lu and F. Porté-Agel. A modulated gradient model for scalar transport in large-eddy simulation of the atmospheric boundary layer. *Physics of Fluids*, 25(1):015110, January 2013. (cit. on pp. 43 and 131).

[Mar94] S. A. Martucci. Symmetric convolution and the discrete sine and cosine transforms. *IEEE Transactions on Signal Processing*, 42(5):1038–1051, 1994. (cit. on p. 30).

[MBG12] F. Morency, H. Beaugendre, and F. Gallizio. Aerodynamic force evaluation for ice shedding phenomenon using vortex in cell scheme, penalisation and level set approaches. *International Journal of Computational Fluid Dynamics*, 26(9-10):435–450, 2012. (cit. on p. 100).

[MC12] A. Magni and G.-H. Cottet. Accurate, non-oscillatory, remeshing schemes for particle methods. *Journal of Computational Physics*, 231(1):152–172, 2012. (cit. on p. 22).

[MCM18] C. Mimeau, G. H. Cottet, and I. Mortazavi. An artificial viscosity model for 3D simulations with vortex methods. In *10th International Conference on Computational Fluid Dynamics*, pages 1–6. ICCFD 2018 - Proceedings, 2018. (cit. on pp. 50 and 129).

[MCW16] Y. Marichal, P. Chatelain, and G. Winckelmans. Immersed interface interpolation schemes for particle–mesh methods. *Journal of Computational Physics*, 326:947–972, 2016. (cit. on p. 17).

[MF00] H. L. Meitz and H. F. Fasel. A compact-difference scheme for the navier–stokes equations in vorticity–velocity formulation. *Journal of Computational Physics*, 157(1):371–403, 2000. (cit. on p. 52).

[MFG+15] C. Mockett, M. Fuchs, A. Garbaruk, M. Shur, P. Spalart, M. Strelets, F. Thiele, and A. Travin. Two non-zonal approaches to accelerate RANS to LES transition of free shear layers in DES. In *Progress in Hybrid RANS-LES Modelling*, Notes on Numerical Fluid Mechanics and Multidisciplinary Design, pages 187–201. Springer International Publishing, 2015. (cit. on p. 40).

[MFR78] N.N. Mansour, J.H. Ferziger, and W. C. Reynolds. Large-eddy simulation of a turbulent mixing layer. Technical report, Stanford University, 1978. (cit. on pp. 45, 48, and 51).

[MFR00] C. Mellen, J. Froehlich, and W. Rodi. Large eddy simulation of the flow over periodic hills. In *Proc. IMACS World Congress (ed. M. Deville & R. Owens), Lausanne*, 2000. (cit. on pp. 80 and 134).

[MFRV20] J. Manzanero, E. Ferrer, G. Rubio, and E. Valero. Design of a Smagorinsky spectral Vanishing Viscosity turbulence model for discontinuous Galerkin methods. *Computers & Fluids*, 200:104440, March 2020. (cit. on pp. 41 and 60).

[MGCM15] C. Mimeau, F. Gallizio, G.-H. Cottet, and I. Mortazavi. Vortex penalization method for bluff body flows. *International Journal for Numerical Methods in Fluids*, 79(2):55–83, 2015. (cit. on p. 19).

[Mim15] C. Mimeau. *Conception and implementation of a hybrid vortex penalization method for solid-fluid-porous media : application to the passive control of incompressible flows*. PhD thesis, Université Grenoble Alpes (ComUE), 2015. (cit. on pp. ix, x, 15, 22, 28, and 95).

[MKM96] J.R. Mansfield, O.M. Knio, and C. Meneveau. Towards lagrangian large vortex simulation. In *ESAIM: Proceedings*, volume 1, pages 49–64. EDP Sciences, 1996. (cit. on pp. 45 and 51).

[MKM98] J. R. Mansfield, O. M. Knio, and C. Meneveau. A Dynamic LES Scheme for the Vorticity Transport Equation: Formulation and a Priori Tests. *Journal of Computational Physics*, 145(2):693–730, September 1998. (cit. on pp. 44, 45, 46, 51, 56, 107, and 129).

[MKM99] J. Mansfield, O. Knio, and C. Meneveau. Dynamic LES of colliding vortex rings using a 3D vortex method. *Journal of Computational Physics*, 152:305–345, June 1999. (cit. on pp. 46, 51, 56, and 129).

[MKT93] Y. Maday, S. M. O. Kaber, and E. Tadmor. Legendre pseudospectral viscosity method for nonlinear conservation laws. *SIAM Journal on Numerical Analysis*, 30(2):321–342, April 1993. (cit. on pp. 41 and 59).

[ML92] O. Métais and M. Lesieur. Spectral large-eddy simulation of isotropic and stably stratified turbulence. *Journal of Fluid Mechanics*, 239:157–194, June 1992. (cit. on pp. 37, 41, and 47).

[MLC96] C. Meneveau, T. S. Lund, and W. H. Cabot. A lagrangian dynamic subgrid-scale model of turbulence. *Journal of Fluid Mechanics*, 319:353–385, 1996. (cit. on p. 39).

[MM21] C. Mimeau and I. Mortazavi. A review of vortex methods and their applications: From creation to recent advances. *Fluids*, 6:68, 2021. (cit. on pp. 11, 12, and 127).

[MMC17] C. Mimeau, I. Mortazavi, and G.-H. Cottet. Passive control of the flow around a hemisphere using porous media. *European Journal of Mechanics-B/Fluids*, 65:213–226, 2017. (cit. on p. 19).

[MMM21] C. Mimeau, S. Marié, and I. Mortazavi. A comparison of semi-Lagrangian vortex method and lattice Boltzmann method for incompressible flows. *Computers & Fluids*, 224:104946, 2021. (cit. on pp. 18, 20, 53, 60, 61, 71, and 83).

[Mon85] J. J. Monaghan. Extrapolating B splines for interpolation. *Journal of Computational Physics*, 60(2):253–262, 1985. (cit. on p. 13).

[MT89] Y. Maday and E. Tadmor. Analysis of the spectral vanishing viscosity method for periodic conservation laws. *SIAM Journal on Numerical Analysis*, 26(4):854–870, August 1989. (cit. on pp. 41 and 132).

[ND99] F. Nicoud and F. Ducros. Subgrid-scale stress modelling based on the square of the velocity gradient tensor. *Flow Turbulence and Combustion*, 62:183–200, 09 1999. (cit. on p. 38).

[NLdLK21] G. Novati, H. Lascombes de Laroussilhe, and P. Koumoutsakos. Automating turbulence modelling by multi-agent reinforcement learning. *Nature Machine Intelligence*, 3(1):87–96, 2021. (cit. on p. 1).

[NVA+17] G. Novati, S. Verma, D. Alexeev, D. Rossinelli, W. M. van Rees, and P. Koumoutsakos. Synchronisation through learning for two self-propelled swimmers. *Bioinspiration & biomimetics*, 12(3):036001, 2017. (cit. on pp. 2 and 19).

[Pas05] R. Pasquetti. Spectral vanishing viscosity method for LES: sensitivity to the SVV control parameters. *Journal of Turbulence*, 6:N12, January 2005. (cit. on pp. 41, 60, and 61).

[Pas06] R. Pasquetti. Spectral vanishing viscosity method for large-eddy simulation of turbulent flows. *Journal of Scientific Computing*, 27(1):365–375, June 2006. (cit. on p. 41).

[PCML91] U. Piomelli, W. H. Cabot, P. Moin, and S. Lee. Subgrid-scale backscatter in turbulent and transitional flows. *Physics of Fluids A: Fluid Dynamics*, 3(7):1766–1771, 1991. (cit. on pp. 58 and 131).

[Pra28] W. Prager. Die Druckverteilung an Korpern in ebener Potentialstromung. *Physikalische Zeitschrift*, 29:865–869, 1928. (cit. on pp. 1 and 7).

[PWS+02] P. Ploumhans, G. S. Winckelmans, J. K. Salmon, A. Leonard, and M. S. Warren. Vortex methods for direct numerical simulation of three-dimensional bluff body flows: application to the sphere at Re= 300, 500, and 1000. *Journal of Computational Physics*, 178(2):427–463, 2002. (cit. on p. 17).

[RBCK10] D. Rossinelli, M. Bergdorf, G.-H. Cottet, and P. Koumoutsakos. Gpu accelerated simulations of bluff body flows using vortex particle methods. *Journal of Computational Physics*, 229(9):3316–3333, 2010. (cit. on p. 2).

[RCW11] J. T. Rasmussen, G.-H. Cottet, and J. H. Walther. A multiresolution remeshed vortex-in-cell algorithm using patches. *Journal of Computational Physics*, 230(17):6742–6755, 2011. (cit. on p. 30).

[Rey95] O. Reynolds. Iv. on the dynamical theory of incompressible viscous fluids and the determination of the criterion. *Philosophical transactions of the royal society of london.(a.)*, 186:123–164, 1895. (cit. on p. 35).

[RHvR+15] D. Rossinelli, B. Hejazialhosseini, W. van Rees, M. Gazzola, M. Bergdorf, and P. Koumoutsakos. MRAG-I2D: Multi-resolution adapted grids for remeshed vortex methods on multicore architectures. *Journal of Computational Physics*, 288:1–18, 2015. (cit. on p. 30).

[Ric22] L. F. Richardson. *Weather prediction by numerical process*. University Press, 1922. (cit. on p. 32).

[RK08] D. Rossinelli and P. Koumoutsakos. Vortex methods for incompressible flow simulations on the gpu. *The visual computer*, 24:699–708, 2008. (cit. on p. 23).

[RLBO13] I Rodríguez, O Lehmkuhl, R Borrell, and A Oliva. Flow dynamics in the turbulent wake of a sphere at sub-critical reynolds numbers. *Computers & Fluids*, 80:233–243, 2013. (cit. on pp. xi, 95, 96, 97, 98, 99, 100, 102, 138, 139, and 140).

[RM11] C. Rapp and M. Manhart. Flow over periodic hills: an experimental study. *Experiments in Fluids*, 51(1):247–269, July 2011. (cit. on pp. 81, 90, 91, 92, 93, 136, 138, and 139).

[Rog81] R.S. Rogallo. *Numerical Experiments in Homogeneous Turbulence*. NASA technical memorandum. National Aeronautics and Space Administration, 1981. (cit. on p. 74).

[Ros31] L. Rosenhead. The formation of vortices from a surface of discontinuity. *Proc. R. Soc. Lond.*, 134:170–192, 1931. (cit. on p. 7).

[RS94] G. Russo and J. Strain. Fast triangulated vortex methods for the 2D Euler equations. *Journal of Computational Physics*, 111(2):291–323, 1994. (cit. on p. 12).

[Sag06] P. Sagaut. *Large Eddy Simulation for Incompressible Flows: An Introduction*. Springer Science & Business Media, 2006. (cit. on pp. 36, 53, and 128).

[SAK01] S. Stolz, N. A. Adams, and L. Kleiser. An approximate deconvolution model for large-eddy simulation with application to incompressible wall-bounded flows. *Physics of fluids*, 13(4):997–1015, 2001. (cit. on p. 42).

[SB95] M. V. Salvetti and S. Banerjee. A priori tests of a new dynamic subgrid-scale model for finite-difference large-eddy simulations. *Physics of Fluids*, 7(11):2831–2847, 1995. (cit. on p. 42).

[Sch46] I. J. Schoenberg. Contributions to the problem of approximation of equidistant data by analytic functions. Part B. On the problem of osculatory interpolation. A second class of analytic approximation formulae. *Quarterly of Applied Mathematics*, 4(2):112–141, 1946. (cit. on p. 13).

[SG88] J. A. Sethian and A. F. Ghoniem. Validation study of vortex methods. *Journal of Computational Physics*, 74(2):283–317, 1988. (cit. on p. 16).

[SGS10] M. Stock, A. Gharakhani, and C. Stone. Modeling rotor wakes with a hybrid OVERFLOW-vortex method on a GPU cluster. In *28th AIAA applied aerodynamics conference*, page 4553, 2010. (cit. on p. 51).

[SJSA97] P. Spalart, W.-H. Jou, M. Strelets, and S. Allmaras. Comments on the feasibility of LES for wings, and on a hybrid RANS/LES approach. In *Proceedings of the First AFOSR International Conference on DNS/LES*, pages 137–147, 01 1997. (cit. on pp. 34 and 40).

[SK19] S. Samarbakhsh and N. Kornev. Simulation of a free circular jet using the vortex particle intensified LES (vπ LES). *International Journal of Heat and Fluid Flow*, 80:108489, 2019. (cit. on pp. 50 and 129).

[Sma63] J. Smagorinsky. General circulation experiments with the primitive equations: I. the basic experiment. *Monthly Weather Review*, 91(3):99 – 164, 1963. (cit. on pp. 37 and 128).

[SMLGM23] A. Suss, I. Mary, T. Le Garrec, and S. Marié. Comprehensive comparison between the lattice Boltzmann and Navier–Stokes methods for aerodynamic and aeroacoustic applications. *Computers & Fluids*, 257:105881, 2023. (cit. on p. 20).

[Sob01] I.M. Sobol. Global sensitivity indices for nonlinear mathematical models and their monte carlo estimates. *Mathematics and Computers in Simulation*, 55(1):271–280, 2001. The Second IMACS Seminar on Monte Carlo Methods. (cit. on p. 66).

[Spe87] C. G. Speziale. On the advantages of the vorticity-velocity formulation of the equations of fluid dynamics. *Journal of Computational Physics*, 73(2):476–480, 1987. (cit. on p. 52).

[SRCDB24] L. P. Saavedra, C. E. N. Radburn, A. Collard-Daigneault, and B. Blais. An implicit large-eddy simulation perspective on the flow over periodic hills. *Computers & Fluids*, 283:106390, 2024. (cit. on p. 81).

[SRS10] B. Schrader, S. Reboux, and I. F. Sbalzarini. Discretization correction of general integral PSE operators for particle methods. *Journal of Computational Physics*, 229(11):4159–4182, 2010. (cit. on p. 12).

[SS88] P.A. Smith and P.K. Stansby. Impulsively started flow around a circular cylinder by the vortex method. *Journal of Fluid Mechanics*, 194:45–77, 1988. (cit. on p. 16).

[STL20] J.-E. Schumann, S. Toosi, and J. Larsson. Assessment of Grid Anisotropy Effects on Large-Eddy-Simulation Models with Different Length Scales. *AIAA Journal*, 58(10):4522–4533, 2020. (cit. on p. 40).

[Str68] G. Strang. On the construction and comparison of difference schemes. *SIAM journal on numerical analysis*, 5(3):506–517, 1968. (cit. on p. 23).

[Str97] J. Strain. Fast adaptive 2D vortex methods. *Journal of computational physics*, 132(1):108–122, 1997. (cit. on p. 12).

[Tad89] E. Tadmor. Convergence of spectral methods for nonlinear conservation laws. *SIAM Journal on Numerical Analysis*, 26(1):30–44, February 1989. (cit. on pp. 41 and 132).

[TG37] G.I. Taylor and A.E. Green. Mechanism of the Production of Small Eddies from Large Ones. *Proceedings of the Royal Society of London Series A*, 158(895):499–521, February 1937. (cit. on pp. 46, 55, and 60).

[TGS+17] F. X. Trias, A. Gorobets, M. H. Silvis, R. W. C. P. Verstappen, and A. Oliva. A new subgrid characteristic length for turbulence simulations on anisotropic grids. *Physics of Fluids*, 29(11):115109, November 2017. (cit. on p. 40).

[TPDT05] C. Tenaud, S. Pellerin, A. Dulieu, and L. Ta Phuoc. Large eddy simulations of a spatially developing incompressible 3D mixing layer using the v-ω formulation. *Computers & Fluids*, 34(1):67–96, 2005. (cit. on pp. 48, 52, and 129).

[Val24] J. Valentin. *Multi-Fidelity Vortex Particles Coupling with Lifting Line and Eulerian Methods for 3D Viscous Aeronautical Simulations*. PhD thesis, INSA Rouen Normandie, 2024. (cit. on pp. 46 and 51).

[VBC16] A. Vollant, G. Balarac, and C. E. Corre. A dynamic regularized gradient model of the subgrid-scale stress tensor for large-eddy simulation. *Physics of Fluids*, 28(2):025114, 2016. (cit. on pp. 43 and 131).

[VCL23] R. Vicente Cruz and E. Lamballais. Physical/numerical duality of explicit/implicit subgrid-scale modelling. *Journal of Turbulence*, pages 1–45, 2023. (cit. on p. 59).

[VM22] A. Vela-Martín. Subgrid-scale models of isotropic turbulence need not produce energy backscatter. *Journal of Fluid Mechanics*, 937, April 2022. (cit. on p. 36).

[Vre95] A.W. Vreman. *Direct and Large-Eddy Simulation of the Compressible Turbulent Mixing Layer*. PhD thesis, University of Twente, Netherlands, December 1995. (cit. on pp. 43, 56, and 129).

[Vre04] A. W. Vreman. An eddy-viscosity subgrid-scale model for turbulent shear flow: algebraic theory and applications. *Physics of Fluids*, 16(10):3670–3681, October 2004. (cit. on p. 37).

[vRGK13] W. M. van Rees, M. Gazzola, and P. Koumoutsakos. Optimal shapes for anguilliform swimmers at intermediate Reynolds numbers. *Journal of Fluid Mechanics*, 722:R3, 2013. (cit. on p. 19).

[vRLPK11] W. M. van Rees, A. Leonard, D. I. Pullin, and P. Koumoutsakos. A comparison of vortex and pseudo-spectral methods for the simulation of periodic vortical flows at high Reynolds numbers. *Journal of Computational Physics*, 230(8):2794–2805, 2011. (cit. on pp. 18 and 60).

[VV03] RWCP Verstappen and AEP Veldman. Symmetry-preserving discretization of turbulent flow. *Journal of Computational Physics*, 187(1):343–368, 2003. (cit. on p. 95).

[WB21] G. R. Whitehouse and A. H. Boschitsch. Investigation of grid-based vorticity-velocity large eddy simulation off-body solvers for application to overset CFD. *Computers & Fluids*, 225:104978, July 2021. (cit. on pp. 46, 51, and 52).

[WFA+13] Z. J. Wang, K. Fidkowski, R. Abgrall, F. Bassi, D. Caraeni, A. Cary, H. Deconinck, R. Hartmann, K. Hillewaert, H. T. Huynh, et al. High-order CFD methods: current status and perspective. *International Journal for Numerical Methods in Fluids*, 72(8):811–845, 2013. (cit. on p. 20).

[WG06] D. Wee and A. F. Ghoniem. Modified interpolation kernels for treating diffusion and remeshing in vortex methods. *Journal of Computational Physics*, 213(1):239–263, 2006. (cit. on p. 14).

[Win95] G. S. Winckelmans. Some Progress in Large-Eddy Simulation using the 3-D Vortex Particle Method. In *Center for Turbulence Research Annual Research Briefs: 1995*, December 1995. (cit. on pp. 45, 51, and 129).

[WJ01] G. S. Winckelmans and H. Jeanmart. Assessment of some models for LES without/with explicit filtering. In *Direct and Large-Eddy Simulation IV*, pages 55–66. Springer Netherlands, Dordrecht, 2001. (cit. on p. 57).

[WLCW96] G. S. Winckelmans, T. S. Lund, D. Carati, and A. A. Wray. A priori testing of subgrid-scale models for the velocity-pressure and vorticity-velocity formulations. In *Summer Program, Center for Turbulence Research, Stanford University and NASA Ames*, pages 309–328, December 1996. (cit. on pp. 45, 51, and 129).

[WWXS21] R. Wang, F. Wu, H. Xu, and S. J. Sherwin. Implicit large-eddy simulations of turbulent flow in a channel via spectral/ *hp* element methods. *Physics of Fluids*, 33(3):035130, March 2021. (cit. on pp. 81 and 132).

[XC19] H. Xiao and P. Cinnella. Quantification of model uncertainty in rans simulations: A review. *Progress in Aerospace Sciences*, 108:1–31, 2019. (cit. on pp. 1 and 65).

[XK02] D. Xiu and G. E. Karniadakis. The wiener–askey polynomial chaos for stochastic differential equations. *SIAM Journal on Scientific Computing*, 24(2):619–644, 2002. (cit. on pp. 2, 56, and 65).

[YM07] D. You and P. Moin. A dynamic global-coefficient subgrid-scale eddy-viscosity model for large-eddy simulation in complex geometries. *Physics of Fluids*, 19(6), 2007. (cit. on p. 39).

[YWXW21] Z. Yuan, Y. Wang, C. Xie, and J. Wang. Dynamic iterative approximate deconvolution models for large-eddy simulation of turbulence. *Physics of Fluids*, 33(8), 2021. (cit. on p. 48).

[Zhi15] Y. Zhiyin. Large-eddy simulation: Past, present and the future. *Chinese journal of Aeronautics*, 28(1):11–24, 2015. (cit. on p. 1).

[ZSK93] Y. Zang, R. L. Street, and J. R. Koseff. A dynamic mixed subgrid-scale model and its application to turbulent recirculating flows. *Physics of Fluids A: Fluid Dynamics*, 5(12):3186–3196, December 1993. (cit. on pp. 42 and 129).

Résumé étendu de la thèse

Introduction

Nous utilisons des methodes vortex remaillées (MVR) pour résoudre les équations de Navier-Stokes. Il s'agit d'une méthode semi-lagrangienne qui consiste à discretiser le fluide sur des particules numériques puis à "remailler" ces particules sur une grille cartésienne, passant ainsi d'un point de vue lagrangien à un point de vue eulérien.

Ces méthodes ont fait leurs preuves dans de nombreux domaines. Cependant, afin d'être compétitives pour des applications industrielles, elles doivent être capable de simuler des écoulements turbulents à de haut nombres de Reynolds. Ces écoulements demandent une puissance de calcul trop importante pour être résolus de manière réaliste, dû à l'importance des petites échelles dans la physique de ceux-ci. Un modèle de turbulence est donc essentiel afin de pouvoir utiliser des tailles de maillage réalisables. Les méthodes vortex, connues pour leur faible diffusion numérique, sont de bonnes candidates pour la simulation des grandes échelles de turbulence (LES).

Chapitre 1 : Méthodes vortex

Les méthodes vortex [CKS00] ont été initialement proposées pour résoudre les équations d'Euler en formulation vorticité ($\boldsymbol{\omega}$)-vitesse($\mathbf{u}$)

$$\frac{\partial \boldsymbol{\omega}}{\partial t} + \mathbf{u} \cdot \nabla \boldsymbol{\omega} - \boldsymbol{\omega} \cdot \nabla \mathbf{u} - \frac{1}{Re} \Delta \boldsymbol{\omega} = 0 \tag{6.4}$$

$$-\Delta \mathbf{u} = \nabla \times \boldsymbol{\omega}, \tag{6.5}$$

Le terme $(\mathbf{u} \cdot \nabla)\boldsymbol{\omega}$ représente l'advection du champs de vorticité et $(\boldsymbol{\omega} \cdot \nabla)\mathbf{u}$ son étirement (le "stretching"), seulement présent en dimension trois. L'équation de Poisson obtenue à partir de la définition de la vorticité et de la condition d'incompressibilité $\nabla \cdot \mathbf{u} = 0$

$$\nabla \times \boldsymbol{\omega} = \nabla \times \nabla \times \mathbf{u} = \nabla(\nabla \cdot \mathbf{u}) - \Delta \mathbf{u} = -\Delta \mathbf{u}$$

permet de déduire la vitesse du champ de vorticité.

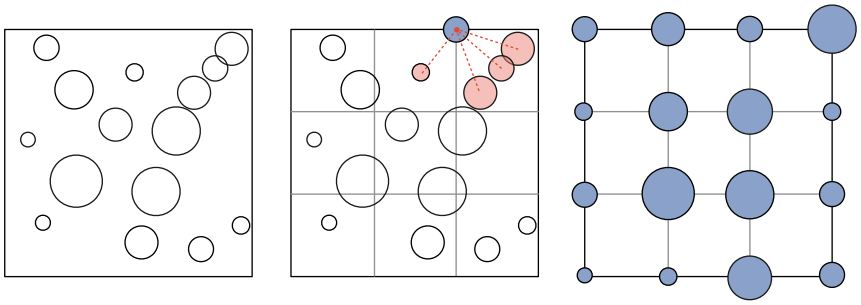

Figure 6.1: Illustration de la procédure de remaillage 2D. Les cercles vides représentent les particules avant remaillage et les cercles bleus les particules remaillées, la taille des cercles étant proportionnelle à l'intensité de la vorticité qu'ils transportent. Lors de l'étape de remaillage (figure du milieu), la vorticité en chaque point de la grille est calculé comme la somme des vorticités portés par les particules de la grille voisines, situées dans le support du noyau de remaillage, à l'aide de l'équation (6.8).

Les méthodes vortex sont des méthodes particulaires, c'est à dire que l'on adopte une vision lagrangienne du fluide où le champ de vorticité est discrétisé sur des particules numériques. En un point $\mathbf{x}$ du domaine et en un temps t, le champ de vorticité est discrétisé par

$$\boldsymbol{\omega}^h(\mathbf{x},t) = \sum_p \alpha_p^h \zeta_\varepsilon(\mathbf{x} - \mathbf{x}_p^h(t)). \tag{6.6}$$

où ζ_ε est une fonction lisse, à symétrie radiale et décroissance rapide qui converge vers la distribution de Dirac δ quand ε tend vers 0 et $\mathbf{x}_p^h$ est la position de la particule p donnée par

$$\frac{d\mathbf{x}_p^h}{dt} = \mathbf{u}^h(\mathbf{x}_p^h(t),t). \tag{6.7}$$

Remaillage

Un des inconvénients majeurs des approches purement lagrangiennes réside dans la perte de convergence de la méthode lorsque la distorsion du champ de particules devient trop importante (typiquement avec la raréfaction ou la concentration des particules dans certaines régions). Il est donc nécessaire de contrôler la distance entre deux particules. Une des manières de le faire est de remailler les particules, c'est à dire de les reprojeter régulièrement sur une grille sous-jacente, comme schématisé sur la figure 6.1. Pour ce faire on utilise des noyaux de remaillage, dans notre cas des fonctions polynomiales par morceaux, notées Λ, qui vérifient des propriétés de régularité et de conservation de moments. La vorticité au nœud j du maillage est alors définie comme la somme des valeurs pondérées de la vorticité portée par les particules p voisines

$$\boldsymbol{\omega}_j^{n+1}(x) = \sum_p \boldsymbol{\omega}_p^n(x) \Lambda\left(\frac{x_p^{n+1} - x_j}{\Delta x}\right). \tag{6.8}$$

Méthodes vortex hybrides pour les équations de Navier-Stokes incompressibles

Les méthodes vortex remaillées (MVR) [KL95, MM21] sont des méthodes semi-lagrangiennes, ou hybrides, caractérisées par l'utilisation d'approches lagrangiennes et eulériennes pour résoudre numériquement les équations de Navier-Stokes, permettant ainsi de bénéficier des avantages des deux approches. En effet, bien que les méthodes vortex soient par construction une approximation plus naturelle de l'écoulement et particulièrement adaptées à la simulation d'effets d'advection, elles rencontrent des difficultés pour représenter de manière efficace et précise les effets de diffusion; par ailleurs la résolution de l'équation de Poisson par la loi de Biot-Savart implique une complexité de calcul en $\mathcal{O}(N^2)$, avec N le nombre de particules. Le cadre eulérien nous permet donc d'utiliser des méthodes spectrales pour résoudre la diffusion et l'équation de Poisson. L'utilisation d'une grille facilite également l'implémentation de conditions aux bords et le couplage avec d'autres modèles.

Dans cette approche, basée sur un algorithme à pas fractionnaire, le problème est divisé en différentes étapes, résolues successivement au sein d'un pas de temps : l'advection est résolue sur les particules par la méthode vortex (lagrangienne) et le stretching, la diffusion et l'équation de Poisson sont résolues par des méthodes eulériennes (différences finies, méthodes spectrales) sur une grille cartésienne. L'étape de remaillage a donc une double fonction dans ce type d'approche : empêcher la distortion du champ de particules et servir de pont entre les deux approches. Par ailleurs, les méthodes vortex ont l'avantage d'offrir une condition de stabilité relaxée sur l'advection des particules comparée à une condition CFL classique. Le pas de temps adaptatif est ainsi défini par

$$\Delta t_{\text{adapt}} = \text{LCFL}/\|\nabla \mathbf{u}\|_\infty$$

où LCFL (pour Lagrangian CFL) doit être inférieur à 1.

HySoP

HySoP est un acronyme pour **Hy**brid **S**imulati**o**n using **P**articles. Il s'agit une bibliothèque Python interfacée avec du Fortran, OpenCl et C++ dédiée à la résolution des équations de Navier-Stokes avec la méthode vortex hybride. Développée depuis 2012, ses développement récents [Kec19] se sont concentrés sur son optimisation par l'utilisation du calcul hybride CPU/GPU et de graphes d'opérateurs orientés acycliques. Les méthodes numériques utilisées pour chaque étape de résolution dans les simulations de ce travail de thèse sont décrites dans le tableau 6.1.

Chapitre 2 : Modélisation des grandes échelles de la turbulence

Modèles de turbulence

Les écoulements turbulents sont caractérisés par un mélange de différentes échelles de tourbillons. Pour simuler de manière précise un écoulement turbulent il est essentiel de représenter toutes les échelles jusqu'à l'échelle dite de Kolmogorov où l'énergie se dissipe en chaleur. Résoudre ces écoulements par simulation numérique directe (ou Direct Numerical Simulation (DNS)) est en pratique très difficilement réalisable car trop coûteux numériquement.

Etapes de l'algorithme à pas fractionnaires		Intégration temporelle	Discretisation spatiale
1) Reprojection solénoïdale	$\Delta\boldsymbol{\omega} = \Delta\boldsymbol{\omega}^* - \nabla(\nabla \cdot \boldsymbol{\omega}^*)$	-	méthode spectrale (`FFTW`) (grille)
2) Équation de Poisson	$\Delta\mathbf{u} = -\nabla \times \boldsymbol{\omega}$	-	méthode spectrale (`FFTW`) (grille)
3) Diffusion	$\partial_t\boldsymbol{\omega} = \frac{1}{Re}\Delta\boldsymbol{\omega}$	Euler implicite	méthode spectrale (`FFTW`) (grille)
4) Advection-remaillage (directionnel)			
a) Advection	$\begin{cases} d_t\mathbf{x}_p & = \mathbf{u}(\mathbf{x}_p(t), t) \\ d_t\boldsymbol{\omega} & = 0 \end{cases}$	RK2	Lagrangien (particules)
b) Remaillage	$\boldsymbol{\omega}(\mathbf{x}) = \sum_p \boldsymbol{\omega}_p(\mathbf{x})\Lambda(\frac{\mathbf{x}_p - \mathbf{x}}{\Delta\mathbf{x}})$	-	noyau $\Lambda_{4,2}$ (particules vers grille)
5) Stretching (directionnel)	$\partial_t\boldsymbol{\omega} = (\boldsymbol{\omega} \cdot \nabla)\,\mathbf{u}$	RK3	DF centrées d'ordre 4
6) Pas de temps adaptatif	$\Delta t(t)$	-	DF centrées d'ordre 4

Table 6.1: Résumé de l'algorithme présentant les différentes étapes de la résolution des équations de Navier-Stokes dans la présente approche MVR.

Deux grandes familles de méthodes permettent de modéliser la turbulence : RANS et LES. Ces méthodes se basent sur les équations de Navier-Stokes à échelle séparées. Les champs sont décomposés en deux parties : $\boldsymbol{\omega} = \overline{\boldsymbol{\omega}} + \boldsymbol{\omega}'$ et $\mathbf{u} = \overline{\mathbf{u}} + \mathbf{u}'$. En RANS le terme $\overline{(\cdot)}$ représente la valeur moyenne du champ et le terme $(\cdot)'$ ses fluctuations. En LES, la partie $\overline{(\cdot)}$ représente les grandes échelles du champ qui sont séparées de la partie $(\cdot)'$, les petites échelles, via un filtre passe-bas.

Dans nos travaux, nous nous intéressons à la mise en œuvre d'approches de type LES, basées sur les équations de Navier-Stokes filtrées. En formulation vorticité-vitesse, ces équations s'écrivent

$$\frac{\partial\overline{\boldsymbol{\omega}}}{\partial t} + \nabla \cdot (\overline{\boldsymbol{\omega}} \otimes \overline{\mathbf{u}} - \overline{\mathbf{u}} \otimes \overline{\boldsymbol{\omega}}) = \nu\Delta\overline{\mathbf{u}} - \nabla \cdot \mathbf{R} \tag{6.9}$$

où $\overline{\mathbf{u}}$ et $\overline{\boldsymbol{\omega}}$ sont les grandes échelles des champs $\mathbf{u}$ et $\boldsymbol{\omega}$ et avec

$$\mathbf{R} = \underbrace{\overline{\boldsymbol{\omega} \otimes \mathbf{u}} - \overline{\boldsymbol{\omega}} \otimes \overline{\mathbf{u}}}_{advection} - \underbrace{\overline{\mathbf{u} \otimes \boldsymbol{\omega}} + \overline{\mathbf{u}} \otimes \overline{\boldsymbol{\omega}}}_{stretching} \tag{6.10}$$

le tenseur de sous-maille, qu'il faut modéliser.

Pour modéliser le tenseur de sous-maille, deux grandes familles de modèles existent [Sag06]:

- Les modèles de type **fonctionnels**, qui sont les premiers à être apparus avec le plus connu, celui de Smagorinsky [Sma63]: ces modèles cherchent à imiter le comportement de dissipation des petites échelles par l'ajout d'une viscosité artificielle.
- Les modèles de type **structurels**, qui cherchent à modéliser le tenseur de sous-maille en réalisant des développements mathématiques (de type développements en séries de Taylor) des filtres utilisés pour les grandes échelles. Un des modèles structurels les plus connus est le modèle de type "gradient". Bien que ces modèles soient plus précis dans des tests a priori, ils ne sont pas assez dissipatifs et demandent souvent des modifications (couplage avec un modèle fonctionnel, procédure de clipping...)

Les travaux sur les modèles de sous-mailles en vorticité-vitesse sont peu nombreux. On peut citer les modèles fonctionnels proposés par Winckelmans *et al.* [Win95, WLCW96] et Mansfield *et al.* [MKM98, MKM99], dans le cadre de méthodes purement Lagrangiennes, que l'on peut relier au modèle de Smagorinksy avec un coefficient dynamique [GPMC91, Lil92, GLMA95]. Plus récemment Cocle *et al.* [CDW07, CBW08, CBW09] ont travaillé, dans le cadre d'approches hybrides similaires à notre méthode, sur des modèles de type Variational Multi-Scale (VMS) [HMOW01] en prenant en compte les plus petites échelles des champs de vitesse et de vorticité. Enfin, on peut citer [TPDT05, HCY$^+$25] qui utilisent des modèles de sous-maille pour la résolution de Navier-Stokes en vorticité-vitesse par une approche purement Eulérienne.

Une approche différente est celle de Cottet *et al.* [Cot96, CJM03] qui propose un modèle structurel en deux dimensions en analysant l'erreur de troncature liée à l'approximation des champs de vorticité et de vitesse par la méthode vortex. Ce modèle se rapproche de modèles de type gradient (voir [Leo75a, CFR79, Vre95, ZSK93]) et a été utilisé dans le cadre de simulations de type "bilevel" [MCM18], où la vitesse et la vorticité sont résolues sur des grilles de tailles différentes avec une résolution grossière pour la vitesse et une résolution fine pour la vorticité. Ce modèle est anisotrope et est beaucoup moins diffusif que les modèles fonctionnels usuels. Récemment, Alvarez *et al.* [AN24] ont repris l'idée de Cottet pour développer un modèle de sous-maille dynamique afin de modéliser les effets de stretching dans le cadre d'une méthode purement lagrangienne. Cette méthode est peu diffusive, stable, précise et surtout très rapide comparée à une LES sur grille.

Enfin on peut citer l'approche de Kornev *et al.* [Kor17, KS19, SK19, KSD24], appelée VπLES, consistant à résoudre les grandes échelles de la turbulence sur une grille avec une approche eulérienne et les petites échelles sur des particules avec une méthode vortex purement lagrangienne. Cette méthode est basée sur le couplage de deux équations de transport, sur la grille et sur les particules, les deux communiquant en permanence. Cette approche montre une précision similaire à celle d'une LES classique avec un modèle de Smagorinsky sur une grille 10 fois plus fine.

Ce travail bibliographique s'est complété par des simulations numériques explorant plusieurs modèles adaptés au formalisme de la méthode vortex remaillée afin de trouver ceux les plus approprié à des LES précises et relativement peu coûteuses.

Modèles de viscosité artificielle

On rappelle ici l'expression des équations de Navier-Stokes filtrées en formulation vorticité-vitesse

$$\frac{\partial \overline{\boldsymbol{\omega}}}{\partial t} + \nabla \cdot (\overline{\boldsymbol{\omega}} \otimes \overline{\mathbf{u}} - \overline{\mathbf{u}} \otimes \overline{\boldsymbol{\omega}}) = \nu \Delta \overline{\mathbf{u}} - \nabla \cdot \mathbf{R}$$

D'après Winckelmans *et al.* [Win95, WLCW96] et Mansfield *et al.* [MKM98, MKM99], un modèle de type Smagorinsky pour cette formulation est obtenu en prenant le rotationnel de $\nabla \cdot \tau_{SGS}$ où τ_{SGS} représente la forme habituelle du tenseur de sous-maille en formulation vitesse-pression, ce qui donne

$$-\nabla \cdot \mathbf{R} \approx \nabla \times \nabla \cdot (\nu_{SGS}(\nabla \mathbf{u} + \nabla \mathbf{u}^T)) \approx -\nabla \times (\nu_{SGS} \nabla \times \overline{\boldsymbol{\omega}}) = \nabla \cdot (\nu_{SGS}(\nabla \overline{\boldsymbol{\omega}} - \nabla \overline{\boldsymbol{\omega}}^T)) \quad (6.11)$$

et donc :

$$\mathbf{R} \approx -\nu_{SGS}(\nabla \overline{\boldsymbol{\omega}} - \nabla \overline{\boldsymbol{\omega}}^T) \quad (6.12)$$

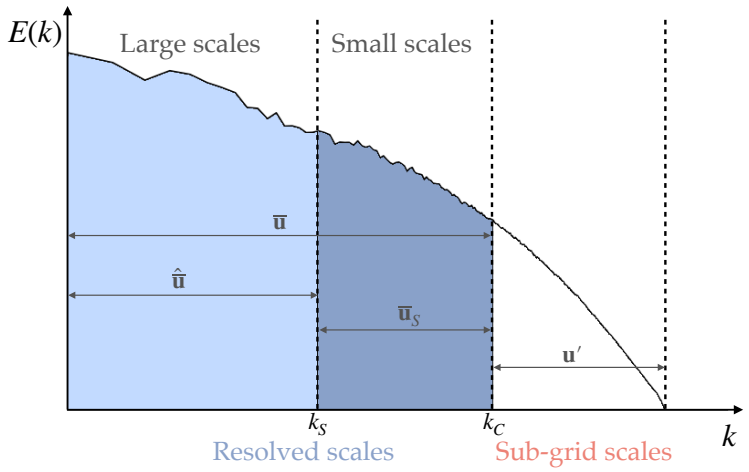

Figure 6.2: Utilisation des plus petites des échelles résolues dans le modèle de sous-maille

avec la viscosité artificielle ν_{SGS} donnée par

$$\nu_{SGS} = (C_S\Delta)^2|\mathbf{S}| \tag{6.13}$$

où C_S est un coefficient à choisir, $\mathbf{S} = \frac{1}{2}(\nabla\overline{\mathbf{u}} + \nabla\overline{\mathbf{u}}^T)$ et $\sqrt{2\mathbf{S}_{ij}\mathbf{S}_{ij}}$ est la magnitude du tenseur S.

Le modèle de Smagorinsky étant connu pour être trop dissipatif, plusieurs stratégies pour l'améliorer sont possibles. Une possibilité est, comme l'ont déjà fait Cocle *et al.* [CDW07, CBW08, CBW09] d'après une méthode de Hughes *et al.* [HMOW01], de se concentrer sur les petites échelles (résolues) de l'écoulement, représentées en bleu foncé sur la figure 6.2. On note $\overline{\boldsymbol{\omega}}_S$ les plus petites échelles du champ de vorticité résolu. Le modèle de Smagorinsky en version VMS (et antisymétrique) devient alors

$$\mathbf{R} \approx -\nu_{SGS}(\nabla\overline{\boldsymbol{\omega}}_S - \nabla\overline{\boldsymbol{\omega}}_S^T) \tag{6.14}$$

Modèles structurels adaptés à la formulation vorticité-vitesse

Comme expliqué précédemment, une autre approche pour un modèle de turbulence est un modèle de type structurel, cherchant à approcher directement le tenseur de sous-maille, comme le modèle de gradient, basé sur un développement de Taylor:

$$\mathbf{R}_g(i,j) = \frac{\bar{\Delta}^2}{12}(\partial_k\overline{\boldsymbol{\omega}}_i\partial_k\overline{\mathbf{u}}_j - \partial_k\overline{\boldsymbol{\omega}}_j\partial_k\overline{\mathbf{u}}_i) \tag{6.15}$$

Ce modèle est connu pour ses bonnes performances dans des tests a priori et présente un faible coût mais surrestime les effets de backscatter, il doit donc être adapté, avec une procédure de clipping comme celle proposée ici

$$\mathbf{R}_g^{clip}(i,j) = \frac{\bar{\Delta}^2}{12}(\partial_k\overline{\boldsymbol{\omega}}_i\partial_k\overline{\mathbf{u}}_j - \partial_k\overline{\boldsymbol{\omega}}_j\partial_k\overline{\mathbf{u}}_i) \times \begin{cases} 1 & \text{si } \mathbf{R}_g(i,j)\Omega_{ij} < 0 \\ -1 & \text{sinon.} \end{cases} \tag{6.16}$$

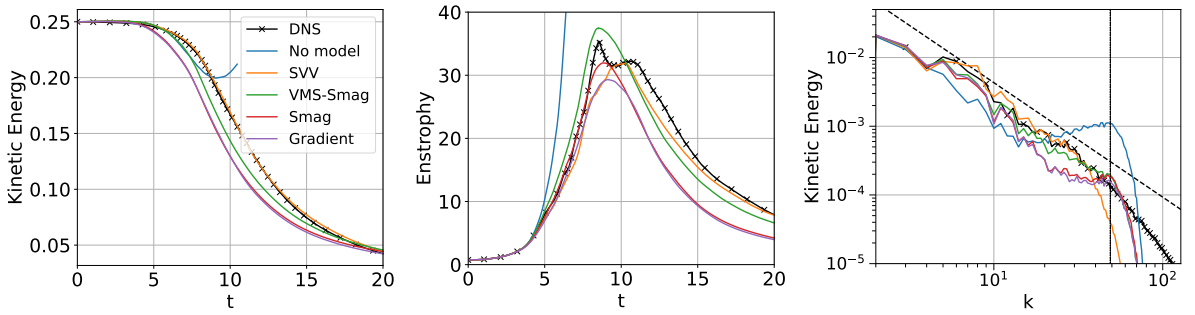

(a) (b) (c)

Figure 6.3: Évolution temporelle de (a) l'énergie cinétique, (b) l'enstrophie et (c) le spectre d'énergie cinétique à $t = 8,5$ pour le TGV avec $Re = 5000$ et $N_{LES} = 96$. Comparaison avec une DNS de résolution 768^3 (filtrée pour (a) et (b)).

avec $\Omega_{ij} = \frac{1}{2}(\partial_j \overline{\boldsymbol{\omega}}_i - \partial_i \overline{\boldsymbol{\omega}}_j)$. Dans cette première approche simple de clipping, on regarde les endroits où le modèle entraîne un transfert d'énergie des petites aux grandes échelles : en vitesse-pression, on peut montrer que ce sont les directions où $\tau_{ij} S_{ij} > 0$ (voir Piomelli et al [PCML91]). En vorticité-vitesse, en considerant les directions de production d'enstrophie, $R_{ij}\Omega_{ij}$ semble être l'équivalent de cet indicateur. Des approches plus sophistiquées existent bien sûr, voir [LPA13, VBC16] par exemple.

Chapitre 3 : Cas tests homogènes isotropes

Comparaison sur le cas test de Taylor-Green

Le tourbillon de Taylor-Green est un des cas test les plus simples de développement de turbulence à partir de conditions initiales simples. Le domaine est un cube de côté 2π aux bords périodiques. Les conditions initiales sont données par

$$\boldsymbol{\omega}(x, y, z, t = 0) = \begin{pmatrix} -\cos(x)\sin(y)\sin(z) \\ -\sin(x)\cos(y)\sin(z) \\ 2\sin(x)\sin(y)\cos(z) \end{pmatrix} \tag{6.17}$$

Ce cas a été testé pour plusieurs nombres de Reynolds : $Re = 1600, 3000$ et 5000. On présente ici les résultats pour $Re = 5000$ avec une résolution de 96^3 pour les simulations LES; ce choix permet de mettre en évidence l'intérêt d'un modèle de sous-mailles, cette résolution étant trop grossière pour permettre de résoudre les plus petites échelles de l'écoulement.

La figure 6.3 présente l'évolution de l'énergie cinétique, de l'enstrophie $\frac{1}{2}\int_\Omega \|\boldsymbol{\omega}\|^2 d\mathbf{x}$ au cours du temps et un spectre d'énergie à $t = 8$ pour les différents modèles LES présentés précédemment. L'enstrophie est comparée à l'enstrophie calculée à partir des plus grandes échelles (96^3) d'une DNS en résolution 768^3. On note que les modèles étudiés améliorent grandement la solution comparés à une LES sans modèle, et permettent de se rapprocher des résultats obtenus en DNS.

On remarque que le modèle le plus précis est le modèle VMS-Smag, appliqué aux petites échelles de la vorticité. Par ailleurs, le modèle de gradient, qui diffère des trois autres par sa construction, présente de bons résultats sur la première partie de l'écoulement (cascade énergétique et pic de dissipation).

Modélisation de la turbulence avec SVV

Ls méthodes de régularisation de type SVV (spectral vanishing viscosity) deviennent de plus en plus populaires comme alternatives aux modèles de sous-mailles classiques [DLLV17, WWXS21, FDLS21], en particulier dans les méthodes spectrales. Notre code résolvant la diffusion de la vorticité avec une méthode spectrale et de précédents tests ayant montré l'avantage des méthodes se concentrant sur les plus petites échelles des échelles résolues de la vorticité (celles où l'enstrophie est la plus importante dans un écoulement turbulent), il est donc naturel d'intégrer de telles approches dans notre code, qui permettent une modélisation précise des écoulements turbulents à bas coût. Bien que ces méthodes sont souvent considérées comme des méthodes implicites, elles nécessite en réalité un terme supplémentaire, généralement intégré dans l'opérateur de diffusion.

La SVV a été introduite en premier par [Tad89, MT89] afin de régulariser des problèmes hyperboliques résolus par des méthodes spectrales. Elles ont ensuite été utilisées pour des LES de Navier-Stokes [KK00, KK02, KS06].

L'idée de la SVV est d'ajouter progressivement de la viscosité artificielle à la fin du spectre résolu, là où des oscillations non-physiques apparaissent. Les plus grandes échelles ne sont donc pas affectée, ce qui rend cette approche similaire en pratique à notre modèle VMS-Smag (qui est lui appliqué dans l'espace physique).
Dans l'espace de Fourier, on écrit

$$\partial_t \hat{\boldsymbol{\omega}} = -(k_x^2(\nu + \nu_S(k_x)) + k_y^2(\nu + \nu_S(k_y)) + k_z^2(\nu + \nu_S(k_z)))\hat{\boldsymbol{\omega}} \tag{6.18}$$

avec

$$\nu_s(k) = \begin{cases} 0 & \text{if } k < k_m \\ \nu_0 \exp\left[-\left(\frac{k_c - k}{k_m - k} \right)^2 \right] & \text{if } k_m \leq k \leq k_c \end{cases} \tag{6.19}$$

Généralement, on prend ν_0 proportionnel à $1/k_c$, ce qui signifie que la viscosité artificielle devient négligeable quand la résolution de la simulation augmente.

Quantification des incertitudes avec le chaos polynomial

Pour étudier la sensibilité de nos modèles à leur paramètres, nous avons utilisé la méthode d'extension par chaos polynomial (PCE). L'idée de cette méthode est de considérer les paramètres de notre modèle comme des variables aléatoires. On choisit une base de polynômes $\{\Psi_p\}$ et écrit la surface de réponse (une quantité u dépendant du vecteur de paramètres $\mathbf{y}$ à évaluer) comme

$$u(\mathbf{y}) = \sum \hat{u}_p \Psi_p(\mathbf{y}) \tag{6.20}$$

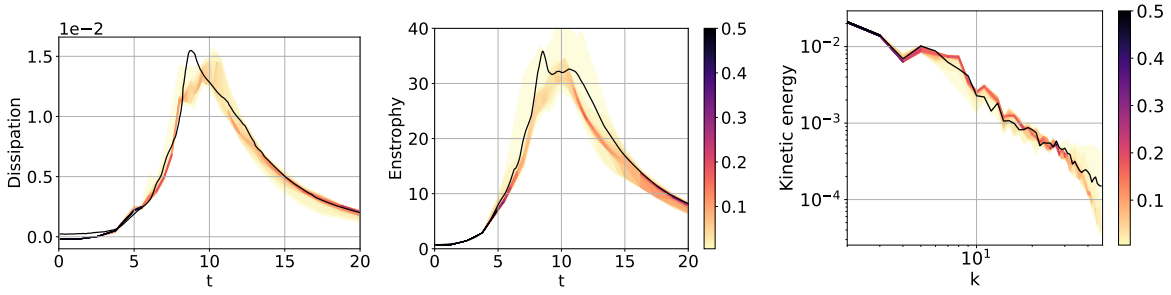

(a) (b) (c)

Figure 6.4: Analyse de sensibilité du modèle SVV sur le cas test TGV à $Re = 5000$ avec $N_{LES} = 96$. Fonctions de densité de probabilité pour l'évolution temporelle de la dissipation d'énergie cinétique (à gauche), de l'enstrophie (au milieu) et du spectre d'énergie cinétique à $t = 8.5$ (à droite). Comparaison avec un DNS de référence (courbe noire continue) : (a) DNS 1280^3 non filtré de [DLLV17], (b) DNS 768^3 filtrée et (c) DNS 768^3 non filtrée.

les coefficients $\hat{u}_p$ sont égaux à

$$\hat{u}_p = \int u(\mathbf{y})\Psi_p(\mathbf{y})dy \tag{6.21}$$

et sont calculés avec une méthode de quadrature à partir des valeurs $u(\mathbf{y})$ obtenues par des simulations avec des paramètres $\mathbf{y}$ discrets. Utiliser cette approximation permet de simplifier les analyses statistiques de la surface de réponse.

La méthode PCE est également utile pour optimiser les paramètres d'un modèle. En effet, en construisant une surface de réponse correspondant à l'erreur entre notre simulation et une référence, on peut interpoler les simulations réalisée et trouver un coefficient optimal pour un coût réduit. L'étude de sensibilité a été réalisée sur le cas test classique du tourbillon de Taylor Green à une résolution de 96^3 et un nombre de Reynolds $Re = 5000$.

Étude de paramètres pour la SVV

Pour harmoniser les résultats avec ceux du modèle VMS-Smag et avoir un filtre dépendant d'un paramètre continu, on modifie l'opérateur SVV en remplaçant le filtre par celui utilisé dans notre modèle VMS-Smag.

$$\nu_s(k) = \nu_0 \exp\left[-\left(\frac{k_c - k}{k_m - k}\right)^2\right](1 - \mathcal{G}^n(k)) \tag{6.22}$$

avec $\mathcal{G}^n(k) = (1 - \sin^{2n}(k/2))$.

On choisit aussi d'étudier des viscosités ν_0 de la forme $\nu_0 = \frac{c}{k_c}$, où k_c est le nombre d'onde à la coupure et c un coefficient à déterminer. On fixe $k_m = 0.3k_c$. Les deux paramètres explorés dans l'étude sont donc c et n. La bibliothèque Dakota est utilisée. Cette première étude (figure 6.4) montre la faible sensibilité du modèle à l'ordre du filtre et que les plus petites valeurs de viscosités sont les plus adaptées.

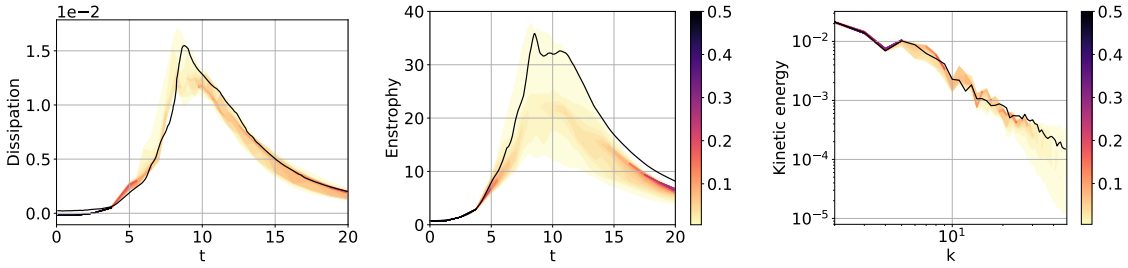

(a) (b) (c)

Figure 6.5: Analyse de sensibilité du modèle VMS-Smag sur le cas test TGV à $Re = 5000$ avec $N_{LES} = 96$. Fonctions de densité de probabilité pour l'évolution temporelle de la dissipation d'énergie cinétique (à gauche), de l'enstrophie (au milieu) et du spectre d'énergie cinétique à $t = 8.5$ (à droite). Comparaison avec un DNS de référence (courbe noire continue) : (a) DNS 1280^3 non filtré de [DLLV17], (b) DNS 768^3 filtrée et (c) DNS 768^3 non filtrée.

Etude de paramètre pour VMS-Smag

On rappelle l'expression du modèle VMS-Smag (qui est le modèle de Smagorinsky appliqué aux plus petites des échelles résolues) :

$$\mathbf{R}_{SGS} = -\nu_{SGS}(\nabla\overline{\boldsymbol{\omega}}_S - (\nabla\overline{\boldsymbol{\omega}}_S)^T) \tag{6.23}$$

avec $\nu_{SGS} = (C_S\Delta)^2|\mathbf{S}|$ et où $\mathbf{S} = \frac{1}{2}(\nabla\mathbf{u} + (\nabla\mathbf{u})^T)$ et C_S et un coefficient à déterminer. Les petites échelles de la vorticité sont filtrées avec le filtre $\mathcal{G}^n(k)$ défini plus haut. Les paramètres dont dépend le modèle qui seront étudiés sont donc n et C_S. L'étude du modèle montre une plus grande dispersion des résultats des simulations et donc une plus grande sensibilité aux paramètres. Les surfaces de réponse montrent que le coefficient optimal n'est pas le même selon la quantité évaluée (voir figure 6.5).

Simulations avec les coefficients optimaux

Les simulations avec coefficients obtenus (on prend $C_{SVV} = 0.09$ et $n = 6$ pour SVV et $C_S = 0.41$ et $n = 6$ pour VMS-Smag) donnent de bons résultats sur le cas test du tourbillon de Taylor-Green sur plusieurs Reynolds et résolutions (figure 6.6).

Chapitre 4 : Cas test avec parois

Ecoulement sur des collines

Un premier cas test avec parois consiste en un écoulement dans un canal sur un profil de collines comme montré en figure 6.7. Des conditions périodiques sont imposées en entrée et en sortie du domaine ainsi que sur les côtés. Des parois solides sont imposées au-dessus et en-dessous du domaine. Il s'agit d'un cas de référence bien connu introduit par [MFR00] qui a été étudié à la fois en DNS, LES et expérimentalement sur une variété de nombres de Reynolds

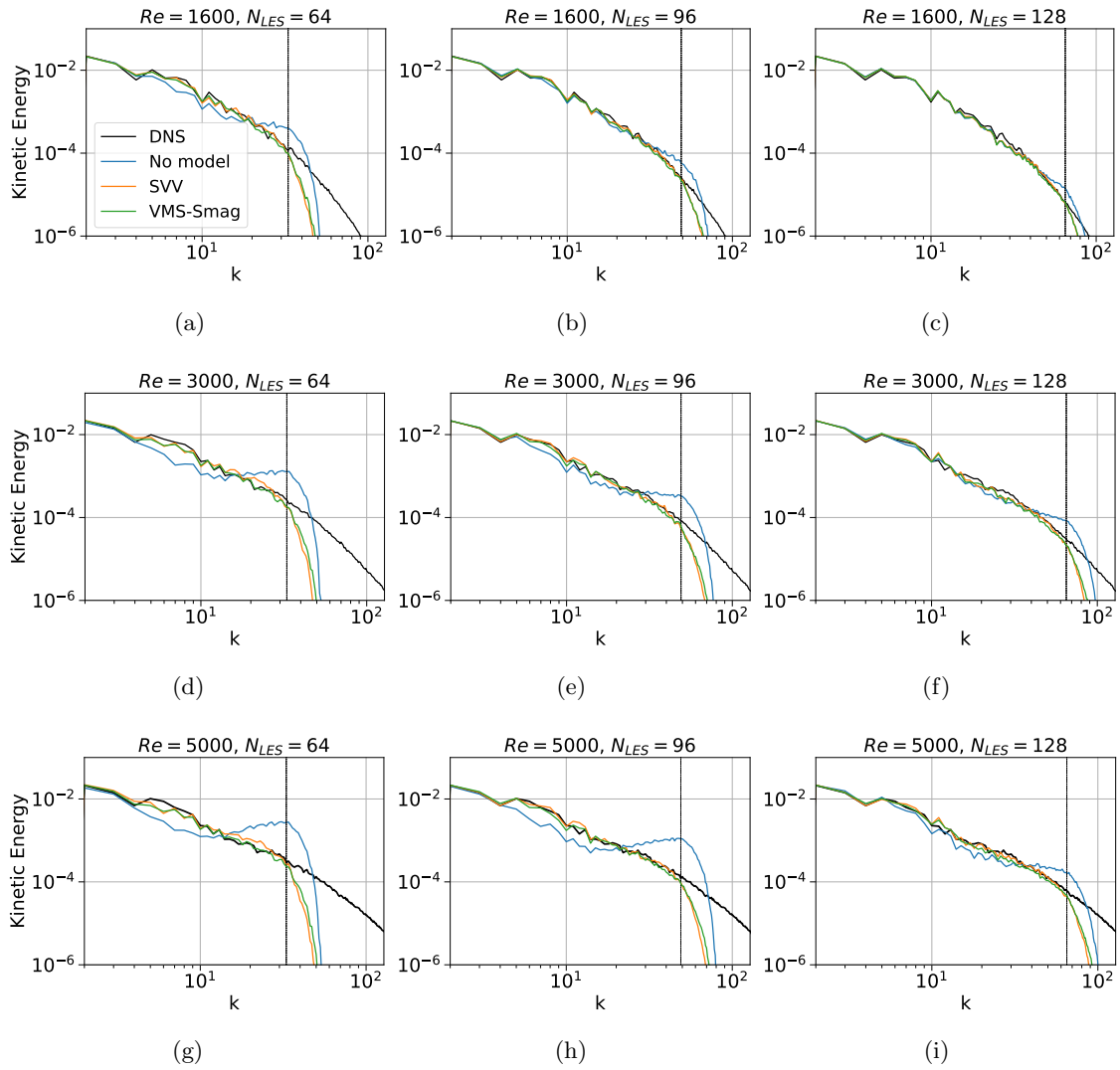

Figure 6.6: Spectre d'énergie cinétique à $t = 8,5$ pour TGV, comparaison avec une DNS de résolution (a)-(c) 512^3, (d)-(i) 768^3. La quantification des incertitudes a été réalisée sur le cas (h).

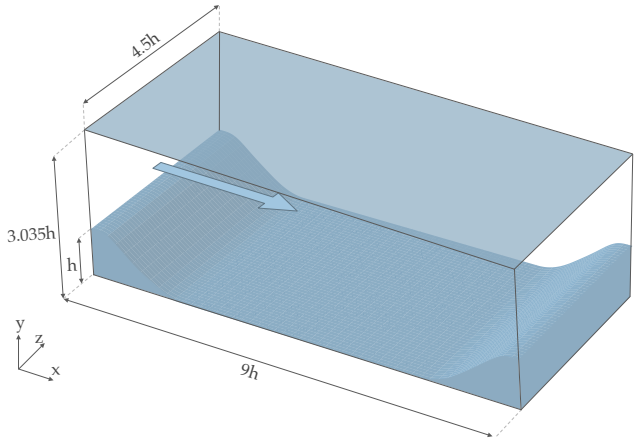

Figure 6.7: Configuration du cas test de l'écoulement sur des collines periodiques.

[BPRM09]. La turbulence se développe rapidement avec la séparation de la couche limite au niveau de la première colline, ce qui rend ce cas test simple à implémenter. La taille du domaine est de $4.5h \times 3h \times 9h$ où h est la hauteur du relief, les conditions aux bords sont périodiques dans la direction de l'écoulement et dans la largeur. Le nombre de Reynolds est basé sur h et U_b, la vitesse moyenne au sommet de la colline. Nous étudions les cas $Re = 2800$ et $Re = 10595$. Les conditions de non-glissement sur les parois solides du canal (paroi supérieure plane et paroi inférieure au profil de collines) sont traitées avec une méthode de pénalisation de Brinkman à l'ordre 1 [Cal94, ABF99, KG01, CC08a].

DNS avec Re=2800

Nous considerons quatre grilles ayant les mêmes proportions, avec une résolution dans la direction de l'écoulement du fluide et dans la direction de la largeur étant respectivement deux fois et trois fois plus faible que dans la direction verticale, $G : N_{vert} \times N_{stream} \times N_{span}$: G_1 : $252 \times 168 \times 84$, $G_2 : 288 \times 192 \times 96$, $G_3 : 384 \times 256 \times 128$ et $G_4 : 512 \times 342 \times 170$.

Les quantités étudiées sont la vitesse et les stress de Reynolds moyennés dans la largeur et en temps à partir de $T_{start} = 20$ passages et pour $\Delta T_{av} = 60$ passages. Les résultats sont comparés avec la DNS de Breuer et al. [BPRM09] dans les figure 6.8 et 6.9. Notre simulation est désavantagée par la grille cartésienne uniforme imposée par notre code, cependant, même à une résolution grossière les résultats sont proches de la référence, avec un comportement proche des parois solides correctement reproduit.

LES avec Re=10595

Pour le cas $Re = 10595$, nous testons nos modèles de sous-maille sur une grille de taille $128 \times 256 \times 128$. Les figures 6.10 et 6.11 montre les profils de vitesse et de stress de Reynolds pour les modèles WALE, VMS-WALE, VMS-Smag et SVV, où l'on applique pour les modèles VMS-Smag et SVV les paramètres (i.e. coefficient et ordre du filtre) calibrés précédemment sur le cas test du Taylor-Green Vortex (TGV). Les résultats sont comparés avec trois références issues de la litérature : une DNS de Krank *et al.*[KKW18], une LES de Breuer *et al.* [BPRM09] et des données expérimentales de Rapp and Manhart [RM11]. Comme pour le cas test du TGV, les

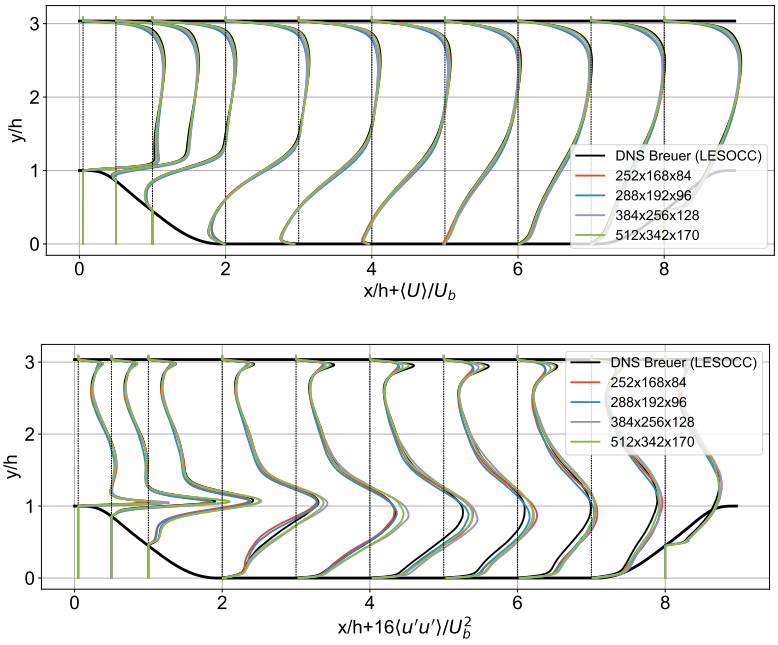

Figure 6.8: Profils moyennés de la vitesse dans le sens de l'écoulement ($\langle U \rangle / U_b$) et de contrainte de Reynolds normale ($\langle u'u' \rangle / U_b^2$) pour les différentes résolutions de grille utilisées dans la DNS de l'écoulement sur des collines périodiques à $Re = 2800$, comparaison avec [BPRM09].

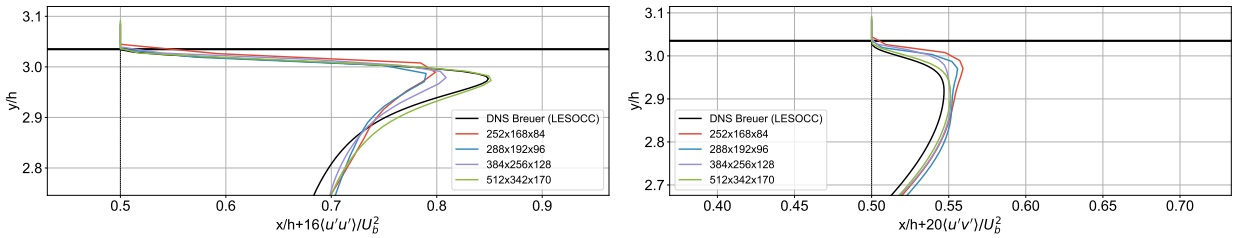

Figure 6.9: Vues rapprochées des profils $\langle u'u' \rangle / U_b$ (à gauche) et $\langle u'v' \rangle / U_b$ (à droite) à $x/h = 0,5$ pour les différentes résolutions de grille utilisées dans la DNS de l'écoulement sur des collines périodiques à $Re = 2800$, comparaison avec [BPRM09].

modèles sélectionnant les petites échelles de la vorticité performent mieux qu'un modèle WALE qui agit sur toutes les échelles résolues et est trop dissipatif. Les paramètres calibrés sur TGV semblent être adéquats pour ce nouveau cas test très différent, mais en comparant la longueur de la bulle de recirculation le modèle VMS-Smag s'avère plus précis : cette longueur est en effet de 4.51 avec VMS-Smag en accordance avec la littérature [KKW18] mais seulement de 3.89 avec SVV. Cela est également en conformité avec nos résultats précédents qui montraient que la calibration des coefficients de VMS-Smag était plus robuste que celle de SVV, les coefficients

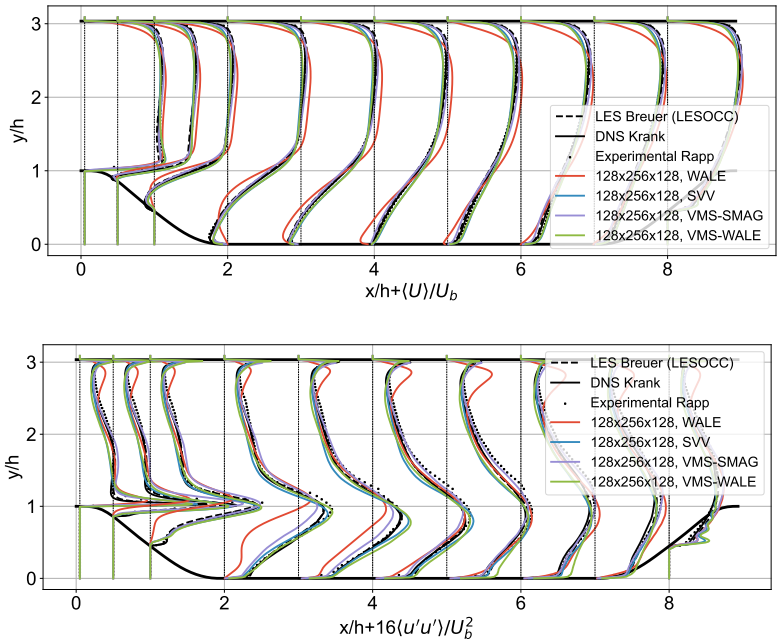

Figure 6.10: Profils moyennés de la vitesse dans le sens de l'écoulement ($\langle U \rangle / U_b$) et de contrainte de Reynolds normale ($\langle u'u' \rangle / U_b^2$) pour les différents modèles utilisés dans la LES de l'écoulement sur des collines périodiques à $Re = 10595$, comparaison avec [BPRM09, KKW18, RM11].

optimaux pour VMS-Smag étant les mêmes pour les deux cas tests précédemment étudiés (TGV et THI).

Quantification des incertitudes pour l'écoulement autour d'une sphere

Enfin, nous considérons un autre écoulement avec parois : le cas d'un écoulement autour d'une sphère à $Re = 3700$. La même procédure de quantification des incertitudes est effectuée sur le modèle VMS-Smag, qui s'est révélé le plus performant sur le cas test des collines périodiques, et sur sa sensibilité au coefficient du modèle C_S^2 et à l'ordre du filtre à petite échelle n. La figure 6.12 présente l'analyse de sensibilité du modèle VMS-Smag avec une résolution $320 \times 128 \times 128$. Les quantités d'intérêt ici sont les spectres d'énergie des fluctuation de la vitesse radiale à $r/D = 0,6$ et $x/D = 1$ et $x/D = 3$, comparée à [RLBO13].

Le premier spectre (à gauche), évalué près de la sphère à $r/D = 0,6$ et $x/D = 1$, représente les instabilités dans la couche de cisaillement. Cette région étant très instable, les LES sont très sensibles aux coefficients de leur modèle et présentent une grande variance sur la plupart des fréquences. Le second spectre (à droite), quant à lui, est évalué plus en aval à $r/D = 0,6$ et $x/D = 3$, où la turbulence est plus développée comme le montre la loi -5/3 dans le domaine inertiel. Les LES sont moins sensibles dans cette zone et recouvrent la plus grande échelle de la turbulence, avec une baisse d'amplitude, en particulier aux fréquences les plus élevées.

Enfin, nous essayons d'utiliser notre procédure de quantification de l'incertitude pour trouver un coefficient optimal la modélisation avec VMS-Smag de l'écoulement autour d'une sphère à

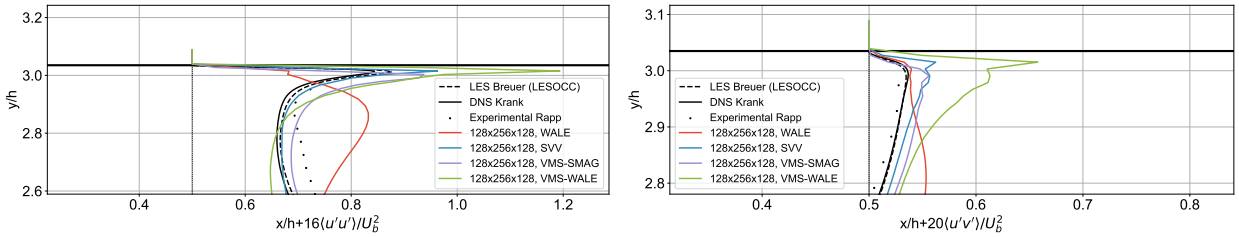

Figure 6.11: Vues rapprochées des profils $\langle u'u' \rangle / U_b$ (à gauche) et $\langle u'v' \rangle / U_b$ (à droite) à $x/h = 0,5$ pour les différents modèles utilisés dans la LES de l'écoulement sur des collines périodiques à $Re = 10595$, comparaison avec [BPRM09, KKW18, RM11].

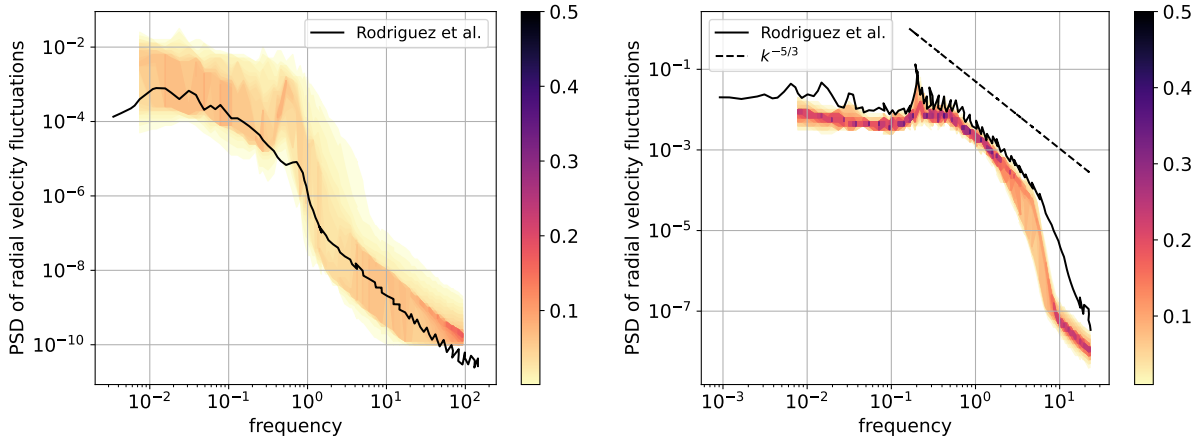

Figure 6.12: Fonctions de densité de probabilité pour les spectres d'énergie des fluctuations de vitesse radiale à $r/D = 0,6$ et $x/D = 1$ (à gauche) et $x/D = 3$ (à droite) pour les simulations VMS-Smag de l'écoulement autour d'une sphère avec $Re = 3700$ et une résolution de $320 \times 128 \times 128$. Comparaison avec [RLBO13].

$Re = 3700$. Nous prenons $C_S^2 = 0,7$ et $n = 4$ comme le meilleur compromis entre les deux spectres. Trois simulations avec ces coefficients ont ensuite été réalisées à des résolutions de $240 \times 96 \times 96$, $320 \times 128 \times 128$ (à laquelle l'UQ a été réalisée) et $640 \times 256 \times 256$. La figure 6.13 présente les spectres d'énergie des fluctuations de vitesse radiale de l'écoulement pour les trois résolutions considérées. Sur le premier spectre, la simulation avec une résolution de $320 \times 128 \times 128$ est la plus performante. La fréquence Kelvin-Helmholtz à plus haute résolution semble mieux alignée avec la référence, mais le spectre est décalé vers le haut, révélant une amplitude de fluctuations trop élevée. Ceci nous amène à conclure que les fluctuations de la couche de cisaillement sont très sensibles à la résolution de la grille. En revanche, le spectre de droite, correspondant à un point plus en aval de la sphère est mieux représenté par la simulation à plus haute résolution.

La calibration n'est donc pas entièrement robuste à un changement de résolution, contraire-

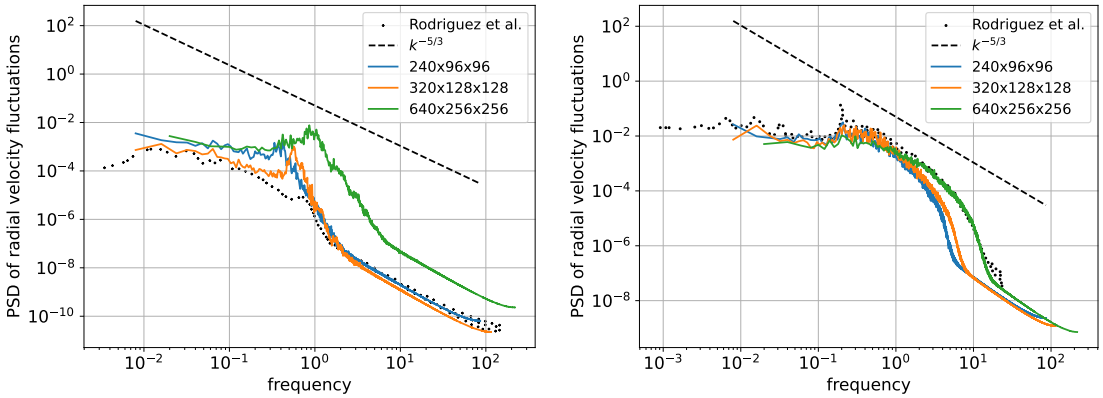

Figure 6.13: Spectres d'énergie des fluctuations de vitesse radiale à $r/D = 0,6$ et $x/D = 1$ (à gauche) et $x/D = 3$ (à droite) pour les simulations VMS-Smag de l'écoulement autour d'une sphère avec $Re = 3700$ et differentes resolutions avec $C_S^2 = 0.7$ et $n = 4$. Comparaison avec [RLBO13].

ment aux cas tests TGV et THI précédents, à l'exception des fluctuations dans les régions plus en aval de la sphère. Cela est dû à la grille cartésienne uniforme, qui est trop grossière pour résoudre correctement la couche limite à un tel Re et les effets de cisaillement près de la surface de la sphère.

Conclusion

Une étude approfondie de divers modèles sous-maille a été menée dans des simulations aux grandes échelles à l'aide d'une méthode vortex remaillée, motivée par le fait que l'impact de la modélisation de sous-maille en LES avec RVM a été beaucoup moins exploré que pour les formulations classiques basées sur la vitesse. De plus, un avantage clé du RVM est sa faible diffusivité, grâce au traitement lagrangien de l'étape d'advection. Il est crucial que le modèle sous-maille adopté ne compromette pas cette caractéristique.

Une étude de la littérature et une étude comparative sur le tourbillon de Taylor-Green ont montré que l'application de modèles de viscosité artificielle uniquement aux plus petites échelles de vorticité permettait des simulations efficaces et précises. Deux modèles ont ensuite été sélectionnés. Comme ils dépendent tous deux de deux paramètres, une procédure de quantification de l'incertitude a été utilisée pour évaluer leur sensibilité à ces paramètres et trouver une configuration optimale. Les coefficients se sont révélés robustes à une variation de Reynolds et de résolution, et, dans le cas de VMS-Smag a donné d'assez bons résultats sur d'autres cas tests, y compris des cas plus complexes à parois. Enfin, un écoulement turbulent au-delà d'une sphère a été considéré. Cette fois, la quantification de l'incertitude était moins robuste et, bien que les résultats obtenus soient satisfaisants, compte tenu de la résolution très grossière utilisée, ils ne s'adaptaient pas bien à une augmentation de la résolution.

Globalement, le MVR combiné aux modèles VMS s'est avéré assez robuste, adapté aux écoulements transitionnels et hautement turbulents, isotropes et anisotropes, et capable de mod-

éliser des écoulements à parois avec des résolutions très grossières, comparativement aux données de la littérature. L'implémentation actuelle du MVR est cependant limitée aux grilles uniformes cartésiennes pour les opérateurs eulériens, ce qui complexifie notre procédure de quantification de l'incertitude pour les écoulements à parois, car les simulations sont impactées par la résolution grossière de la frontière solide.